Energie & Umwelt
Energy & Environment

374

Oxidation induced lifetime prediction for FCC

Ran Duan

Mitglied der Helmholtz-Gemeinschaft

JÜLICH
FORSCHUNGSZENTRUM

Prediction of Oxidation Induced Life Time for FCC Materials at High Temperature Operation

Ran Duan

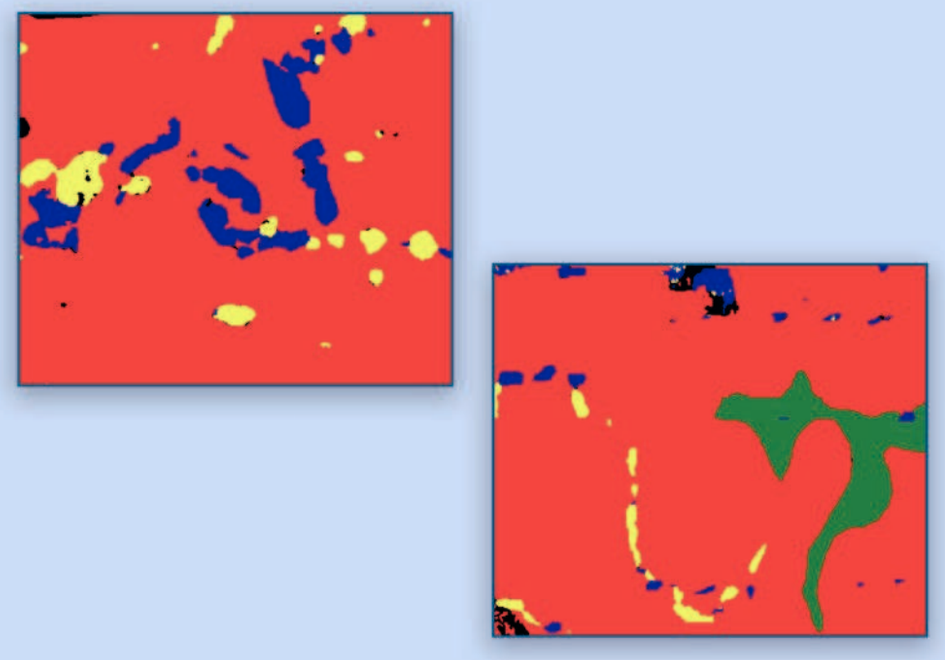

Energie & Umwelt /
Energy & Environment
Band / Volume 374
ISBN 978-3-95806-230-6

JÜLICH
FORSCHUNGSZENTRUM

Energie & Umwelt /
Energy & Environment
Band / Volume 374
ISBN 978-3-95806-230-6

JÜLICH
FORSCHUNGSZENTRUM

Schriften des Forschungszentrums Jülich
Reihe Energie & Umwelt / Energy & Environment Band / Volume 374

Forschungszentrum Jülich GmbH
Institute of Energy and Climate Research (IEK)
Microstructure and Properties of Materials (IEK-2)

Prediction of Oxidation Induced Life Time for FCC Materials at High Temperature Operation

Ran Duan

Schriften des Forschungszentrums Jülich
Reihe Energie & Umwelt / Energy & Environment Band / Volume 374

ISSN 1866-1793 ISBN 978-3-95806-230-6

Bibliographic information published by the Deutsche Nationalbibliothek.
The Deutsche Nationalbibliothek lists this publication in the Deutsche
Nationalbibliografie; detailed bibliographic data are available in the
Internet at http://dnb.d-nb.de.

Publisher and Distributor: Forschungszentrum Jülich GmbH
Zentralbibliothek
52425 Jülich
Tel: +49 2461 61-5368
Fax: +49 2461 61-6103
Email: zb-publikation@fz-juelich.de
www.fz-juelich.de/zb

Cover Design: Grafische Medien, Forschungszentrum Jülich GmbH

Printer: Grafische Medien, Forschungszentrum Jülich GmbH

Schriften des Forschungszentrums Jülich
Reihe Energie & Umwelt / Energy & Environment, Band / Volume 374

D 82 (Diss. RWTH Aachen University, 2016)

ISSN 1866-1793
ISBN 978-3-95806-230-6

The complete volume is freely available on the Internet on the Jülicher Open Access Server (JuSER)
at www.fz-juelich.de/zb/openaccess.

Acknowledgement

This doctoral thesis was written by me at the Institute of Energy and Climate Research, Microstructure and Properties (IEK-2), at the Forschungszentrum Jülich GmbH. I would like to express my gratitude to Prof. Dr. L. Singheiser from IEK-2 for the supervision of my work and his excellent support.

I would like to sincerely thank Dr. B. A. Pint from Oak Ridge National Laboratory (ORNL) for his support by exchanging experimental and for the fruitful discussions during the FZJ - ORNL workshops. The valuable comments on the results were essential for this thesis. I also express many thanks to the other colleagues at ORNL, especially K. Unocic, for a very successful cooperation.

I am very grateful to my scientific supervisor at IEK-2 Prof. Dr.-Ing. W. J. Quadakkers for his continuous excellent support during my work. Many of the very valuable discussions about the progress of the investigations were very helpful for interpreting my results and extensively broadened my technical knowledge. I would like to thank Dr.-Ing. P. Huczkowski for his daily support during my work, especially his patience and assistance with his scientific and experimental know-how. My sincere gratitude to Dr.-Ing. A. Jalowicka for carrying out part of the Thermocalc calculations and especially for her excellent assistance in the experimental work which let the project run fluently during my maternity leave.

This project would not have been possible without the support of my colleagues in carrying out oxidation experiments as well as the characterization of the materials: I would like to thank H. Cosler, R. Mahnke and A. Kick for carrying out the oxidation experiments, V. Gutzeit and J. Bartsch for metallographic investigations, Dr. E. Wessel and Dr. D. Grüner for SEM (with EDX and EBSD) analysis and Dr.-Ing. W. Nowak for GDOES measurements. Assistance with ICP-OES analysis provided by H. Lippert and V. Nischwitz from the Central Institute for Engineering, Electronics and Analytics, ZEA-3, at the Forschungszentrum Jülich GmbH is greatly appreciated. A special gratitude to Dr. A Chyrkin for carrying out the DICTRA calculations as well as his helpful discussions related to thermodynamics and kinetics of phase transformations. I am grateful to Dr. R. Pillai‟s advises in respect to MATLAB programming.

I express my sincere gratitude to all the other colleagues in the High Temperature Corrosion group: D. Naumenko, V. Shemet, J. Zurek, E. Hejrani, M. Schiek and T. Galiullin for assistance and fruitful discussions, nice concern and greetings during my pregnancy and maternity leave, and for a great time in the institute.

The continuous support and patience of my parents and my parents-in-law and especially my husband Mr. Pengfei Liu were essential for my successful work. Thanks to my lovely sons Alexander and William for bringing me motivation and hope in my life and work.

I would also like to acknowledge the “Bundesministerium für Bildung und Forschung” (BMBF) for the financial support of this work under Grant No. 03EK3032.

Publications and presentations

Part of the results presented in this thesis has already been published in the following articles and at the following conferences:

A. Jalowicka, R. Duan, P. Huczkowski, A. Chyrkin, D. Grüner, B. A. Pint, K. A. Unocic and W. J. Quadakkers, “Effect of Specimen Thickness on Microstructural Changes During Oxidation of the NiCrW Alloy 230 at 950-1050°C”, *JOM*, vol. 67, no. 11, pp. 2573-2587, 2015.

R. Duan, A. Jalowicka, P. Huczkowski, A. Chyrkin, D. Grüner, B. Pint, K. Unocic, W. J. Quadakkers, “Predicting Oxidation-Limited Lifetime of Thin-Walled Components of NiCrW Alloy 230”, *Oxidation of Metals*, vol. 87, no. 1, pp. 11-38, 2017.

Poster presentation at Gordon Conference High Temperature Corrosion, New London, NH, USA, 26 - 30 July 2015: A. Jalowicka, R. Duan, P. Huczkowski, A. Chyrkin, D. Grüner, B. A. Pint, K. A. Unocic, M. J. Lance, W. J. Quadakkers. “Effect of wall thickness on oxidation induced microstructural changes of Ni-Cr-W alloy 230 in the temperature range 950-1100°C”

Poster presentation at EUROCORR, Graz, Au, 7 - 11 September 2015: R. Duan, A. Jalowicka, P. Huczkowski, A. Chyrkin, D. Grüner, B. Pint, W. J. Quadakkers, “Prediction of oxidation induced lifetime limits of thin-walled components of Ni-based superalloys in the temperature range 950-1050°C”.

Abstract

With an increasing application of high temperature alloys, especially Ni-based superalloys in automobile and other industrial fields, the ability to predict components‟ lifetime becomes a predominant demand from both safety and energy consumption aspects. In the present investigation, an attempt was made to develop a generalized oxidation lifetime model for chromia-forming FCC alloys that can be incorporated into alloy data sheets and easily understood and employed by component designers. The model captures the most important damaging oxidation effects relevant for component design: wall thickness loss, scale spallation and the occurrence of “breakaway” oxidation. The material used for development of the concept was the wrought NiCrW base alloy 230.

For deriving modeling input parameters and for verification of the model approach, specimens of this alloy with different thicknesses were exposed cyclically for different times at temperatures in the range 950 - 1050°C in static laboratory air. The studies concentrated on thin specimens (thickness 0.2 - 0.5 mm) to obtain data for critical subscale depletion processes resulting in “breakaway” oxidation within reasonably achievable test times up to 3000 h. The oxidation kinetics and oxidation induced subscale microstructural changes from the long term tests were combined with results from thermogravimetric analyses (TGA), scanning electron microscopy (SEM) with energy dispersive x-ray (EDX) spectroscopy and electron backscatter diffraction (EBSD), as well as glow discharge optical emission spectroscopy (GDOES).

Oxidation induced microstructural changes as function of specimen thickness, time and temperature were estimated and modeled using the software packages Thermocalc and DICTRA. The modeling of the oxide scale spalling and re-formation was based on the cyclic oxidation spallation program (COSP), which was published previously. The program was modified to adapt the approach to the present experimental observations. A new model was developed to describe accelerated oxidation occurring after longer exposure times in case of the thinnest specimens. The calculated oxidation kinetics was correlated with the Cr reservoir equation, by means of which the relation between the consumption and the remained concentration of the scale forming element (Cr) in the alloys is established as a function of temperature and specimen thickness. The results obtained by the reservoir approach were compared with calculations of Cr concentration profiles using a finite difference model. Based on this approach, a generalized lifetime diagram is proposed in which wall thickness loss as function of time, specimen thickness and temperature as well as times to reaching a critical chromium subscale depletion are presented. The same approach was subsequently applied to the nickel base alloys X and NiCr 8020 as well as the austenitic steel Nicrofer 2020. Both Ni base alloys showed shorter times to critical subscale depletion than alloy 230; alloy X mainly due to higher scale growth rates, alloy NiCr 8020 due to poorer scale adherence and a lower initial Cr content. The austenitic steel showed the shortest lifetime mainly due to Mn and Ti induced high growth rates of the chromia scale and resulting low Cr interface concentrations.

Kurzfassung

Wegen des zunehmenden Einsatzes von Hochtemperaturwerkstoffen, insbesondere von Nickelbasislegierungen im Automobilbau und anderen industriellen Anwendungen, werden zuverlässige Modelle zur Lebensdauervorhersage von immer größerer Bedeutung. In der vorliegenden Arbeit wurde ein allgemein anwendbares Modell entwickelt, das die Vorhersage der oxidationsbedingten Lebensdauergrenzen von chromoxidbildenden kubisch flächenzentrierte (KFZ) Legierungen ermöglicht. Mit dem Modell sollte eine Darstellung zur Verfügung gestellt werden in dem Oxidationsschädigung nach standardisierten Verfahren quantitativ beschrieben wird und somit in Werkstoffdatenblätter aufgenommen werden kann. Es ist somit ein einfach anwendbares Tool für die Berücksichtigung von Oxidationsschädigung bei der Komponentenauslegung. Das Modell berücksichtigt die wichtigsten oxidationsbedingten Schädigungsmechanismen die für die Komponentenauslegung relevant sind, nämlich Wanddickenverlust, Deckschichtabplatzen und Auftreten von „Breakaway-Oxidation“. Für die Entwicklung des Modells wurde die wurde die NiCrW-Basislegierung 230 verwendet. Zur Ermittlung der Eingabeparameter für das Rechenmodell und zur Verifikation der Langzeitextrapolationen erfolgten zyklische Oxidationsversuche in ruhender Laborluft mit Proben unterschiedlicher Dicke im Temperaturbereich 950 - 1050°C. Um zu gewährleisten, dass kritische Chromverarmungen und somit „Breakaway-Oxidation“ innerhalb vertretbarer Versuchszeiten von maximal 3000h erreicht werden konnten, lag der Schwerpunkt der Untersuchungen bei dünnen Proben (Dicke 0.2 - 0.5 mm). Die Oxidationskinetik und die oxidationsbedingte Chromverarmung unterhalb der oxidischen Deckschichten wurden mittels Langzeitversuchen ermittelt. Die Resultate wurden mit Resultaten aus thermogravimetrischen Analysen (TGA), Glimmentladungsspektroskopie (GDOES), Raster-Elektronenmikroskopie (REM) mit energiedispersiver Röntgenanalyse (EDX) und Elektronenrückstreubeugung (EBSD) korreliert. Oxidationsbedingte Änderungen der Legierungsmikrostruktur als Funktion der Probendicke, Zeit und Temperatur wurden mit Hilfe der Softwarepakete Thermocalc und DICTRA modelliert. Die mathematische Beschreibung der Abplatzkinetik und nachfolgender Neubildung der oxidischen Deckschichten basierte auf dem früher publizierte Programm COSP. Letzteres wurde modifiziert zur Anpassung des mathematischen Ansatzes an die in der vorliegenden Arbeit gemachten experimentellen Beobachtungen. Zur Beschreibung der beschleunigten Oxidation die nach Langzeitauslagerung bei den dünnsten Proben (0.2 mm) auftrat, wurde ein neues mathematisches Modell entwickelt. Die berechnete Oxidationskinetik wurde mit dem Cr-Reservoir in der Legierung korreliert. Hierdurch erfolgte eine Beziehung zwischen Verbrauch und verbleibender Konzentration des schichtbildenden Legierungselementes (hier Cr) als Funktion von Zeit, Temperatur und Probendicke. Die mit diesem Reservoir-Ansatz ermittelten Ergebnisse wurden mit den Cr-Profilen, welche mittels eines Finite-Differenzen-Programms berechnet wurden, verglichen. Basierend auf diesen mathematischen Ansätzen wurde ein allgemein anwendbares Lebensdauerdiagramm erarbeitet, in dem Wanddickenverlust als Funktion von Zeit, Probendicke und Temperatur, sowie die Zeit bis zum Erreichen einer kritischen Chromkonzentration an der Grenzfläche Oxid/Legierung, dargestellt wird.

Der gleiche Ansatz wurde anschließend auf die Nickelbasislegierungen X und NiCr 8020 sowie den austenitischen Stahl Nicrofer 2020 angewendet. Beide Ni-Basislegierungen zeigten kürzere Zeiten bis zum Auftreten einer kritischen Chromverarmung als Legierung 230. Bei Legierung X war dies vorwiegend auf einer höheren Oxidwachstumsrate zurückzuführen. Bei NiCr 8020 auf die schlechtere Oxidhaftung und den geringeren Ausgangs-Cr-Gehalt der Legierung.

Der austenitische Stahl Nicrofer 2020 zeigte die kürzeste Lebensdauer der untersuchten Legierungen. Die wichtigste Ursache dafür waren die durch Mn und Ti induzierten höheren Wachstumsraten der Chromoxidschichten und die dadurch bedingten sehr niedrigen Cr-Konzentrationen an der Grenzfläche Oxidschicht/Legierung.

Content

1 Introduction

1.1 Current applications of high temperature superalloys

High-temperature alloys have been widely used in many industrial applications, including power generation, chemical plants, and engine technologies. In the family of high-temperature alloys, the superalloys are high performance nickel-, iron-nickel-, and cobalt-base alloys, which are used at temperatures above approximately 540°C due to an outstanding oxidation and creep resistance [1]. The group of iron-nickel-based superalloys is an extension of common stainless steels. From the viewpoint of oxidation resistance [2] an approximate indication of maximum application temperatures can be defined: austenitic stainless steels that form a Cr_2O_3 external scale during high temperature service may be applied as construction material up to 850°C, nickel-based Cr_2O_3 forming alloys up to about 950°C, while Ni-based Al_2O_3 forming alloys can be used even at temperatures as high as 1100°C. However, the actual applicable maximum operating temperatures depend on numerous parameters such as detailed alloy composition, service environment, required lifetime, component design, etc. The excellent high temperature strength makes nickel-based superalloys to be the ideal materials in the manufacture of gas turbine components used in both commercial and military aircraft, power generation, and marine propulsion. Other application fields include space vehicles, submarines, nuclear reactors, military electric motors, chemical processing vessels, and heat exchangers [3].

Due to the high oxidation and creep resistance of nickel-based superalloys, new jet engines perform more efficiently at higher temperatures, and their emission is also reduced as a result of a more complete combustion. **Figure 1.1** shows the application of nickel-based superalloys in the hot section of a jet engine. The superalloys are also widely used for thin-walled high temperature components such as micro heat exchangers for Solid Oxide Fuel Cell (SOFC) made by a nickel-based superalloy shown in **Figure 1.2**, here with a typical wall thickness of 0.3 mm.

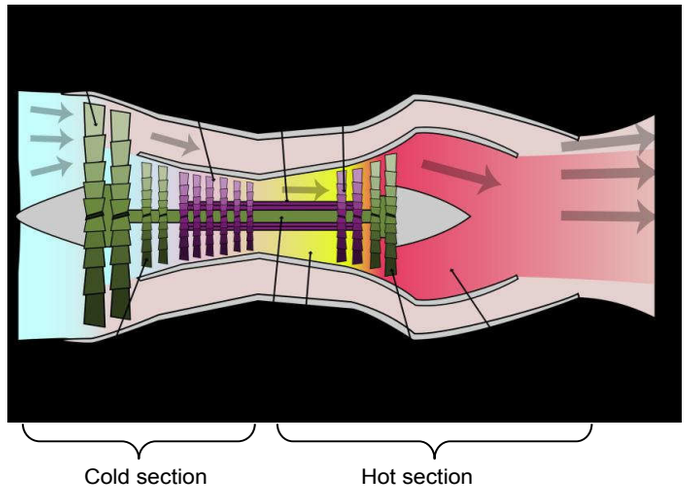

Figure 1.1: Schematic illustrating application of nickel-based superalloys as construction materials for various components, mostly in hot section of a jet engine [4].

Figure 1.2: Micro high temperature heat exchanger for SOFC system fabricated using NiCr-base alloy [5].

The use of nickel has increased over time and is correlated with the worldwide economic development. Although the main usage of nickel is nowadays the production of stainless steels, the consumption of nickel in producing superalloys is significantly growing. **Figure 1.3** illustrates the first use of nickel in 2011, where "first use" means the use of newly produced nickel. The usage of nickel in superalloys is included in the category of nonferrous

alloys. Following the category of plating, this category is becoming one of the most important application sectors for nickel and accounts for 8% of the total nickel use [4].

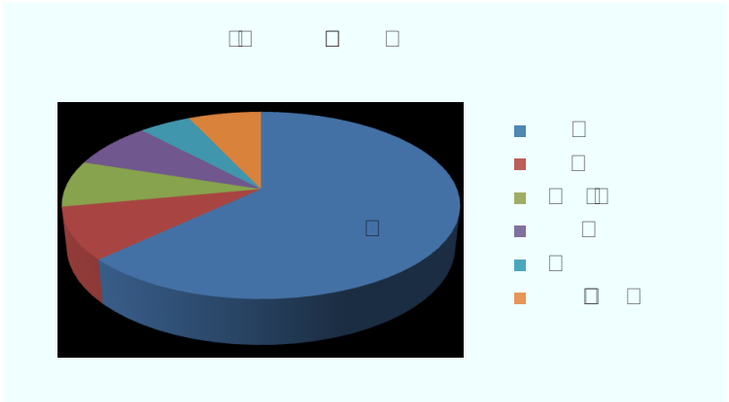

Figure 1.3: The world first use of nickel in 2011 [3].

1.2 Classification of high temperature superalloys

The nickel based alloys can be classified into wrought and cast alloys [1]. Wrought alloys are alloys, which are commonly forged or rolled to sheet or other semi-finished products. Higher alloyed, so-called cast nickel based alloys cannot be manufactured into semi-finished products by the standard methods described above and are therefore used in the as-cast condition. Among the cast alloys, special groups of materials are directionally solidified and single crystal superalloys. From the viewpoint of strengthening, the wrought alloys can be divided into solid-solution-strengthened and precipitation-strengthened alloys. In solid-solution-strengthened alloys, the alloying elements exist as substitutional or interstitial atoms in the base face centered cubic (FCC) lattice. In precipitation-strengthened alloys, a second phase, such as carbides of alloying elements, γ', γ'' or oxide precipitates in ODS (oxide-dispersive-strengthened) superalloys, is precipitated and/or dispersed at the grain boundaries in the alloy matrix [1]. **Table 1.1** lists selected typical wrought and cast supperalloys.

Table 1.1: Classification of typical iron-nickel- and nickel-base superalloys [1, 6]

	Alloys	**Nominal composition(in wt. %)**
Wrought alloys		
Solid-solution strengthened alloys:		
Iron-nickel-base	Haynes 556	21Ni-29Fe-22Cr-20Co-3Mo-2.5W
	Incoloy 800	32.5Ni-45.7Fe-21Cr
Nickel-base	Haynes 214	Ni-16Cr-4.5Al-3Fe
	Haynes 230	Ni-22Cr-14W-5Co-2Mo
	Haynes 617	Ni-22Cr-14.1Fe-12.5Co-9Mo-1.35Al
	Hastelloy X	Ni-22Cr-15.8Fe-9Mo-1.5Co
Pricipitation-hardening alloys:		
Iron-nickel-base	Incoloy 925	44Ni-29Fe-20.5Cr-2.8Mo-2.1Ti
Nickel-base	Astroloy	Ni-15Cr-15Co-5.25Mo-3.5Ti-4.4Al
	Haynes 242	Ni-8Cr-25Mo-2.5Co-2Fe
	Rene 41	Ni-19Cr-11Co-10Mo-3.1Ti-1.5Al
	Waspaloy	Ni-19.5Cr-13.5Co-4.3Mo-3Ti-1.4Al-2Fe
Cast alloys		
Nickel-base	Rene 80	Ni-14Cr-9.5Co-4Mo-5Ti-3Al
	Inconel 738	Ni-16Cr-8.5Co-1.95Mo-2.6W-3.4Al-3.4Ti
Directional solidified alloy	Siemet DS	Ni-12Cr-9Co-5Ta-1.9Mo-3.8W-3.6Al-4.2Ti
Single crystal alloy	CMSX-4	Ni-6.5Cr-9Co-1Ti-5.6Al-0.6Mo-6W-6.5Ta
	CMSX-6	Ni-10Cr-5Co-4.8Al-4.7Ti-3Mo-2Ta

1.3 Oxidation resistance of nickel base superalloys

Wrought nickel-base alloys combine properties that make them ideally suited for a wide variety of elevated temperature applications including the aerospace, power generation and chemical processing industry [6-8]. The high temperature creep resistance of this class of alloys mainly relies on solid solution strengthening by alloying additions such as Cr, Mo, Co and W as well as precipitation strengthening by carbides (e.g. $M_{23}C_6$ or M_6C), which form with C additions of ~0.05 - 0.1% [9, 10]. Depending on alloy composition, intermetallic phases also may contribute to the creep strength. Most wrought Ni-base alloys form slow-growing, protective chromia-base surface scales during high temperature exposures due to selective Cr oxidation [11, 12]. This scale formation is based on typical Cr contents of 20 - 25%. These alloys are therefore commonly termed chromia-formers, although other alloying

elements (e.g. Mn, Ti, Si, Al, Nb) participate in the oxide formation which may result in multiphase surface scales.

Investigation and quantification of oxidation resistance is commonly done by combining gravimetric results with data of a variety of characterization tools such as light and electron microscopy as well as surface analysis methods [11-14]. Weight changes are a measure of oxide growth kinetics during steady state scale growth as well as an indicator of scale spallation, mainly occurring as a result of thermal cycling [15]. The disadvantage of using the measured weight change data for characterization of the oxidation behavior is that these data do not provide information, which is directly usable in the design of high temperature components. For component design, more relevant oxidation induced damage processes are:

- Loss in wall thickness resulting in loss of load carrying cross section [16].

- Spallation of the scales especially occurring as a result of thermal stresses in combination with void formation/cracking in the scale during temperature cycling [14]. Spalled oxides may block narrow gas passages which may inhibit heat transfer and thus cause local overheating.

- Subsurface loss of Cr as a result of consumption by scale growth and re-healing after spallation. This process may eventually lead to a decrease of the Cr concentration at the alloy/scale interface to such a low level that the growth of the protective chromia scale can no longer be sustained. This leads to formation of other less protective oxide phases, which is frequently termed “breakaway oxidation” [17] and is often correlated with the end of component life.

1.4 Status of studies on lifetime prediction

Although it is widely known, that the oxidation resistance is an important characteristic of nickel-based superalloys, design relevant quantitative data related to oxidation resistance are hardly provided in data sheets of superalloys. The common information about oxidation resistance is usually presented by mentioning a maximum temperature at which safe application may be expected.

Considering the wide application of nickel-based superalloys in a variety of components used in both civil and military applications, the designer of the component should always stand in

the safe side. Therefore, the lifetime of the superalloy turns out to be a very important reference to the designer.

Apart from the above mentioned design relevant damage processes, oxidation may also result in microstructural changes, which affect mechanical properties. This is the result of changing the amount and distribution of precipitates in the component as a result of depletion of the scale forming element. It is obvious that depletion-induced processes will be more significant in thin- than in thick-walled components. For accurate modeling of long-term component lifetime, these oxidation-related damage processes must all be included.

In the literature, numerous papers give modeling approaches providing (semi-)quantitative descriptions of scale growth kinetics [12], scale spallation and healing [18-20] as well as predicting breakaway oxidation [21-24]. **Table 1.2** summarizes the existing models concerning oxidation behavior and/or lifetime prediction with their publication time and principles. However, no generally applicable quantitative model or standardized method has been established where the above mentioned damage mechanisms are all included. Additionally, alloy data sheets from manufacturers contain mostly qualitative descriptions of the relative oxidation behavior of a given alloy, e.g. providing a maximum operating temperature or presenting relative differences in oxidation behavior among a group of similar alloys. However, this information does not provide component designers with the quantitative data needed, for example, to specify the wall thickness of a heat exchanger for 25,000 h service at 900°C.

Table 1.2: Models concerning growth of protective oxide and lifetime limit of high-temperature alloys.

Model	Year of first publication	Principle
FZJ model [21,25-33]	1994	Estimation of Lifetime limit by equating the rate of element consumption with its supply in the bulk alloy
Multistage model [34]	2001	Development of FZJ model to account for different stages of the oxidation process
Whittle"s model [13,14,22,23][35-37]	1972	Solving the equation of Fick"s second law analytically to calculate depletion profiles during isothermal oxidation
FZJ concept [24]	2012	Estimation of lifetime limit of Cr_2O_3 forming nickel base alloys under isothermal oxidation based on Wittle"s model

Table 1.2 (continued).

Finite Differenc Method (FDM) [38-41]	1989	Use finite difference techniques to solve diffusion problem and predict depletion profiles
Tedmon"s model [42]	1966	Simulating weight change curve with paralinear kinetics of materials forming volatile oxide species
COREST [43]	1976	Computer program to calculate weight change of the materials forming volatile oxide species
Wajszel"s model [44]	1963	Simulating weight change curve considering volatile species
COSP [45-48]	1991	Cyclic oxidation spallation program: parabolic growth of oxide, iterative calculation
DICOSM [49]	2003	Deterministic interfacial cyclic oxide spallation model
p-Kp model [20,50,51]	2003	Cyclic oxidation spallation model using probability of spallation as model parameter

2 Aim of present study

In the present investigation an attempt is made to develop a generalized method for presenting oxidation induced damage of nickel base wrought alloys whereby the above mentioned, most important design relevant oxidation induced damage processes are being considered. Final aim of these studies would be, to provide a tool which allows incorporating quantitative information on oxidation induced damage processes in material data sheets, in a similar standard manner as is e. g. common for a number of physical and mechanical materials properties.

The material selected for the development of this approach is the commercial Cr_2O_3 forming Ni-base alloy 230 frequently used in high temperature service [52]. For deriving input data for the modeling and for verification of the developed model, oxide growth and spallation kinetics as well an occurrence of critical chromium depletion phenomena were studied during air oxidation in the temperature range 950-1050°C, using specimens of different thickness. Main emphasis was put on the behavior of thin walled components thus allowing the experimental detection of breakaway oxidation as function of oxidation temperature, within a reasonable time limit. The oxidation induced microstructural changes of the studied alloys are also discussed. The present study deals with static conditions, i.e. conditions where the formation of volatile chromium species is not of great importance.

Subsequently, the results of similar studies will be illustrated obtained for the commercial nickel base alloy X, a material which contains a substantial amount (approximately 18 wt. %) of iron. Then results of alloy 230 and X will be compared with those obtained for alloy NiCr 8020, i.e. a material which is close to a binary model NiCr alloy containing hardly any strengthening alloying additions. Finally, the results obtained for the three chromia forming nickel base alloys will be compared with those of a Fe-base material, i.e. the austenitic steel Nicrofer 2020.

3 Basics of oxidation

3.1 Thermodynamics of oxidation

The general oxidation reaction of a metal can be written as

□□□□□□□□□ (3.1)

From the second law of thermodynamics, the change of Gibbs free energy (G′) is a function of the reaction enthalpy and the entropy, expressed as [2, 53]

□′=□′-T□′ (3.2)

where H′ is the enthalpy, T the temperature, and S′ the entropy of the system. Whether reaction (3.1) proceeds from left to right or vice versa is determined by the change of Gibbs free energy ΔG′. If ΔG′<0, spontaneous reaction is expected, if ΔG′=0, the system is in equilibrium, if ΔG′>0, the oxidation reaction does not occur [2].

For a chemical reaction in the form of:

□ □ □ (3.3)

ΔG′ is expressed as [2, 53]:

Δ□′ □ Δ□□ □ $\left(\frac{\square\square\square}{\square\square\square}\right)$ (3.4)

where ΔG° is the free-energy change when all species are present in their standard states; R is the gas constant; a is the thermodynamic activity, which may be expressed for a given species i as [2]:

□□□ $\frac{\square\square}{\square\square}$ (3.5)

Here p_i is either the vapour pressure over a condensed species or the partial pressure of a gaseous species; p^{o}_{i} is the vapour pressure corresponding to the standard state of species i.

If equilibrium prevails, ΔG′=0 and **Eq. (3.4**) is reduced to **Eq. (3.6)**,

$$\Delta G^{\circ} = -RT \ln\left(\frac{a_M \cdot a_{O_2}}{a_{MO_2}}\right) \quad (3.6)$$

The term in parentheses is called the equilibrium constant (K) and is used to describe the equilibrium state of the reaction system [53].

Therefore the change of the Gibbs free energy for reaction (3.1) is expressed as:

$$\Delta G = \Delta G^{\circ} + RT \ln\left(\frac{a_M \cdot a_{O_2}}{a_{MO_2}}\right) \quad (3.7)$$

If the activities of metal M and metal oxide MO_2 are taken as unity, the oxygen partial pressure at which the metal and oxide coexist, i.e., the dissociation pressure of the oxide MO_2 [53], can be derived:

$$p_{O_2/MO_2} = \frac{\Delta G^{\circ}}{RT} \quad (3.8)$$

In considering alloy oxidation, the actually prevailing activity of the metal and oxide must be taken into account.

$$p_{O_2} = \frac{\Delta G^{\circ}}{RT} + \frac{a_M \cdot a_{O_2}}{a_{MO_2}} \quad (3.9)$$

The dissociation pressure of the respective oxide thus can be calculated using **Eq. (3.8)** or **(3.9)** taking known temperature dependent ΔG° values of text books [12] or thermodynamic databases from softwares like Thermo-Calc [54] or FactSage [55]. When assuming metal and oxide to exist as pure phases, i.e. their activities are taken as unity, then the values of p_{O_2/MO_2} as given by **Eq. (3.8)** may be obtained directly from the so-called Ellingham diagram (**Figure 3.1**).

In this type of diagram, the standard free energy of formation (ΔG°) is plotted versus temperature for the compounds of a type, e.g., oxides, sulphides, carbides etc.. The values of ΔG° are expressed in **Figure 3.1** as $kJ.mol^{-1}$ O_2 so the stabilities of various oxides may be compared directly, i.e. at a given temperature, the lower the position of the line in the diagram, the lower the dissociation pressure of the oxide, and thus the more thermodynamically stable is the oxide [53]. The dissociation pressure can be obtained by drawing a straight line from the origin marked “O” through the free-energy line at the temperature of interest and reading

the oxygen partial pressure from its intersection with the scale at the right side labeled "pO_2" [53].

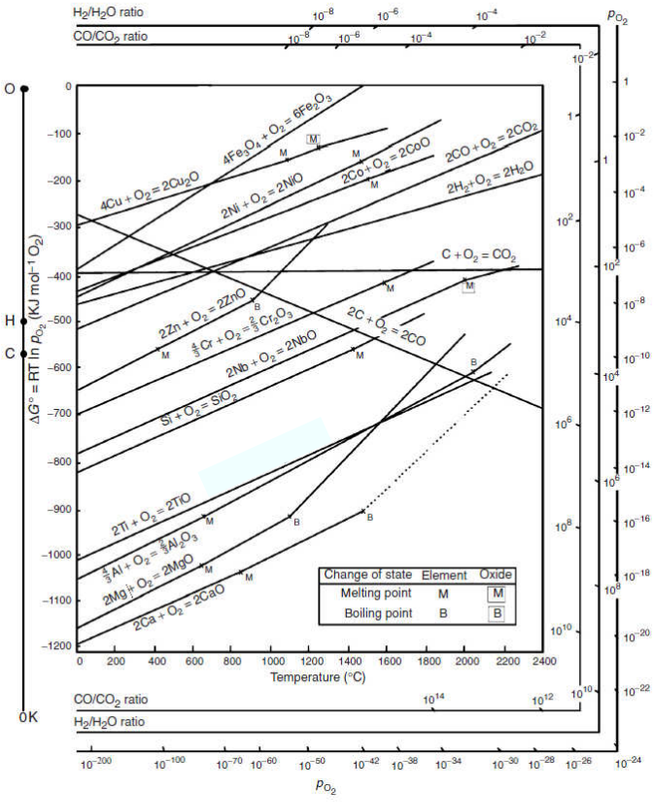

Figure 3.1: Ellingham diagram showing standard free energy of formation (ΔG°) of selected oxides as a function of temperature [2, 53].

A more convenient way of presenting the dissociation pressures is illustrated in **Figure 3.2** showing e.g. that the dissociation pressure of Cr_2O_3 is substantially lower than that of NiO. This means that Cr_2O_3 is thermodynamically substantially more stable than NiO. In turn, Cr_2O_3 is less stable than MnO, SiO_2 or Al_2O_3.

If various pieces of metal would be exposed in an atmosphere in which the oxygen partial pressure equals for instance 10^{-14} bar at 1300°C, then Cr, Mn, Si and Al would oxidize whereas Ni and Fe would remain metallic.

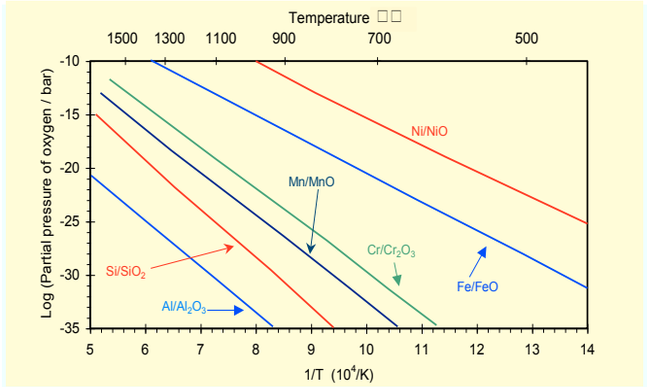

Figure 3.2: Diagram showing the dissociation pressures of various oxides as function of temperature assuming unit activities for metals and oxides [53].

Low oxygen partial pressures can be established in high vacuum systems. With presently used systems, the lowest partial pressures practically achievable are in the range 10^{-9} to 10^{-10} bar. NiO is a borderline case, i.e. the oxide could be reduced at temperatures well above 1000°C, whereas oxides of Fe, Cr, Al, Si can even under such high vacuum conditions not be reduced [55]. Much lower oxygen partial pressures than in a technologically achievable vacuum can be obtained by using suitable gas mixtures.

In a given atmosphere with mixed gases, the establishment of the oxygen partial pressure of oxygen pO_2 is usually based on the equilibrium of redox reactions of CO/CO_2, H_2/H_2O or SO/SO_2. To take the H_2/H_2O equilibrium as an example: at 900°C, in the gas mixture of Ar-4%H_2-2%H_2O, the calculation of the equilibrium pO_2 is as follows [2]:

$$H_2O(g)=H_2+\frac{1}{2}O_2 \qquad (3.10)$$

$$K=\frac{p_{H_2}\left(p_{O_2}\right)^{\frac{1}{2}}}{p_{H_2O(g)}} \qquad (3.11)$$

Taking the known value of K=□□□ □ $^{-\square}$[55] at 900°C,

$$\square\square=\left(\frac{K\cdot p_{H_2O(g)}}{p_{H_2}}\right)^2=\frac{\left(7.1\times10^{-9}\times0.02\right)^2}{0.04}=1.26\times10^{-17}\text{bar} \qquad (3.12)$$

Even lower oxygen partial pressures can be obtained in gas mixtures with a higher $H_2^{(g)}$

and/or lower $H_2O^{(g)}$ content. Important to note that the equilibrium oxygen partial pressure in the gas mixture changes with temperature and depends on the $H_2O^{(g)}/H_2^{(g)}$-ratio, not on the absolute partial pressures of the individual species [53]. The $H_2O^{(g)}/H_2^{(g)}$-ratio in equilibrium with a given metal and oxide may be derived from the Ellingham diagram in **Figure 3.1** by drawing a straight line from the origin marked “H” through the free-energy line at the temperature of interest and reading the oxygen partial pressure from its intersection with the scale at the right side labeled “H_2/H_2O ratio” [2].

3.2 Kinetics of oxidation

3.2.1 Diffusion controlled oxide growth

Differences in thermodynamic stability of various oxides which have been discussed in Section 3.1 do not allow drawing conclusions in respect to the differences in growth rate of these oxides [53].

If a metal, e.g. pure Ni is exposed at elevated temperature (e.g. 1000°C) in a gas (e.g. air) which possesses an oxygen partial pressure which is higher than the dissociation pressure of NiO at that temperature (10^{-10} bar), then reaction of Ni with the atmosphere results in Ni-oxide formation, according to the general reaction [2]:

$$\square \frac{\square}{\square} \square_{\square}(\square) \quad \square \quad \square \qquad (3.13)$$

In the very early stage of exposure, NiO nuclei start to form randomly distributed on the Ni surface. The rate of oxidation is in that stage of the process controlled by the rate of reaction of the Ni specimen surface with individual oxygen molecules (i.e. kinetics of surface reaction) [2]. Upon prolonged exposure, the number and size of the nuclei grow until eventually, a closed layer of NiO covers the complete surface of the Ni specimen and the oxidation product NiO separates the metallic Ni from the gaseous environment. Further reaction, thus growth of the NiO layer, then requires a transport of nickel and/or oxygen across the oxide scale so that the oxidation reaction can continue [2]. If a certain oxide thickness is reached, the transport of Ni- and/or O-species becomes limited with the result that no longer the kinetics of the surface reaction is the rate limiting (i.e. the slowest) step in the oxidation process, but the transport of Ni- and/or O-species across the scale [2]. In many oxide scales this situation already occurs quite early in the oxidation process, i.e. after the scales reach a thickness of a few tenths of a

micrometer. The long term oxidation behavior is thus governed by transport processes in the oxide layers [53].

The mechanism of oxidation of metal always involves the ionization of metal atoms. The metal atoms loose electrons and become cation [2]. For most oxides relevant here, such as $Fe_{0.95}O$, NiO, Cr_2O_3, Al_2O_3 and CoO [12], the cations transport to the oxide/gas interface and attract an oxygen anion to form oxide at the interface with the gas. For the oxide with chemical formula of MO, the ionization process is simply expressed with a chemical reaction as [2]:

□ □ □□□ □ □□ (ß.14)

The oxidation process can be further divided into three sub-processes [2]:

a) Adsorption of oxygen
b) Chemisorption
c) Ionization

Taking the oxidation of Ni as an example, these sub-processes are schematically shown in **Figure ß.3**. First, the oxygen atom is physically adsorpted on the oxide/gas interface, shown as O(ad) [2]. Then the adsorpted oxygen atom captures an electron and becomes an oxygen anion and, because of the loss of an electron, one nickel cation in the nickel-sub-lattice obtains an excessive positive charge [2]. Finally, the oxygen anion captures another electron, one nickel cation in the nickel-sub-lattice is activated and jumps to the oxide/gas interface and combines with the oxygen anion forming further oxide [2]. A vacancy is formed due to the jumping of the nickel cation, and awaits for an ionized nickel atom from the bulk metal, or leaves as a point defect in the oxide scale [2].

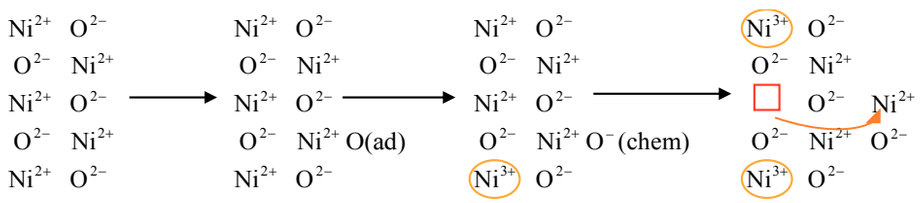

Figure ß.3: Representation of diffusion controlled oxidation process of Ni including surface adsorption, ionization and transportation of iron in the scale (based on [2]).

The diffusion processes in the oxide thus occur via point defects [53]. Except for the major types of cation vacancies existing in NiO, other point defects like anion vacancies or cation interstitials may exist in the regular lattice of various oxides [2].

If we assume the oxide scale to be perfectly gas tight (i.e. it does not allow penetration by oxygen molecules) the rate of oxidation is governed by diffusion of metal and/or oxygen ions through the oxide layer. Upon scale thickening the diffusion distance will increase and the extent of ion transport will thus decrease with increasing time. The thickening rate at a given time is thus expected to be inversely proportional to the thickness of the oxide (x) at time (t) [2]:

(ß.15)

Integration yields

(ß.16)

in which k_p (unit e.g. $\mu m^2.s^{-1}$) is the parabolic rate constant of the oxidation process.
In the most simple form, i.e. if C=0 at t=0,

(ß.17)

The rate constant k_p can be derived from oxide thickness measurements in metallographic cross sections after different oxidation times. However, this is quite a time consuming procedure and especially for thin oxide scales (in the range of a µm thick or less) this method is quite inaccurate [53]. Therefore, oxidation kinetics is frequently measured using weight change measurements [53]. If the specimen oxidizes, it takes up oxygen from the atmosphere resulting in a weight increase. The latter is directly correlated with the amount of oxide formed and therefore, for a given oxide, it is proportional to the thickness of the oxide scale. The weight measurements can be accomplished in two ways [53]:

- discontinuously, i.e. measurements using a standard electronic balance after cooling the specimens to room temperature at different oxidation intervals.

- continuously, i.e. using weight recording in-situ during the oxidation process. This so-called thermogravimetric (TG) analysis is far more accurate than the discontinuous method and it additionally prevents a possible effect of the intermediate specimen cooling on the oxidation process.

When the experimental data are based on gravimetric results, the parabolic oxidation kinetics is commonly expressed in terms of area specific weight gain (Δm) as a result of oxygen uptake:

$$(\Delta\square)^{\square}\square\ \square\square\square\cdot\square \qquad (3.18)$$

In many cases the oxidation kinetics does not obey an ideal parabolic behavior. This may be related to a significant contribution of grain boundary diffusion in combination with changing oxide grain size in the overall oxidation process [56, 57]. In case of alloy oxidation the time dependent incorporation of minor alloying additions with high oxygen activity (e.g. Mn, Si, Al, Ti, Nb) into the oxide scale may result in deviations from ideal parabolic behavior [58，59]. In such cases, the oxidation behavior can frequently be described with reasonable accuracy by sub-parabolic kinetics [12]:

$$\Delta\square\ \square\ \square\cdot\ \square^{\square} \qquad (3.19)$$

in which k is the power law rate constant and n the oxidation exponent whereby n<0.5.

For oxidation with significant formation of volatile species, e.g. in case of pure Cr or chromia forming alloy, paralinear kinetics prevail and **Eq. (3.15)** changes to **Eq. (3.20)**, where k_v is the linear rate constant indicating the loss of the oxide due to surface evaporation of volatile species [12].

$$-\square\ \frac{\square\square}{\square}-\square\square \qquad (3.20)$$

3.2.2 Oxidation rates of common metals

Metallic materials are frequently termed as “oxidation resistant” when comparing the respective metals or alloys with other types of materials, exhibiting higher oxidation rates. However, the expression “oxidation resistant” is only a relative expression [53]. As the dissociation pressures of commonly used metallic materials are usually lower than the partial pressure of oxygen provided by most service environments in practical applications at elevated temperatures, oxidation of the materials can in most applications not be prevented. Therefore, the aim of selection and design of oxidation resistant materials is not to prevent oxidation, but to slow down the oxidation kinetics to reduce the oxidation induced damages to acceptable limits [53].

As explained above, diffusion in a gas tight scale primarily occurs via point defects. Therefore it can generally be said that, although also differences in mobility of point defects are of importance for oxidation kinetics [60], oxides with high concentrations of point defects commonly exhibit higher growth rates than oxides with low concentrations of point defects [2, 53]. **Figure 3.4** shows experimentally determined parabolic rate constants k_w (here expressed in the unit $g^2.cm^{-4}.s^{-1}$) for oxide formed on various metallic materials.

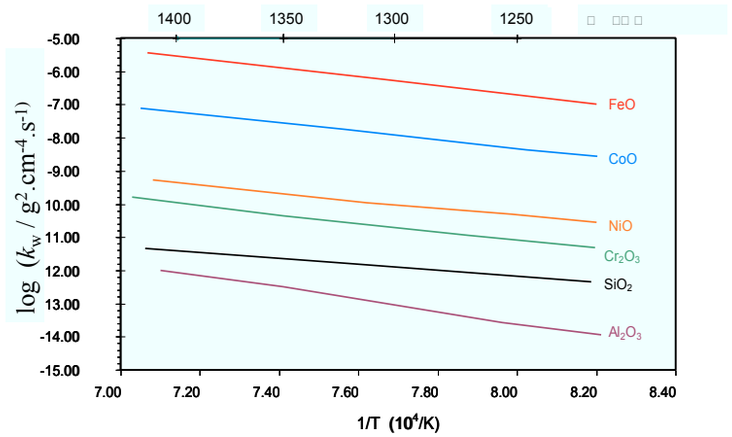

Figure 3.4: Parabolic rate constants k_w for the growth of various oxides as function of reciprocal temperature. Upper horizontal axis indicates temperatures in K ([53], based on [2]).

To be noted is that the parabolic oxidation rates k_w for the various oxides are not correlated with the dissociation pressures shown in **Figure 3.2**. For instance, FeO and Cr_2O_3 both possess a lower dissociation pressure than NiO but the growth rate of NiO is higher than that of Cr_2O_3 lower than that of FeO. It is also apparent from the above diagram that the oxidation rates increase with increasing temperature. Considering that the oxidation process is governed by diffusion processes in the oxide scale, it is not surprising that the oxidation rates exhibit a similar (Arrhenius type) temperature dependence as for diffusion processes in general [2]:

□□ □ □□□ □ $\left(\frac{-\square}{\square\square}\right)$ (3.21)

where k_w^0 is the pre-exponential factor and Q the activation energy of the oxidation process.

3.3 Oxidation of alloys

3.3.1 From internal to protective external oxidation

Oxidation protection of high temperature alloys is commonly based on the so-called "selective oxidation", which means that a dense, continuous, relatively slow growing external oxide scale of one or more alloying elements is formed. In describing selective oxidation, it is important to consider the dissociation pressures and the growth rates of the different metal oxides. Besides, the contents of alloying elements in the alloy systems play a critical role in the oxidation behavior. Internal oxidation of a solute in a binary alloy will occur if the following conditions are fulfilled [2]:

- The oxide of the solute element is thermodynamically more stable than the oxide of the base metal.
- Sufficient solubility and diffusivity of oxygen to establish a necessary oxygen partial pressure in the alloy.
- The concentration of the solute is lower than that required for forming an external oxide.

Considering for example, a low alloyed Ni-3 wt. % Cr alloy exposed in air at 1000°C, the oxygen partial pressure in the atmosphere is much higher than either the dissociation pressure of NiO or that of Cr_2O_3 (see **Figure 3.2**). In this case, pure NiO will form as external oxide on top of the alloy, whereas the Cr is oxidized in the sub-surface region. The internal precipitation of oxides frequently occurs along grain boundaries. **Figure 3.5** illustrates the cross section of an oxidized Ni-3 wt. % Cr alloy, showing formation of external NiO, and only a small amount of Cr_2O_3 precipitate is formed beneath the NiO layer [53].

Increasing the chromium content in the nickel alloy has as consequence that the amount of internal oxide precipitates is increased and, in parallel, the increased oxide is concentrated in a thinner zone [2]. Therefore, a steady increase of the Cr content in the alloy will have as result that above a critical Cr content in the alloy, the internal oxidation zone changes to a closed layer, thus forming a dense Cr_2O_3 layer. The oxygen partial pressure at the Cr_2O_3/alloy interface equals the dissociation pressure of Cr_2O_3 (in equilibrium with the Cr activity in the alloy). As this dissociation pressure is much lower than that of NiO, the external Cr_2O_3 scale prevents the base metal (Ni) from further oxidation. The void formation in the scale and/or at

the alloy/scale interface is frequently related to condensation of inwardly moving cation vacancies [12].

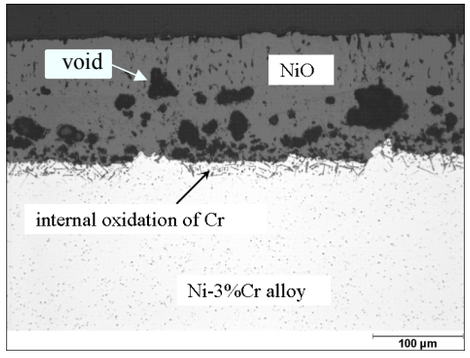

Figure 3.5: Metallographic cross section of oxide scale and internal oxidation zone formed on Ni-3 wt. %Cr alloy during oxidation at 1000°C for 100 h in air [53].

An exact treatment [2] reveals for the chromium mole fraction (N_{Cr}) required for obtaining external rather than internal oxidation:

$$\square \quad \square \left[\frac{\pi \square^{*}}{\square} \square(\square) \frac{\square\square\square}{\widetilde{\square} \quad \square \quad \square\square\square}\right]^{\square/\square} \qquad (3.22)$$

where $\square_{\square}^{(2)}$ is the oxygen solubility in the alloy, D_O the diffusivity of oxygen in the alloy, $\widetilde{\square}\square$ the Cr inter-diffusion coefficient in the alloy, and $\square_{\square}$ and $\square_{\square\square}$ are the molar volumes (e.g. in cm^3/mole) of the alloy and oxide, respectively. The factor g* is generally approximated as about 0.3 [2].

However, strictly speaking, **Eq. (3.22)** is only valid for a system where only Cr can be oxidized, for example if the environmental oxygen partial pressure is lower than the dissociation pressure of NiO but higher than that of Cr_2O_3. The exact mathematical treatment [12] for the case that both Ni and Cr may be oxidized reveals for the critical chromium content at which the change from internal to external oxidation of Cr occurs, a slightly higher value than that given by **Eq. (3.22)**, however the dependence of the critical concentration depends in a qualitatively similar manner on $\square_{\square}^{(2)}$, D_O and $\widetilde{\square}\square$ as described for **Eq. (3.22)**.

If a thin and protective oxide scale is formed, it covers the alloy substrate and protects it from rapid oxidation of the base metal. Generally, the protective scale should meet the properties of

slow growth rate, high thermal stability, continuity, free of crack and pores, good coherence and adherence to the substrate alloy. For austenitic steels and nickel-based alloys, Cr or Al are mostly used as alloying additions which lead to formation of a protective external scale in the form of Cr_2O_3 or Al_2O_3, respectively [53]. In the present study, the main focus is on Cr_2O_3 forming nickel-based alloys and austenitic steels, which possess a FCC lattice.

3.3.2 Main stages of oxidation for chromia forming alloys

The oxidation of so-called chromia forming alloys at high temperature in a high pO_2 gas such as air undergoes several separate stages; the terms of the stages will be marked in bold in the following text.

At the very beginning of oxidation, a short period of **transient oxidation** [61] occurs, which is a stage before the establishment of stable formation of the protective chromia scale. In this stage, all the common alloying elements and the base metal can be oxidized. The oxidation products are usually called transient oxides and may form a thin outer oxide layer (see **Figure 3.6**). For a Cr_2O_3 former, the protective Cr_2O_3 grows together with the transient oxides. After the Cr_2O_3 forms into a continuous layer beneath the multiphase transient oxides, the transport of base metal to the alloy/gas interface is suppressed, and the transient oxidation stage ceases [61]. After the transient stage of oxidation, **steady state growth of the protective chromia scale** occurs whereby diffusion of cations and/or anions in the scale is the rate determining step of the scale growth process. The kinetics and mechanisms have already been discussed in Section 3.2.1.

The consumption of the scale forming element Cr results in subscale depletion of this element and thus in formation of concentration gradients in the alloy beneath the oxide scale. If ideal parabolic kinetics (**Eq. (3.18)**) prevail, the concentration (C_i) of the scale forming solute (Cr) at the alloy/scale interface is virtually time independent before the depletion front reaches the center of the specimen (first stage of depletion), provided that the specimen is sufficiently thick [22]. The subscale Cr concentration profile is described by [14]:

$$\frac{C_o - C_i}{C_o} \cdot \frac{M}{M_{alloy}} \cdot \frac{1}{\nu} \left(\frac{\pi k_p}{x} \right)^{\frac{1}{2}} \qquad (3.23)$$

Here C_o is the initial solute concentration, C_i the interface solute concentration, M the atomic weight of the solute, M_{alloy} the average atomic weight of the alloy, ν the Pilling-Bedworth

ratio (molar volume of oxide divided by the molar volume of the solute metal), and $\tilde{D}$ the inter-diffusivity of the solute in the alloy.

If sub-parabolic kinetics prevail (i.e. n in **Eq. (3.19)** is smaller than 0.5), the value of C_i is not time independent but increases with increasing oxidation time [22]. In contrary, "super-parabolic" kinetics prevail, i.e. if the value of n in **Eq. (3.19)** is larger than 0.5, then C_i decreases with increasing oxidation time [22].

A very frequently observed phenomenon during oxidation of high-temperature alloys is the formation of voids in the alloy substrate as well as at the alloy/scale interface. **Figure 3.7** shows an example of the void formation in both the bulk metal and along the grain boundaries of a Ni-30 wt. % Cr model alloy. There are mainly two mechanisms of void formation [62]. Firstly, the injection of cationic vacancies; and secondly, the Kirkendall [63] effect.

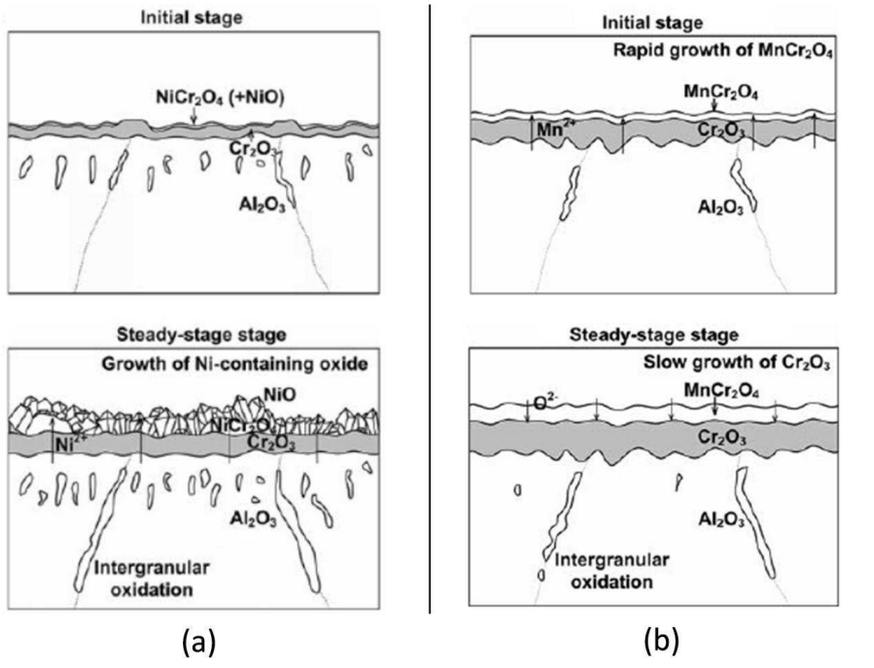

Figure 3.6: Schematic graph showing the oxides grown on typical wrought nickel base alloys, here a) Alloy 617 and b) Haynes 230 at 900°C in air during transient and steady state of oxidation [61].

The outward movement of the metal cations in the oxide is accompanied by an inward diffusion of vacancies. To keep the lowest energy level of the system, the concentration of vacancies would increase at preferable areas, where the density of dislocations is low, resulting in the aggregation and super saturation of the vacancies and finally the formation of porosity and voids occurs [62]. The vacancy condensation may occur in the oxide, at the alloy/scale interface or within the alloy [12].

The Kirkendall effect is known as the mismatch of the diffusion coefficient between two diffusing elements which leads to a vacancy flux of one element in the opposite direction of the flux of the fastest element. This mechanism often causes voids in the bulk alloy [62].

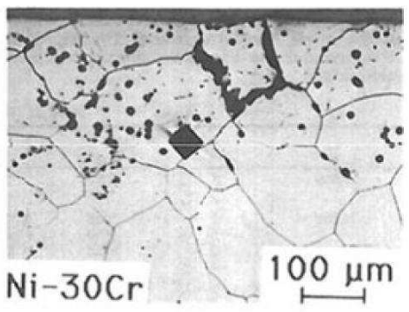

Figure 3.7: Void formation during oxidation of Ni-30 wt.% Cr model alloy exposed in air at 1200°C for 100 h [64].

The formation of voids at the alloy/scale interface may be the source of cracks which deteriorate the high temperature oxidation resistance of the materials by initiation of scale spallation [15]. In studies of oxidation of Ni-Cr binary alloys, it is found that the coalescence of the vacancies may initiate microcracks, and leads to the ingress of oxygen, so that a duplex-scale is formed, of which the inner layer is porous oxide with equiaxed grains [65]. In contrary to the common remarks about the consequence of void formation, the porous oxide with small equiaxed grains is thought to act as mediate between the alloy substrate and the outer columnar grains to improve maintenance of interface adhesion [66].

In studies related to oxidation of pure Cr, it is also revealed that a certain contribution of inward growth of oxide can decrease void formation at the alloy/scale interface [67, 68].

In addition to formation of voids at the alloy/scale interface, also thermally induced stresses occurring during cooling due to the mismatch of the thermal expansion coefficients between

alloy and oxide and even oxide growth stresses may lead to scale micro damage [15, 69, 71]. After formation of scale defects with a critical size, compressive stresses in the scale induced during cooling from oxidation to room temperature may eventually lead to **scale spalling** [15]. During re-heating the protective chromia scale may re-form, provided that the concentration C_i (**Eq. (3.23)**) is sufficiently high for external oxidation of Cr to be favored over internal oxidation [12, 72].

The scale spalling will result in enhanced loss of the scale forming element and thus the Cr consumption rate is faster than that given by **Eq. (3.23)**. Consequently the value of C_i will decrease with time and may eventually become substantially smaller than the value given by **Eq. (3.23)**. Upon re-heating after cooling, the formation of the protective scale may then be no longer possible. In case of typical Ni-Cr base wrought alloys discussed here, this "**breakaway oxidation**" may lead to formation of less protective, Ni-containing oxides. However, this generally does not lead to a sudden, catastrophic oxidation frequently observed e.g. in FeCrAl alloys [73] as long as the reservoir of the solute chromium in an adequately thick specimen is sufficiently high to (partly) re-form the inner chromia scales beneath the less protective oxide formed during re-heating.

In thin specimens (e.g. of a few tenths of a mm thickness) the subscale solute concentration profiles may within relatively short times reach the center of the specimen. This will generally more rapidly occur in BCC (e.g. ferritic steels) than in FCC materials (e.g. NiCr base alloys, austenitic steels) because the solute diffusivities are generally smaller in the latter than in the BCC type alloys [12]. If the diffusion profile reaches the center of the specimen, the second stage of depletion starts, and the value of C_i (**Eq. (3.23)**) will then, even during steady state scale growth, decrease with increasing oxidation time. The subscale concentration profiles then become relatively flat, as e.g. frequently observed during growth of alumina scales on FeCrAl base alloys [21, 26] and chromia scales on high-Cr ferritic steels [32, 74]. Upon ongoing scale formation the solute concentration over the whole specimen thickness will decrease with increasing time. The interface concentration of the solute may finally reach concentrations which are so low that external formation of the protective scale is no longer possible. For alumina forming ferritic steels at temperatures in the range 1000 - 1200°C [21, 26] and chroma forming ferritic steels at 800 - 900°C [32, 74] it could be shown that the time for occurrence of breakaway oxidation (t_B) can with reasonable accuracy be described by correlating the Cr (or Al) consumed by the growth of the oxide scale with the Cr (or Al)

reservoir in the alloy. This lead to the following expression for the time (t_B) till occurrence of breakaway oxidation [21]:

$$t_B \approx \left[\frac{\pi}{16} \cdot (C_0 - C_B) \cdot \frac{\rho \cdot d}{k_p} \right]^{\frac{1}{n}} \tag{3.24}$$

Here C_B is the critical solute concentration for occurrence of breakaway, ρ the density of the alloy, d the wall thickness, k_p the rate constant of oxidation and n the oxidation exponent as defined in **Eq. (3.19)**. The value $\frac{\pi}{16} = 0.1963$ is a constant valid for alumina formers, whereas for chromia formers the value of this constant is $\frac{\pi}{24} = 0.1309$.

Assuming a simple scale spalling model the value of t_B could be estimated by [21]:

$$t_B \approx \frac{\pi}{16} \cdot (C_0 - C_B) \cdot \rho \cdot d \cdot (k_p)^{-\frac{1}{n}} \cdot (\Delta m^*)^{\frac{1}{n}-1} \tag{3.25}$$

where the Δm^* is the area specific weight gain at the time when a complete scale spallation starts to occur.

This approach allowed constructing lifetime diagrams showing times to breakaway as function of component thickness for various temperatures [21].

The nearly flat solute depletion profiles are, however, up to quite long exposure times not observed in chromia forming FCC materials, due to the higher oxidation rate and the lower interdiffusivity of the solute. An extensive mathematical treatment to describe the subscale depletion as function of time and oxidation rate for alloys forming non-flat solute depletion profiles was provided by Bastow et al. [75].

Young et al. [24] showed that the Bastow/Whittle approach can be numerically approximated, revealing an expression to calculate the time till occurrence of breakaway oxidation, i.e. the time at which C_i becomes lower than a critical value C_B:

$$t_B \approx \frac{\pi}{24} \left[\left(\frac{C_0 - C_B}{2} \cdot \frac{\rho}{\mu} \right)^2 \frac{k_p}{D} - \frac{\sigma}{2} \right] \tag{3.26}$$

Here, μ is the metal/oxygen weight ratio of the scale forming oxide, k_p the parabolic rate constant (**Eq. (3.18)**), σ is a constant equal to $\frac{\pi}{24} = 0.1309$, and D the diffusion coefficient of the solute Cr in the alloy in $cm.s^{-1}$.

However, both the Bastow/Whittle approach as well as **Eq. (3.26)** are only valid in case of steady state oxide growth obeying parabolic kinetics. Prediction of the time to breakaway if

deviations of ideal parabolic kinetics prevail and especially accounting for occurrence of scale spalling is not possible on the basis of the concepts in reference [24].

3.3.3 Volatilization of oxide

The oxidation of Cr_2O_3 forming alloys can undergo scale loss due to reactive evaporation of chromium containing gas species [42]. A number of possible Cr-containing gas species can be formed in O_2 and H_2O containing environment, such as various chromium oxides, chromium hydroxides and chromium oxy-hydroxides. In dry air, the predominate gaseous species formed is $CrO_3(g)$. The accelerated degradation due to water vapor as well as steam environments was firstly described by Kofstad [76, 77] in the beginning of the 1990s. In last decades, the evaporation of Cr from protective scales of stainless steels [78-87] and other alloys [88-94] were further studied. The effects of water vapor on chromia forming alloys are mostly marked for Fe-based alloys, its influence on Ni-based alloys are seem to be less severe [95]. One of the differences between Fe-base and Ni-base alloys is possible formation of $Fe(OH)_2(g)$ in wet air, which then may convert into haematite or magnetite thus contributing to a higher rate of oxidation [80]. For Ni-base alloys, the formation of $NiCr_2O_4$ spinel can reduce the Cr evaporation by a factor of 2 at temperatures up to 1000°C [96]. For high-Cr ferritic steels the formation of outer $MnCr_2O_4$ has been shown to reduce Cr evaporation [97, 98].

It is well established that the effect of volatile species formation on the overall oxidation process increases with increasing gas flow rate [99, 100]. Under static condition in oxygen rich gases with low water vapor contents, such as ambient air, the contribution of volatile species on the scaling process is limited and can thus up to quite long exposure times be neglected.

3.3.4 Effects of alloying elements

In design of high-temperature alloys, a wide variety of alloying elements are added to FCC alloy systems in order to optimize mechanical properties, such as high-temperature creep strength. However, these alloying elements may also influence the oxidation behavior of the alloy.

Addition of W, Mo, Cr and Co increases the creep resistance of Ni-base alloy by solid solution strengthening, and to some extend slowing down the diffusion of atoms in the base

alloy. In Ni-base alloys, W, Mo, Cr and Co tend to form carbide precipitates, thus affecting creep strength [101, 102].

Si and Al form oxides which are thermodynamically far more stable than chromia. Therefore, these elements mostly prevail in internal oxides rather than being incorporated into the scale. If the Al and/or Si contents are increased to beyond 1 wt. %, the internal silica and/or alumina precipitation may change into protective, external scale formation. Due to the extremely low growth rates of silica and alumina, this effect is accompanied by a strong increase in oxidation resistance [103]. It is also generally admitted that Si addition decreases the probability of breakaway oxidation. First, during the initial stages of oxidation, internal precipitates of silica form, which sustains internal precipitates of chromia settlement. Silica forms beneath the chromia scale and the discontinuous layer of silica acts as a partial diffusion barrier and leads to a decrease in the oxidation rate [104, 105].

Ti and Mn are incorporated in the scale and finally diffuse to outer scale, mostly forming TiO_2 and $MnCr_2O_4$, respectively [106]. The formation of the spinel type oxide of Mn in the outer part of the surface scale may reduce the evaporation of the Cr in oxidation of chromia forming alloys at high temperatures [96]. It was found that Mn has a very minor solubility in Cr_2O_3 which depends on pO_2 [107]. It has also been found that at high-pO_2, Mn can replace a substantial amount of Cr in the Cr/Mn-spinel [107]. Mn additions increase the oxidation rate of NiCr-alloy in the high-pO_2 environment, partly by forming a spinel layer in addition to Cr_2O_3 [108]. However, the rapid incorporation of Mn in the oxide will easily lead to complete exhaustion of the Mn reservoir in the oxidized specimen especially for thin specimens oxidized at high temperatures, which will alter the described effect of Mn on the oxidation kinetics [109]. Ti is an alloying element with a large influence on the oxidation rate [106, 110]. For example, by adding 2 wt. % of Ti to an alloy containing 10 wt. % of Cr, the chromia growth rate in steam reforming gas was found to increase by a factor of about 4 due to the Wagner-Hauffe doping effect [106, 110]. It was also found that the enrichment of Ti in the outer chromia increases with increasing pO_2 in the surrounding atmosphere, which is, similar to Mn, probably a result of a pO_2 dependent Ti solubility in chromia scale [110-112].

A variety of studies on the effects of so-called reactive elements (RE) on the formation of protective scale were published [113-118]. The reactive elements are the elements in Group II to Group V in the periodic table, including La, Y, Ce, Hf, Zr, Mg, Ca, etc. The buckling and resulting poor adhesion of the scale can be minimized by the addition of RE either in metallic

form or in the form of an oxide dispersion [116, 117]. The most commonly used RE‟s, which are added in concentrations of a few hundredths or tenths of a percent, are Y, La, Ce and Zr. Apart from the improved scale adhesion, the dispersed oxides of RE may in the early stages of oxidation, promote oxide nucleation thus shortening the time to obtaining steady state oxidation. Thus, RE additions tend to promote selective external oxidation of Cr [113].

4 Experimental

4.1 Materials

Four commercial high-temperature alloys were chosen for the present study, three of which are Ni-base alloys, namely alloy 230, alloy X, and NiCr 8020. The fourth alloy studied is the high temperature austenitic steel Nicrofer 2020.

Alloy 230 is a material frequently used as construction material for a variety of high temperature components [52], including thin-walled components such as honeycomb structures and heat exchangers. Alloy X is recommended to be used in furnace application as well as in the field of aircraft, such as the jet engine tailpipes, afterburner components, cabin heaters and other aircraft parts [119]. The high temperature Ni-base alloy NiCr 8020 is also commonly named Nichrome 8020, which was firstly patented in 1905 as the oldest resistance heating alloy [120]. Because of its oxidation resistance and high melting temperature (1400°C), NiCr 8020 is still used in a very wide variety of devices where electric heating is required. The common chemical composition is simply 80 wt. % Ni and 20 wt. % Cr, whereas some other alloying elements are inevitably present or intentionally added during the production. Nicrofer 2020 is a commercial high temperature austenitic steel provided by VDM Metals. It is widely known that this type of stainless steel represents Fe-based alloys with high heat resistance. This alloy has good oxidation resistance in air and is applied in automotive and electronic or electrical industries as well as heating elements for household applications [121].

The nominal compositions of the alloys are listed in **Table 4.1**. The chemical compositions of the studied batches will be shown in the respective chapters in which the experimental and modeling results of the corresponding alloys are presented.

The chemical composition analyses of the as-received materials were performed using inductively coupled plasma-optical emission spectroscopy (ICP-OES) after completely dissolving the metal in aqua regia. The concentrations of C, N, O and S were obtained from combustion infrared analysis.

Table 4.1: Nominal compositions of studied alloys

Alloy 230[52]	Ni	Cr	W	Mo	Fe	Mn	Si	Al	Co	La	C
	Bal.	22.0	14.0	2.0	3.0#	0.5	0.4	0.3	5.0#	0.02	0.10
Alloy X [121]	Ni	Cr	Fe	Mo	Co	W	Si	Mn	P	B	C
	Bal.	20.5* 23.0#	17.0* 20.0#	8.00* 10.00#	0.50* 2.50#	0.20* 1.00#	1.00#	1.00#	0.04#	0.01#	0.05* 0.15#
NiCr 8020 [121]	Ni	Cr	Fe	Mn	Si	Mg	C				
	Bal.	19.0* 20.0#	0.20#	0.05#	0.1* 0.2#	0.01* 0.02#	0.20#				
Nicrofer 2020 [121]	Fe	Ni	Cr	Si	Mn	Ti	Al	C			
	Bal.	19.0* 22.0#	19.0* 22.0#	1.0 #	1.0#	0.6#	0.6#	0.05#			

*:minimum, #:maximum

4.2 Preparation of specimens

The as-received alloys prevailed in form of sheet materials of different thicknesses. The sheet materials were laser-cut into specimens with the size of 10 mm × 20 mm. The specimens were then ground to thicknesses of 0.2, 0.3, and 0.5 mm (1 mm) with a final surface finish up to P1200. Before the oxidation tests the specimens were degreased with ethanol.

4.3 Oxidation testing

4.3.1 Discontinuous exposure

The prepared specimens with thicknesses of 0.2, 0.3, 0.5 mm, and in few cases 1 mm, were subjected to discontinuous air oxidation tests for exposures up to 3000 h at temperatures of 950, 1000 and 1050°C. For the austenitic steel Nicrofer 2020 additional tests were carried out at 900°C. For the 1000 and 1050°C tests carried out at Forschungszentrum Jülich, the specimens were air cooled and weighed every 48 h. During the oxidation, the specimens were hung on thin alumina rods in alumina crucibles, which allowed the measurement of the weight changes of the specimen (in the following designated as “net weight change”) as well as the weight change of the specimen including the spalled oxide scale (“gross weight change”). During the oxidations tests at 950°C carried out at Oak Ridge National Laboratory (ORNL) in dry air the cycle was 10 h and only the net weight was measured.

4.3.2 Thermogravimetry

In addition to the discontinuous long-term oxidation experiments, selected 0.2 and 0.5 mm specimens were isothermally oxidized (TG tests) using a SETARAM thermo balance at 900°C for 72 h, 1000°C for 100 h and 1050 °C for 72 h to obtain more information about the oxidation and Cr depletion kinetics in the early stages of oxidation.

4.4 Characterization methods of oxidized specimens

Before mounting the oxidized specimens for metallographic cross section analyses, the specimens were sputtered with a thin gold layer and subsequently electroplated with nickel. This nickel coating provides protection of the surface oxide layer during grinding and polishing and it ensures better optical contrast between oxide and mounting material during the light and electron optical investigations. The coated specimens were mounted in a resin and the cross sections of the specimens were polished to a mirror like surface with diamond paste with diameters down to 1 µm; a SiO_2 suspension with particle size of 0.5 - 0.7 µm was used for the final polishing.

The oxide scale and microstructure of the alloy were characterized with scanning electron microscopy (SEM: Zeiss Supra 50VP or Zeiss Merlin) with energy dispersive X-ray analysis (EDX) with an accelerating voltage of 15 kV. The element depletion profiles of oxidized specimens were investigated with EDX, whereas for part of the specimens these depletion profiles were investigated with glow discharge optical emission spectroscopy (GDOES). For selected samples, electron backscatter diffraction (EBSD) was used to characterize the precipitate phases in the alloy.

5 Effect of specimen thickness on microstructural changes during oxidation of alloy 230

5.1 Analyzed chemical composition

The alloy 230 specimens were all fabricated from 1.2 mm thick sheet in the solution-annealed condition, supplied by Haynes International. Bulk chemical analyses were performed by inductively coupled plasma-optical emission spectroscopy (ICP-OES) after completely dissolving the metal in aqua regia. The concentrations of C, N, S and O were determined using combustion-infrared analysis. **Table 5.1** shows that the composition was very close to the nominal values, however, the Co and Fe contents were much lower than the maximum values and La was not unequivocally detected by the ICP-OES process.

Table 5.1. Chemical composition (in wt. %) of the studied alloy 230 batch determined by ICP-OES and combustion infrared analysis compared with nominal composition supplied by manufacturing data sheet [52].

	Cr	W	Mo	Fe	Mn	Si	Al	Co	La	C	N	O	S
Nominal	22.0	14.0	2.0	3.0 (max)	0.5	0.4	0.3	5.0 (max.)	0.02	0.10	-	-	-
Analyzed	22.2	14.3	1.28	1.23	0.49	0.41	0.37	0.14	<0.01	0.092	0.060	0.002	<0.01

5.2 Example of oxidation kinetics and subscale chromium depletion

Figure 5.1 shows an example of the mass change data during oxidation at 1000 and 1050°C in laboratory air illustrating the typical effect of specimen thickness on oxidation kinetics. The oxidation kinetics at 950℃ showed similar trends and will be presented in the following chapter. The mass change at 1000°C was found to be independent of specimen thickness until approximately 400 h of exposure (**Figure 5.1**). After longer exposure times, the specimen and total mass changes for the 0.3 and 0.5 mm specimens began to deviate indicating scale spallation. The total mass gains for both specimens remained similar, but the extent of scale spallation was slightly more pronounced for the thicker specimen.

For the 0.2 mm thick specimen, there was only a minor difference between the specimen and total mass gains indicating that little or no scale spallation occurred up to 3000 h. However,

after ~500 h, the total weight gain deviated from near-parabolic behavior to “super-parabolic” or almost linear kinetics.

The results in **Figure 5.1** show, as expected, similar trends of weight gain curves at 1050°C, but increasing oxidation rates with increasing temperature. For example, the weight gain of the 0.2 mm specimen after 500 h oxidation is about 1.2 mg.cm^{-2} at 1000℃ , whereas the weight gain of the 0.2 mm specimen is about 2 mg.cm^{-2} at 1050℃ after the same oxidation time.

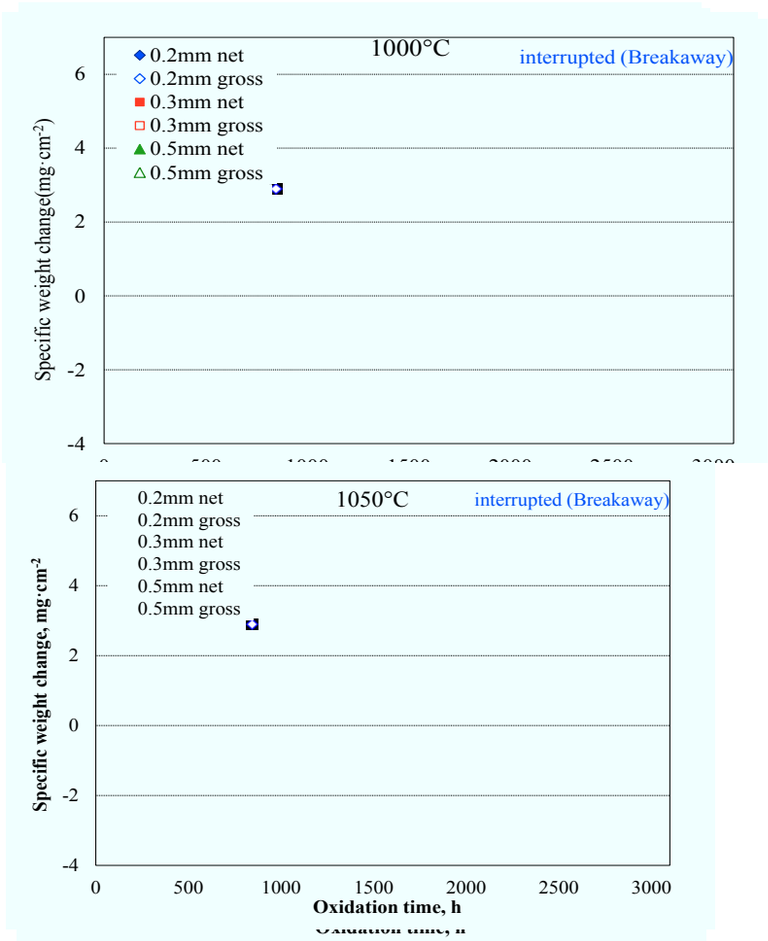

Figure 5.1. Typical example of net and gross weight change of alloy 230 (with specified specimen thicknesses) during oxidation in laboratory air at 1000 and 1050°C. The open and closed symbols indicate the total and specimen mass changes, respectively.

In interpreting the mass change data (**Figure 5.1**), it has to be borne in mind that oxidation of chromia forming alloys in high pO_2 gases (such as air) will be affected by the formation of volatile Cr species, such as CrO_3 and $CrO_2(OH)_2$ in the presence of H_2O [42, 122, 123], as discussed in Section 3.3.3. Based on relevant data [67], the mass loss induced by this effect in static laboratory air in the temperature range considered would be in the range of a few tenths of a $mg \cdot cm^{-2}$ for a pure chromia scale up to the maximum exposure time of 3000 h and thus should not fundamentally alter the mass change kinetics in the present study. It also should be mentioned that the Mn in alloy 230 (**Table 5.1**) is known to form a thin outer layer of $(Cr, Mn)_3O_4$ on top of the chromia scale [61]. This spinel layer has been shown [124] to reduce the formation of volatile Cr species. Thus, formation of volatile Cr species certainly occurs, but it is not expected to substantially affect the measured kinetics and related subscale depletion phenomena under the prevailing experimental conditions.

Considering the O/Cr mass ratio and the well known density of chromia (5.2 $g.cm^{-3}$) [124] it is easy to derive, that for growth of a pure chromia scale an area specific oxygen uptake of 1 $mg.cm^{-2}$ corresponds to a scale thickness of 6.07 µm [53]. Ignoring the very minor amounts of spinel phase and the oxygen uptake by internal oxidation, the scale thicknesses derived from weight gains may be compared with the actually prevailing scale thicknesses visible in the metallographic cross sections (**Figure 5.2**). As example: the 0.2 mm specimen exhibited a mass gain of 1.95 $mg.cm^{-2}$ after 1000 h at 1000°C, which would correspond to a scale thickness of 11.8 µm. This is in good agreement with the value seen in the metallographic cross section (**Figure 5.2 a**). It is easy to verify that, in spite of the mentioned sources of inaccurcy, in all cases very reasonable agreement prevails between the metallographically measured scale thicknesses and the thicknesses derived from the weight gain data. The weight gain related to oxygen uptake by internal oxidation of mainly Si and Al can thus be neglected.

Not only at 1000°C (**Figure 5.1**) but also at 950 and 1050°C, oxide adherence was found to increase with decreasing specimen thickness. This is in qualitative agreement with previous results and theoretical considerations related to the effect of specimen thickness on oxide scale adherence [125]. Whereas no indication for oxide spallation for the 0.2 mm specimens was found, the 0.3 and 0.5 mm specimens exhibited an onset of scale spallation after approximately 300 h at 1050°C, 600 h at 1000°C (**Figure 5.1**) and 2000 h at 950°C. At the times at which the thicker specimens started to exhibit scale spallation, the 0.2 mm specimen showed oxidation kinetics which were faster than parabolic. This enhanced oxidation might

be related to relaxation of growth stresses by plastic deformation of the metallic substrate [126, 127], rapid exhaustion of the reservoir of the reactive element La [126, 128] or, more likely, to tensile microcracking occurring upon re-heating after repeated specimen cooling, as described in references [125, 129]. The mechanisms will be extensively discussed in Section 6.2. A similar specimen thickness dependence of oxidation kinetics was also found for alloy X and NiCr 8020, as will be shown later in Chapter 8 and 9.

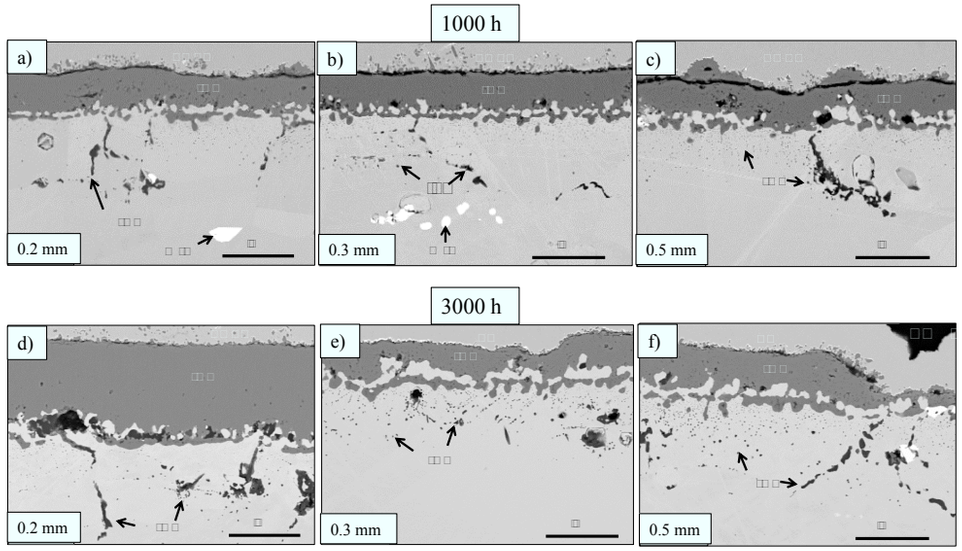

Figure 5.2: BSE image of cross sections showing the oxide scale morphology of alloy 230 specimens of different thicknesses oxidized at 1000°C for 1000 h a-c) and 3000 h d-e) air oxidation.

Figure 5.3 shows Cr profiles measured by EDX for specimens of different thickness after 1000 h and 3000 h exposure at 1000°C. It should be noted that the EDX point analyses measured the Cr concentration in the alloy matrix and do not take into account Cr tied up in precipitate phases which possess a size that are clearly visible in the SEM image. After 1000 h, a subscale Cr depletion was apparent and the Cr mass fraction at the scale-alloy interface for all of the specimens shown in **Figure 5.3 a** was ~17 %. After 3000 h (**Figure 5.3 b**) the Cr concentrations at the scale-alloy interface for the thicker specimens were quite similar, i.e. ~15%. However, for the 0.2 mm specimen, the depletion profile reached the center of the sample. With a severely depleted Cr reservoir, the result was a substantial decrease in the Cr interface concentration, as expected from theoretical considerations (see Section 3.3.2 and

reference [75])

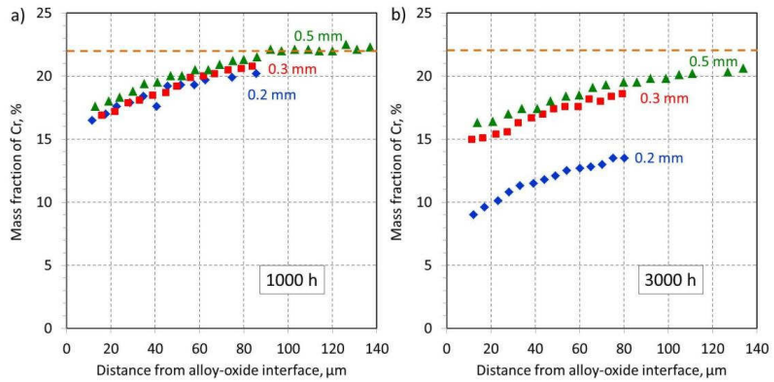

Figure 5.3: Cr profiles measured by EDX (measured in γ-Ni matrix) for specimens of different thicknesses after a) 1000 h and b) 3000 h exposure at 1000°C (Dashed line indicates the original Cr concentration in alloy 230)

5.3 Oxidation induced microstructural changes

In order to obtain information about the alloy microstructure without it being affected by the subscale depletion process, a 0.5 mm specimen was isothermally exposed at 1000°C for only 100 h. **Figure 5.4** shows that the alloy exhibited a three phase microstructure consisting of a face-centered cubic γ-Ni matrix and two types of precipitates. EDX revealed one of the precipitates (black arrows) to be rich in W and Ni, likely M_6C [131, 132] whereas the other type of precipitate (white dashed arrows) was a Cr-rich nitride with typical composition with respect to metallic constituents in atomic percent: 37Cr-34Ni-15W-4Mo-10Si. Only traces of a Cr-rich carbide, probably $M_{23}C_6$ [133] were found, mainly at alloy grain boundaries. These precipitates were too small for quantitative analysis by EDX at this stage.

The typical microstructural features of alloy 230 specimens after prolonged oxidation are shown in **Figure 5.5**, using the 0.3 mm specimen after 3000 h exposure at 1000°C as an example. Apart from the internal aluminum oxide, three types of precipitates were observed in the alloy (in the BSE image appearing white and grey, respectively). These precipitates were absent beneath the scale and were mainly present in the center of the specimen. Comparing **Figure 5.4** and **Figure 5.5**, the volume fraction of precipitates appeared to increase with increasing exposure time.

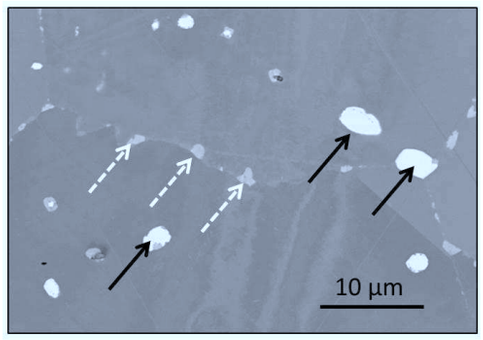

Figure 5.4: BSE image showing cross-section of bulk alloy microstructure (0.5 mm thick sample) of alloy 230 after 100 h isothermal exposure in synthetic air at 1000°C (Black and white arrows indicate W-rich and Cr-rich precipitates respectively)

The precipitates formed after prolonged exposure could be unequivocally identified by EDX and EBSD. **Figure 5.6 a** shows a BSE image from the center of the 0.3 mm specimen oxidized at 1000°C for 3000 h and **Figure 5.6 b-g** are element maps from this region. The carbide appearing bright in the BSE image is rich in Ni and W (similar to **Figure 5.4** and **Figure 5.5**) with some Mo present, whereas the other carbide is Cr-rich.

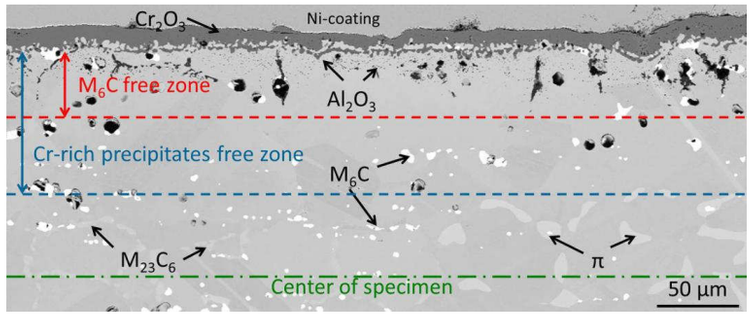

Figure 5.5: BSE cross-section image of 0.3 mm thick alloy 230 specimen after reaction for 3000 h in laboratory air at 1000°C. Designations of phases are based on EDX and EBSD results in **Figure 5.6** and **Figure 5.7**.

The result of the EBSD phase map for the same specimen is shown in **Figure 5.7 a**, confirming the presence of $M_{23}C_6$ and M_6C phases after long-term oxidation at 1000°C. EDX analyses indicated typical compositions of the metallic constituents in the two carbide

precipitates (in wt. %) to be 63W-20Ni-12Cr-5Mo for M_6C and 40Cr-32Ni-24W-4Mo for $M_{23}C_6$.

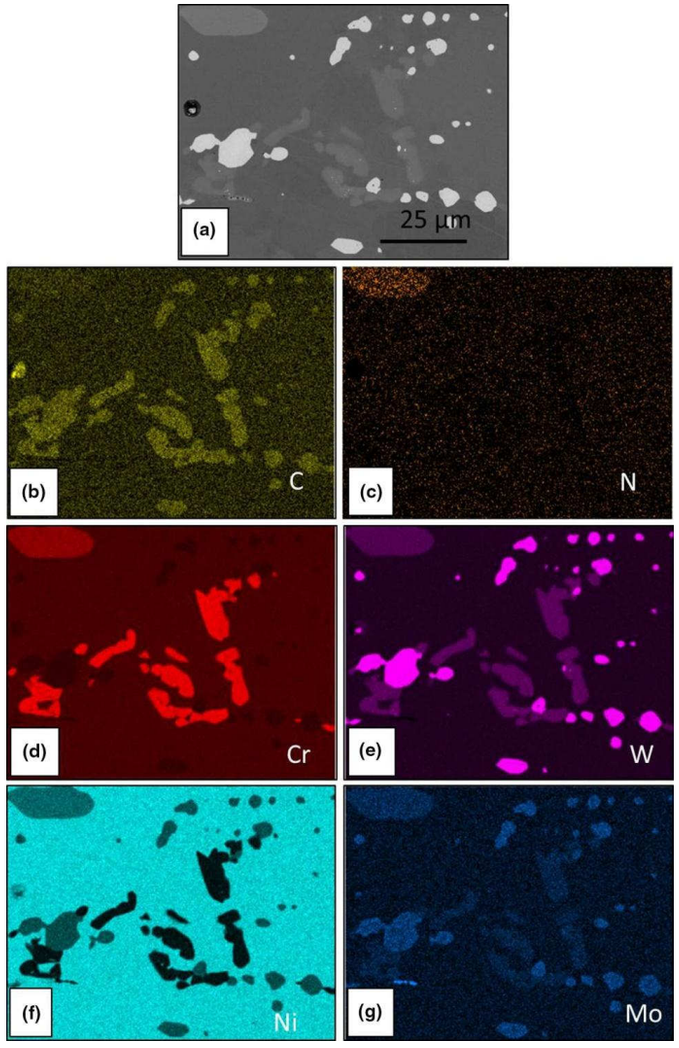

Figure 5.6: BSE image a) with EDX element maps b-g) from the center of a 0.3 mm thick alloy 230 specimen oxidized for 3000 h at 1000°C in laboratory air. The location used for the measurement corresponds to the left side of **Figure 5.5**.

Additionally, nitride precipitates could be identified (**Figure 5.6 c** and **Figure 5.7 b**) which were isostructural with Ni_2W_3N (π-phase) [134, 135] with typical concentrations of the

metallic constituents (in wt. %) 39Cr-32Ni-24W-4Mo. Unlike the nitride phase observed in the specimen exposed for only 100 h (**Figure 5.4**), no Si was found in the π-phase precipitates. In some specimens and/or specimen areas, the Cr-rich carbides and nitrides coexisted (**Figure 5.6 a**) whereas in some places only carbides or nitrides were present.

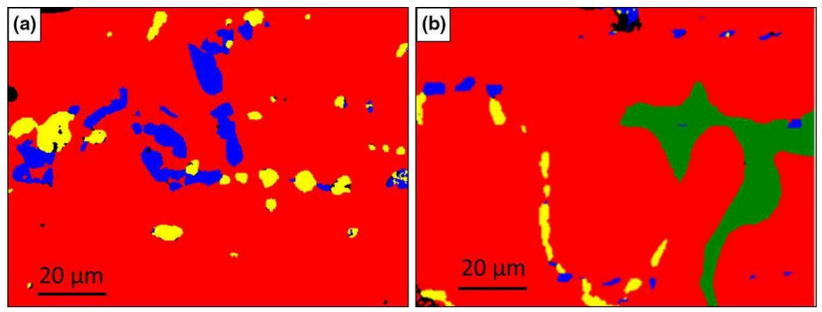

Figure 5.7: EBSD phase maps for Alloy 230 in two different places (a, b) in the center of 0.3 mm specimen of alloy 230 after 3000 h oxidation at 1000°C in laboratory air. In the EBSD phase map red color corresponds to γ-Ni matrix, yellow to $M_{23}C_6$, blue to M_6C and green to π-Ni_2W_3N. The location used for the measurement in Fig. a) corresponds to the left side of **Figure 5.5**; the location used for the measurement in Fig. b) corresponds to the right side of **Figure 5.5**.

The microstructural evolution of alloy 230 as a function of time and specimen thickness at 1000°C is shown in **Figure 5.8**. The trends of microstructural evolution were found to be qualitatively similar for all three temperatures. The cross sections of the specimens after oxidation at 950 and 1050℃ are shown in **Figure 5.10** and **Figure 5.11**, respectively.

In all cases, the scale was predominantly Cr_2O_3 with minor amounts of alumina internal oxidation, which preferentially nucleated along alloy grain boundaries. This morphology is very common for commercial Ni-Cr alloys with high (>20%) Cr contents and low Al contents [136]. (The Al may be intentional or an impurity associated with commercial alloy manufacturing). On top of the chromia layer, a very thin Mn-rich oxide, likely $MnCr_2O_4$, was found to be present. However, due to the very limited Mn reservoir in the specimens, no unequivocal indications for spinel formation were found after longer exposures, especially in the thinnest specimens. The scale thickness varied from 6 - 30 µm. The scale on the 0.2 mm specimens was substantially thicker than that on the 0.3 and 0.5 mm specimens, in agreement with the gravimetric data (**Figure 5.1**). Additionally, minor void formation was found in the

subsurface zone, probably related to the Kirkendall effect [12]. **Figure 5.5** and **Figure 5.8** clearly show that the width of the region, which was free of Cr-rich carbide and nitride precipitates (blue dashed lines), is slightly wider than that of the M_6C depletion zone (red dashed line). For the 0.2 mm specimen, almost all of the M_6C precipitates were consumed after 3000 h at 1000°C (**Figure 5.8 f**).

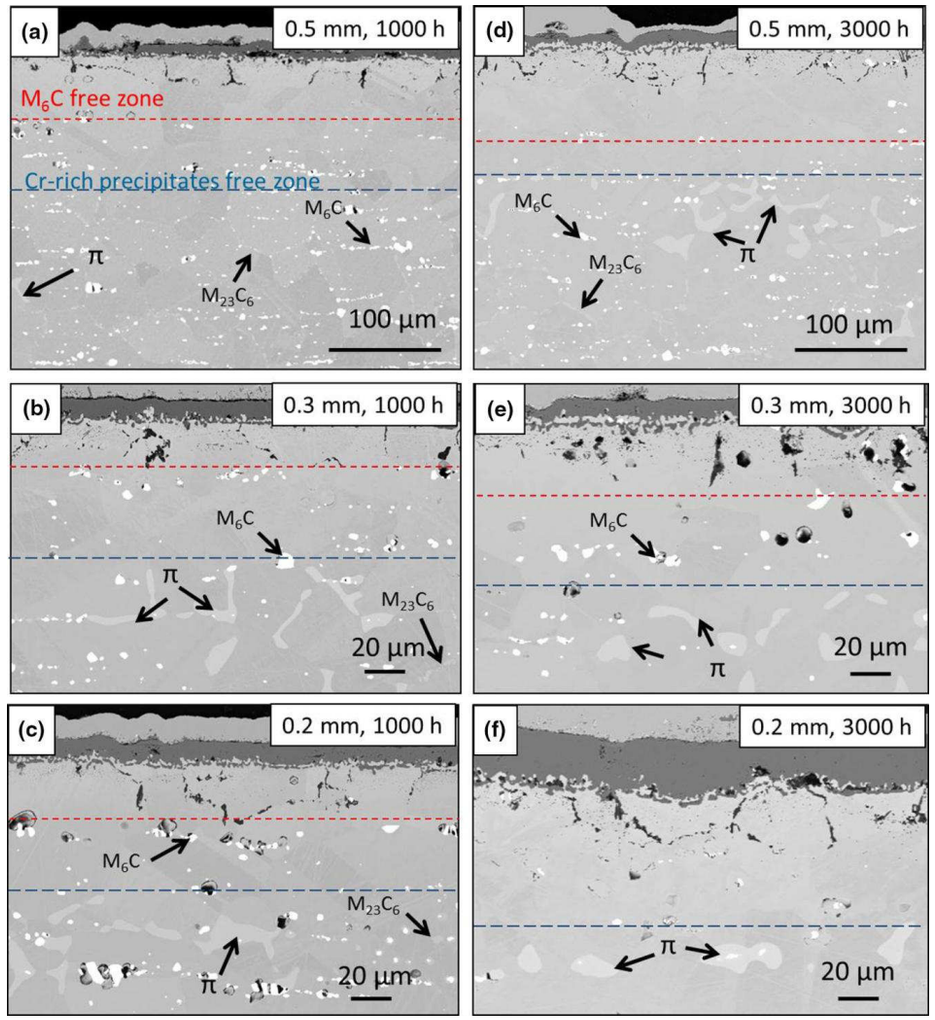

Figure 5.8: BSE images of a, d) 0.5 mm, b, e) 0.3 mm and c, f) 0.2-mm-thick alloy 230 specimens after reaction for a-c) 1000 h and d-f) 3000 h in laboratory air at 1000°C (blue and red dashed lines indicate the width of the zones depleted in M_6C and Cr-rich precipitates, respectively).

Table 5.2 summarizes measured volume fractions, expressed as a percentage of M_6C and the Cr-rich precipitates formed at 1000°C after 1000 and 3000 h for the three specimen thicknesses. Particularly for the thin specimens, the quantitative estimation of the volume fractions of the various precipitates in the specimen center was difficult, due to the limited width of the precipitate containing zone. Also, in the BSE images, it was difficult to distinguish between the two types of Cr-rich precipitates ($M_{23}C_6$ and Cr-nitrides) in the AnalySIS pro 5.0 software due to similarity in contrast. Thus, these precipitates were summed together in **Table 5.2**. In spite of the quantification difficulties, the results show that the volume fraction of Cr-rich precipitates in the center of the specimen increased with exposure time and the volume fraction of M_6C tended to decrease. As illustrated e.g. in **Figure 5.6** and **Figure 5.7**, Cr-rich $M_{23}C_6$ and π-phase co-existed in the core of some specimens. However, there was a clear trend that with increasing exposure time and decreasing specimen thickness the relative amount of nitride increased at the expense of $M_{23}C_6$, until in the thinnest specimen after 3000 h the Cr-rich precipitates consisted solely of nitrides (**Figure 5.8 f**).

Table 5.2: Volume fraction (%) of various types of precipitates in the specimen center after oxidation at 1000°C (see text for detailed explanation).

	Exposure time, h			
	1000	3000	1000	3000
Specimen thickness, mm	M_6C		Cr-rich precipitates	
0.2	22	13	4	6
0.3	15	9	3	9
0.5	10	8	2	12

The width of the M_6C-free subsurface zone in the 0.5 and 0.3 mm thick specimens was smaller than that of the zone free of Cr-rich precipitates (**Figure 5.8 a-e**). In the 0.2 mm specimen, a similar trend was observed in the specimen oxidized for 1000 h (**Figure 5.8 c**). However, the area in which Cr-rich precipitates (here π-phase) were present after 3000 h was limited to a narrow zone of approximately 50 µm around the center of the specimen. Hardly any precipitates of M_6C were found (**Figure 5.8 f**).

Table 5.3 summarizes the widths of the carbide/nitride free subsurface zones after the 1000°C exposures shown in **Figure 5.8**. The data illustrate that the widths of the zones which were free of Cr-rich precipitates increased with increasing exposure time and specimen thickness. An exception is the thickest specimen in which the Cr-rich precipitate free zone after shorter

exposure time was larger than after 3000 h. That however, may be caused by the fact that the Cr-rich precipitates in the specimen oxidized for 1000 h were very small and the measurements might be subject to a larger error.

Table 5.3: Depth of the subsurface zones (in µm) which were free of M_6C and Cr-rich precipitates (carbides and nitrides) in specimens oxidized at 1000°C.

	Exposure time, h			
	1000	3000	1000	3000
Specimen thickness, mm	M_6C		Cr-rich precipitates	
0.2	41	67	77	90
0.3	49	79	96	121
0.5	74	91	134	126

To illustrate the effect of temperature, **Figure 5.9** shows the microstructures of 0.2 mm thick alloy 230 specimens oxidized for 1000 and 3000 h at 950°C as well as 1000 and 2000 h at 1050°C. At both temperatures, a subscale region free of carbide and nitride precipitates developed as a result of Cr consumption by oxide scale formation, like at 1000°C. However, the widths of these precipitate free zones were much less pronounced at the lowest oxidation temperature. After 1000 h oxidation, the enrichment of the Cr-rich precipitates in the specimen center at 950°C (**Figure 5.9 a**) was, as expected, far less significant than observed after exposure at 1000°C (**Figure 5.8 c**) and at 1050°C (**Figure 5.9 c**). To compare the size and amount of the precipitates after long time of oxidation at 950°C (**Figure 5.9 b**) with that at 1000°C (**Figure 5.8 f)** and 1050°C (**Figure 5.9 d**), the temperature effect on the enrichment of the Cr-rich precipitates becomes more significant. (Note that the 1050°C specimen was stopped after 2000 h due to occurrence of breakaway oxidation at the specimen corners, as will be further discussed in Chapter 6.)

Both the 0.2 and 0.5 mm thick specimens exposed at 950°C contain M_6C and Cr-rich precipitate phases (**Figure 5.10**). The images in **Figure 5.10** indicate that the volume fraction of the Cr-rich precipitates near the specimen center increased with increasing oxidation time (compare **Figure 5.10 a** with **Figure 5.10 b** and **Figure 5.10 c** with **Figure 5.10 d**) and decreasing specimen thickness (compare **Figure 5.10 a** with **Figure 5.10 c** and **Figure 5.10 b** with **Figure 5.10 d**) as was already observed for the specimens oxidized at 1000°C.

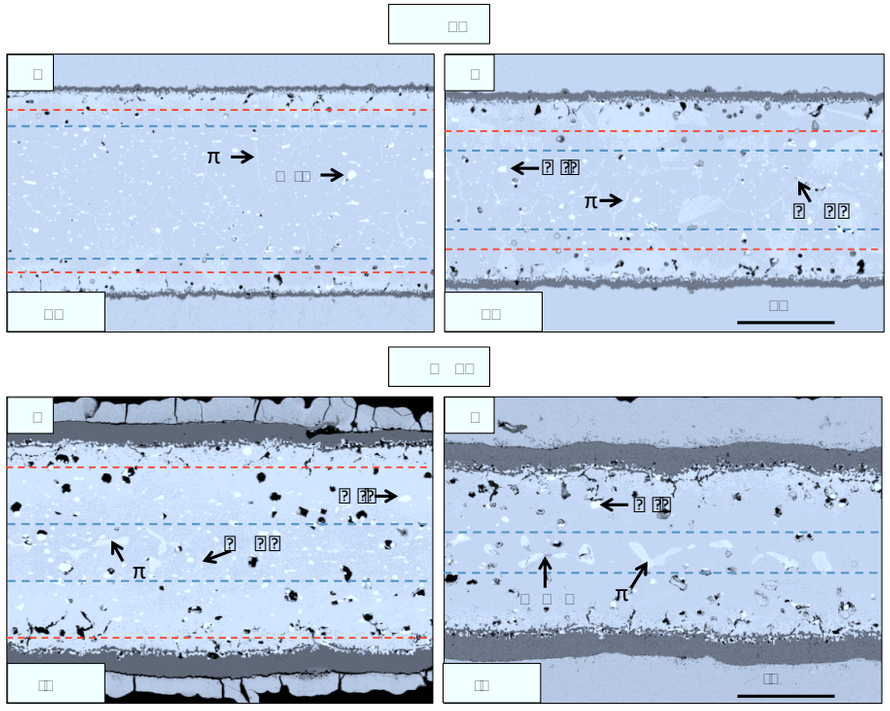

Figure 5.9: BSE images of 0.2 mm thick alloy 230 specimens after reaction for a) 1000 h and b) 3000 h at 950°C h and c) 1000 h and d) 2000 h at 1050°C in laboratory air (Blue and red dashed lines indicate the width of the zones free of M_6C and Cr-rich precipitates respectively)

It is interesting to note that for the 0.2 mm specimens after 1000 and 3000 h as well as for the 0.5 mm specimen after 3000 h precipitates of M_6C as well as Cr-rich carbide and nitride were found. However, for the 0.5 mm specimen after 1000 h, no indications of the presence of Cr-rich carbides could be detected.

At 1050°C, for the 0.5 mm specimen, the dissolution of the M_6C carbides in the subscale region was similar to the observations at 1000°C. A subsurface zone depleted in carbide and nitride was clearly apparent after the 1000 h exposure (**Figure 5.11**). The Cr-rich precipitates in the center after 3000 h exposure mainly consisted of nitride. There was a tendency that some M_6C precipitates appeared again after 3000 h (**Figure 5.11**) in the subsurface zone. A similar observation was made for the 0.3 mm specimen. For the 0.2 mm specimen after 2000 h, only a very narrow Cr-nitride layer was present in the specimen center, showing similar features as after 3000 h at 1000°C (**Figure 5.8 f** and **Figure 5.9 d**).

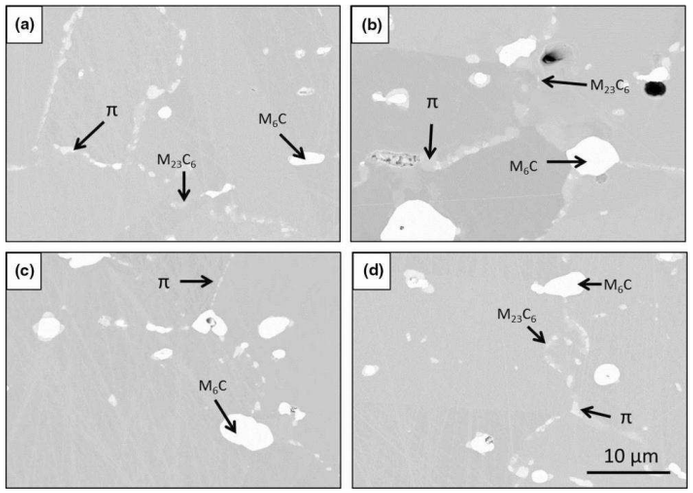

Figure 5.10: BSE images showing microstructure in center of alloy 230 specimens after reaction for a, c) 1000 h and b, d) 3000 h at 950°C in laboratory air. Specimen thickness: a, b) 0.2 mm and c, d) 0.5 mm. Grey appearing phases are Cr-rich precipitates, light appearing phases are Ni/W-rich M_6C.

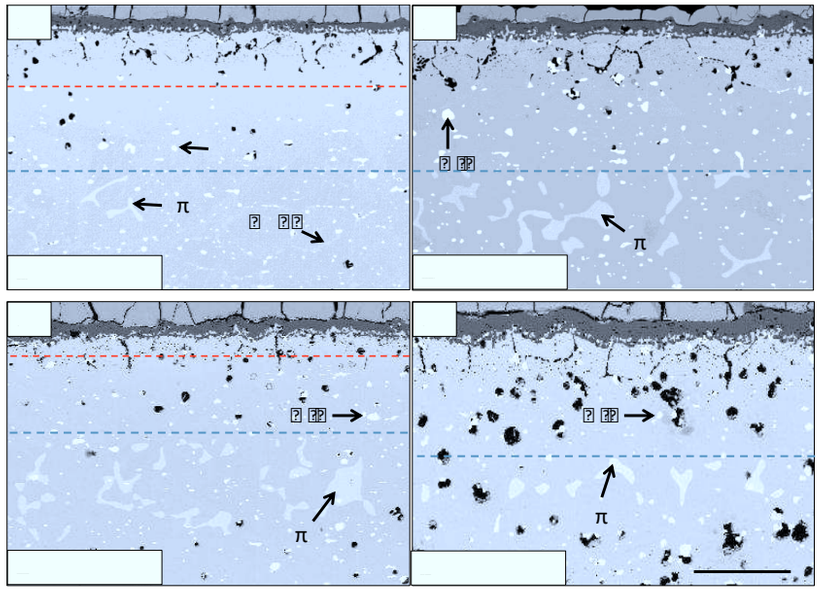

Figure 5.11: BSE images of a, b) 0.5 mm, c, d) 0.3 mm after reaction for a, c) 1000 h and b, d) 3000 h in laboratory air at 1050°C (blue and red dashed lines indicate the width of the zones depleted in M_6C and Cr-rich precipitates, respectively).

5.4 Modeling dissolution of M_6C and enrichment of $M_{23}C_6$

It is well established that long term, high temperature exposure of Ni base alloys generally results in precipitate coarsening [130]. In the present case, however, the precipitate size and morphology was mainly affected by subscale changes in alloy composition, especially due to the Cr depletion for these relatively thin specimens oxidized at high temperature. The experimental results show that the Cr depletion leads to formation of precipitate free subscale zones and the widths of these zones for the various precipitate types (carbides and nitrides) differ substantially. Also, the volume fraction of Cr-rich precipitates ($M_{23}C_6$ and Cr-nitrides) in the specimen center increased with time. In most samples, the amount of $M_{23}C_6$ was larger after 1000 h than after 3000 h, where mainly nitrides were found. These effects increased with increasing temperature and decreasing specimen thickness. At the extreme of the 0.2 mm thick specimen after 3000 h at 1000°C and 2000 h at 1050°C, the M_6C carbide tended to vanish completely.

Thermodynamic calculations using Thermo-Calc and the data base TTNI7 [137] revealed that for the C content (i.e. 0.09 wt. %) prevailing in the as-received alloy 230, only γ-Ni and M_6C exist in addition to a very minor amount of Cr-rich nitride. Based on the experimental findings (**Figure 5.7**), it was assumed in the calculations that π-phase was the only Cr-rich nitride which may be formed. If the C content was increased to ~0.16 wt. %, the calculation predicted $M_{23}C_6$ formation with a corresponding decrease in M_6C fraction as the C content further increased (**Figure 5.12**). As the major precipitate phase in the as-received material is M_6C carbide, the first part of the following discussion focuses on the carbides and initially ignores the nitrides.

To assist in understanding the mechanism of the observed microstructural changes in alloy 230 during oxidation, a section of the Ni-Cr-W-Mo-C phase diagram at 1000°C was calculated with fixed 14 wt. % W and 2 wt. % Mo. The trends discussed for 1000°C are qualitatively similar for the range of temperatures studied. The phase diagram together with C iso-activity lines are shown in **Figure 5.13**. (An iso-activity line is a locus of compositions in the phase diagram for which the chemical potential (i.e. activity) of the selected element (here C) is constant.) Point A in **Figure 5.13** indicates that the bulk composition of alloy 230 is located in a two-phase field in which the Ni-matrix is in equilibrium with the W-rich M_6C carbide, as shown in **Figure 5.12**.

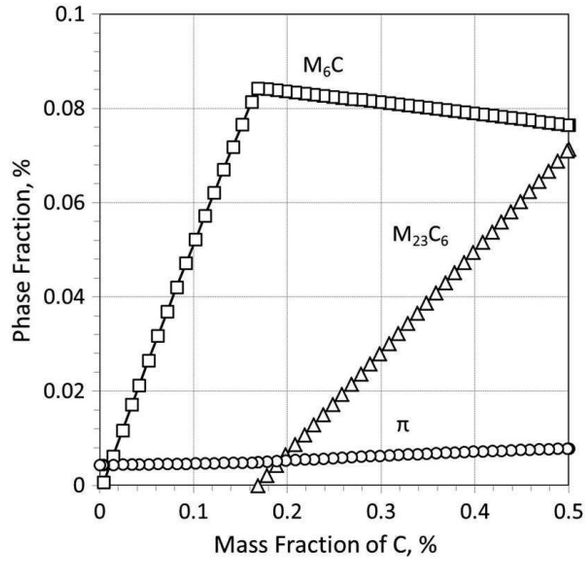

Figure 5.12: Molar fractions of different phases in alloy 230 as a function of C content at 1000°C (calculated by Thermo-Calc using database TTNI7). For details see text.

During high temperature oxidation, the Cr concentration at the scale-alloy interface decreases due to the continuous Cr depletion related to the scaling process (**Figure 5.3**). Moving from point A to point P in **Figure 5.13** as the Cr content decreases, results in an increase in the solubility and thus a de-stabilizing of the M_6C carbide. This may at first sight be surprising as the carbide mainly contains Ni, W and some Mo, but hardly any Cr. The reason for this dependence of M_6C solubility on Cr content is related to the thermodynamic interactions of the alloying elements in the γ-Ni matrix, specifically, the effect of Cr content on the activity of C and W. The thermodynamic calculations in **Figure 5.14** show that the W activity decreases with decreasing Cr content, thus de-stabilizing the M_6C carbide. The effect of Cr on the thermal stability of M_6C in a Ni-base alloy has been extensively discussed elsewhere [138]. **Figure 5.14** also shows that Cr depletion leads to an increased C activity. The Cr-depleted near surface region of the alloy is thus an area of high C activity compared to that in the middle of the specimen. The resulting C activity gradient creates a driving force for C to diffuse from the Cr-depleted surface region to the specimen center in order to maintain equilibrium. In **Figure 5.13**, it means that the diffusion path for this transformation will be close to the iso-activity line from point A to point B.

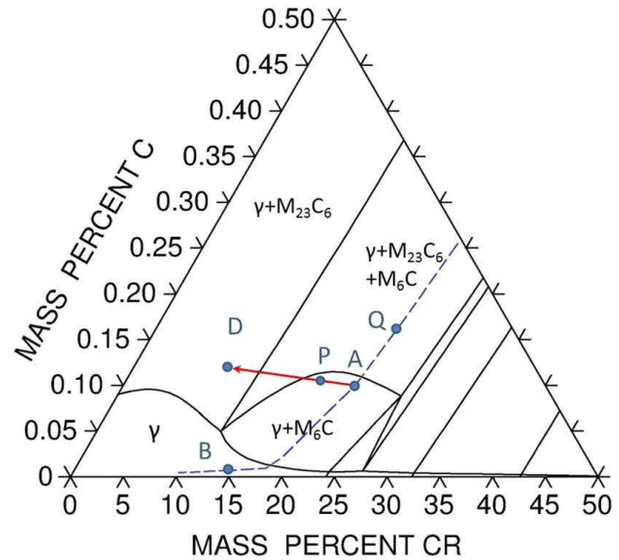

Figure 5.13: Section of the Ni-Cr-W-Mo-C phase diagram at 1000°C for constant W and Mo contents of 14 wt. % and 2 wt. %, respectively, calculated in Thermo-Calc using the TTNI7 database. The dashed line indicates iso-activity for which the chemical potential (activity) of the C is constant (a_C = □□□ □ $^{-□}$).

Back diffusion of C as a result of oxidation induced Cr-depletion has been described in previous studies, e.g. for the Ni-base alloy 617 [139-143]. The back diffusion was generally explained to be the result of the Cr-depletion induced dissolution of the Cr-rich carbide. The dissolution of the carbide obviously results in an increase of the C activity in the matrix [144], thus providing a composition gradient driving force for C diffusion towards the specimen center. The mechanisms why the higher C activity in the subsurface regions results in this case in C back diffusion rather than in decarburization is discussed elsewhere [145].

The back diffusion of C occurring during air oxidation of alloy 230 is not related to a composition gradient as frequently described for cases that Cr depletion results in dissolution of Cr-rich carbides [139]. Here the back diffusion occurs due to an activity gradient which drives diffusion. The increased C activity is mainly due to the effect of Cr loss on M_6C stability (as described above) and the thermodynamic interaction among Cr, C and W in the γ-Ni matrix.

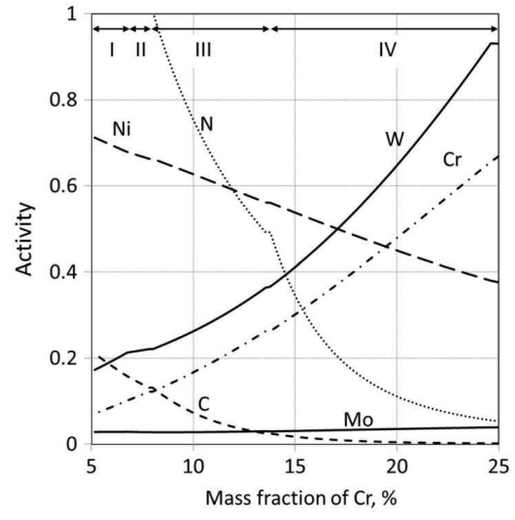

Figure 5.14: Activities of different elements in alloy 230 as a function of Cr content at 1000°C, calculated by Thermo-Calc. Areas indicated I–IV relate to phase fields γ+$M_{23}C_6$, γ+ $M_{23}C_6$ + M_6C, γ+ M_6C+M(N,C) and γ+ M_6C +π, respectively.

Obtaining quantitative experimental confirmation of the C enrichment in the specimen center is not possible from EDX or WDX measurements e.g. due to the multiphase character of the microstructure. A suitable method for measuring the total C content is GDOES. However, depth profiling by sputtering through the surface scale and the relatively wide subscale depletion zone results in a very deep sputter crater. It is well established that the measurement accuracy may substantially decrease with increasing crater depth, because of crater side effects and non-flatness of the sputter crater [146, 147]. Therefore, a different approach was used to measure the C and N contents in the specimen center. Specimens of 0.5 mm thickness after exposure at 1000°C for 1000 and 3000 h (compare microstructures in **Figure 5.8 a** and **b**) were carefully ground till reaching the center of the specimen. This procedure was unfortunately not possible for the 0.3 and 0.2 mm specimens due to the limited accuracy of the grinding method and the very limited width of the precipitate containing zones (**Figure 5.8**)

The ground surfaces, corresponding to the center of the 0.5 mm specimens, were analyzed by GDOES. For obtaining the relative sensitivity factors [148] for the various elements, a non-exposed alloy 230 specimen was analyzed using the same sputtering parameters as used for the two oxidized specimens, taking into account the known bulk alloy composition

(**Table 5.1**). The quantified depth profiles as a function of sputtering time for the specimen exposed for 3000 h in **Figure 5.15 b** shows that the average C content in the specimen center was 1.03 at. % (compared to 0.48 at. % present in the as-received material). For the 1000 h exposure shown in **Figure 5.15 a** the C content in the specimen center was 0.74 at. %. **Figure 5.15 b** also indicates that for the 3000 h specimen at a depth corresponding to a sputtering time of approximately 1300 s the C content decreased, eventually reaching values which were even lower than the C content in the as received material. The sputter time at which this effect occurs thus corresponds to the interface with the subscale carbide free zone shown in **Figure 5.8 d**. These results clearly illustrate that indeed a C back diffusion occurred as a result of the mechanisms described above. After the 3000 h exposure at 1000°C, this resulted in an approximate doubling of the C content in the center of the 0.5 mm specimen.

Specimen or component thickness is an important consideration for the discussion of the oxidation induced microstructural changes. In thin specimens, as were studied here, the Cr reservoir was limited. In addition, the C diffusing from the surface near regions will enrich in the center. For a component several millimeters thick, the C released from the subsurface depletion zone will only make a minor change in the C content of the wide zone at the center of the component. However, for the very thin specimens studied here, the width of the subsurface depletion zone becomes eventually similar or larger than the width of the remaining carbide-containing zone after long times and/or at the highest temperatures, e.g. **Figure 5.8 f**. Even for the 0.5 mm specimen, the C content in the specimen center after a 3000 h exposure approximately doubled compared to that in the as-received material, as shown in **Figure 5.15**. In **Figure 5.13**, this increase in C content would correspond to movement on the iso-activity line to point Q. Once the C concentration exceeds 0.14 wt. %, Cr-rich $M_{23}C_6$ becomes stable with a resulting decrease in the Cr concentration in the γ-Ni matrix. For simple geometrical reasons it is apparent that the relative enrichment of C in the specimen center will tend to be even larger for the 0.3 and 0.2 mm specimens.

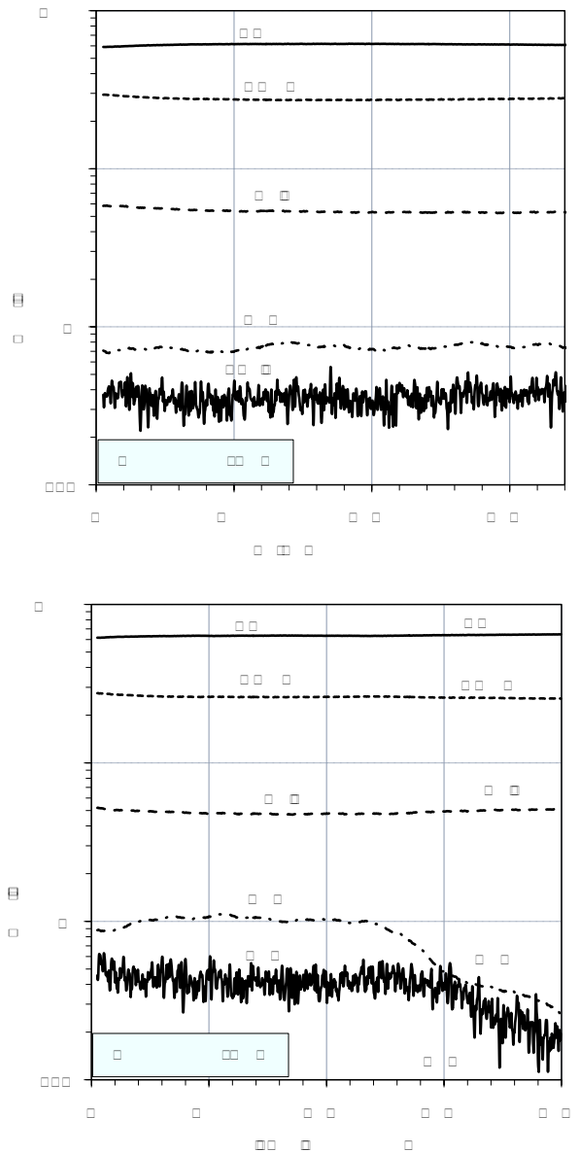

Figure 5.15: Element concentrations as function of sputter time for 0.5 mm alloy 230 specimen after 1000 and 3000 h exposure at 1000°C. Before the GDOES measurement, the specimens were ground to half thickness. Thus, the left part of the diagram (sputter time equals 0 s) corresponds to the center of the specimen. Averaged concentrations of the various elements in the respective regions are inserted in the graphs.

For the case when the W-rich M_6C carbides completely dissolved in the 0.2 mm thick specimen after 3000 h at 1000°C (**Figure 5.8 f**), the Cr profile showed significant Cr depletion across the entire specimen, such that the average Cr content in the specimen had dropped from 22 down to ~12 wt.% (**Figure 5.3 b**). In **Figure 5.13**, that depletion corresponds to the red arrow path from point A to point D and a transition from the three-phase field γ-Ni + M_6C + $M_{23}C_6$ region towards the two-phase field γ-Ni+$M_{23}C_6$ region with no M_6C present. One assumption in **Figure 5.13** is that the concentration of W and Mo remain at the original levels of 14 wt. % and 2 wt. % respectively. In reality, however, the Cr depletion may affect the activities of these elements (**Figure 5.16**), thus establishing W and Mo activity gradients between the subscale depletion zones and the specimen center.

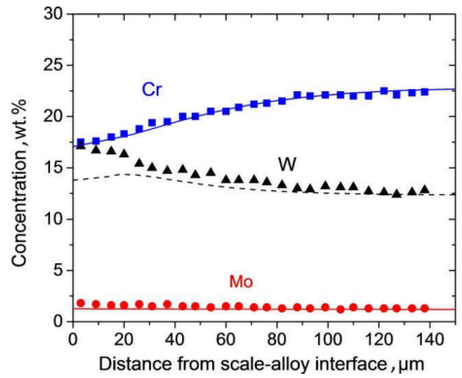

Figure 5.16: Cr, W and Mo concentration profiles in the γ-Ni matrix measured by EDX (symbols) in the 0.3 mm thick specimen of alloy 230 compared with DICTRA calculations (lines) after 1000 h oxidation at 1000°C in laboratory air. Measured oxidation kinetics used as input for the calculation was taken from the gravimetric data in **Figure 5.1**.

For developing a more detailed description of the mechanism of the $M_6C/M_{23}C_6$ transformation discussed above, a set of calculations was performed in DICTRA to simulate the experimentally observed oxidation-induced phase transformations. Similar to the thermodynamic calculations, five elements were taken into account, i.e. Ni, Cr, W, Mo, and C. A time-dependent outward Cr flux, derived from the experimentally determined oxidation data, was set as a boundary condition to simulate the oxidation induced Cr depletion, using the procedure described in reference [144]. **Figure 5.16** shows the calculated and measured concentration profiles in a 0.3 mm thick specimen after oxidation for 1000 h at 1000°C. Good agreement between the measured and calculated Cr profiles was obtained, which implies that

the Cr depletion kinetics were accurate. However, the calculated W profile did not completely match with the experimental one in the near-surface region, although the W subsurface enrichment was qualitatively correct. The reason for the inaccuracy is likely related to the inability of DICTRA to take into account the interface displacement due to metal consumption by the scaling process. While this effect is virtually negligible for thick specimens, the moving boundary effect distorts the depletion calculations in a 0.3 mm thick specimen. For a better quantitative description of the depletion kinetics, interface displacement has to be implemented into the model. However, commercial software packages like DICTRA do not provide this option so far. Modeling approaches developed to account for this effect were described elsewhere [140, 144], but fall outside the scope of the present investigation.

According to the thermodynamic calculations (see **Figure 5.12**), the $M_{23}C_6$ carbide is not stable in the as-received condition in alloy 230. Based on the above considerations, it formed in the specimen center after back diffusion has resulted in an overall C content higher than the critical value of 0.16 wt. %. The C migration from the Cr depleted zone towards the specimen core is a dynamic process and it requires a certain time until the C enrichment in the center of the foil exceeds the threshold for $M_{23}C_6$ formation, which is 0.14 wt. % at 1000°C, according to the calculated phase diagram (**Figure 5.13**). For a given oxidation condition (i.e. depth of Cr depleted zone) the critical C concentration required for formation of the Cr rich carbide will be reached after shorter oxidation times in a thin than in a thick specimen. This is in agreement with the 950°C results presented in **Figure 5.10**.

The DICTRA calculations in **Figure 5.17** thus at least qualitatively correctly describe:

(1) the formation of a subscale M_6C depleted zone,

(2) the formation of initially unstable Cr-rich $M_{23}C_6$ carbide in the specimen center due to the subscale Cr depletion and the C back diffusion, and

(3) the accompanied decrease in the M_6C volume fraction.

The total calculated decrease in volume fraction of M_6C was smaller than experimentally observed. This discrepancy is related to the formation of nitride along with oxidation induced Cr depletion in the specimen center, as will be illustrated in the following section.

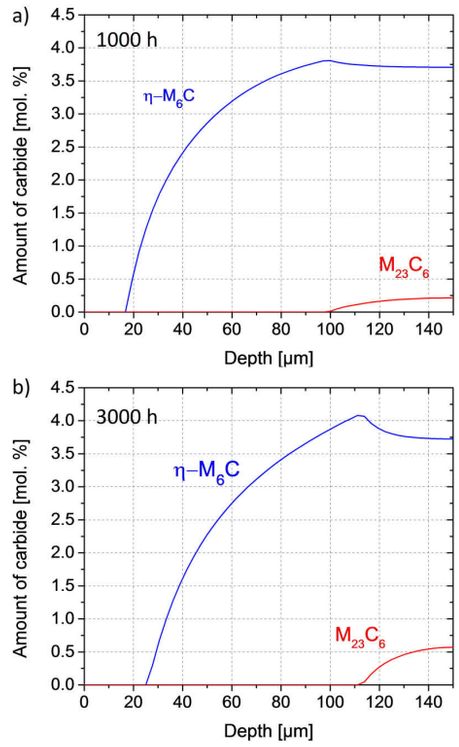

Figure 5.17: DICTRA calculation profiles showing volume fractions of M_6C and $M_{23}C_6$ in the 0.3-mm-thick specimen of alloy 230 after a) 1000 h and b) 3000 h at 1000°C in laboratory air. Input kinetics was taken from **Figure 5.1**, starting alloy composition from **Table 5.1**, and calculations in **Figure 5.12**.

5.5 Modeling the formation of nitride in the center of specimen

The high volume fractions of nitride especially in the thin specimen after long exposure time are indicative of nitridation. Apart from back diffusion of N similar to that of C, there was also substantial N ingress from the environment. In the current type of experiments involving oxide growth, oxide spallation and N uptake it was virtually impossible to accurately estimate the nitridation kinetics and the incubation time before nitridation appears to occur after the occurrence of certain Cr depletion. With so many experimental unknowns, diffusion calculations would be extremely inaccurate and inconclusive.

Therefore, another attempt was made to rationalize the experimentally observed microstructural changes, on the basis of phase equilibria calculated by Thermo-Calc using the data base TTNI7. Based on the activity data in **Figure 5.14** the subscale Cr depletion would result in a back diffusion of N in a similar manner as described for C. This was confirmed by the GDOES results shown in **Figure 5.15**. Although the measured concentrations for N were nearer to the detection limits (as indicated by the larger noise to signal ratio) than is the case for C, the results clearly revealed that an increase of the N content in the specimen center occurred whereby the N content increased with increasing exposure time. The database TTNI7 considers various types of nitride phases, i.e. mainly Cr_2N. The nitride phase present after a very short (100 h) exposure time (**Figure 5.4**) could, as described in previous sections, not unequivocally be identified. The nitride in the specimen center, however, could clearly be correlated with π-phase (see **Figure 5.7 b**). The composition of this phase at 1000°C for the alloy 230 composition in the data base TTNI7 is 57Cr-36Ni-2Mo-5N (in wt.%). Compared to the actually measured nitride composition (39Cr-32Ni-24W-4Mo-1N in wt. %) the database TTNI7 did not take into account W solubility, however, Mo solubility was correctly described.

Assuming in the calculations that π-phase is the only nitride formed, alloy 230 should at 1000°C exhibit a microstructure consisting of γ-Ni matrix, W-rich M_6C and very minor amounts of π-phase (**Figure 5.12**). A doubling of the C and N content (see **Figure 5.15**) by back diffusion resulted in the formation of a four phase microstructure consisting of γ-Ni matrix, W-rich M_6C, Cr-rich $M_{23}C_6$ and π-phase (**Figure 5.18 a**).

Considering the densities of the mentioned phases (9 $g.cm^{-3}$ for γ-Ni [149], 14.2 $g.cm^{-3}$ for M_6C [150] and 6 $g.cm^{-3}$ for π-phase [151]) reveals that the volume fraction of M_6C in the alloy region which is not affected by oxidation induced depletion processes, is approximately 2.7 vol. % whereas the volume fraction of π-phase is extremely small. If one assumes that the back diffusion of N would in the 0.3 and 0.2 mm specimens result in a N content of 0.18 wt. %, i.e. even higher than found for the 0.5 mm specimen after 3000 h (**Figure 5.15**), the volume fraction of π-phase would be 3.9 %. This is substantially lower than that experimentally observed for the thinnest specimens after 3000 h at 1000°C (**Table 5.3**).

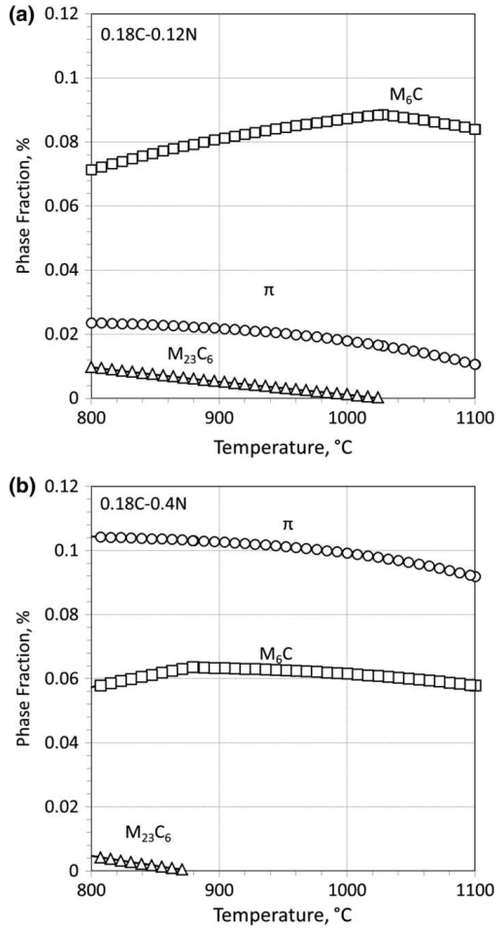

Figure 5.18: Calculated phase fractions in alloy 230 as function of temperature for various C and N contents. For details, see text.

This leads to the conclusion that upon increasing exposure time and decreasing specimen thickness the high volume fraction of nitride in the specimen center was not only related to back diffusion of N but additionally to uptake of N from the atmosphere (**Figure 5.18 b**). This is probably related to the fact that the substantial decrease in Cr interface concentration substantially lower than ~15 wt. % occurred during long term exposure (**Figure 5.3**) resulted in a loss of protective properties of the surface oxide scale, which then may become prone to transport of gas molecules such as N_2.

Assuming a doubling of C content (due to back diffusion) and an even greater than doubling of the N content in the specimen core, the resulting calculated phase fractions are shown in

Figure 5.18. Here the C content was set at twice the original value and the N content arbitrarily to a high value of 0.4 wt. %, i.e. substantially higher than twice the original value used in **Figure 5.18**. This resulted in a substantial increase in the phase fraction of π-phase and at 1000°C, a slight decrease in phase fraction of M_6C as well as a vanishing of the $M_{23}C_6$, which is in agreement with the experimental observations (**Figure 5.8 e** and **f**). The dissolution of the Cr-rich carbide will obviously result in an increase of the C activity in the center of the specimen. This is expected to result in a re-distribution of C in the specimen. This may be the qualitative explanation for the observations illustrated in **Figure 5.11** where after 1000 h a subscale M_6C-free zone was clearly found, whereas after 3000 h this was not the case.

The thermodynamic calculations in **Figure 5.18 b** do not predict that the formation of large volume fractions of Cr-rich nitrides after long times in the thinnest specimens is accompanied by the experimentally observed vanishing of M_6C (**Figure 5.8 f** and **Figure 5.9 b**). The effect occurs when the overall Cr content in the specimen core starts to decrease (**Figure 5.3**). The discrepancy between calculation and experiment might be related to the fact that the π-phase in the database TTNI7 does not consider W solubility. This is contrary to the experimentally observed composition in which typically 24 wt. % W was present in the π-phase. Due to this high W solubility, formation of π-phase is expected to substantially decrease the W content in the γ-matrix which obviously should have a destabilizing effect on the Ni/W-rich M_6C phase. The vanishing of the M_6C phase (**Figure 5.8 f** and **Figure 5.9 b**) in the specimen core is thus likely caused by a combination of the substantial oxidation induced Cr loss and the consumption of W by formation of the W-containing nitride.

6 Development of lifetime diagram for alloy 230

6.1 Current approach

In the following an attempt will be made to develop a generalized, pragmatic approach which aims to cover the three main oxidation related damage processes mentioned in Section 3.3. Previous approaches for alumina forming FeCrAl base ferritic steels [32] and chromia forming ferritic steels [26] present graphically solely times to breakaway as function of component thickness and temperature. For this type of materials this approach is useful because the oxidation induced wall thickness loss is in many practical applications extremely small due to the very low growth rates of the (reactive element doped [25, 30]) alumina (and chromia) surface scales. Thus, for these materials a critical aluminium (or chromium) depletion resulting in breakaway oxidation mostly occurs before wall thickness loss and/or scale spalling become practically significant. Also, the time to occurrence of a critical solute depletion (resulting in "breakaway" oxidation) is easy to be determined experimentally. Because of the large difference in k_w value of Al- and Cr- oxide compared to Fe-oxide (**Figure 3.4**), occurrence of breakaway is accompanied by a sudden, dramatic increase in scale growth rate due to a change from alumina (or chromia) scale formation to Fe-base oxide formation.

Due to an earlier tendency for spalling of the chromia base surface scales, the situation is different in case of NiCr-base wrought alloys. For thicker specimens (e.g. in the mm range) wall thickness loss and/or scale spalling may become life limiting factors for a component in service far before breakaway type oxidation occurs. Additionally, the definition of the "time to breakaway" is for NiCr based alloys far less obvious than e.g. in case of the above mentioned FeCrAl alloys because a critical chromium depletion leads to a change from chromia growth to growth of (chromium containing) nickel rich spinel types oxides. This causes an increase of the growth rate, however, because of the relatively small k_w-value of these mixed oxide and NiO (**Figure 3.4**) the change tends to occur gradually, i.e. not abrupt as known from the FeCrAl base alloys and, to a lesser extent, the FeCr base alloys.

For FeCr- and FeCrAl alloys [26, 32], the time at which breakaway oxidation occurs was termed t_B. For NiCr alloys, a sudden rapid increase in growth rate does generally not occur and therefore the expression "critical depletion" seems for these alloys to be more appropriate

than “breakaway”, The time at which the Cr content at the alloy/scale interface reaches a pre-defined critical concentration is therefore in the following designated as t*. A second critical time, t_C indicates the time when the Cr depletion profile reaches the center of the specimen [24].

According to reference [152], t_C can be estimated with **Eq. (6.1)** [24].

$$\approx \frac{l^2}{D} \tag{6.1}$$

where l is the half thickness of the specimen in cm and D the diffusion coefficient of Cr in the alloy in $cm^2.s^{-1}$. The schematic in **Figure 6.1** illustrates a comparison of t_C and t*. It illustrates that generally t_C provides a conservative prediction of the lifetime limit. Additionally, **Eq. (6.1)** shows that t_C is independent of the oxide growth rate. Thus, for a given alloy, the time till reaching a critical Cr interface concentration would be independent of the scale growth rate; this would obviously not be in agreement with experimentally observed oxidation degradation mechanisms.

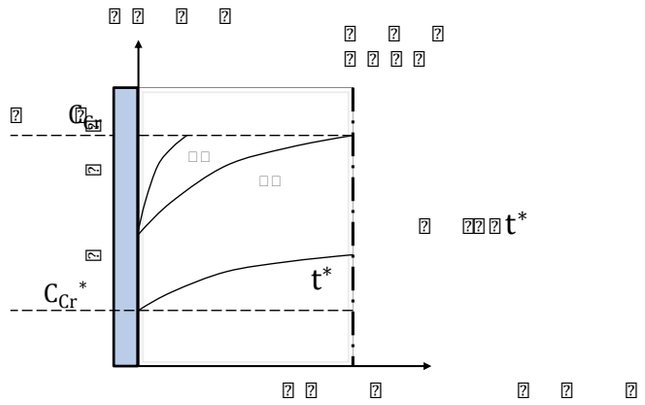

Figure 6.1: Schematic graph showing concentration profiles of scale forming element after different oxidation times in case of steady state scale growth illustrating difference in definition of times to critical subscale depletion (t_C and t*).

Based on the above discussions, a different way of graphically presenting the design relevant oxidation damage will be attempted, i.e. presenting wall thickness loss as function of time and temperature, thereby indicating in the graphs times (t*) for occurrence of breakaway type oxidation as function of specimen thickness.

6.2 Oxidation and depletion kinetics

The area specific (net) weight changes of the specimens during 3000 h discontinuous oxidation are shown as a function of oxidation time in **Figure 6.2**. The data were, in a different way of presentation, already shown in Section 5.2, but are summarized here again for easier readability of the text.

Figure 6.3 - Figure 6.5 show polished cross sections of alloy 230 specimens with different thicknesses after oxidation at temperatures of 950, 1000 and 1050°C. The scales formed on the specimens at 1000°C were already shown in Section 5.2, but are presented here again for easier readability of the text. As explained in Section 5.2 a continuous external Cr_2O_3 scale formed on top of the alloy and minor internal Al_2O_3 was present along the alloy grain boundaries. In some cases, minor amounts of $MnCr_2O_4$ spinel phase were found on top of the chromia. In agreement with the gravimetric data in **Figure 6.2 b c,** the 0.2 mm specimen has the thickest Cr_2O_3 layer (**Figure 6.4 b** and **Figure 6.5 a b**), whereas the Cr_2O_3 layer on the top of the 0.3 mm and especially the 0.5 mm specimen after 3000 h at 1000°C and 1000 h at 1050°C, exhibit local scale spallation. The latter is in agreement with the gravimetric data.

During the earlier stages of oxidation at these temperatures, the area specific weight change did, as explained in Section 5.2 not exhibit a clear specimen thickness dependence (**Figure 6.2**). At 1000°C, similar behavior was observed for all three specimen thicknesses up to ~600 h. At 1050°C, this period was much shorter (~200 h) whereas at 950°C it took approximately 2000 h before clear differences in weight change between thick and thin specimens became apparent.

In case of the 0.2 mm specimens, the weight change curves increased after this initial steady state oxidation period, continuously following a “super-parabolic” oxidation behavior at all temperatures. The decrease of the net weight changes of the 0.3 and 0.5 mm thick specimens occurring after this steady state scale growth was the result of scale spallation as corfirmaed by the grow weight change data (**Figure 5.1**). The amount of spalled oxide of the 0.5 mm specimen was larger than that of the 0.3 mm specimen. For the 0.2 mm specimens at 1000-1050°C, the scale did not spall significantly until the maximum exposure time of 3000 h. In other words, the thinnest specimens exhibited far better scale adhesion than the thicker ones.

a)

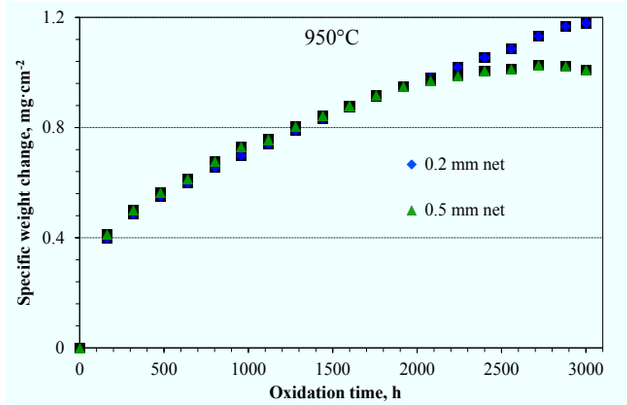

b)

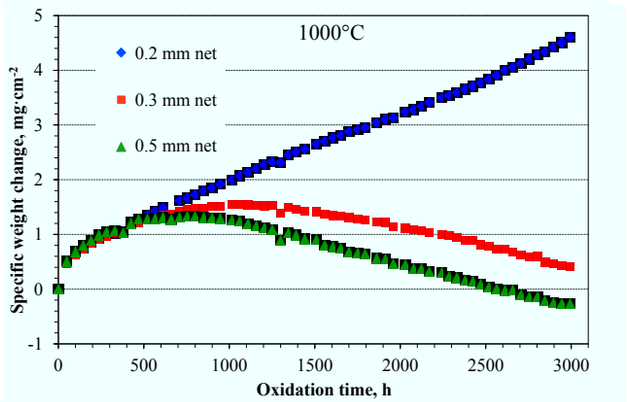

c)

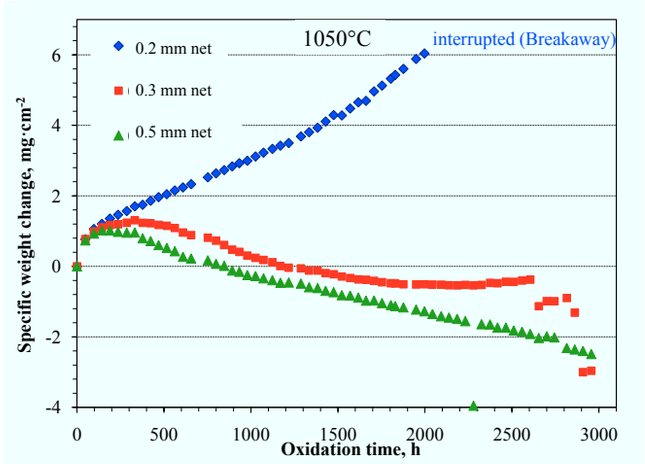

Figure 6.2: Area specific net weight change curves of alloy 230 specimens with different thicknesses during oxidation for 3000 h at a) 950°C (10 h cycle), b) 1000°C (48 h cycle), and c) 1050°C (48 h cycle).

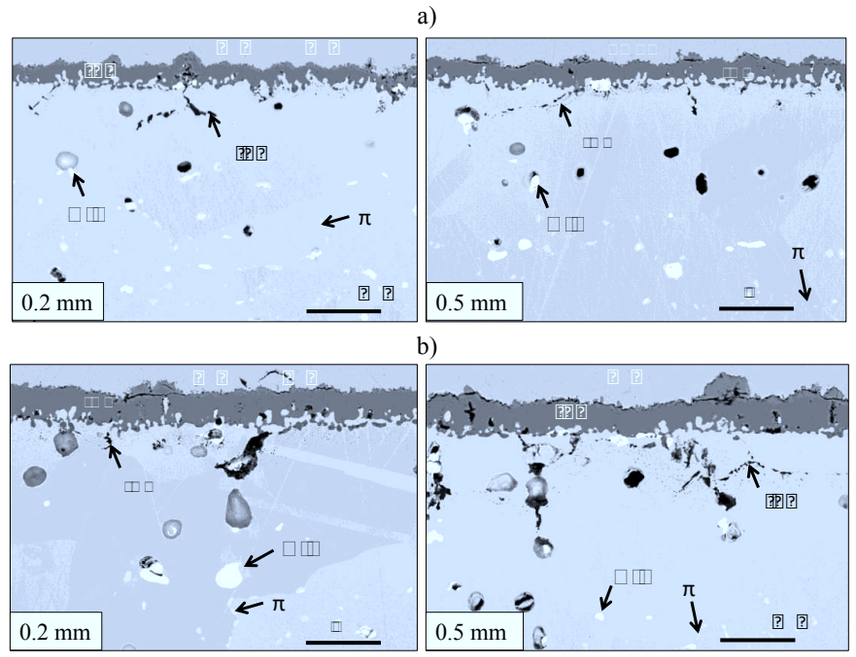

Figure 6.3: BSE images showing cross sections of alloy 230 specimens with different thicknesses oxidized at 950°C in air for a) 1000 h, and b) 3000 h.

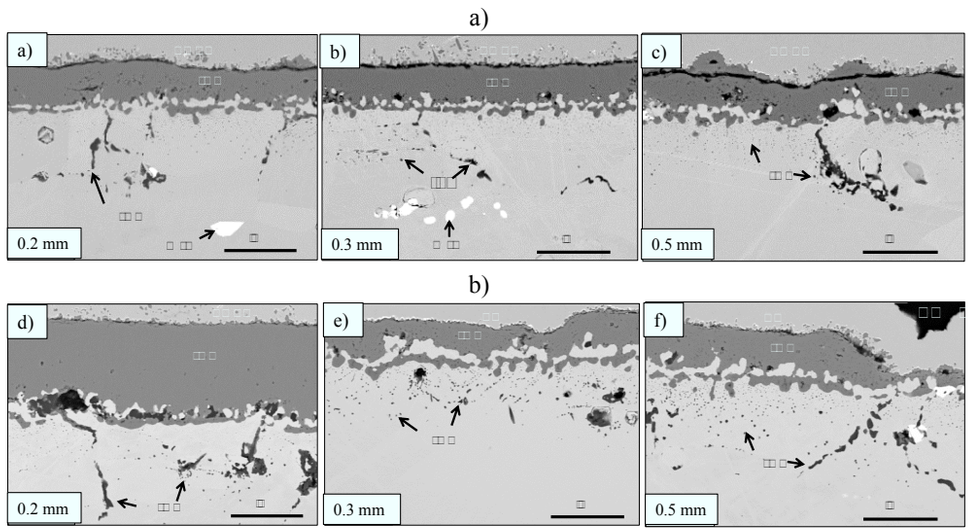

Figure 6.4: BSE images showing cross sections of alloy 230 specimens with different thicknesses oxidized at 1000°C in air for a) 1000 h, and b) 3000 h.

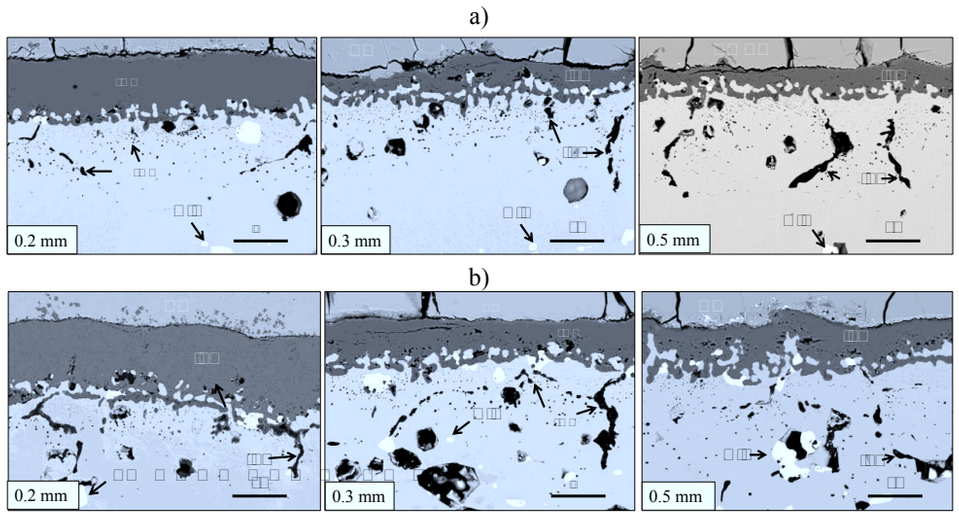

Figure 6.5: BSE images showing cross sections of alloy 230 specimens with different thicknesses oxidized at 1050°C in air for a) 1000 h, and b) 3000 h.

This is in qualitative agreement with findings of other authors [53, 126, 153, 154]. It is generally assumed that this difference in adherence is related to different modes of stress relaxation. The thermal stresses produced by thermal cycling in the scale and the bulk alloy of the thicker specimens are relaxed by scale cracking eventually resulting in scale spallation [15, 125, 155, 156]. For the 0.2 mm specimens, the stress was likely relaxed by substrate creep in the high temperature range during cooling of the sample, resulting in better scale adherence [155]. It is interesting to note that the 0.2 mm specimens started to exhibit "super-parabolic" oxidation after a given oxidation time, which increased with decreasing temperature. In Section 5.2 it was proposed that this enhanced oxide growth rate may be related to depletion of the reactive element La in the alloy [58, 113], to relaxation of growth stresses [129], or, more likely, to formation of micro tensile cracks in the oxide after specimen re-heating, which allows ingress of oxygen through the cracks resulting in faster oxide formation.

Figure 6.6 is a schematic of the generation of different stress states in the scale depending on specimen thickness. The horizontal axis represents the temperature, here using as an example 1000°C as the target temperature. The vertical axis represents the stress in the oxide, where σ_T indicates a tensile stress, and σ_C a compressive stress. Because the thermal expansion coefficient of the alloy (approximately $16 \cdot 10^{-6}$ K^{-1}) is larger than that of the chromium oxide ($6.5 \cdot 10^{-6}$ K^{-1}), the alloy substrate undergoes more volume contraction than the scale during

cooling, resulting in generation of a tensile stress in the alloy and a compressive stress in the scale [125, 155]. At the beginning of the cooling process, i.e. at relatively high temperature, the thinner specimen tends to creep due to the tensile stress generated in the substrate [155]. This effect will be far less pronounced in the thicker specimen because of the smaller tensile stress in the substrate [129]. The creep of the thin substrate causes partial relaxation of the compressive stress in the scale. The rate of creep deformation slows down with decreasing temperature and finally ceases; then both the alloy and the oxide follow elastic behavior.

Upon subsequent rapid heating to the oxidation temperature, thinner specimens, for which the residual compressive stress in the oxide at room temperature is smaller than for thicker specimens, will finally generate tensile stresses in the oxide upon approaching the target temperature (see the dashed lines in **Figure 6.6**). The tensile stress reached in the oxide at the target temperature increases with decreasing specimen thickness [129]. Therefore, the scales on thinner specimens have a larger tendency to exhibit micro-tensile-cracking than those on thicker specimens [129]. The tensile stress in the metal in case of the thick specimen is not large enough to cause substantial creep during cooling. The room temperature residual stress in the scale is sufficient that the oxide is prone to spallation when the scale reaches sufficient thickness in combination with existing micro-damage (e.g. voids) [15].

The substrate creep during cooling and thus the resulting tensile cracking of the oxide scale occurring during reheating in case of the thinnest specimens will only become significant after the oxide has reached a certain thickness [71, 129], i.e. after the tensile stress in the substrate exceeds a certain critical value. The tendency to spalling observed for the thicker specimens is well known to increase with increasing specimen thickness and is affected by formation of microstructural defects within the scale and/or at the scale/alloy interface as a result of the scale growth process [156]. This explains why the specimens of different thickness do not initially show any differences in oxidation kinetics and spallation behavior at the three test temperatures (**Figure 6.2**). The effect of specimen thickness on scale spallation vanishes beyond a certain specimen thickness, here apparently around 0.5 mm (see explanation in Section 9.2) based on experiment for 1 mm specimen.

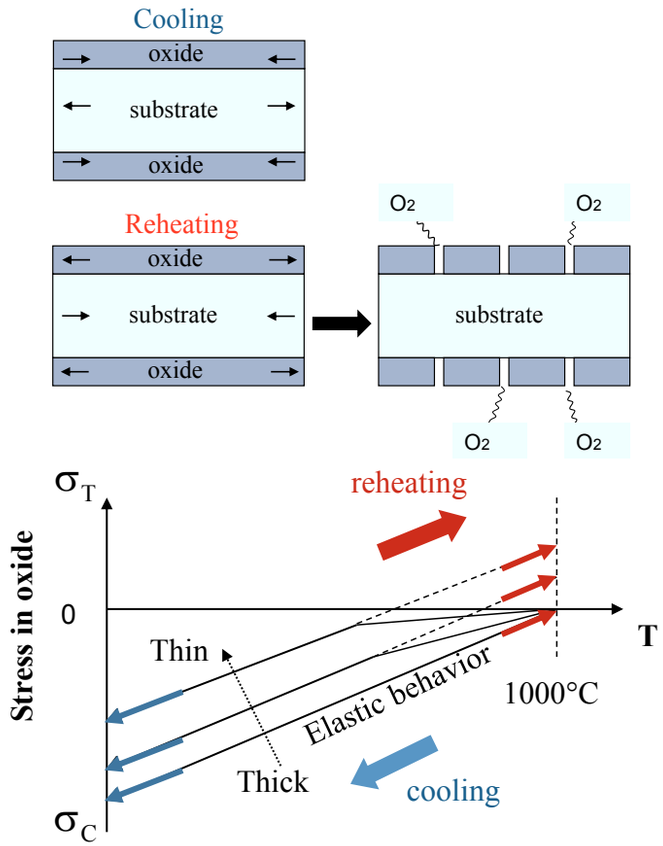

Figure 6.6: Schematic illustration of stress formation in the oxide scale during thermal cycling of specimens with three different thicknesses (based on reference [129]). Solid lines indicate behavior during cooling, dashed lines show behavior during re-heating to oxidation temperature.

6.3 Subscale depletion process

Figure 6.7 illustrates an example of the concentration profiles of Ni, Cr, W, and Mo in the bulk alloy, for a 0.5 mm specimen after 3000 h exposure at 950, 1000 and 1050°C. The concentration of Ni slightly increased in the subsurface where the Cr is depleted. The W concentration also noticeably increased in the subsurface which may be caused by a correlation between the activities of Cr and W (see Section 5.4). Depletion of Cr results in a decrease of the W activity thus providing a driving force for W to diffuse towards the surface.

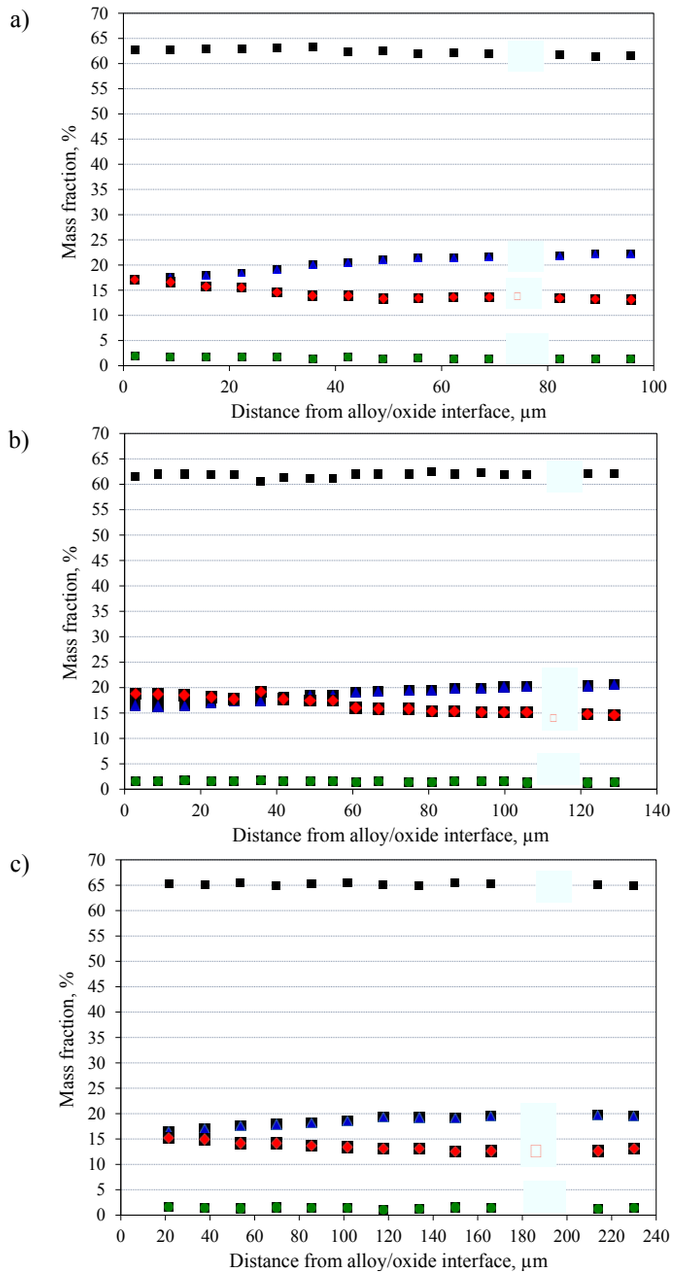

Figure 6.7: Examples of concentration profiles of Ni, Cr, W, and Mo in oxidized alloy 230 here showing the 0.5 mm specimens after 3000 h air oxidation at a) 950, b) 1000 and c) 1050°C.

The subscale Cr concentration profiles of specimens with different thicknesses after 1000 and 3000 h oxidation at 1000°C were shown in Section 5.2. **Figure 6.8** compares these data with the results obtained at 950 and 1050°C after exposure times of 1000 and 3000 h. At all temperatures the Cr profiles after 1000 h show hardly any specimen thickness dependence. Especially at 950 and 1000°C, the concentration profiles did not yet reach the centers of the 0.3 and 0.5 mm specimens, i.e. they are still in the first stage or at the beginning of the second stage of the depletion process described in Section 3.3.2. The Cr concentration at the center of the 0.2 mm specimen at 1000°C has already very slightly decreased. It should be mentioned that this slightly lower Cr content also may be caused by the back diffusion of C and N (Section 5.4 and 5.5). This process results in an enrichment of Cr rich carbide and nitride precipitates in the specimen center (see Section 5.3) and thus in a Cr depletion of the γ-Ni matrix, i.e. the value actually measured by EDX. The difference between the actual total Cr content and the matrix Cr content will increase with increasing C and/or N content in the specimen center.

The 1050°C results after 1000 h (**Figure 6.8 c**) display the critical state when the specimen thickness clearly starts to affect the Cr content at the alloy/scale interface as well as in the specimen center. The Cr profiles at the same temperatures but after longer term (3000 h) oxidation are shown in **Figure 6.8 d-f**. At 950°C (**Figure 6.8 d**), the depths of the Cr depletion zones are approximately 80 µm, which is close to the center of the 0.2 mm specimen. The Cr concentration at the alloy/scale interface of the 0.2 and 0.5 mm specimens are similar. Based on the considerations in Section 3.3.2, this suggests that the oxide growth and thus the Cr consumption obey a near parabolic time dependence. Upon longer oxidation times, the Cr depletion profile will reach the center of the 0.2 mm specimen and it is expected that then the interface Cr concentration of the 0.2 mm specimen will start to decrease, while that of the 0.5 mm specimen will remain at approximately the same level because of the adequate reservoir of Cr. This means that the width of the depletion zone will still be substantially smaller than the half thickness of the specimen.

With the faster Cr consumption rate at 1000°C (**Figure 6.8 e**), the Cr concentration at the alloy/scale interface of the 0.3 and 0.5 mm specimens do not show a significant specimen thickness dependence after 3000 h. However, the Cr interface concentration in the 0.2 mm specimen is much lower than that of the thicker specimens because the diffusion profile has clearly reached the center of the specimen.

The specimen thickness dependence of the Cr interface concentration was more pronounced after exposure at 1050°C (**Figure 6.8 f**). The Cr depletion revealed behavior typical for the second stage of the depletion process (see Section 3.3.2) for all three specimen thicknesses, wherein both the Cr concentrations at the alloy/scale interface and at the center of the specimen decreased, and resulted in relatively flat profiles with increasing oxidation time. At 1050°C not only the 0.2 mm but also the 0.3 mm specimen clearly exhibited an interface Cr concentration which is much lower than that after the 1000 h exposure. For both specimens, the diffusion profile has clearly reached the specimen center. The 0.2 mm specimen showed indications of breakaway oxidation at the edges of the specimen after only 2000 h (**Figure 6.9**), so the oxidation test of that specimen was interrupted after the mentioned exposure time.

Figure 6.8 clearly shows that the diffusion process of Cr is time and specimen thickness dependent. Thicker specimens have larger Cr reservoirs and it takes more time for the diffusion front to reach the center of the specimen, and thus also a longer time for the interface Cr content to be decreased to a critical value at which growth of the protective chromia base scale can no longer be maintained. For the 0.2 mm specimens, the times were quite short due to the small Cr reservoir. These observations are in qualitative agreement with the considerations in Section 3.3.2.

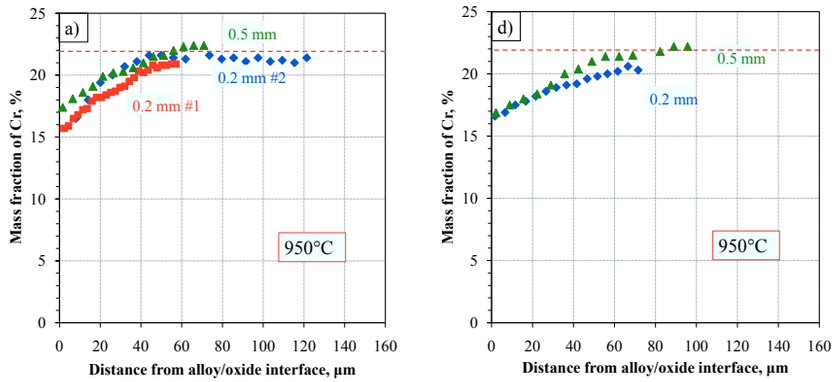

Figure 6.8: Concentration profiles of Cr in γ-Ni matrix (measured by EDX) of alloy 230 for specimens of different thicknesses at different temperatures after air oxidation for a-c) 1000 h and d-f) 3000 h

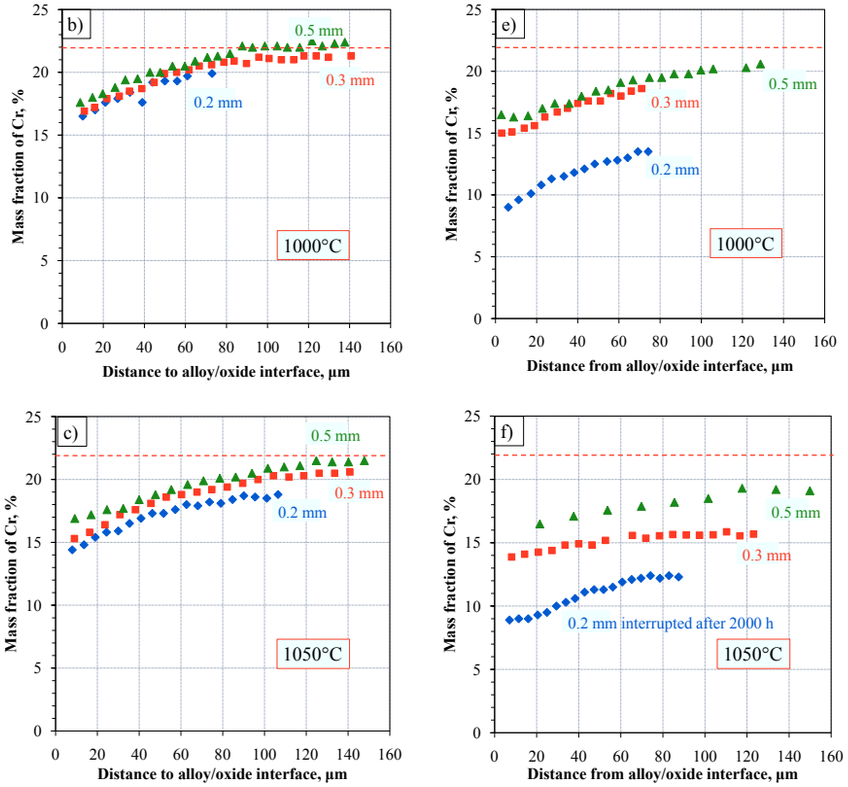

Figure 6.8 (continued)**.**

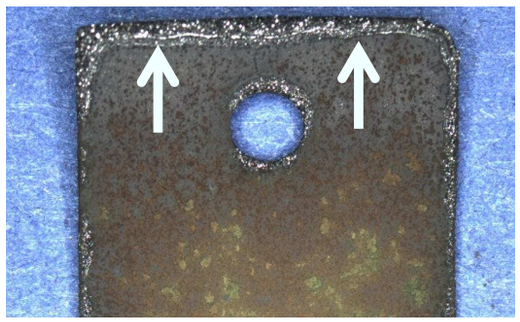

Figure 6.9: Macro image of 0.2 mm specimen of alloy 230 showing breakaway oxidation (arrows) at the specimen edges after air oxidation of 2000 h at 1050°C.

6.4 Modeling oxidation induced damage and lifetime limits

6.4.1 Modeling oxidation kinetics

The gravimetric data shown in **Figure 6.2** were used for evaluation of the oxidation kinetics. It was found that for these experimental conditions, alloy 230 exhibited only a slight deviation from parabolic kinetics during the steady state scale growth period; a good description of the experimental data could be obtained assuming power law oxidation kinetics (see **Eq. (3.19)**) with n=0.4 (**Eq. (6.2)**). The R^2 to the power law with n=0.4 is nearest to 1. An example of the data fitting is shown in **Figure 6.10**.

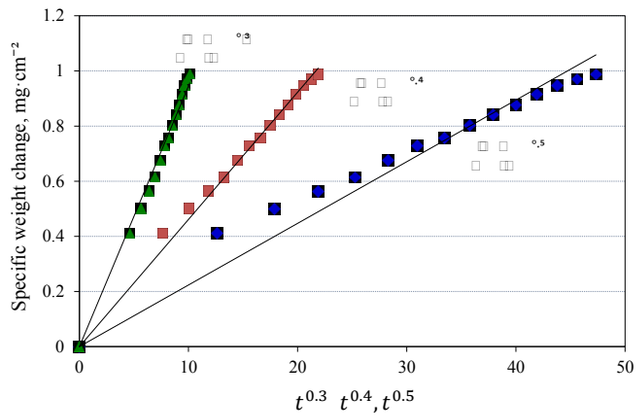

Figure 6.10: Fitting of the specific net weight change data of 0.5 mm alloy 230 specimen oxidized at 950°C to t^n.

Similar fitting results were obtained for all specimens. Therefore, the growth of the oxide is described here with the following power law expression:

$$\Delta \quad (6.2)$$

Because no apparent specimen thickness dependence of the growth rate was observed during steady state oxidation (before the appearance of scale spallation or "super-parabolic" oxidation), the rate constant k is taken as an average of the rate constants obtained for the different specimen thicknesses. **Figure 6.11** shows a double logarithmic plot of the fitting curves of the area specific net weight change during the steady state oxidation stage, compared with the experimental data at the three test temperatures. The functions expressing the oxidation kinetics with the averaged k for each temperature as well as the schematic straight lines representing the functions are also shown in the figure.

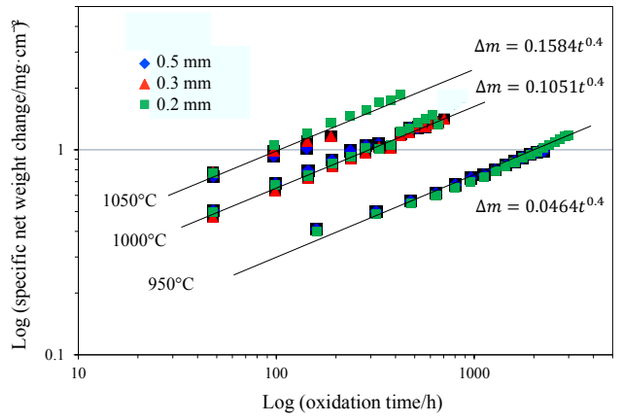

Figure 6.11: Double logarithmic plot of area specific net weight changes as function of time for specimens of different thicknesses at different temperatures during "steady state oxide growth", i.e. before onset of scale spallation for the thick specimens and enhanced scale growth rate for the 0.2 mm specimens. Inserted lines illustrate fitting of the data using **Eq. (6.2)**.

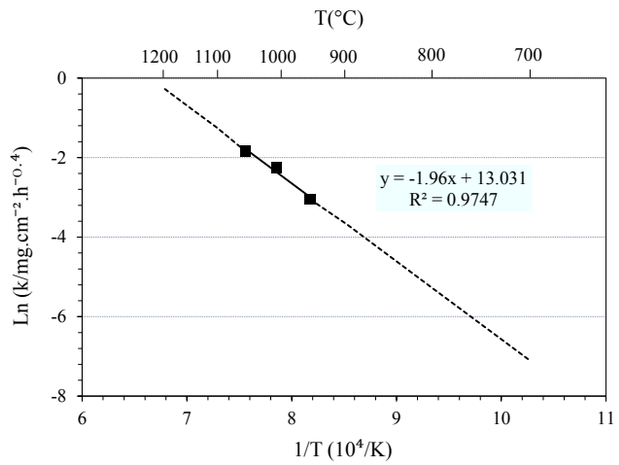

Figure 6.12: Rate constant k (**Eq. (6.2)**) during steady state oxide growth for alloy 230. Symbols indicate measured data, dashed line indicates extrapolation assuming an Arrhenius relationship (**Eq. (6.3)**).

The relationship between the rate constant k and temperature typically can be described by an Arrhenius function [157, 158], as has been mentioned in Section 3.2.2. The oxidation rate

constant then can be extrapolated to other temperatures, shown in **Figure 6.12** using the expression:

$$\square\square - \frac{\square}{\square} \square \quad \square\square \tag{6.3}$$

6.4.2 Modeling oxide spallation and re-healing

In order to describe the net weight change curves, a modified COSP modeling approach was applied. The traditional COSP model [18] assumes that initially parabolic kinetics prevails and a fraction of the scale spalls already after the first cooling step. The equations used in the COSP model are as follows [18].

$$\square_{\square}\square \ \square_{\square} \cdot \square_{\square\square}' \tag{6.4}$$

$$\square_{\square\square}' \ \square \cdot \square_{\square}^{\square/\square} \cdot \tau^{\square/\square} \tag{6.5}$$

$$\square_{\square\square}\square \ \square_{\square} \cdot \square_{\square\square}' \ \square \ \square_{\square} \cdot \square^{\square} \cdot \square_{\square} \cdot \tau \tag{6.6}$$

$$\square_{\square\square}\square \ \square_{\square\square}' - \square_{\square\square} \tag{6.7}$$

where $\square_{\square}$ is the fraction of oxide grown during the first heating that will spall after cooling, $\square_{\square}'\square$ the area specific weight of the grown oxide during the first heating cycle, $\square\square$ the ratio of molecular weight of oxide to oxygen (for Cr_2O_3, $\square = 3.167$), τ the duration of one heating period and $\square_{\square}\square$ the area specific weight of spalled oxide after the first cooling. It is apparent from **Eq. (6.4)** that the fraction of spalled oxide is assumed to be a monotonic function of the existing oxide. Due to the spallation of oxide, the time for oxide growth in the subsequent heating cycles should be corrected with a so-called „„effective time" $\square_{\square}$, which indicates the equivalent time spent for the oxide to grow to $\square_{\square\square}$ on bare metal. The $\square_{\square}\square$ and the grown oxide after the second heating can be calculated using the following equations:

$$\square_{\square\square}\square \ \square \cdot (\square\square_{\square})^{\square/\square} \cdot \square_{\square\square}^{\square/\square} \tag{6.8}$$

$$\square_{\square\square}' \ \square \cdot (\square\square_{\square})^{\square/\square} \cdot (\square_{\square\square} \square \tau)^{\square/\square} \tag{6.9}$$

The mass balance to calculate the area specific net weight change of the specimen after cycle i (**Eq. (6.10)**) and the total amount of Cr consumed (**Eq. (6.11)**) are as follows:

$$\Delta\square_{\square}\square \left(\frac{\square}{\square}\right) - \left(\square - \frac{\square}{\square}\right) \cdot \sum \square \tag{6.10}$$

$$\square \quad \square\left(\square-\frac{\square}{\square}\right)\left(\square \quad \square\sum\square\right) \tag{6.11}$$

However, in the present study, the oxidation kinetics appeared to be sub-parabolic; therefore, the first modification is to change the power law time dependence, such that **Eq. (6.5)** is re-written as:

$$\square\square\square'\square \quad \square\cdot\square\cdot\tau^{\square\square} \tag{6.12}$$

With **Eqs. (6.4)** and **(6.12)**, the $\square_{\square\square}$ and $\square_{\square\square}$ assuming a power law time dependence of the scale growth, can be calculated. Accordingly **Eqs. (6.8)** and **(6.9)** are reformulated to **Eqs. (6.13)** and **(6.14)**, respectively:

$$\square_{\square\square}\square \quad \square\cdot\square\cdot\square_{\square\square}^{\square\square} \tag{6.13}$$

$$\square_{\square\square}' \quad \square\cdot\square\cdot(\square_{\square\square}\square\tau)^{\square\square} \tag{6.14}$$

The second modification is to set Q_0=0 before onset of spallation occurs for the 0.3 and the 0.5 mm specimens. **Figure 6.13** shows the regime schematically. In the steady state oxidation stage, there is no decrease of the net weight change due to spallation. After a certain number of cycles, spallation starts to occur and the weight change curve shows an inflection point. Subsequently the net weight change decreases while the gross weight change increases. It is obvious that the increase of the gross weight change should accelerate due to the oxide spalling and re-healing process [41].

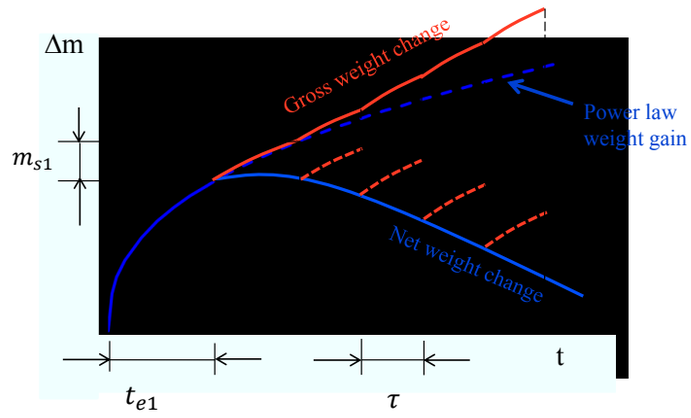

Figure 6.13: Schematic illustration of net and gross weight change calculated with the modified COSP model.

To describe the “super-parabolic” oxide growth observed after longer oxidation times for the thinnest specimens (0.2 mm) as discussed in the previous sections, a new parameter θ with a value between 0 and 1 is introduced. This parameter indicates that after each thermal cycle, micro-tensile-cracks cause a fraction θ of the total surface area of the specimen to be exposed to oxygen. Taking the first three cycles as example, the additional oxide □ □can be calculated using **Eqs. (6.15) - (6.17)**. Similar to spallation, the cracking effect is assumed to occur after a certain number of cycles; so, during the steady-state oxidation stage the value of θ□ is set to zero.

1st cracking: □ □□ θ · □· □· τ□□ (6.15)

2nd cracking: □ □□ θ · □· □· [(□τ)□□ □ τ□□] (6.16)

3rd cracking: □ □□ θ · □· □· [(□τ)□□ □ (□τ)□□ □ τ□□] (6.17)

With the additional weight of oxide, **Eq. (6.7)** is rewritten as:

□ □□ □ □ □□′ □ □ □□ − □ □□ (6.18)

No spallation of oxide was observed in the case of the 0.2 mm specimen (**Figure 5.1**), so the value of □ □in **Eq. (6.18)** equals zero.

The model was programmed in Matlab version 8.4 (R2014b), and the weight change data were calculated for all three temperatures. **Figure 6.14** shows the results of the modelled weight change curves for the alloy 230 specimens of different thickness at 1000°C. The dashed lines represent the results calculated with the modified COSP model using different optimized values of the parameters □ □and θ. The optimization was done by changing the values of □ □and θ with an accuracy level of 0.0001. When the calculated points clearly deviated from the experimental data, the parameters were changed to make the curve fit again and the maximum root mean square error (RMSE) between the calculated and experimental data was limited to 0.15 $mg.cm^{-2}$.

For the 0.2 mm specimen at 1000°C, □ □=0, but after 7 cycles, micro-tensile-cracking started to occur with θ=0.0033. For the 0.3 mm specimen, the oxide started to spall with □ □=0.0014 after 14 cycles. For the 0.5 mm specimen, after 13 cycles, the oxide started to spall with □ □=0.0025, and after 2000 h, □ □had to be changed to 0.0022 in order to obtain an optimum fit with the experimental data. The decrease of □ □with time suggests a reduction of the scale

spallation rate, perhaps as a result of the slight reduction in specimen thickness during prolonged oxidation.

The results of the modeling showed that in the studied temperature range, □□increases with specimen thickness, which is in agreement with the assumption that the tendency of scale spallation increases with increasing specimen thickness [126]. Another observation is that the calculated gross weight change curves are slightly higher than those measured. The reason might be the loss of spalled oxide out of the crucible due to „„explosive" spallation.

As described in Section 5.2, it is easy to derive that for growth of a pure Cr_2O_3 scale, an oxygen uptake of 1 mg.cm^{-2} (gross weight change) corresponds to a scale thickness of 6.07 µm and a corresponding wall thickness loss of about 3.01 µ on one side of the specimen. In this manner, the gross weight change curves can be converted into the loss of wall thickness. By extrapolation with the optimized estimated model parameters (□□and θ), the loss of wall thickness for longer oxidation times can be predicted (see the solid lines in **Figure 6.15**). For all studied temperatures, the 0.2 mm specimens exhibit the most pronounced loss in wall thickness. This enhanced wall thickness loss due to the accelerated oxidation rate is thus more pronounced than that related to oxide spallation and re-growth for the thicker specimens. The 0.5 mm specimen shows a higher loss of wall thickness than the 0.3mm specimen because of the larger tendency to scale spallation.

Because the oxidation rates decrease with decreasing temperature (**Figure 6.11**), the 0.2 mm specimen at 950°C starts to show "super-parabolic" oxidation just before the end of the experiment (**Figure 6.2**), i.e. after approximately 2000 h. Therefore the exposure time of 3000 h is relatively short for the 950°C test and for verification of the extrapolated values after 3000 h, the experiments have to be confirmed in experiments with longer exposure times in the future.

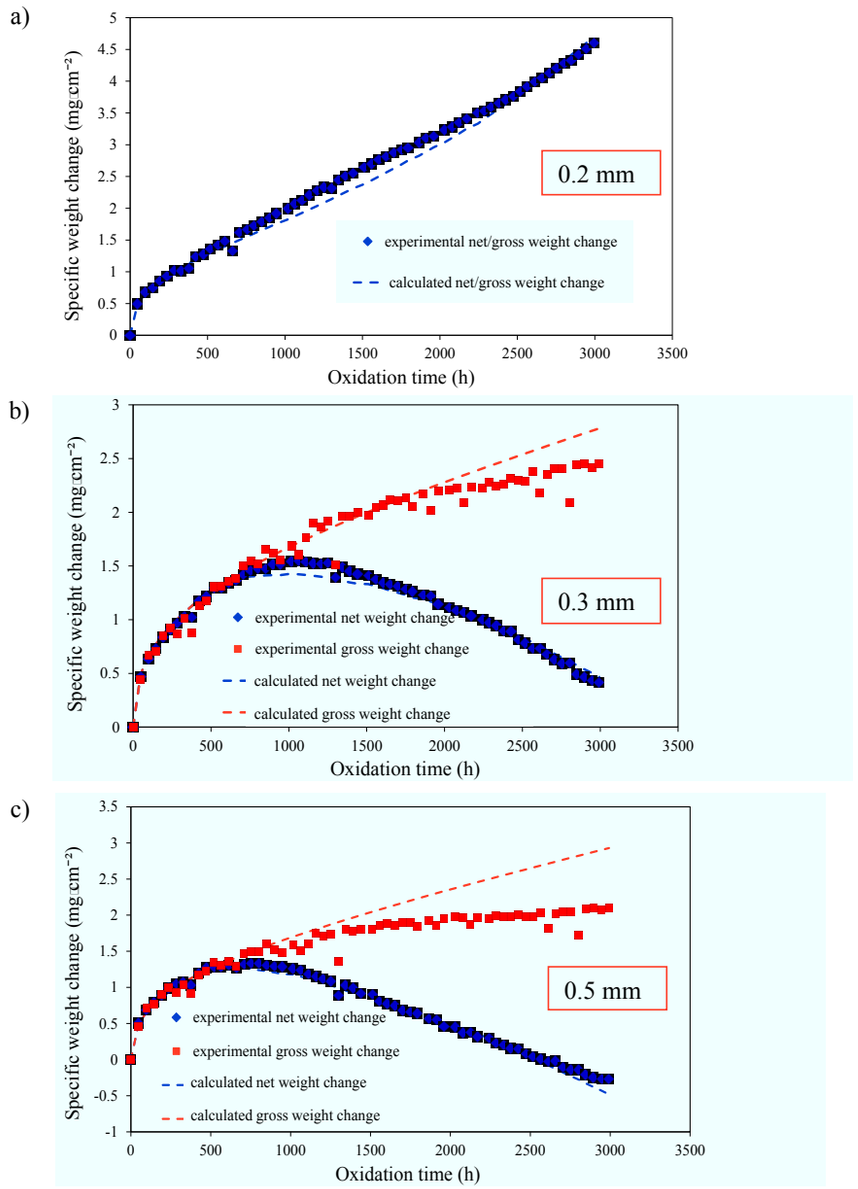

Figure 6.14: Comparison between experimental (symbols) and calculated (dashed lines) area specific net and gross weight change curves of alloy 230 for specimens of a) 0.2 mm b) 0.3 mm and c) 0.5 mm thickness here showing the results of the 1000°C experiments as examples.

6.4.3 Correlating oxidation kinetics and Cr depletion

As mentioned in Section 6.1, wrought NiCr-base alloys do commonly not exhibit a sudden, rapid increase in oxidation rate if a critical interface concentration of the scale forming element is reached, as frequently observed if e.g. a critical Al depletion occurs in case of FeCrAl base alloys [73]. In reference [2, 12] it is frequently mentioned that a Cr concentration of approximately 10 wt. % is required to obtain external chromia formation on NiCr base alloys in the temperature range considered in the present study.

From the results in **Figure 6.9** it is apparent that the 0.2 mm specimen showed indications for "breakaway" type oxidation at the specimen edges when the Cr content at the scale/alloy interface is about 9 wt. % (**Figure 6.8 e**). So, it is apparently reasonable to use 10 wt. % as the critical Cr interface concentration corresponding to the lifetime t*. Also, the extent of internal nitridation seemed to significantly increase (see Section 5.3) if the Cr concentration was depleted to a level around 10 wt. %. Therefore it seems appropriate to define a Cr interface concentration as a critical value which, for pragmatic reasons, may be considered as an end of life of the component. The effect of interface Cr concentrations different from 10 wt. % on t* will be illustrated later.

The subscale Cr concentration profiles are initially quite steep (**Figure 6.8 a-c**) but their slope generally decreases with increasing oxidation time (see e.g. **Figure 6.8 d-f**). Especially beyond the exposure time t_C and thus approaching t*, the Cr concentration profiles become quite flat (see **Figure 6.8 f**). Therefore, as a reasonable approximation, the Cr concentration in the alloy may be assumed to be the same as the Cr concentration at the alloy/scale interface throughout the specimen upon reaching t*. The reservoir equation (**Eq. (6.19)**) rearranged from **Eq. (3.26)** developed in previous studies for Al_2O_3 forming FeCrAl alloys [21] can thus be implemented. In analogy to the approach in reference [21], the left hand side of **Eq. (6.19)** expresses the gross weight gain by oxygen uptake (for the case of solely steady state oxidation (**Eq. (6.2)**) at the time when the exposure duration equals t*. The right hand side indicates the weight of oxygen combined with Cr in the form of Cr_2O_3.

$$\square \cdot (\square^*) \square \square \frac{(\square\square - \square^*)}{\square} \cdot \frac{\rho}{\mu} \cdot \frac{\square}{\square} \qquad (6.19)$$

Here C* is the remaining Cr concentration at t*, μ the metal/oxygen weight ratio in the scale (for Cr_2O_3, μ=2.167), ρ the density of the alloy in $mg.cm^{-3}$ (for alloy 230, ρ=8970 $mg.cm^{-3}$), d

the specimen thickness in cm. If the ratio μ is deleted from the right hand side of **Eq. (6.19)**, the expression represents the consumption of Cr.

With the modified COSP model and the model for describing the "super-parabolic" oxidation (**Eqs. (6.15) - (6.17)),** the total consumption of Cr after cycle i is calculated as □ (**Eq. (6.11)**). To equal □ □ to the right hand side of **Eq. (6.19)** but omitting□μthe new equation is written as:

$$\square\,\square\,\square \frac{(\square\square - \square^*)}{\square} \cdot \rho \cdot \frac{\square}{\square} \qquad (6.20)$$

It is clear that for a given alloy, the total consumption of Cr at t* is for a given temperature only dependent on the wall thickness of the component. For a 0.2 mm specimen, the total loss of wall thickness (i.e. accounting for oxidation at both sides of the specimen) at t* is 29.80 μm; for the 0.3 and 0.5 mm specimens the values are 44.70 and 74.50 μm, respectively.

To insert into the cyclic calculation in the modified COSP approach, **Eq. (6.20)** can be re-written in the form:

$$\square\quad\square \frac{(\square\square - \square\square)}{\square} \cdot \rho \cdot \frac{\square}{\square} \qquad (6.21)$$

The time until □□□ □* is the time t*. The calculation was done with 48 h or 10 h cycles for the experiments at 1000/1050°C and 950°C, respectively, so the calculated values of □□are series of points with time intervals of 48 h or 10 h.

6.4.4 Construction of lifetime diagram

Figure 6.15 shows a lifetime diagram for alloy 230 based on the considerations in the previous sections. The solid lines were derived from the weight gain data using the conversion from weight change into total metal loss, as described above. The values of t* obtained from the calculations based on **Eq. (6.21)** are inserted as solid symbols. The critical Cr interface concentration is assumed here to be 10 wt. %; the critical exposure times t* are therefore designated as t_{10}. Due to the lack of experimental data, the t_{10} of the 0.3 mm specimen at 950°C is interpolated, resulting in a location near the line of the 0.5 mm specimen.

The open symbols in **Figure 6.15** indicate the approximate times to occurrence of local breakaway observed from the appearance of the oxidized specimens. The 0.2 mm specimen

oxidized at 1050°C showed obvious local breakaway oxidation (**Figure 6.9**) at 2000 h, which means that 2000 h has already exceeded the time t_{10}. So in the diagram, the observed open symbol is located slightly higher than the calculated closed symbol. The 0.2 mm specimen oxidized at 1000°C did not yet show apparent breakaway oxidation. It should, however, be very close to the critical time t_{10} after 3000 h, based on the measured Cr profile in the alloy (**Figure 6.8 e**) and the presence of coarsened nitride in the microstructure as discussed in Section 5.3. So the inserted open symbol is located slightly lower than the calculated closed one.

Taking the 1000°C results as an example, the thicknesses of remaining metal after 3000 h oxidation were measured from metallographic cross section images using the software AnalySIS Pro. 5.0 and are compared to the calculated metal thicknesses (**Table 6.1**). The calculated remaining metal thicknesses of the 0.2, 0.3 and 0.5 mm specimens in **Table 6.1** correspond to the closed symbols of green, red and blue colors at 1000°C in **Figure 6.15**, respectively. For the 0.2 and 0.3 mm specimens the calculated remaining metal thicknesses are slightly larger than the metallographically measured thicknesses, which might be explained by creep of the thin specimens occurring under thermal cycles and by the limited accuracy of the thickness measurements with AnalySIS Pro. 5.0. The calculated and measured metal thicknesses of the 0.5 mm component agree very well, which implies that the thicker specimen has better creep resistance than the thinner ones, and thus, the only uncertainty is the error in thickness measurement.

The lifetime diagram can be extrapolated to other temperatures (dotted lines in **Figure 6.16**) using the extrapolated data of k shown in **Figure 6.12**. It can be observed that the deviation of the weight change curves from the steady state oxidation occurs when the weight gain reaches approximately 1 $mg.cm^{-2}$ at all three temperatures in **Figure 6.2**, which approximately corresponds to the level of 6 µm of wall thickness loss in **Figure 6.15**. Based on this observation, the deviated dotted lines from the straight dotted lines in **Figure 6.16** are plotted assuming that the times for the occurrence of the deviation of the weight gain curves from steady state oxidation at other temperatures also occurs at a level of wall thickness loss of 6 µm. In this way, at 900°C and lower temperatures, the non-steady-state oxidation (phenomena involving scale spallation and “super-parabolic” oxidation due to “tensile-crack-effect”) obviously occur substantially later than at higher temperatures. Whereas at temperatures higher than 1050°C, the non-steady-state oxidation starts after very short exposure, e.g. 50 h

at 1200°C, and even cannot be plotted in the used double logarithmic diagram for temperatures higher than 1200°C.

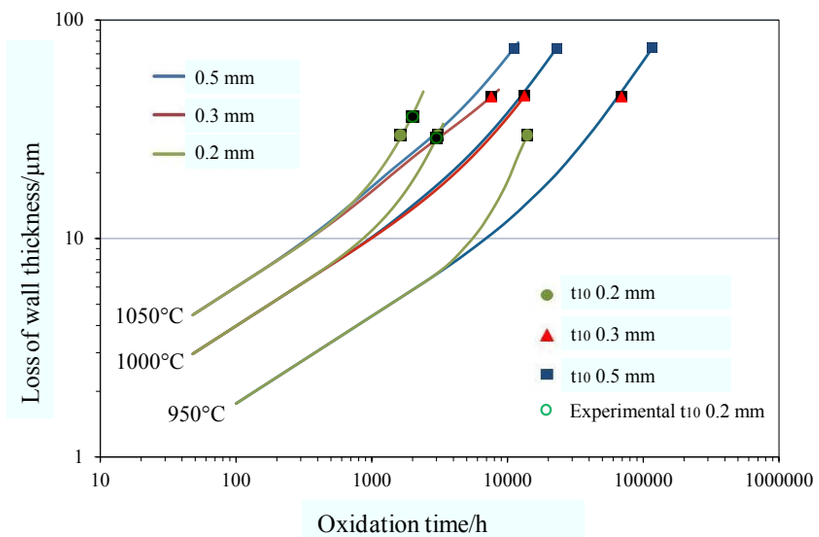

Figure 6.15: Lifetime diagram of alloy 230 showing calculated total loss of wall thickness as function of time at different temperatures. Calculations are based on assumption that wall thickness loss occurs on both specimen sides in the same manner. Inserted are solid symbols indicating times t_{10} for specimens of different thickness (0.2, 0.3 and 0.5 mm). Open symbols indicate experimentally observed times close to t_{10}.

Table 6.1: Comparison between measured and calculated remaining thickness of metal after 3000 h oxidation at 1000°C.

Specimen thickness(mm)	Measured metal thickness(µm)	Calculated metal thickness(µm)
0.2	162 ± 6	172
0.3	265 ± 4	284
0.5	484 ± 3	483

It is important to note that one cannot exactly predict below which specimen thickness the “super-parabolic” behavior will occur at a given temperature. However the trend is that at higher temperatures, specimens thicker than 0.2 mm also tend to show “super-parabolic”

behavior. This phenomenon could be observed for alloy X as will be discussed in Chapter 8. At lower temperatures specimens thinner than 0.2 mm may tend not to present "super-parabolic" behavior. Therefore the deviated lines at temperatures higher than 1050°C are assumed to be parallel to the slopes of the lines calculated for the 0.2 mm specimen at 1050°C for all specimen thicknesses, whereas the slopes of the deviated lines at temperatures lower than 950°C are assumed to be parallel to the slopes of the lines calculated for the 0.5 mm specimen at 950°C for all specimen thicknesses. In order to make sure that the extrapolated lines are arranged parallel to the reference lines, new model parameters had to be estimated. For example, the fitted value of the parameter for the "super-parabolic" θ (**Eq. (6.15)**) is 0.02 at 1100°C, larger than the value of θ (0.0063) at 1050°C, which is in accordance with the trend that the "tensile-crack-effect" is for a given specimen thickness enhanced with increasing temperature. At 900°C, the fitted value of Q_0 (**Eq. (6.4)**) is 0.00008, compared to the value of 0.00013 at 950°C, which is in agreement with the expectation that the rate of scale spallation decreases with decreasing exposure temperature.

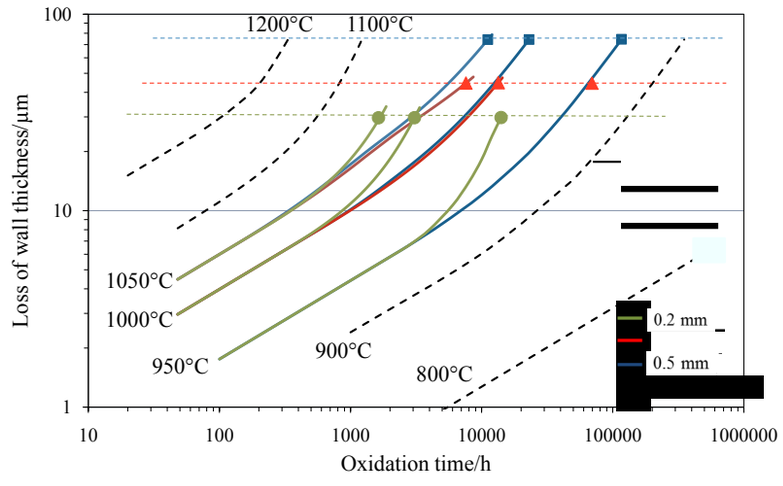

Figure 6.16: Lifetime diagram of alloy 230 showing data from **Figure 6.15** (solid lines) and extrapolations to other temperatures (dashed lines), using procedures described in text.

Figure 6.17 shows, for clearer visibility, the calculated times t_{10} as function of specimen thickness at different temperatures, i.e. a similar way of presenting critical depletion processes in a manner used earlier for FeCrAl based alloys [21, 26] and high-Cr ferritic steels [32, 74]. As mentioned above, the time t_{10} of the 0.3 mm specimen at 950°C is interpolated using the

experimental results of the 0.2 and 0.5 mm specimens. The kinks of the lines (change of slopes) at 0.3 mm indicate the change of oxidation mechanism from mainly scale spallation occurring for thicker specimens to the “super-parabolic” oxidation observed for thinner specimens.

In **Figure 6.18**, the times t_{10} have been extrapolated to other component thicknesses (0.1 and 1 mm with open symbols) and temperatures (1100 and 900°C). At a given temperature, the lifetimes t_{10} of the 1 mm thick specimen are calculated by setting the same model parameters as for the 0.5 mm specimens, because no apparent difference of oxidation kinetics including the rate of spallation was found in a similar test of a 1mm specimen of alloy 230 at 1050°C (see **Figure 6.19**).

Therefore, the calculated t_{10} are located approximately on the extrapolated straight lines at all the studied temperatures. As an approximation, the t_{10} of the 0.1 mm specimen were calculated by setting the same model parameter, i.e. θ (**Eq. (6.15)**), as for the 0.2 mm specimen. Considering that the 0.1 mm specimen would suffer from a more significant “tensile-crack-effect” than the 0.2 mm specimen during the cooling and reheating process, the value of the parameter θ might be underestimated by taking the same value as that of the 0.2 mm specimen, which may lead to a slight overestimation of the t_{10} for the 0.1 mm specimen.

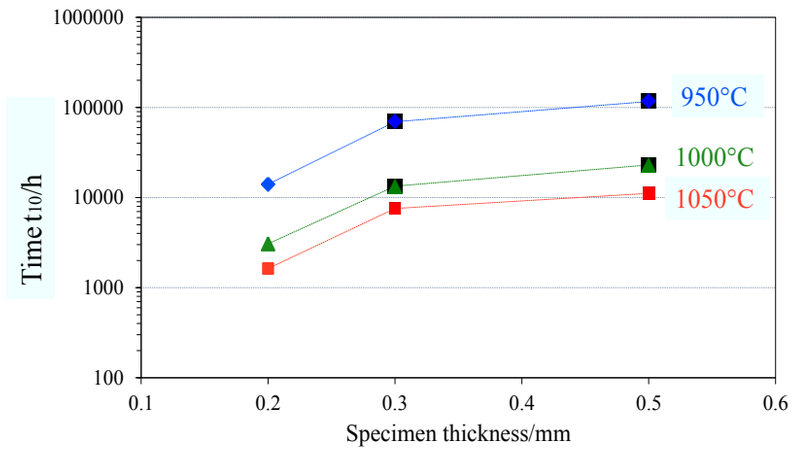

Figure 6.17: Calculated times t_{10} as function of specimen thickness for alloy 230 at different temperatures.

The procedures of the extrapolations to higher and lower temperatures are the same as those described in the text related to **Figure 6.16**. The intersections of the black dashed lines and the horizontal dotted lines in **Figure 6.16** represent part of the values in **Figure 6.18**. Because at 1100°C the specimens with all thicknesses are assumed to show "super-parabolic" behavior, the extrapolated values of t_{10} for thick specimens (0.5 and/or 1 mm) might be underestimated. Vice versa, it was for all specimen thicknesses at 900°C assumed that scale spallation instead of "super-parabolic" oxidation occurred. The extrapolated values of t_{10}forthin specimens (0.1, 0.2 and/or 0.3 mm) might therefore be overestimated. Consequently, there is no apparent kink of the slope in the extrapolated lines of 900 and 1100°C.

Figure 6.20 shows the effect of using a different value of critical interface Cr concentration (here 8 and 12 wt. % respectively) on the times t*, here using as example the data at 1000°C. The differences between t_8, t_{10}, and t_{12} decrease with decreasing specimen thickness. Especially for 0.2 mm, the difference between t_8 and t_{12} is less than 2000 hours. One reason is that the Cr reservoir of the thinnest specimen tested is smaller than that of the thicker specimens. Therefore the absolute amount of 4 wt. % Cr (difference between 12 wt. % and 8 wt. %) in the thinner specimen is less than that in the thicker specimens. The other reason is that the rate of Cr consumption in the 0.2 mm specimen is significantly faster than that of the thick specimen due to the "super-parabolic" oxidation, as discussed above.

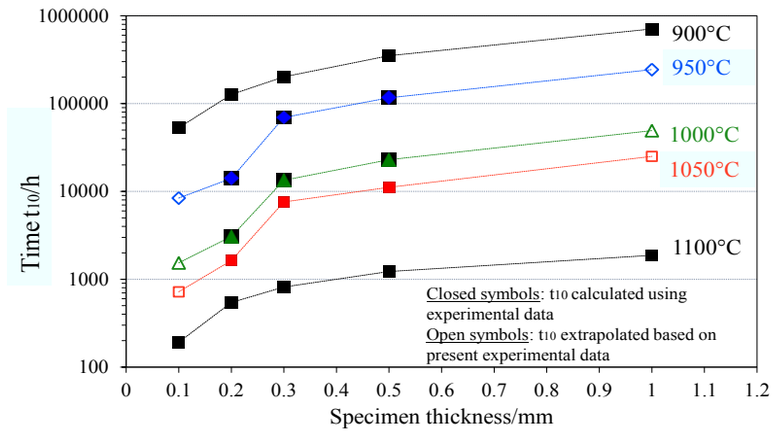

Figure 6.18: Calculated times t_{10} as function of specimen thickness for alloy 230 with extrapolations (open symbols) to other temperatures and specimen thicknesses based on experimental results of specimens oxidized at studied temperatures. See text for details used in the calculation.

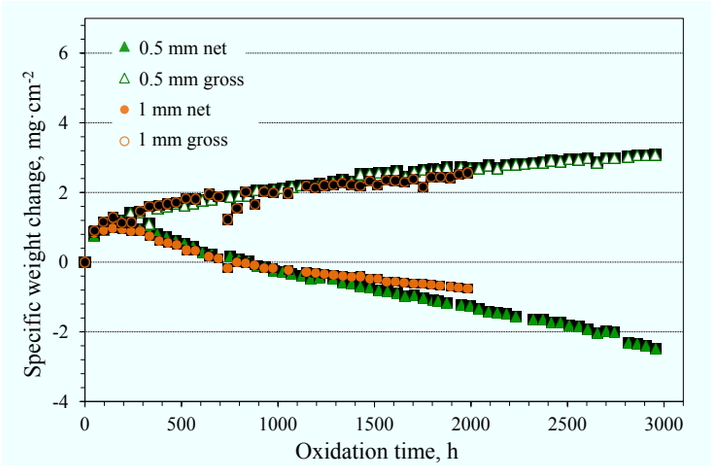

Figure 6.19: Comparison of net and gross weight changes of 0.5 and 1 mm specimens of alloy 230 during oxidation at 1050°C.

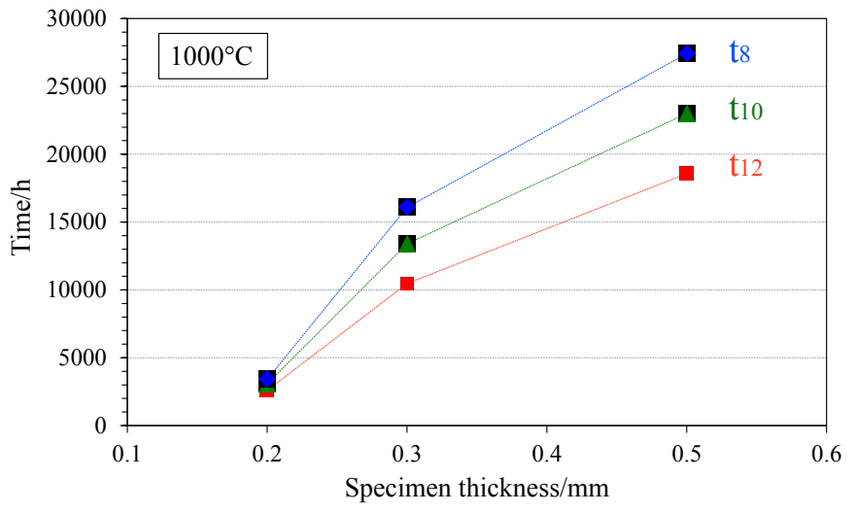

Figure 6.20: Time to reaching critical Cr interface concentration (t_{10}) as function of specimen thickness compared with times t_8 and t_{12} for oxidation at 1000°C.

7 Modeling oxidation induced lifetime limits with non-steady-state finite difference method

7.1 General remarks

For the calculation of the time t* it was assumed in the previous section that the Cr concentration profiles in the alloy were ideally flat. This seemed to be justified because the initially steep subscale Cr profiles became gradually less steep upon approaching t*. In the following sections it will be estimated, in how far the calculated time t* differs if a more precise description of the time dependence of the shape of the Cr depletion profiles is taken into account.

7.2 Background

The finite difference method (FDM) is a useful and commonly used tool to solve partial differential equations. It is widely applied to solve transportation problems such as heat transport and diffusion in different substance states (gas, liquid and solid) [159, 161]. The outward diffusion of a protective scale forming element (here Cr) of high temperature alloys driven by the oxidation of this element from the bulk alloy to the alloy surface results in a subscale depletion of the element. In terms of oxidation induced chemical failure of the high temperature component, the failure occurs when a critical solute (Cr) concentration is reached. Several studies related to oxidation of metallic materials have been carried out by solving diffusion equation (Fick"s second law [161]) analytically [13, 14, 22, 23, 35-37] or numerically with FDM [38-41], in order to predict the solute depletion profiles or the lifetime of the component. The analytical approach can only calculate the solute depletion during steady-state parabolic oxidation, mostly prevailing under isothermal conditions. With a numerical approach, also non-steady state conditions can be modeled and the effective diffusion coefficient [162, 163] of the solute can be derived by fitting calculated results to the experimental data if no independent data are available from literature. In previous studies, programs which enable to apply the FDM to oxidation under thermal cycling including scale spallation have been developed [38, 43] and programmed with Fortran. However this program is still not widely applied as a pragmatic tool to prediction of component lifetime. In the following section an FDM model will be described for prediction of component lifetime defined by critical solute depletion in alloy 230 by incorporation of one dimensional FDM to

the modified COSP which has been described in Chapter 6. The calculated values of t* will then be compared with the results obtained using the reservoir approach presented in Section 6.4.4.

7.3 Time dependent subscale depletion

The calculation of this chapter is based on the same experimental oxidation kinetics presented in Chapter 6 (see **Figure 6.2**). In Chapter 6, the subscale Cr depletion profiles measured by EDX are shown as function of specimen thickness (**Figure 6.8**). Here the time dependent Cr profiles for a certain specimen thickness and temperature are illustrated in **Figure 7.1** in order to more clearly illustrate the diffusion process as a function of time. Additionally, the Cr concentration profiles after TG tests are included because after the short test times used in these experiments the subscale Cr profiles are quite steep and thus show the largest deviation from the assumption of flat profiles made in the previous section. The results of 0.3 mm specimens are not included here because the exposures at 950°C as well as the TG tests were conducted only for the 0.2 and 0.5 mm specimens. Besides, the specimen thickness dependent Cr depletion profiles including the 0.3 mm specimens have already been shown in **Figure 6.8**. This figure shows that the difference of the Cr profiles between the 0.3 and 0.5 mm specimens is not very apparent especially after the shorter oxidation time of 1000 h. Therefore it will be sufficiently clear to explain the modeling of the depletion process by comparing the experimental as well as the calculated results of merely the 0.2 and 0.5 mm specimens in the present chapter.

The short term TG tests indicate that the Cr interface concentration during steady state scale growth very slightly decreases with increasing temperature **Figure 7.1**. However, this temperature dependence is quite small; the interface concentration of Cr during this oxidation stage is approximately 16 wt. % (**Figure 7.1**). Even after longer time cyclic oxidation up to 3000 h this interface concentration remains approximately constant as long as the diffusion depth does not reach the center of the specimen.

Beyond the studied exposure time the Cr depletion of the 0.2 mm specimen proceeds much faster than that of the 0.5 mm specimen due to the smaller reservoir of Cr. This effect of specimen thickness becomes, as expected, more pronounced with increasing temperature.

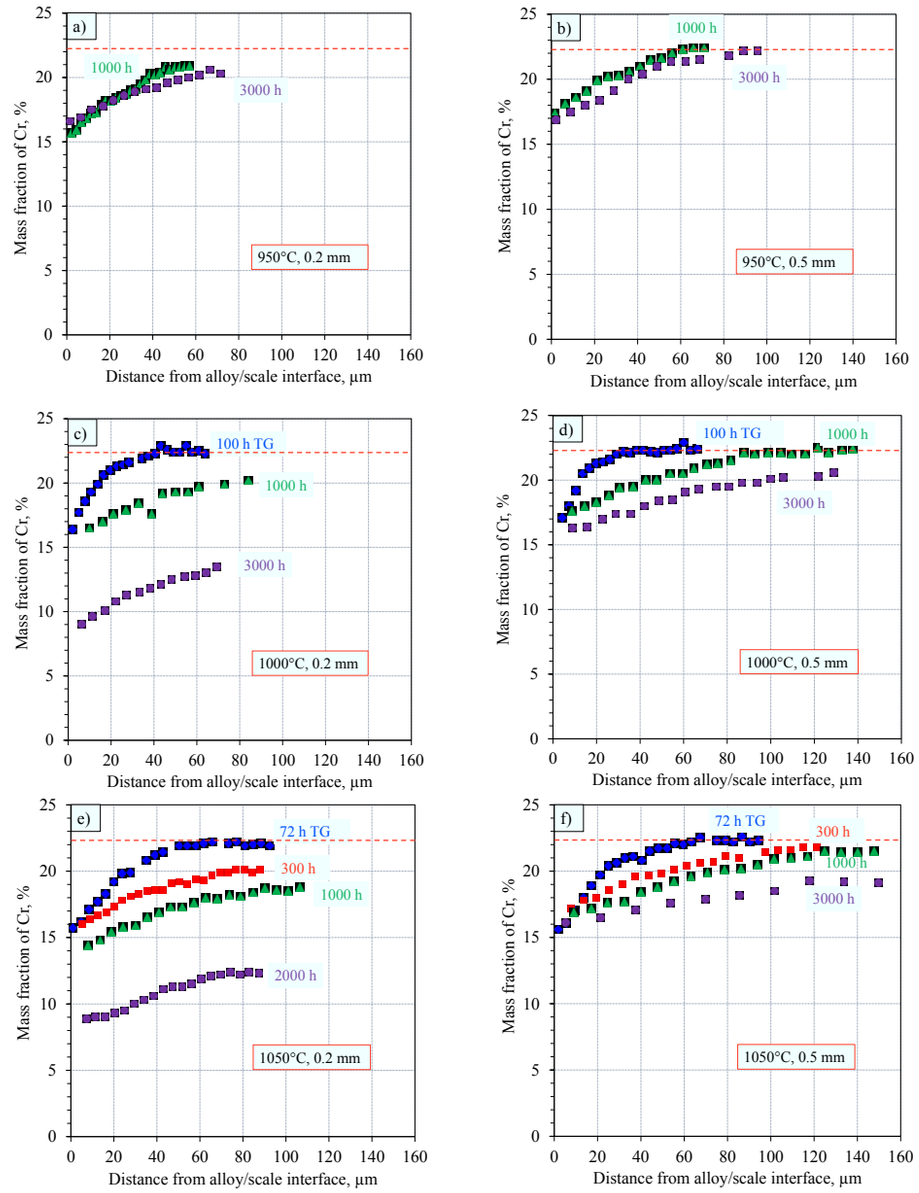

Figure 7.1: Temperature dependence of subscale Cr concentration profiles in alloy 230 specimens of different thicknesses after oxidation at a, b) 950°C, c, d) 1000°C and e, f) 1050°C (dashed lines indicate the original concentration of Cr). Results at 1000 and 3000 h were taken from Section 6.3; results of 72 h and 100 h relate to TG tests. The 300 h data at 1050°C relate to additional exposures mentioned in Section 4.3.

As a result, after 1000 h at 950 and 1000°C and 300 h at 1050°C, the second stage of the Cr depletion process has already started for the 0.2 mm specimens as the Cr concentrations in the center of the specimen are clearly lower than the original value.

For the 0.5 mm specimens the depletion front reaches the center of the specimen after much longer time for each temperature. All the measured interface Cr concentrations of the 0.5 mm specimens are about 16 - 17 wt. % (**Figure 7.1 b-f**). The profiles indicate that the second depletion stage just started after 3000 h. The slight increase of the interface Cr concentration at the beginning of the second stage in the case of power law kinetics (**Eq. (3.19)**) with n<0.5 as mentioned above is not clearly observed. This is likely due to the limited accuracy of the EDX measurement in the immediate vicinity of the alloy/scale interface and due to the interference of the formation of internal Al_2O_3 precipitates in the subscale region. These aspects will further be discussed using the results of the finite difference calculations in Section 7.4.1.

Based on the experimental observations, the 0.2 mm specimen showed indications for "breakaway" type oxidation (Section 6.3) at the specimen edges when the Cr content at the alloy/scale interface is about 10 wt. % (**Figure 7.1 c e)**. Besides, the extent of internal nitridation appeared to significantly increase (see Chapter 5) if the Cr concentration was depleted to a level around 10 wt. %. Therefore, in the pragmatic reservoir approach for lifetime prediction of alloy 230, an interface Cr concentration of 10 wt. % was determined as the critical value, which is considered as the end of the life of the component. This criterion will also be applied to the finite difference modeling in the present chapter whereby more accurate Cr depletion profiles at the end of the lifetime of the components can be predicted with the FD model instead of assuming quasi-flat profiles as described in the reservoir approach.

7.4 Modeling of lifetime limits

7.4.1 FDM for steady-state oxidation

The diffusion of Cr in Ni-based alloys is quite slow because of the FCC lattice structure [24]. Unlike the case for alumina forming FeCrAl or NiCrAl alloys, the depletion profile of the scale forming element, here Cr, is not flat; therefore, the following diffusion equation has to be solved to obtain the depletion profile [161]:

$$\frac{\partial \square}{\partial \square} \square \square \frac{\partial^{\square} \square}{\partial \square^{\square}} \tag{7.1}$$

where N denotes the mole fraction of the oxidizing solute.

The lifetime prediction model with FDM is constructed on basis of the establishment of the traditional steady-state FDM, including the set-up of FD equations, initial and boundary conditions as well as the determination of D_{Cr} by fitting the calculated profile to the experimental Cr profile measured with EDX. **Figure 7.2** shows the used boundary conditions, taking a half of the specimen thickness. Considering the symmetric geometry of the specimen, the flux of Cr is zero in the middle of the specimen, whereas the outward flux of Cr at the alloy/scale interface is a function of the rate of oxidation. The boundary condition at the alloy/scale interface is derived from that used in reference [24] for parabolic oxidation kinetics:

$$-\square \frac{\partial \square}{\partial \square} \square (\square - \square_{\square}) \left(\frac{\square_{\square}}{\square \square}\right)^{\square/\square} \tag{7.2}$$

Here k_c is the parabolic rate constant of the interface alloy recession, and the second term on the right hand side of **Eq. (7.2)** is converted by taking the derivative of x_C to t from the parabolic scaling kinetics where x_C indicates the consumption of alloy thickness on each surface [24]:

$$\square_{\square}^{\square} \square \square \square_{\square} \tag{7.3}$$

In the present study, the scaling kinetics obeys a power law instead of a parabolic time dependence, so **Eq. (7.2)** has to be modified into the following form:

$$-\square \frac{\partial \square}{\partial \square} \square (\square - \square_{\square})(\square \square \square_{\square} \cdot \square^{-\square \square}) \tag{7.4}$$

where k_r is the power law rate constant of the interface alloy recession and can be calculated from the power law rate constant of oxidation (area specific weight gain, i.e. oxygen uptake) k by the following expression:

$$\square_{\square} \square \cdot \frac{\square}{\square} \cdot \frac{\square \square \square}{\square \square \square_{\square}} \cdot \frac{\square}{\square} \tag{7.5}$$

where k is the power law rate constant of oxidation, i.e. given by **Eq. (6.2)** with n=0.4. Here V_{Cr} is the molar volume of chromium in $cm^3.mol^{-1}$, M_{Cr} the molar weight of Cr in $mg.mol^{-1}$,

and □ □ □/ □ □ □the weight ratio of metal to oxygen in the Cr_2O_3 scale, i.e. μ in **Eq. (6.19)** (equal to 2.167). The ratio of molar volume □ □ /□ ≈ ⍰ for alloy 230.

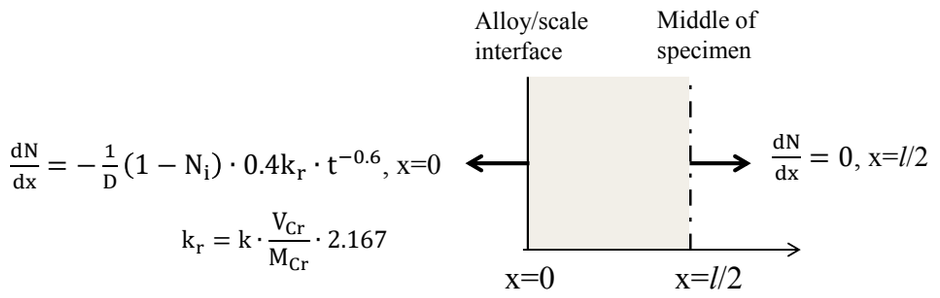

Figure ⍰7.2: Schematic illustration of boundary conditions for Cr flux, i.e. (□—) used in steady-state FDM. (l is the thickness of the specimen)

To avoid an infinitely large value at the beginning of the calculation when taking t=zero, here the initial condition is set by taking the Cr depletion data measured by EDX after the 100 h TG test at 1000°C and the 72 h TG test at 1050°C. However, no short time result of a TG test at 950°C is available. Therefore, the diffusion coefficient of Cr in the alloy at 950°C will be extrapolated based on the data of 1000 and 1050°C for use in later calculations. The initial condition at 950°C can be extrapolated from the Cr concentration profiles after TG test at 1000 and 1050°C based on the relation: □ ∝ √ ⍰[164].

The explicit finite difference method [161] is used for transferring **Eq. (⍰7.4)** into finite difference equations, which has been claimed to be suitable for solving diffusion equations in oxidation problems by other authors [40]. The fictitious point technology [161] is implemented to deal with the end points at both boundaries. The D_{Cr} is assumed to be independent of the concentration gradient of any other alloying element. The programing and the calculations are done in Matlab version 8.4 (R2014b).

With the above described steady-state FDM, the diffusion coefficient of Cr in the alloy can be obtained by fitting the calculated profile to the experimental data. The Cr profiles measured before reaching the specimen center, i.e. after 1000 h at 1000°C as well as the one measured after 300 h at 1050°C were taken for the estimation of D_{Cr}. The obtained D_{Cr} at 1000 and 1050°C as well as the extrapolated D_{Cr} at 950°C for alloy 230 are shown in **Figure ⍰7.3** assuming an Arrhenius type temperature dependence. According to Atkinson [65], the lattice

diffusion coefficients of Cr in Ni-20Cr alloy is about □□ □ − $cm^2.s^{-1}$at 950°C, □□ □ − $cm^2.s^{-1}$ at 1000°C, and □□ □ − $cm^2.s^{-1}$ at 1050°C. In reference [165], the fitted D_{Cr} for a Ni-22Cr-12Co-Mo alloy at 950 °C was found to be □ □ − $cm^2.s^{-1}$. It reveals that the values for D_{Cr} obtained here are in the same range as the data found in literature. The values in the present study are slightly smaller than those in reference [65] at corresponding temperatures, which may suggest that the alloying elements slightly decrease the diffusivity of Cr in alloy 230 compared to that in a binary NiCr alloy.

Using the D_{Cr} value presented in **Figure 7.3**, the calculation of the Cr concentration profiles at the studied temperatures for each specimen thickness has been conducted and compared with the measured data. As expected, the results of the Cr profiles calculated by FDM assuming steady-state oxidation agrees with the experimental results only for short oxidation times, i.e. as long as steady state oxidation prevail. An example of the comparison between calculated and measured profiles (here for a 0.2 mm specimen) is shown in **Figure 7.4**. The Cr profiles after steady-state oxidation for 500, 1000, 1500 and 3000 h are calculated and plotted as solid lines; the experimental data after 1000 and 3000 h oxidation are plotted as data points with the same color as the respective calculated lines for the corresponding times.

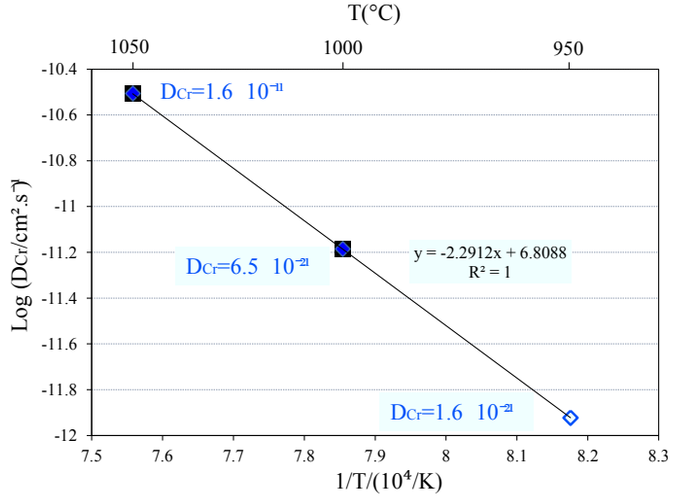

Figure 7.3: Fitted values (at 1000 and 1050°C) and extrapolated value (at 950°C) for the diffusion coefficient of Cr in alloy 230 as function of 1/T.

The oxidation kinetics of the 0.2 mm specimen at 1000°C already starts to deviate from the steady-state power law oxidation after about 600 h (see **Figure 6.2**). The so-called "super-parabolic" oxidation behavior of the 0.2 mm specimen results in a much faster consumption of Cr than during the steady-state oxidation stage (Chapter 6). Therefore, the calculated line after 3000 h is much higher than the measured Cr profile, whereas the calculated line after 1000 h is in good agreement with the measured data. It can be concluded from this result that this FDM calculation approach is only suitable in the steady-state oxidation stage, and the error increases with increasing oxidation time.

The area marked by the gray dashed square in **Figure 7.4** is amplified and shown at the lower right corner. The results illustrate the change of the interface Cr concentration assuming power law oxidation kinetics with n=0.4. With n<0.5, the outward flux of Cr has a larger dependence on time (the flux decreases with time faster than in parabolic kinetics), thus, the depletion profiles tend to be flatter than for the parabolic kinetics. Before the diffusion front reaches the center of the specimen (i.e. for 150 and 300 h), the Cr interface concentration increases slightly with time, in agreement with the consideration in Section 3.3.2.

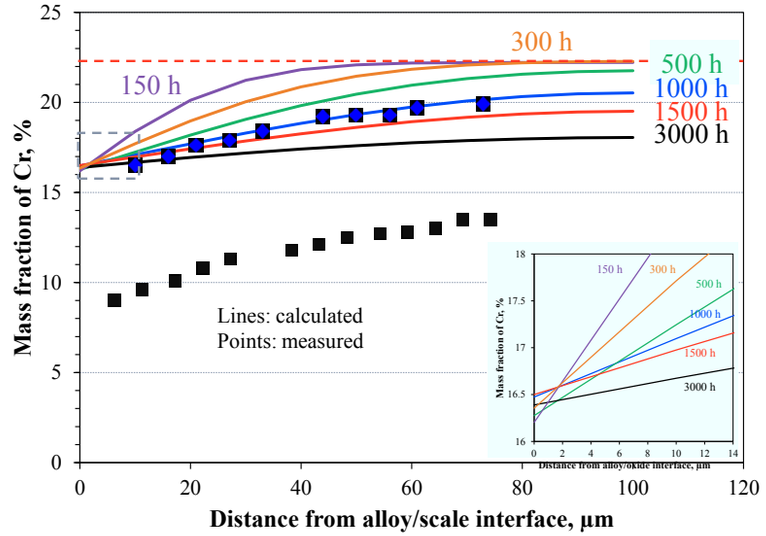

Figure 7.4: Calculated Cr depletion profiles (using FD method) for 0.2 mm specimen of alloy 230 at 1000°C after different times showing comparison with existing experimental data after 1000 h and 3000 h (red dashed line indicates the original Cr concentration). Input data were steady state oxidation kinetics from **Figure 6.11** using k=0.1051 $mg.cm^{-2}.h^{-0.4}$ and n=0.4. Inset shows calculated profiles near alloy/scale interface.

If the diffusion profile reaches the center of the specimen, the interface concentration has to slightly decrease in order to maintain the same flux. So at 500 h, the Cr interface concentration is slightly lower compared to that at 300 h. From 500 to 1500 h, the interface concentration continues to increase and finally decreases with increasing time (e.g. from 1500 to 3000 h). A detailed quantitative explanation of the diffusion mathematics concerning the solute depletion processes falls outside scope of the present study, and will not be discussed in detail here.

7.4.2 Formulation and results of FDM for non-steady-state oxidation

The above results illustrate that the FDM calculation assuming steady-state oxidation cannot be applied for prediction of Cr depletion profiles after long time oxidation due to the inability to describe the complex oxidation behavior (scale spalling and “super-parabolic” scale growth). To make the FD modeling applicable to the cyclic oxidation problem, the steady-state FDM has to be correlated with the cyclic oxidation model, i.e. the modified COSP approach, of which the concept and model formulations have been extensively explained in Chapter 6.

The considerable error of the FDM calculations in describing long time cyclic oxidation appears because the assumed steady-state scale growth neglects the additional outward flux of Cr caused by the scale spallation and re-healing or by the enhanced Cr consumption in case of “super-parabolic” kinetics. Therefore, the way to relate the FDM to the modified COSP is to change the boundary condition at the alloy/scale interface to a more realistic value which has been calculated by the modified COSP model on the basis of the experimentally determined oxidation kinetic data; this condition may be designated as “instantaneous boundary condition”. With the modified COSP model, the total consumption of Cr after each cycle ($m_{m,i}$) can be calculated. After the steady-state oxidation stage, the accelerated consumption of Cr due to scale spalling or due to “super-parabolic” oxidation is taken into account and results in a value for $m_{m,i}$ after each thermal cycle. The mass flux of Cr at the alloy/scale interface at a given time is the derivative of the Cr consumption to time. As an approximation, the flux given in **Eq. (7.4)** can be rewritten into the following expression (see also **Figure 7.5**):

$$\frac{\partial C}{\partial t} \approx \frac{\Delta m_{m,i}}{\Delta t} \cdot \frac{\rho_{Cr,i-1} - \rho_{Cr,i}}{\Delta x} \tag{7.6}$$

Here J_{Cr} is the mass flux of Cr, $m_{m,i}$ the total consumption of Cr after cycle number i, and Δ the increment in time, here equal to the cycle duration (48 h at 1000 and 1050°C, 10 h at 950°C). For converting the mass flux into atomic flux, the instantaneous boundary condition (**Eq. (7.6)**) can be applied to the same explicit finite difference equations as used for the steady-state oxidation stage. In this way, the instantaneous boundary condition finally becomes the bridge between the cyclic oxidation behavior and the finite difference method. With the instantaneous boundary condition, the predicted Cr depletion profile should be flatter and the concentrations of Cr at the alloy/scale interface and the mid-plane of the specimens should decrease faster than calculated using the boundary condition for steady-state oxidation (**Eq. (7.4)**).

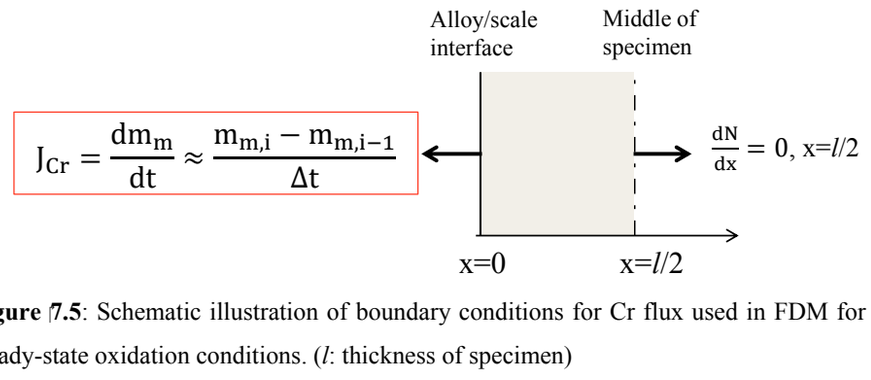

Figure 7.5: Schematic illustration of boundary conditions for Cr flux used in FDM for non-steady-state oxidation conditions. (*l*: thickness of specimen)

Figure 7.6 shows the Cr depletion profiles after long time exposure (1000 and 3000 h) at the studied temperatures calculated with the FDM and are compared with the measured EDX data. At 950°C after both 1000 and 3000 h and at 1000°C after 1000 h, the deviations from steady-state oxidation were, as expected not very significant (**Figure 6.2**). Therefore the Cr depletion profiles can still be described with FDM assuming steady-state oxidation as explained in Section 7.4.1. The profiles calculated by FDM assuming steady-state oxidation are marked as dashed lines in order to be distinguished from the solid lines calculated by FDM for non-steady-state oxidation (**Figure 7.6 a-d**).

At 1050°C the deviation from steady-state oxidation appears already quite early i.e. after about 300 h (**Figure 5.1**). Therefore, the Cr profile after 1000 h has to be calculated by FDM for non-steady-state oxidation; the lines calculated for both times are shown as solid lines in **Figure 7.6 e f**.

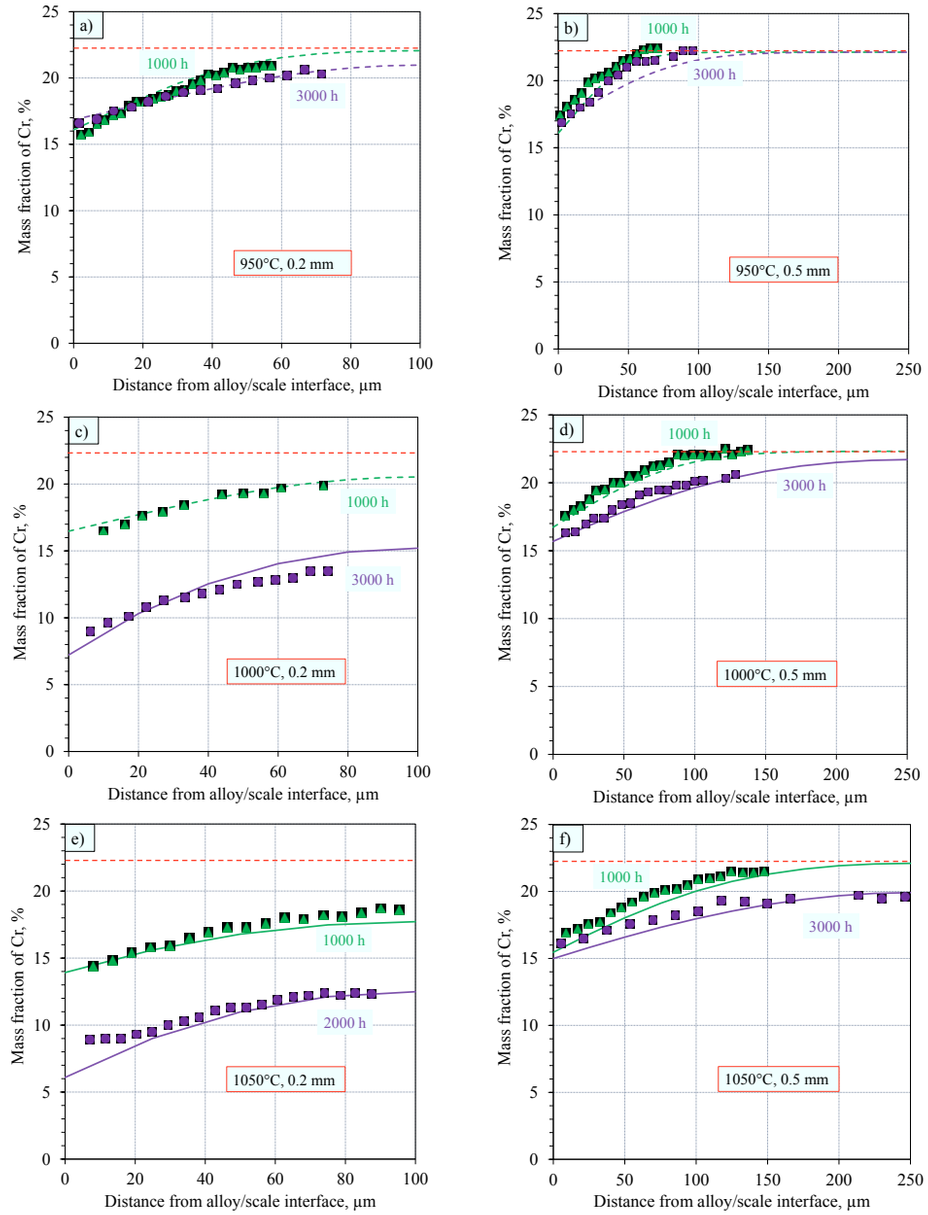

Figure 7.6: Comparision between calculated and measured Cr depletion profiles of alloy 230 at a, b) 950°C, c, d) 1000°C, and e, f) 1050°C. The red dashed lines indicate the original Cr concentration, the solid symbols represent the data measured by EDX. The solid lines relate to calculations by FDM for non-steady-state oxidation, the green and purple dashed lines relate to calculations by FDM assuming steady-state oxidation.

Comparison of **Figure 7.6 c** and **Figure 7.4** reveals for the 0.2 mm specimen after 3000 h at 1050°C that the predicted Cr concentration profile of this specimen (after extensive Cr consumption under cyclic oxidation) by FDM for non-steady-state oxidation shows far better agreement with the experimental data than that predicted by FDM assuming steady-state oxidation. This illustrates that the FDM for non-steady-state oxidation with the instantaneous boundary condition explained in **Figure 7.5** can adequately describe the acceleration of Cr depletion for long term cyclic oxidation conditions. It is apparent that in all the calculated cases good agreement is found between calculated and measured data at all test temperatures for 0.2 and 0.5 mm specimens with acceptable errors, given the common inaccuracies in the EDX measurements and the assumptions made in the modeling. Similar good agreement was found also for the 0.3 mm specimens.

7.4.3 Prediction of critical chromium depletion with FDM for non-steady-state oxidation

The resuls in the previous section show that for long time oxidation the Cr depletion profiles have to be predicted by FDM for non-steady-state oxidation to obtain more accurate results. Therefore, the purpose of predicting times t* of the components should also be realized by the FDM taking non-steady-state kinetics into account.

According to the experimental observations, the end of lifetime is defined as the time when the interface Cr concentration reaches 10 wt. % as discussed in Chapter 6. To distinguish from the notation of t_{10} used in reservoir approach, here the lifetime limit is designated as t_{10}^{F}. The same approach and model parameters for predicting the Cr depletion profiles as explained in Section 7.4.2 are used. The only difference is that, here the calculation is run until a critical number of cycles where the interface Cr concentration has decreased to 10 wt. %.

Figure 7.7 shows the calculated profiles upon reaching t_{10}^{F} for different specimen thicknesses at the studied temperatures. The reference line in **Figure 7.7** indicates the assumption of quasi-flat Cr profiles at the end of lifetime, which was, in analogy to FeCrAl [21, 26] and chromia forming ferritic steels [32, 74] used as the criterion of lifetime limit in the pragmatic reservoir approach for alloy 230 in Chapter 6. As expected, at all temperatures the lifetime limits for the 0.3 and 0.5 mm specimens are much longer than for the 0.2 mm specimen, because of the larger reservoirs of Cr as well as the limited acceleration of Cr consumption caused by scale spallation compared to that caused by “super-parabolic” oxidation of the 0.2 mm specimen (Chapter 6).

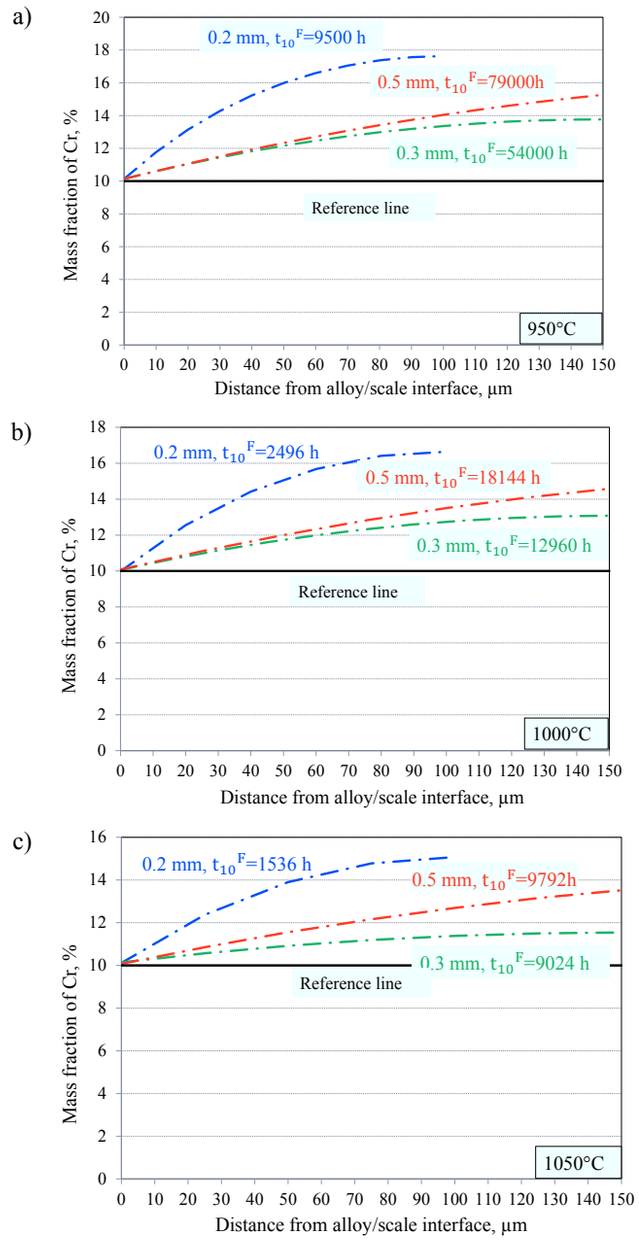

Figure 7.7: Calculated lifetime limits t_{10}^{F} and Cr depletion profiles of alloy 230 specimens with different thicknesses at a) 950, b) 1000, and c) 1050°C. The black line is the reference line which was used as the lifetime criterion (critical solute depletion) in the pragmatic reservoir approach described in Chapter 6.

For the 0.2 mm specimen at 1000°C (**Figure 7.7 b**), the lifetime limit t_{10}^F is 2496 h, which is in good agreement with the experimental observation that breakaway type oxidation was observed at the edges of the specimen after 3000 h with an interface Cr concentration of approximately 10 wt. % (see e.g. **Figure 7.1 c**).

It can be observed that for a given specimen thickness, the Cr profile at t_{10}^F becomes flatter with increasing temperature. For example, with the same interface Cr concentration of 10 wt. %, the mid-plane Cr concentration of the 0.2 mm specimen is 17.6 wt. % at 950°C, 16.6 wt. % at 1000°C, and 15.1 wt. % at 1050°C.

Considering the experimentally observed non-flat Cr profiles prevailing even after very long time oxidation of Ni-Cr alloys, the use of the FDM for non-steady-state oxidation to predict the lifetime should be more accurate than the previously used reservoir approach. The lifetime limits of alloy 230 at all studied thicknesses and temperatures calculated by FDM are compared with the results of the reservoir approach in **Table 7.1** and **Figure 7.8**. Because of the lack of experimental data, the t_{10}^F of the 0.3 mm specimen at 950°C is interpolated (grey numbers in **Table 7.1**) with the same model parameters as for the 0.5 mm specimen assuming similar behavior of scale spallation of the 0.3 and 0.5 mm specimens at 950°C. The lifetime limits obtained by the two approaches are comparable within acceptable relative errors □(□ ^□ – □)□ □□ taking into account the uncertainty in the oxidation induced lifetime prediction. This result suggests that the assumption of a quasi-flat Cr profile at the end of the lifetime in the reservoir approach will not lead to large errors in prediction of t* and is a reasonable method to be applied for a pragmatic lifetime prediction.

Table 7.1: Lifetime limits of alloy 230 specimens comparing calculated results obtained by FDM for non-steady-state oxidation (t_{10}^F) and by reservoir approach (t_{10}). Results of 0.3 mm specimens at 950°C were obtained by using interpolated experimental data (see text for explanation).

Predicted lifetime (h)						
Temperature (°C)	950		1000		1050	
Specimen thickness (mm)	t_{10}^F	t_{10}	t_{10}^F	t_{10}	t_{10}^F	t_{10}
0.2	9500	14070	2496	3072	1536	1623
0.3	54000	69500	12960	13392	9024	7584
0.5	79000	116600	18144	22992	9792	11136

Theoretically, the t_{10}^F values predicted by FDM should be slightly shorter than those predicted by the reservoir approach, because in the latter more Cr has to be consumed to reach the lifetime limit due to the assumption of flat profile. Most of the results obey this expectation; however an exception appears for the 0.3 mm specimen at 1050°C. Many factors can lead to this difference, including the scattering in data caused during the experiment and by the assumptions and approximations in the modeling procedures. Here, for example, the longer t_{10}^F calculated by FDM might result from an underestimation of the Cr flux during long term oxidation.

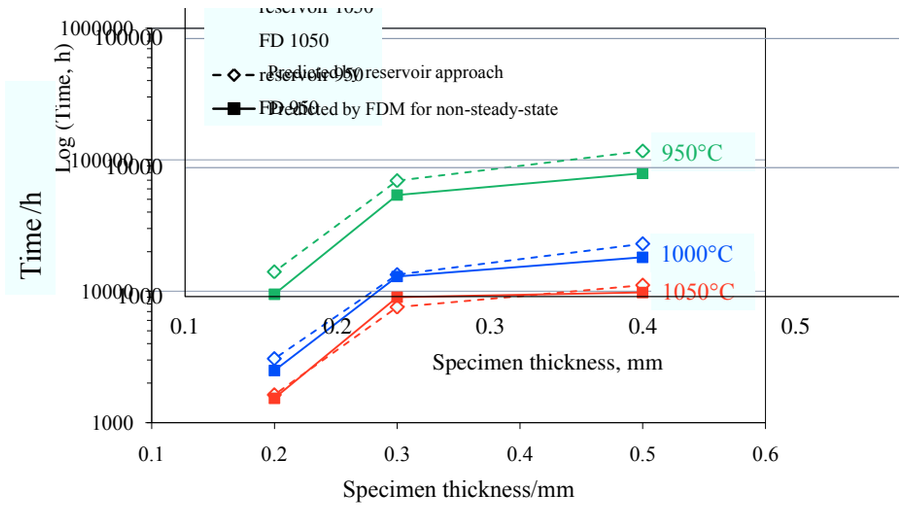

Figure 7.8: Lifetime limits t_{10} predicted by FDM for non-steady-state oxidation and reservoir approach for alloy 230 of different thicknesses at studied temperatures.

To be noted is that the absolute value of the average relative error decreases with increasing temperature, as shown in **Table 7.2**. The total Cr consumption until reaching the lifetime limit calculated by the FDM approach is less than that calculated by the reservoir approach which assumes a quasi-flat Cr concentration profile when the oxidation time approaches t*. For example, the Cr concentration profile of the 0.2 mm specimen at the time t_{10}^F at 950°C is steeper than that at 1050°C (**Figure 8.6 a c**). This results in a larger difference of the calculated Cr consumption between the values obtained by the FDM approach and the reservoir approach at 950°C than that at 1050°C. Therefore the relative difference between t_{10}^F and t_{10} of the 0.2 mm specimen calculated for 950°C is larger than that calculated for 1050°C.

The advantage of the FDM approach is its ability to predict the lifetime limits t* as well as to predict Cr depletion profiles at the same time. The predicted value of t* is in most cases more conservative than those predicted by the reservoir approach.

Table 7.2: Table showing the average relative errors between t_{10}^{F} and t_{10} of alloy 230 at temperatures from 950 to 1050°C.

Temperature (°C)	950	1000	1050
Average relative error	-0.29	-0.14	-0.005

However, compared to the reservoir approach, the calculation of FDM needs more computer time and, thus, longer calculation times to obtain the final result. For example, for the 0.5 mm specimen at 950°C, the t* is more than 100,000 hours and it takes about 10 minutes of calculation to reach this time with 10 h time steps, whereas only several seconds are needed using the reservoir approach. It is apparent that the time for calculation with FDM will increase with increasing specimen thickness, decreasing temperature, and decreasing cycle duration (i.e. smaller time step).

Another limitation imparted by the FDM is the stability criterion (**Eq. (7.7)**) [161] for the explicit finite difference method:

$$\frac{D\Delta t}{\Delta x^2} \leq \frac{1}{2} \qquad (7.7)$$

Here D is the diffusion coefficient, Δt the time step, and Δx the space step. This stability criterion implies that analyzing the results with great detail in space (with a very small Δx), automatically means that the time step should also be small. However in the present model, with the instantaneous boundary condition the time step Δt should be the same as the duration of the thermal cycle used during the experiments (here 48 h or 10 h), which means that the Δt cannot be an arbitrary chosen small value. The problem will especially appear at very high temperatures at which the value of D is quite large. For example, assuming $D = 10^{-4}$ $cm^2.s^{-1}$, according to **Eq. (7.7)**, $\Delta t / \Delta x^2 \leq 0.5$, and an experimental cycle duration of 10 h (36,000 s) results in $\Delta x \geq \sqrt{2 \cdot 10^{-4} \cdot 36000} = 0.085$ cm. To make sure that the half-thickness of the specimen is divided into at least 10 spaces (11 data points for describing the Cr profile), the studied wall thickness should not be thicker than 0.38 mm. The problem of the stability

criterion can be avoided by applying the Crank-Nicholson method for transferring the diffusion equation into finite difference equations without losing accuracy [161], but the model equations will become harder to handle than using the explicit method.

Summarizing it can be said that the FDM for non-steady-state oxidation provides the ability to predict the Cr depletion profiles at the end of the component lifetime in parallel to the prediction of the lifetime limits. It has been found by comparison of the FDM and reservoir approach that in most cases the former results in shorter, thus more conservative lifetime values. However, the reservoir approach has the advantage that it can be, theoretically, applied to all oxidized specimens of NiCr-alloys whose lifetime is limited by a critical Cr depletion without any stability limitations, thereby providing lifetime data which do not differ too significantly from the FDM results; also it describes the dependence of lifetime on oxidation kinetics, time, and specimen thickness in a reasonably accurate manner. Larger difference between results obtained by the two methods are for alloy systems in which the value of k/D is quite large, i.e. if critical Cr interface concentration establishes before a certain “flattening” of the Cr concentration profiles has occurred.

8 Microstructural changes and oxidation induced damage during oxidation of alloy X

8.1 Analyzed chemical composition

Solid solution annealed plate material of alloy X with a thickness of 5 mm was supplied by VDM Metals. The nominal and analyzed chemical compositions of the alloy are listed in **Table 8.1**. The analyzed compositions of Cr, Fe, Mo, Co and C are between the maximum and minimum of the nominal values, however no W was found by the ICP-OES method in the studied batch. Additionally, minor amounts of the elements Ti, N and O, not clearly specified in the nominal composition, were found by ICP-OES or infrared analysis.

Table 8.1: Chemical composition of studied batch of Alloy X (in wt. %) determined by ICP-OES and combustion infrared analysis compared with nominal composition supplied by manufacturing data sheet [121].

		Ni	Cr	Fe	Mo	Co	W	Si	Mn	P	B
Nominal	min.	Bal.	20.5	17.0	8.00	0.50	0.20				
	max.		23.0	20.0	10.00	2.50	1.00	1.00	1.00	0.0015	0.005
Measured		Bal.	22.0	17.8	8.49	1.33	-	-	0.39	-	-

		Al	Ti	C	N	O	S
Nominal	min.		-	0.05	-	-	
	max.	0.10		0.15			0.01
Measured		0.25	0.029	0.061	0.018	0.0014	<0.001

8.2 Oxidation kinetics

Figure 8.1 shows the area specific weight changes of alloy X specimens during oxidation at 950 - 1050℃ . At the three temperatures, no thickness dependence of the oxidation kinetics is apparent during the first stages of exposure. The results in **Figure 8.1** show that the independence of specimen thickness prevails up to about 800 h at 950°C, 500 h at 1000°C, and 200 h at 1050°C. The shortening of this stage with increasing temperature is in qualitative agreement with the results obtained for alloy 230 (Section 6.2).

a)

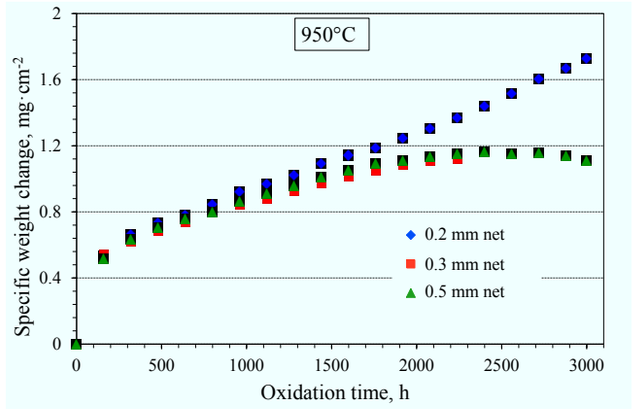

b)

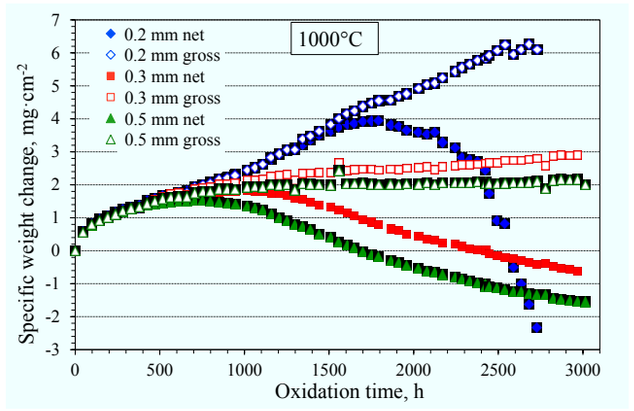

c)

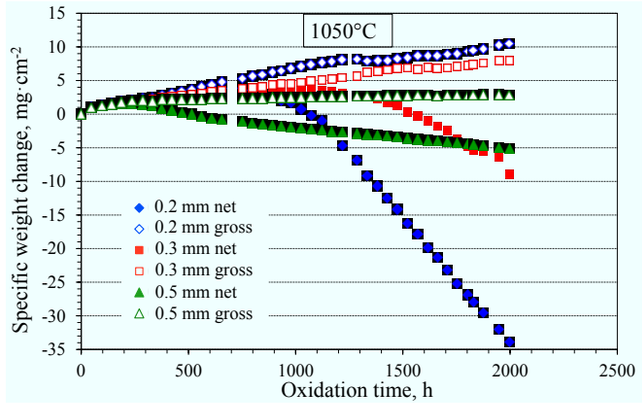

Figure 8.1: Weight change curves of alloy X specimens with different thicknesses during oxidation tests at a) 950°C, b) 1000°C, and c) 1050°C in air.

After the first oxidation stage, the weight change of the thinnest specimens (0.2 mm) always exhibits “super-parabolic” kinetics. The same behavior has been observed for the 0.2 mm specimens of alloy 230, and, as discussed in Section 6.2, the thinner the specimen, the smaller the tendency to scale spallation. As explained in Section 6.4.1, the relaxation of the stress during cooling in the scale of the thinnest specimen will eventually change the stress state in the scale during re-heating from compressive to tensile, resulting in the formation of micro-cracks in the scale, which increases the oxidation rate. Selected experiments were interrupted prior to reaching the final exposure time of 3000 h because of the appearance of breakaway oxidation.

To be noticed is that at 1050°C, not only the weight change of the 0.2 mm but also that of the 0.3 mm specimen shows a short period (see the red points between 200 h and 900 h) of slight “super-parabolic” behavior. At higher temperature, the temperature difference between upper and lower dwell temperature during thermal cycling is larger, which leads to thermal stresses apparently large enough to cause the thicker specimen to creep after a critical number of cycles, i.e. after exceeding a certain scale thickness. As shown in Chapter 6, the 0.3 mm specimen of alloy 230 did at 1050°C not show the “super-parabolic” behavior. This difference between alloy 230 and alloy X at 1050°C may be related to the fact that the creep strength of alloy 230 is higher than that of alloy X, as indicated in the product data sheets [52, 121, 166]. The larger tendency to “super-parabolic” oxidation may also be related to the higher oxidation rate of alloy X compared to that of alloy 230 (as will be further discussed in Section 8.5), which may lead to a larger tensile stress in the substrate at a given time due to a thicker oxide scale.

The drastic scale spallation (rapid drop of the net weight change curves) of the 0.2 mm specimen after 1700 h at 1000°C and 800 h at 1050°C as well as the 0.3 mm specimen after 1200 h at 1050°C is not related to spallation of the protective chromia base scale but indicates failure of the specimens, as will be discussed later in Section 8.3. It is interesting to note that at 1050°C the weight change of an additional test specimen with a thickness of 1 mm is almost the same as that of the 0.5 mm especially after long time exposure (see **Figure 8.2**). This result suggests that at a given temperature, the specimen thickness dependence of oxidation behavior becomes less significant when the specimen thickness is larger than a critical value.

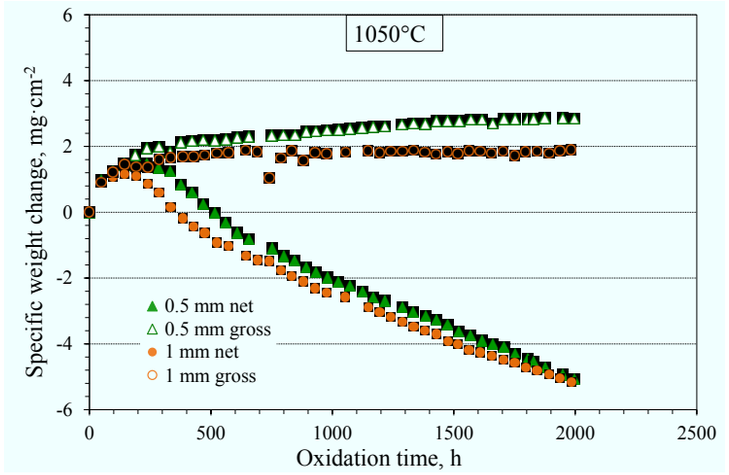

Figure 8.2: Comparison of weight change data of 1 mm and 0.5 mm specimens of alloy X during oxidation at 1050°C in air.

The similarity of the oxidation behavior beyond a critical specimen thickness has also been found for alloy 230 (Section 6.4), and can be explained in the following way:

The main reason of the thickness dependent oxidation rate is the different extent of substrate creep. Therefore if the substrate does ideally not creep or the creep rate is quite slow, the thickness dependence will vanish.

During long term high temperature oxidation, the growth of the oxides on the top of the alloy will create growth stress ($\sigma^{?}$) because of the distortion of the lattice [153, 167-169] and/or oxide formation within the scale [15]. On an alloy substrate with a given thickness, the growth stress increases with increasing oxide thickness [15]. The thermal mismatch due to the difference between the thermal expansion coefficient of the oxide and the alloy ($\alpha \quad - \alpha_{?}$) results during the cooling process in a compressive thermal stress in the scale ($\sigma \quad$) and a tensile thermal stress in the alloy ($\sigma_{?}$). For mechanical equilibrium the force balance dictates [168]:

$$\sigma \quad \sigma \quad \frac{}{} \tag{8.1}$$

where the superscript I indicates the growth stress, II the thermal stress. h_{OX} is the thickness of the oxide layer formed on each side of a flat substrate of thickness $2h_M$.

According to reference [168], the growth stress and the thermal stress in the scale can be expressed by the following equation:

$$\sigma \quad \square \frac{\square}{(\square - \square)} \frac{(\alpha \quad - \alpha_{\square})\Delta\square}{\square\square\ \square} \tag{8.2}$$

Where E is the Young"s modulus, v is the Poisson ratio, and R represents a term including the oxide and alloy thickness:

$$\square\ \square \frac{\square \quad (\square - \square_{\square})}{\square_{\square}(\square - \square\ )} \cdot \frac{\square}{\square_{\square}} \tag{8.3}$$

A conclusion drawn from **Eq. (8.2)** and **(8.3)** is that for a thick alloy substrate, where the oxide/alloy thickness ratio $h_{OX}/h_M \ll 1$, the dependence of thermal stress in the scale as well as the thermal stress in the alloy substrate (**Eq. (8.1)**) on h_{OX}/h_M or on h_M can be neglected.

The creep of the alloy is expressed generally as a power law stress dependence of the creep rate in the metal on the applied stress (for either growth stress or thermally induced stress) as [153, 155]:

$$\frac{\partial\varepsilon}{\partial\square}\square\ \square \cdot \sigma^{\square} \tag{8.4}$$

Here ε is the creep strain, K is constant for a given alloy at a given temperature and n is the creep exponent commonly used when describing an exponential stress dependence of creep rate [153, 170]. The creep rate in the alloy substrate due to the induced tensile stress caused by the compressive growth stress in the oxide can then be described as:

$$\frac{\partial\varepsilon}{\partial\square}\square\ \square \cdot \left(\sigma \quad \cdot \frac{\square}{\square_{\square}}\right)^{n} \tag{8.6}$$

Only when the creep rate exceeds a critical value, the creep of the substrate will be sufficiently large to affect the oxidation kinetics of a specimen with given thickness. According to the above discussions, the growth stress in oxide ($\sigma^{?}$) decreases with decreasing h_{OX}/h_M ratio, therefore according to **Eq. 8.1**, $\sigma^{?}_{?}$ decreases with decreasing h_{OX}/h_M; the thermal stress in the oxide ($\sigma_{?}$) does not depend on the h_{OX}/h_M ratio once the h_M exceeds a critical value. Therefore, the creep rate is approximately only dependent on the ratio of

h_{OX}/h_M. That means, if the thickness of the alloy substrate h_M is larger than a critical value, the creep rate of the substrate is too small to cause a significant influence on the oxidation kinetics.

Therefore, when the substrate thickness is larger than a critical value, the alloy exhibits a "quasi-elastic" behavior during oxidation. In this case, the rate of scale growth as well as the rate of scale spallation will no longer depend on the substrate thickness. This explains the similarities in oxidation kinetics, and the rate of spallation of the 0.5 and 1 mm specimens. It should be mentioned that other authors of reference [15] showed, that the tendency to scale spalling is not only affected by scale thickness but additionally by formation of physical defects (cracks, voids) in the scale and/or at the alloy/scale interface, e.g. as a result of vacancy condensation (see Section 3.3.2). A detailed description of these effects falls outside the present discussion.

It can thus be concluded that, in the studied temperature range, the differences in oxidation kinetics after the steady-state oxidation stage might be classified according to specimen thicknesses: "plastic" behavior for 0.2 mm and thinner specimens, "mixed" behavior for 0.3 mm, and "quasi-elastic" behavior for 0.5 mm and thicker specimens.

8.3 Microstructral changes and subscale depletion

The as-received, solution annealed alloy X consists mainly of a face-centered-cubic γ-Ni matrix and minor amount of M_6C. Exposures at 950 - 1050℃ result in precipitation of more M_6C precipitates within the grains as well as at the grain boundaries. This is illustrated by **Figure 8.3** showing the cross section of a 0.2 mm specimen after a 70 h short term TG test at 1000°C, i.e. conditions under which the microstructure has not been affected by the oxidation process.

Figure 8.4 shows the BSE cross sections of the specimens after 1000 h discontinuous oxidation at 1000°C. According to the EDX element spectra, there is a thin layer of Mn, Fe, Cr-rich spinel phase on top of the pure Cr_2O_3 scale of the 0.2 mm specimen, which was not observed for alloy 230 (Section 5.3). The formation of the continuous Mn-rich chromia spinel has frequently been found to be accompanied by a higher chromia growth rate during air or Ar-O_2 exposure [109]. This might explain the faster oxidation kinetics of alloy X compared to that of alloy 230.

The spinel phase was not observed for the 0.3 and 0.5 mm specimens, which may be the result of scale spallation occurring already after about 500 h of oxidation (**Figure 8.1 b**). The cracks in the upper part of the oxide scale (**Figure 8.4 a, c**) indicate that the scale spallation occurs virtually parallel to the gas/oxide interface. Fine particles of internal Al_2O_3 are scattered in the subscale region as well as along the grain boundaries. The size of the M_6C carbide precipitates increased slightly compared to that found after short time oxidation in the TG test (**Figure 8.3**).

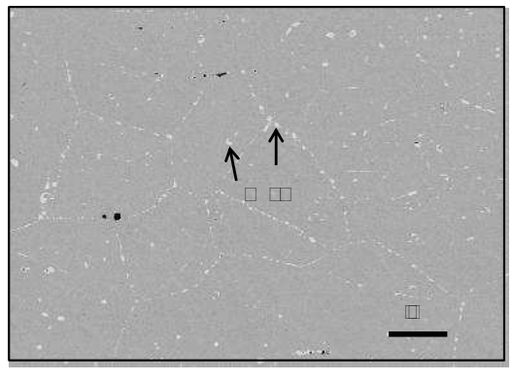

Figure 8.3: BSE image showing the cross section of the 0.2mm alloy X specimen after 70 h TG test at 1000°C.

Figure 8.5 shows the oxide scales as well as the subscale microstructures of the specimens after 3000 h discontinuous oxidation at 1000°C. The laterally variable scale thickness of the 0.2 mm specimen is a result of drastic scale spallation (**Figure 8.1 b**). As mentioned in Section 8.2, the drastic scale spallation is not caused by the spallation of the protective Cr_2O_3 based scale, but by the spallation of the non-protective, “breakaway type” scale incorporating relative large amounts of Fe and Mn, as indicated by the result of point EDX analyses (**Figure 8.5 a**). This observation may suggest that the onset of drastic scale spallation (change of the slope of the net weight change curve after a period of steady scale spallation in **Figure 8.1 b**) approximately corresponds to the time when breakaway oxidation occurs. For the 0.3 mm specimen, instead of a continuous layer, only fragments (e.g. see EDX result of point 2) of Mn, Cr-spinel are observed as a result of scale spallation as discussed above.

The alloy microstructures of the 0.3 and 0.5 mm specimen after 3000 h look quite similar to those of the 0.3 and 0.5 mm specimens after 1000 h oxidation (**Figure 8.4 b c**). However, the carbide precipitates in the 0.2 mm specimen are replaced by the π-phase nitride in the 0.2 mm specimen after 3000 h oxidation (**Figure 8.4 a**). This is another indication of the change of

oxide scale property from protective to non-protective after a critical Cr depletion, in a similar manner as explained for alloy 230 in Section 5.5. Additionally, substantial formation of internal Cr_2O_3 into the bulk alloy occurs in the 0.2 mm specimen after 3000 h oxidation at 1000℃ .

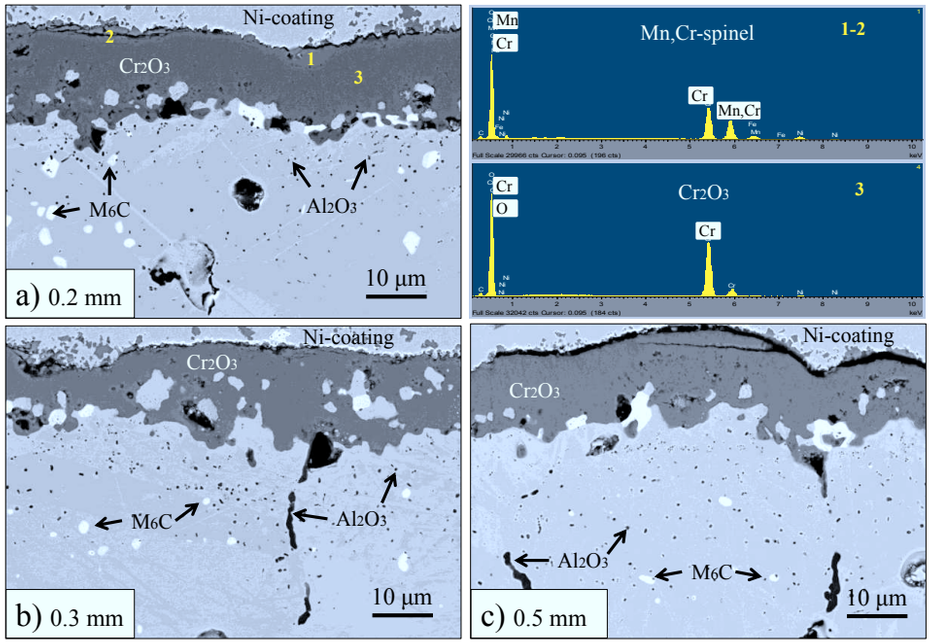

Figure 8.4: BSE cross section images and EDX analysis of selected points of alloy X specimens with different thicknesses after 1000h oxidation at 1000°C.

More cross section images focusing on the microstructures in the center of the specimens after oxidation of 1000 h and 3000 h at 1000℃ are shown in **Figure 8.6**. It is apparent that the particle size and volume fraction of the precipitated phase (white colored) in the bulk alloy increases with decreasing specimen thickness (compare **Figure 8.6 a, b, and c** or **Figure 8.6 d, e, and f**) and increasing oxidation time (compare e.g. **Figure 8.6 b and e**). The quantitative values of volume fractions of the precipitates in the specimens were measured by AnalySIS Pro 5.0 software and are shown in **Table 8.2**. It was found by EDX point analyses and mappings (see **Figure 8.7**) in combination with EBSD analysis that the precipitates in the 0.5 mm specimen after oxidation for 3000 h at 1000℃ are Mo-rich M_6C carbide.

In the 0.3 mm specimen, the precipitate after 3000 h is mostly M_6C carbide and a minor amount of nitride was found. The contrast in **Figure 8.6** does not allow an unequivocal separation between the nitride and carbide phases, whereas the EDX element mapping (**Figure 8.8**) and EBSD phase mapping (**Figure 8.9**) clearly illustrate the presence of nitride at the grain boundary along with the M_6C particles. The data shows that the nitride possesses the Ni_2Mo_3N structure; it is the same type of nitride phase, designated as π-phase found in alloy 230 (Chapter 5).

In the 0.2 mm specimen, the M_6C carbide disappears after long term exposure. Instead, a network of nitride precipitates is formed (**Figure 8.6 b**). With decreasing specimen thickness, the content of N in the precipitate increases and the original M_6C in the alloy becomes eventually replaced by the formation and coarsening of the nitride.

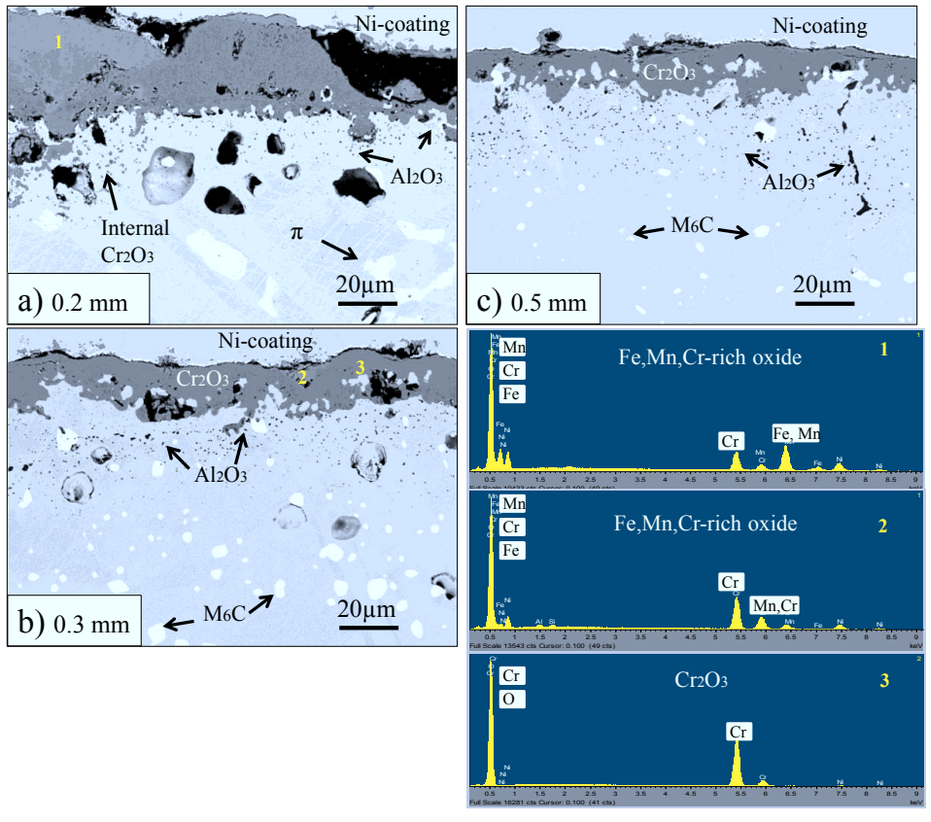

Figure 8.5: BSE cross section images and EDX analysis of selected points of alloy X specimens with different thicknesses after 3000 h oxidation at 1000°C.

Because the reservoir of Cr in the thin specimen is smaller than that in thick specimens, the re-healing ability of the Cr_2O_3 scale after spallation decreases with decreasing specimen thickness. Therefore, after long term exposure, the Cr_2O_3 scale of the thinnest specimen (0.2 mm) loses its protective property.

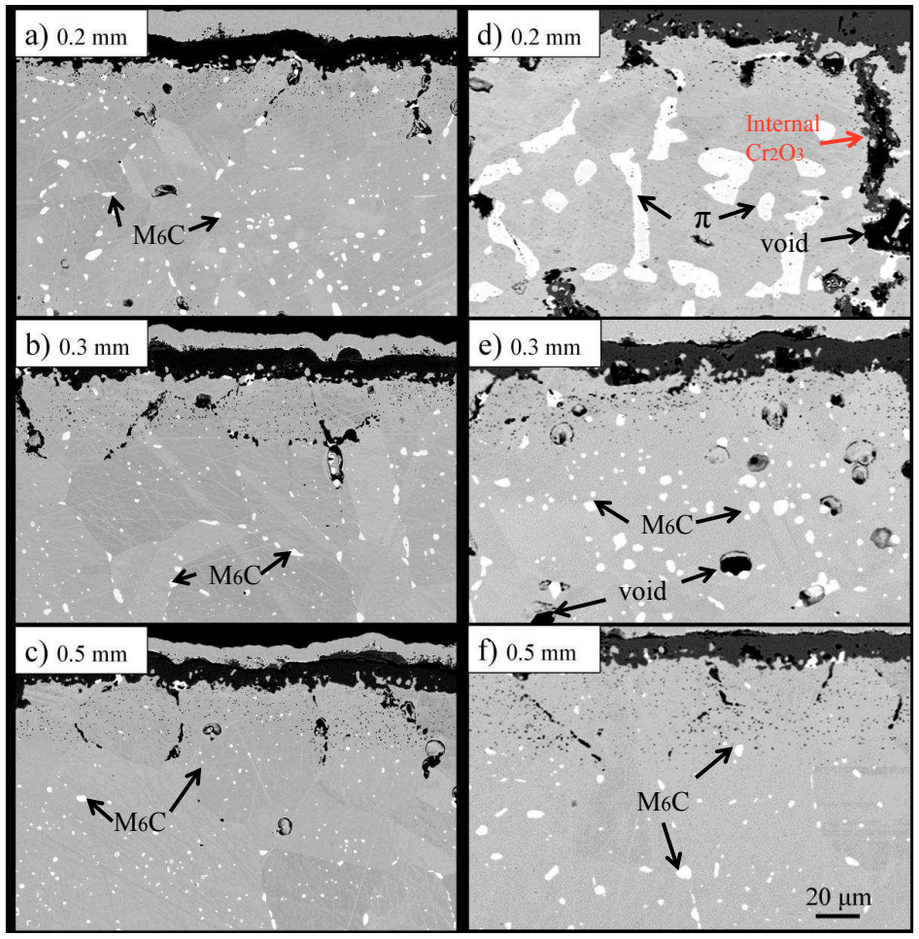

Figure 8.6: BSE cross section images showing the specimen thickness dependent microstructure of alloy X specimens after a-c) 1000 h and d-f) 3000 h oxidation at 1000°C.

The poor protective property of the scale makes the alloy vulnerable to nitridation by allowing the molecular ingress of nitrogen from the atmosphere. This phenomenon of nitride formation is similar to that was found for alloy 230 (see Chapter 5).

The EDX element mappings (**Figure 8.10** and **Figure 8.11**) of the 0.2 mm specimen show again that the precipitates are Ni- and Mo- rich nitride and contain minor amounts of Cr. The randomly dispersed small black particles in the BSE image of **Figure 8.10** are found to be CrN nitride (also see dark blue particles in **Figure 8.12**). Since the Cr is an important element to form the nitrides, the amount of nitride in the alloy depends not only on the property of the protective scale, but also on the reservoir of Cr in the alloy.

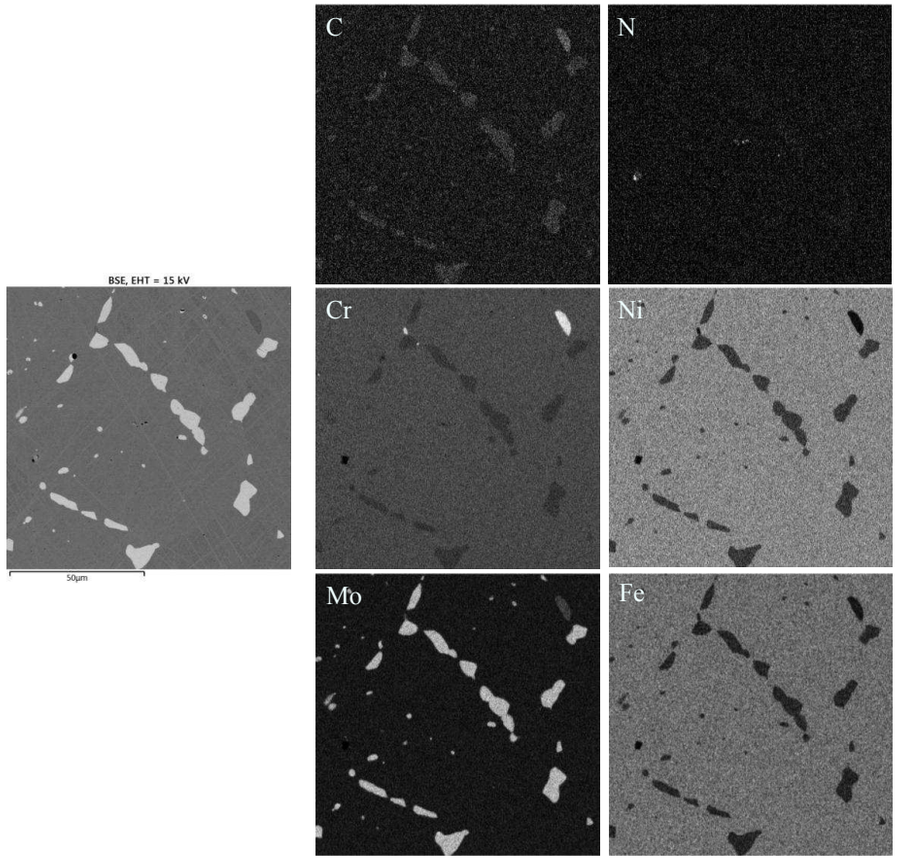

Figure 8.7: BSE image (left) and EDX element mappings in the center of the 0.5 mm specimen of alloy X after 3000 h oxidation at 1000°C (compare **Figure 8.6** and **Figure 8.5 f**).

After 3000 h oxidation (**Figure 8.6 d-f**), thinner specimens (0.2 and 0.3 mm) exhibit more void formation in the bulk alloy than the 0.5 mm specimen. This might be a result of ingress of vacancies produced by outward cation flux in the scale, of Kirkendall voids [62, 63] and/or creep voids [155] due to substrate creep. The latter might occur during cooling (see

discussions in Section 6.2), but also during the high temperature exposure as a result of compressive oxide growth stress initiating tensile stresses in the substrate.

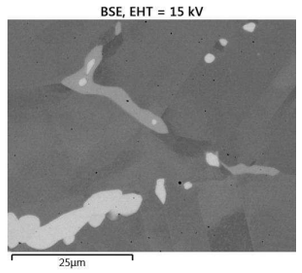

Figure 8.8: BSE image (left) and EDX element mappings in the center of the 0.3 mm specimen of alloy X after 3000 h oxidation at 1000°C (compare **Figure 8.6 e**).

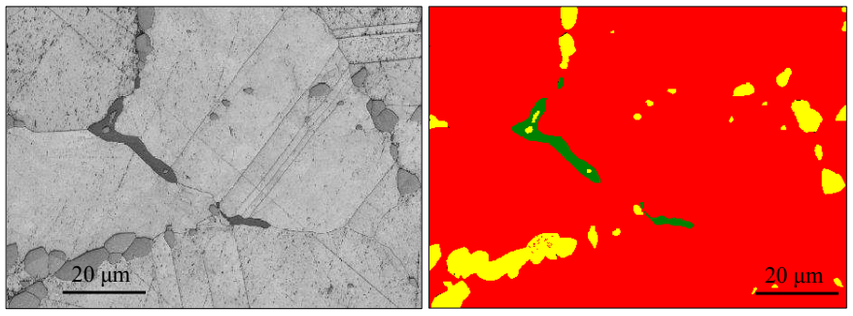

Phase Map: red – γ; yellow – M_6C; green – Ni_2Mo_3N(π phase)

Figure 8.9: EBSD phase mapping in the center of the 0.3 mm alloy X specimen after oxidation for 3000 h at 1000°C (see **Figure 8.8**).

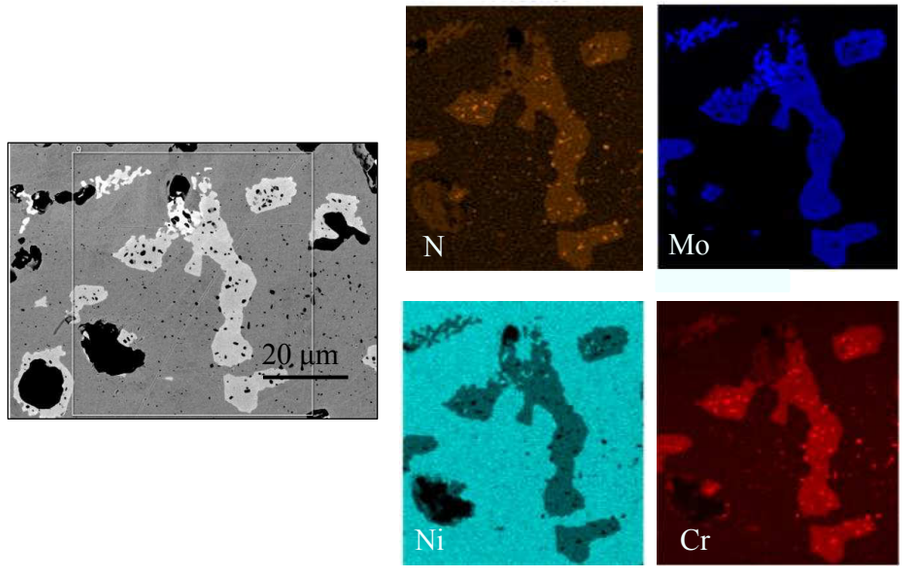

Figure 8.10: BSE image (left) and EDX element mappings in the center of the 0.2 mm specimen of alloy X after 3000 h oxidation at 1000°C (compare **Figure 8.6 d**).

The voids in the 0.2 mm specimen even started to form a network allowing the internal oxidation of Cr along the voids (see **Figure 8.6 d** and the phase in aqua color in **Figure 8.12**). This effect may finally initiate formation of vital transverse cracks. In addition to the indications of the breakaway discussed above, the massive formation of protrusions of internal Cr_2O_3 is supposed to be another sign of failure of the specimen.

Figure 8.13 shows the cross sections of the specimens after 1000 h and 2000 h oxidation at 1050°C. Similar to what has been observed for specimens oxidized at 1000°C, the amount of precipitates in the specimen center after 1000 h oxidation at 1050℃ increases with decreasing specimen thickness (see **Figure 8.13 a-c** and **Table 8.2**). However, the amount of the precipitates of the 0.2 and 0.3 mm specimens seems to decrease with oxidation time, showing an opposite time dependence to that observed at 1000℃ (**Figure 8.13 d e** and **Table 8.2**). Different from the formation of a network of nitride in the 0.2 mm specimen after 3000 h oxidation at 1000°C (**Figure 8.6 d**), here the nitride is nearly completely vanished in the bulk alloy of the 0.2 mm specimen. This suggests an “escape” of nitrogen to the atmosphere after long term oxidation at higher temperature as a result of extensive Cr depletion.

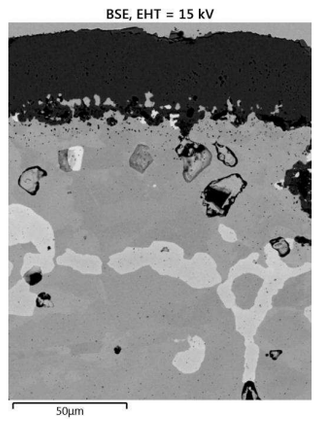

Figure 8.11: BSE image (left) and EDX element mappings in the center of the 0.2 mm alloy X specimen after 3000 h oxidation at 1000°C (compare **Figure 8.7 d**).

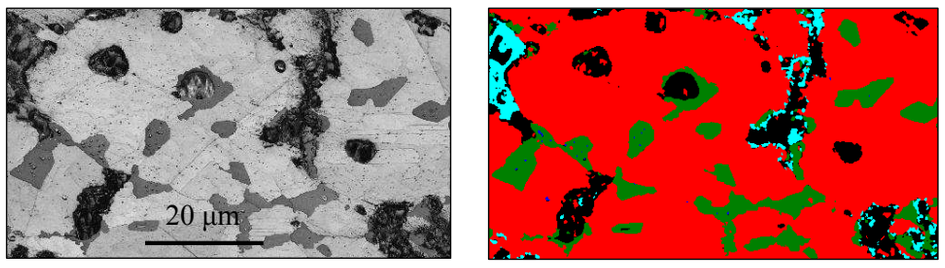

Phase Map: red – γ; blue – CrN; green – Ni_2Mo_3N; aqua – Cr_2O_3

Figure 8.12: EBSD phase mapping in the center of the 0.2 mm alloy X specimen after oxidation of 3000 h at 1000°C (compare **Figure 8.6 d**).

It has been mentioned in Section 8.2 that the experiments at 1050°C were interrupted after 2000 h due to the macroscopically visible failure of some of the specimens. Here the 0.2 and 0.3 mm specimens no longer maintained the original specimen shape after 2000 h, corresponding to the drastic scale spallation shown by the weight change curves in **Figure 8.1 c**. The content of Cr in the 0.3 mm specimen after 2000 h at 1050°C is less than 10 wt. % (**Figure 8.16 e**), and the content of Cr in the 0.2 mm specimen is even less than 5 wt. % (**Figure 8.16 d**). This is likely the main reason for the above mentioned dissolution of nitride. This phenomenon has been verified by thermodynamic equilibrium calculations using Thermal-Calc 5.0 (see Section 8.4).

Figure 8.14 shows the cross sections of the 0.2 and 0.5 mm specimens of alloy X oxidized at 950°C for 3000 h. As was observed for the 0.2 mm specimen oxidized at 1000°C for 1000 h (**Figure 8.4**), a thin layer of Mn/Cr-spinel is present in the outer part of the scale of the 0.2 mm specimen oxidized at 950°C. Neither nitridation nor extensive internal oxidation of Cr was found in the alloy substrate. Therefore no indications of breakaway were apparent after oxidation for 3000 h at 950°C for both specimen thicknesses. The subscale Cr concentration profile of the 0.5 mm specimen after oxidation of 3000 h at 950°C is shown in **Figure 8.15**. The interface Cr concentration is ~15 wt. % and the depletion front has not reached the center of the specimen. This again indicates that the exposure time of 3000 h is far smaller than the lifetime limit of this specimen.

Figure 8.16 shows the time dependent subscale Cr concentration profiles of alloy X specimens of different thicknesses oxidized at 1000 and 1050℃. For obtaining more quantitative information about the time dependence of the Cr depletion kinetics, TG tests were conducted for 0.2 and 0.5 mm specimens and the subscale Cr profiles are also shown in **Figure 8.16**. The profiles relating to specimens with apparent shape change after the experiments are indicated with the word “failure”.

As the result of diffusion controlled Cr depletion, a qualitatively similar time dependence is observed here as that discussed for alloy 230 in Chapter 6 and 7. The interface Cr concentration is around 14 - 15 wt. % before the diffusion front reaches the center of the specimen, as e.g. seen from the profiles after the 100 h TG test at 1000℃ or the 72 h TG test at 1050℃ in **Figure 8.16**.

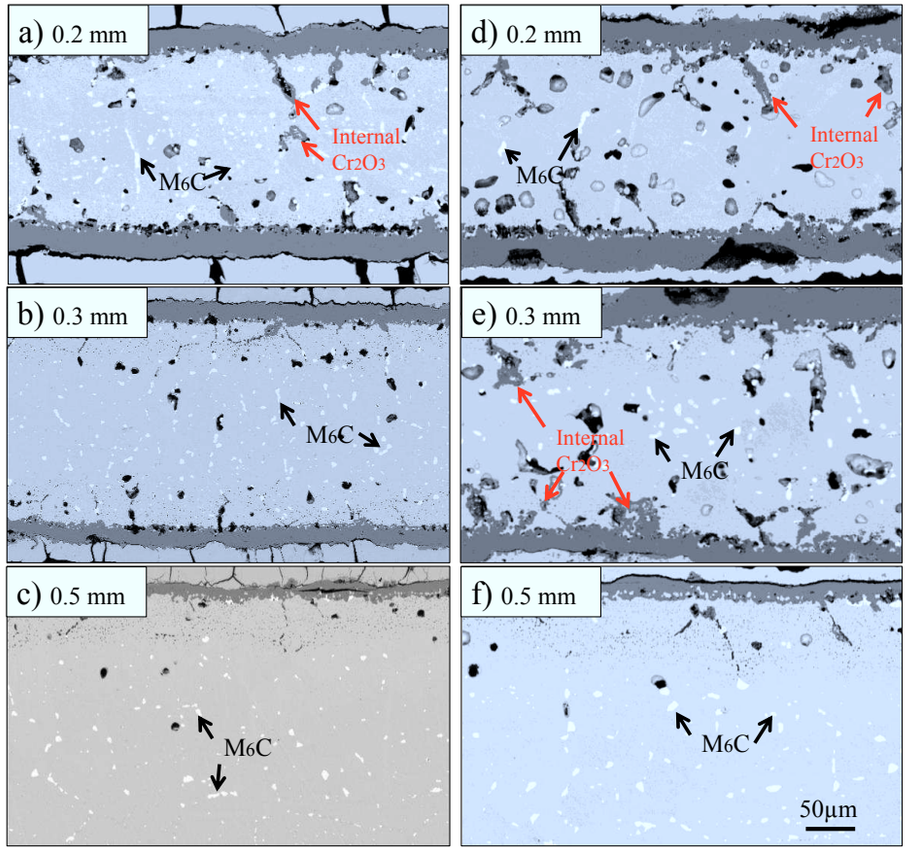

Figure 8.13: BSE cross section images showing specimen thickness dependent oxide scale formation and alloys microstructure of alloy X after a-c) 1000 h and d-f) 2000 h oxidation at 1050°C.

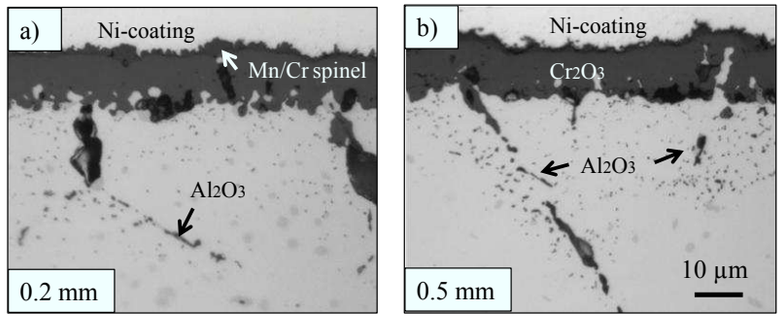

Figure 8.14: BSE cross section images showing scale and microstructure of the a) 0.2 and b) 0.5 mm specimens of alloy X after 3000 h oxidation at 950°C.

Table 8.2: Volume fraction (%) of precipitates (M_6C and/or π) in the specimen center after oxidation at 1000 and 1050°C (red numbers indicate the significant nitridation at 1000°C and the vanishing of nitride at 1050°C in the 0.2 mm specimen; see the text for detailed explanation).

	Exposure time, h			
	1000	3000	1000	2000
Specimen thickness, mm	1000°C		1050°C	
0.2	3.4	27.6	4.7	0.4
0.3	2.6	4.3	3.0	2.8
0.5	1.3	2.5	1.3	2.5

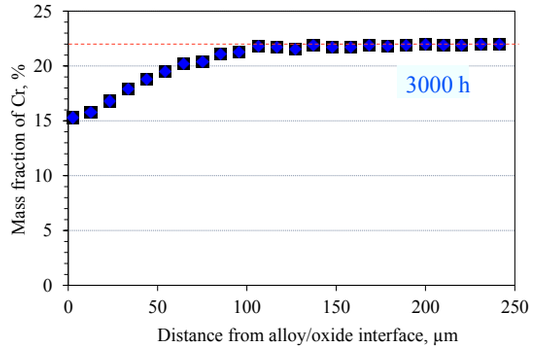

Figure 8.15: Concentration profile of Cr in γ-Ni matrix (measured by EDX) of the 0.5 mm specimen of alloy X oxidized at 950°C for 3000 h.

After the diffusion front reaches the center of the specimens, the mid-plane Cr concentration starts to decrease, whereas the interface Cr concentration increases slightly for a short time period and then decreases again together with the mid-plane Cr concentration. The level of 10 wt. % Cr which was used as the lifetime criterion for t_{10} (in case of alloy 230) is marked with a solid line. Three Cr profiles (in **Figure 8.16 a d e**) are below the solid lines, and one (in **Figure 8.16 d**) is only slightly above, i.e. it almost reaches the critical concentration. The four specimens in which these Cr profiles are found, exhibit significant internal Cr_2O_3 formation (marked with red arrows in **Figure 8.6** and **Figure 8.13**). This finding may verify the consideration made above, that the appearance of significant internal Cr_2O_3 corresponds to a loss in protective properties of the external scale. Although the 0.2 mm specimen oxidized at 1050°C for 1000 h does not show a clear macroscopically visible indication of breakaway

oxidation, it seems reasonable to assume that this specimen is just at the transition time when the breakaway process just begins.

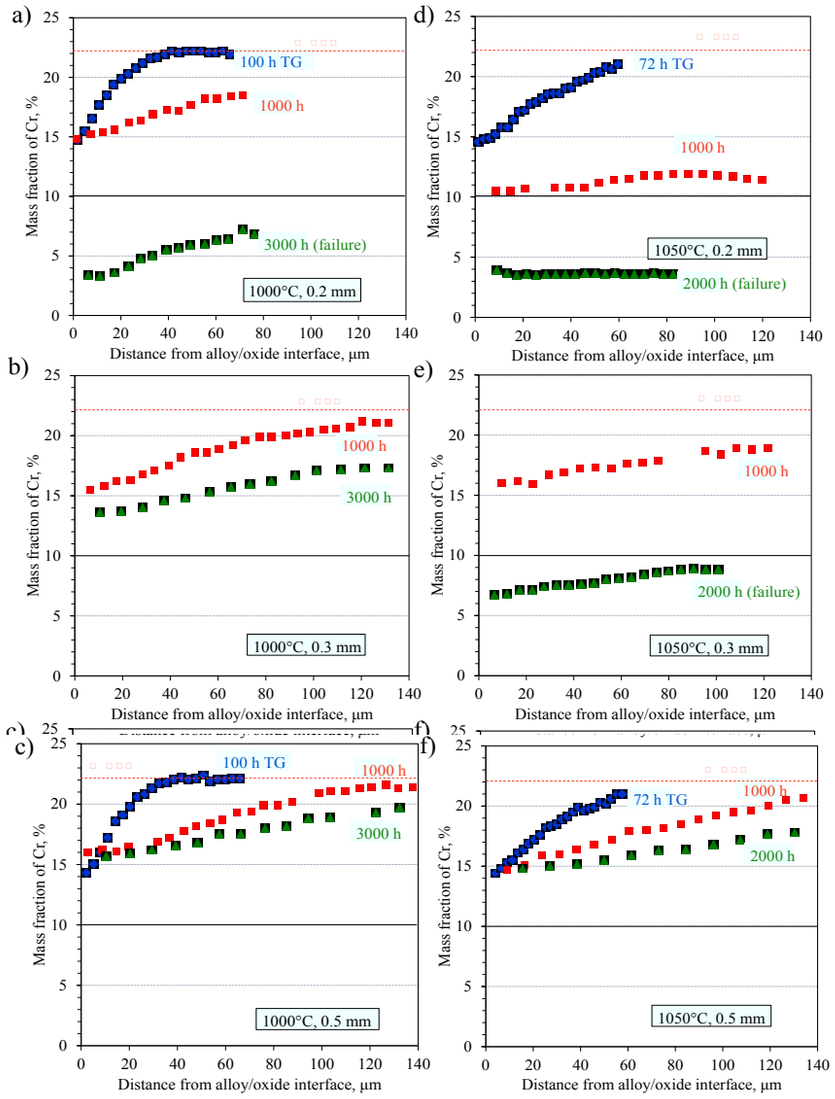

Figure 8.16: Concentration profiles of Cr in γ-Ni matrix (measured by EDX) of alloy X specimens of different thicknesses after different times of air oxidation at a-c) 1000°C and d-f) 1050°C.

8.4 Modeling nitride formation and dissolution

Figure 8.17 illustrates the calculated isothermal section of the phase diagram for the studied batch of alloy X at 1000 and 1050°C. Thus, the concentrations of Fe, Mo, W, C etc. are kept constant at the level of the as-received material (**Table 8.1**). The red dot indicates the composition of the alloy before oxidation. According to the calculations the alloy has a two-phase microstructure consisting of γ-Ni and M_6C, in agreement with the experimental observations shown in **Figure 8.3**. Upon oxidation for 3000 h at 1000°C for the 0.2 mm specimen the concentration of Cr in the specimen center decreases to about 6 - 7 wt. % (**Figure 8.16 a**), whereas the concentration of N should increase. Thus, the composition of the alloy is approximately located in the position indicated by the green dot. The phase diagram at 1000°C shows that after oxidation, the π-phase (calculated composition in wt. %: 60.4Mo-27.5Ni-4.56Cr-7.24N) is formed in addition to the original two-phase microstructure of γ-Ni and M_6C (calculated composition in wt. %: 54.26Mo-22.49Ni-15.8Cr-4.53Fe-0.22Co-2.67C). While at 1050°C, with decreased Cr concentration (here the value of 3 wt. % after 2000 h oxidation in the specimen of 0.2 mm thickness taken from **Figure 8.16 d**), the microstructure transfers from region ① through region ② and ③ to region ④. During this process, the π-phase is initially formed and then becomes subsequently dissolved. The latter results in formation of nitrogen gas which is released into the atmosphere. From the diagram it can be seen that, as long as the concentration of Cr is lower than 7.8 wt. % even if that of N is higher than 0.4 wt. %, the nitride will completely disappear (**Figure 8.17 b**).

Figure 8.18 shows the calculated mole fractions of the stable phases in alloy X as a function of mass fraction of N at a Cr concentration level of 5 wt. %. This value is approximately between 3 wt. % (1000°C) and 6 wt. % (1050°C) of Cr in the center of the 0.2 mm specimens shown in **Figure 8.16**. According to the calculation, γ-Ni, M_6C and hcp-nitride (π-phase) are stable phases at 1000°C. With increasing mass fraction of N, the fraction of M_6C does not change significantly, whereas the fraction of nitride increases. However, the calculated mole fraction of the nitride is much less than experimentally observed, especially for the thinnest specimen. This indicates that in reality, the main reason for the coarsening of the nitride is the ingress of N from the atmosphere. For a Cr concentration of 5 wt. % at 1050°C, the nitride phase no longer exists. Besides, the fraction of M_6C at 1050°C is less than that at 1000°C under the conditions used in the calculation.

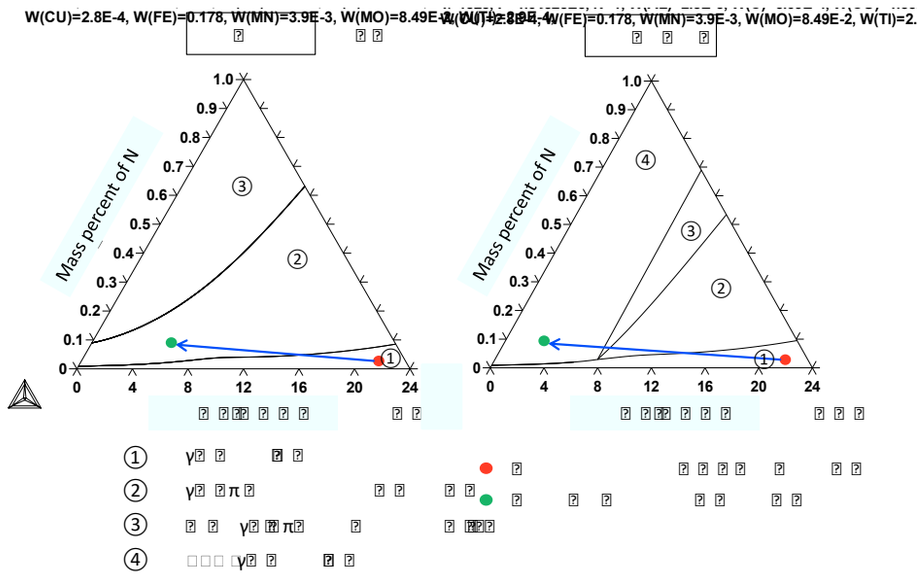

Figure 8.17: Section of the Ni-Cr-Fe-Mo-N phase diagram at 1000°C and 1050°C calculated in Thermo-Calc using the TTNI7 database. Concentrations of Fe, Mo, C were kept constant at the levels given by the initial composition of alloy X (**Table 8.1**).

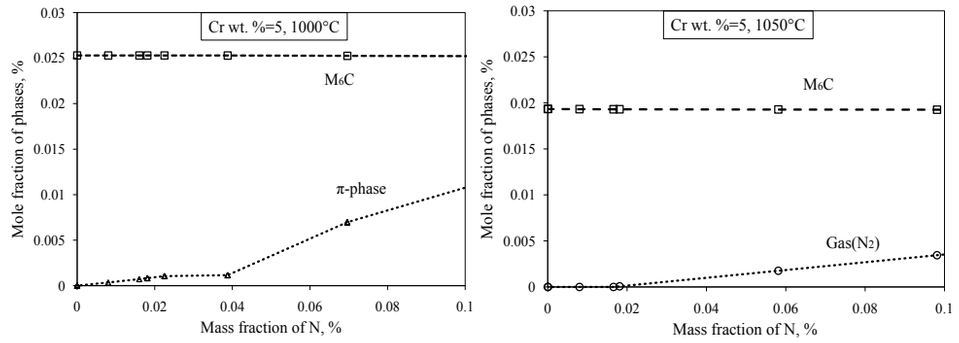

Figure 8.18: Mole fractions of stable phases (in addition to γ-Ni) at 1000°C and 1050°C in alloy X, however with a Cr concentration of 5 wt. % calculated in Thermo-Calc using the TTNI7 database.

At 1000°C, the large amount of nitride formed makes the specimens brittle, resulting in formation of voids and cracks under cyclic stresses, which may finally lead to fracture of the specimen. As discussed in Section 8.3 the voids may partly be related to creep of the substrate. It was also found that, although the 0.2 mm specimen after 1050℃ exposure for 2000 h was

totally destroyed, no “classical” breakaway oxidation has been observed. This is an unusual observation compared to other Fe-rich Ni-Cr alloys [24]. However, substantial amount of Fe-rich oxide were present in the outer layer of the scale. In the present study, the mechanical failure is the main reason for the end of the specimen lifetime, which means that the specimen was structurally damaged by the repeated spallation of the rapidly growing scale, which leads to rapid consumption of the metal.

After the Cr concentration decreased to a sufficiently low level, the property of the scale has changed from protective to non-protective due to incorporation of elements like Fe and Mn to form rapidly growing mixed Fe-rich oxide as discussed in Section 8.3. The rapid spallation of this non-protective oxide leads to much larger weight losses than in case of pure chromia spallation, thus, massive loss of the metal, accompanied by the failure of the specimen.

8.5 Results of lifetime prediction using reservoir approach

The same approach as described for alloy 230 in Section 6.4 was used for construction of a lifetime diagram for alloy X. Although no “classical” breakaway oxidation was observed, the specimen of 0.2 mm after 3000h at 1000°C and the specimens of 0.2 and 0.3 mm after 2000 h at 1000°C clearly failed due to the massive loss of the metal. Additionally, massive nitridation was found in these specimens.

According to the Cr concentration profiles shown in **Figure 8.16** and the experience gained in the treatment for alloy 230, the critical value of 10 wt. % Cr in the alloy seems also here to be a pragmatic criterion of lifetime limit t* for alloy X. **Figure 8.19** shows the calculated times t_{10} at different temperatures for specimens of different thicknesses. The black open symbol shows the experimental oxidation time (1000 h) of the 0.2 mm specimen at 1050°C and it corresponds to an interface Cr concentration of approximately 10 wt. % (**Figure 8.16 d**). The dashed lines represent extrapolations to higher and lower temperatures. The straight part of the dashed line showing the steady-state power law oxidation is calculated according to the Arrhenius law of oxidation kinetics (see **Figure 8.21**) as described in Section 6.4.4. The start of the deviation from the steady-state oxidation as well as the slope of the lines after the deviation are predicted using the same procedures described in Section 6.4.4 for alloy 230. Here the deviation occurs when the weight gain reaches a value of approximately 1.2 $mg.cm^{-2}$ (see **Figure 8.1**).

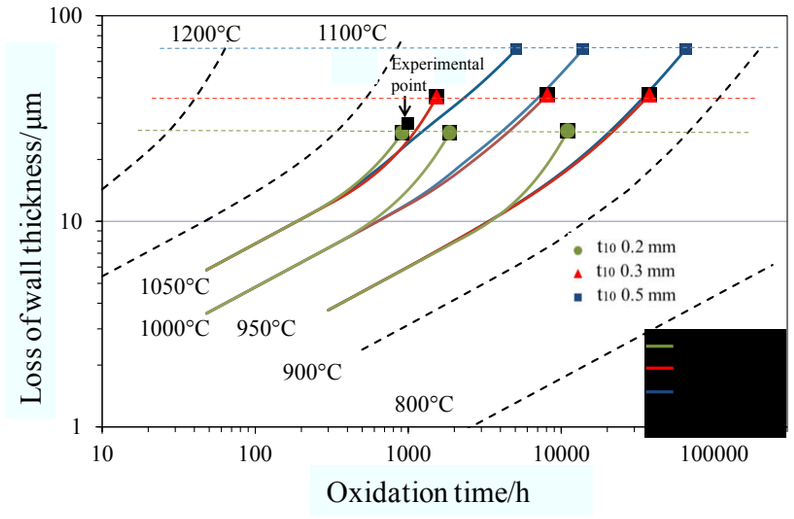

Figure 8.19: Lifetime diagram showing calculated and experimental lifetime limits of alloy X at different temperatures for different wall thicknesses. Dashed lines are extrapolations to higher and lower temperatures based on experimental data and extrapolated data (**Figure 8.20**) using the procedures described in Section 6.4.4.

In the same manner as done for alloy 230 in Section 6.4.4, the calculated lifetime limits t_{10} of alloy X are plotted as a function of specimen thickness with extrapolations to other thickness (0.1 and 1 mm) as well as to other temperatures (900 and 1100°C) in **Figure 8.20**. Based on the experimental results, which showed no significant differences in oxidation kinetics between the 0.5 mm and 1 mm thick specimens (**Figure 8.2**), the extrapolation for the 1 mm specimen used the same model parameters as for the 0.5 mm specimen at the respective temperature. The extrapolation to the 0.1 mm specimen used the same model parameters as used for the 0.2 mm specimen at the corresponding temperatures. As discussed for alloy 230, this assumption may cause a slight overestimation of the lifetime t_{10} of the 0.1 mm specimen.

It has been mentioned in Section 8.2 that the creep strength of alloy X is poorer than that of alloy 230. Besides, alloy X exhibits faster oxidation kinetics and poorer scale adherence than alloy 230. **Figure 8.21** shows a comparison of the steady-state oxidation kinetics as a function of reciprocal temperature for alloy X and alloy 230. The k values for alloy X are slightly higher than those of alloy 230 at all temperatures. The high content of Fe in alloy X leads to the incorporation of Fe into the oxide scale, and increases the concentration of point defects

[53], which increases the oxide growth rate. More Mn/Cr spinel on top of the scale of alloy X, as discussed in Section 8.3, may be another reason for the enhanced chromia growth rate [109]. The poorer scale adhesion on the thicker specimens of alloy X compared to 230 can be explained by the lack of a reactive element, such as La, which has the effect of improving the coherence between the alloy and the oxide (see Section 3.3.4 and e.g. reference [116, 117]).

Figure 8.22 shows a comparison between the calculated values of t_{10} for alloy 230 and alloy X. The times t_{10} of alloy X are shorter than those of alloy 230 at the same temperature for specimens of the same thickness. Most of the lines have "convex inflections" at a specimen thickness of 0.3 mm. This can be explained by the fact that during prolonged oxidation the oxidation kinetics changes from sub-parabolic of the "super-parabolic" for the very thin (0.2 mm) specimens, whereas scale spallation tends to occur for the 0.3 and 0.5 mm specimens. The "super-parabolic" behavior results in a more substantial enhancement of Cr consumption, thus shorter lifetime, than the enhancement of Cr consumption by scale spallation observed for the thicker specimens (**Figure 8.1**). Different from alloy 230, the inflection at 0.3 mm is not clearly apparent for alloy X at 1050°C, because at this high temperature both the 0.2 and the 0.3 mm specimens of alloy X showed "super-parabolic" oxidation kinetics (**Figure 8.1 c**).

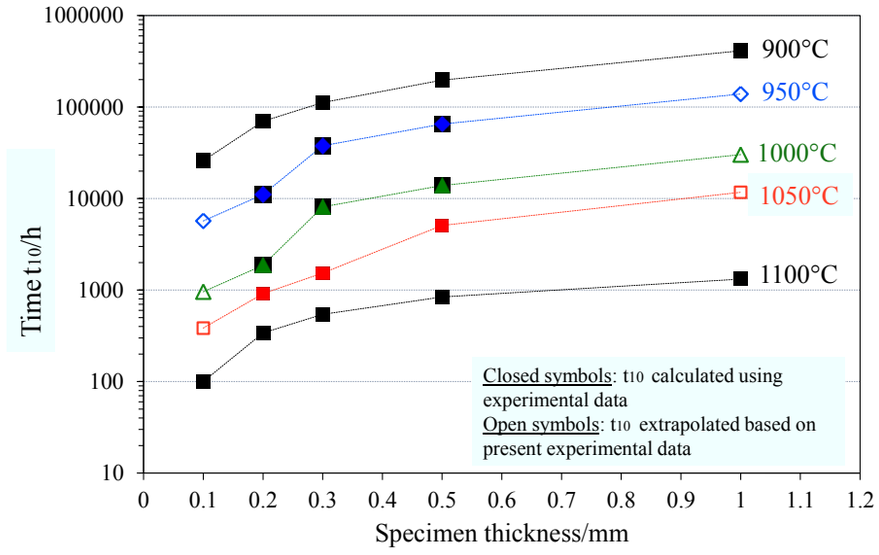

Figure 8.20: Calculated times t_{10} as function of specimen thickness for alloy X with extrapolations (open symbols) to other temperatures and specimen thicknesses based on experimental results of specimens oxidized at studied temperatures (950 - 1050°C).

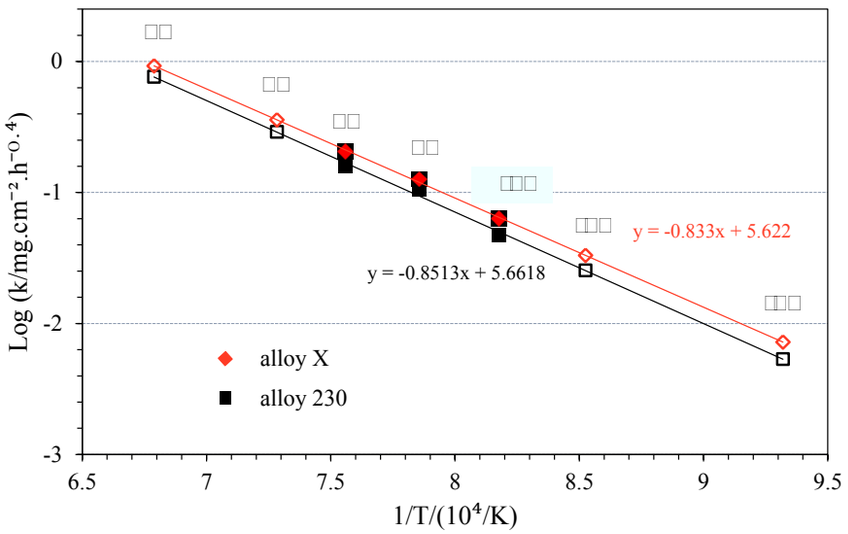

Figure 8.21: Comparison of rate constant of oxidation k (assuming power law kinetics, i.e. **Eq. (3.19)** with n=0.4) during steady state oxidation for alloy X and alloy 230. Closed symbols are derived from experimental data; open symbols are extrapolated values.

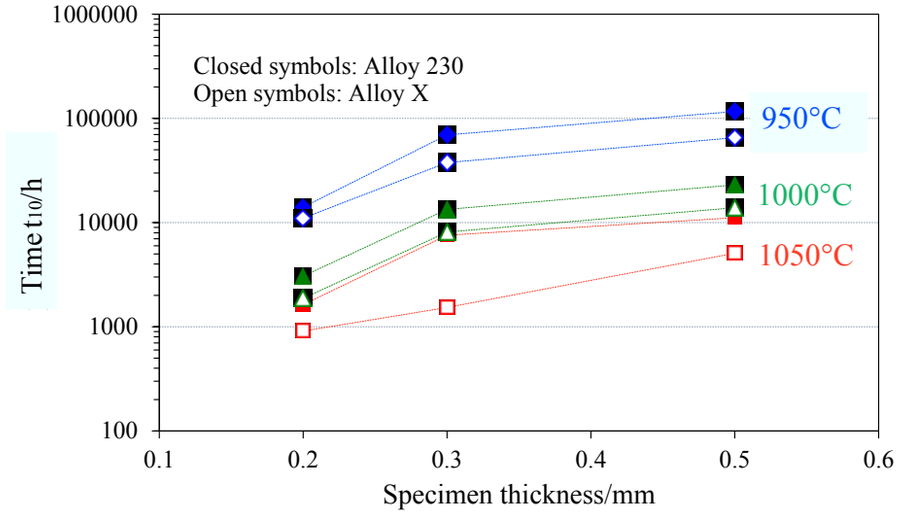

Figure 8.22: Comparison between the times t_{10} of alloy X and alloy 230 calculated using the same "reservoir approach" described in Section 6.4.

9 Oxidation behavior and lifetime of NiCr 8020 SO

9.1 Analyzed chemical composition

The studied sheet material (1 mm thickness) of NiCr 8020 SO alloy was supplied by VDM Metals. The specified chemical composition is simply 80 wt. % Ni and 20 wt. % Cr, whereas some minor alloying elements are inevitably or intentionally added during the production. The nominal [121] and analyzed compositions are presented in **Table 9.1**.

Due to its simple composition and the very low carbon content, the alloy exhibited under all test conditions a single phase microstructure consisting of γ-Ni. Therefore, no details of changes in alloy microstructure as function of time, temperature and specimen thickness will in the following be discussed.

Table 9.1: Chemical composition of studied alloy NiCr 8020 (in wt. %) determined by ICP-OES and combustion infrared analysis compared with nominal composition from manufacturing data sheet [121].

	Cr	Fe	Mn	Si	Mg	C	N	S
Nominal	19.0~20.0	0.20(max)	0.05(max)	0.1~0.2	0.01~0.02	0.20(max)	-	-
Measured	19.9	0.061	0.011	0.19	-	0.0018	0.0129	0.0018

9.2 Oxidation kinetics

The net weight change curves measured during oxidation at 950°C (10 h cycle) show inflections for both specimen thicknesses after about 400 h with weight gains of about 0.3 $mg.cm^{-2}$, which indicate earlier occurrence of scale spallation compared to the performance at higher temperatures (**Figure 9.1**). The higher frequency of thermal cycling (10 h) at 950°C may contribute to the rapid establishment of the scale spallation period [171].

The weight change curves do not show a specimen thickness dependence during the early stages of oxidation at 1000 and 1050°C (**Figure 9.1 b c**). At 1000°C, the scale on the 0.3 and 0.5 mm specimens starts to spall after about 1000 h, while for the 0.2 mm the spallation initiates later, and the rate of spallation is apparently slower than that of the 0.3 and 0.5 mm specimens.

a)

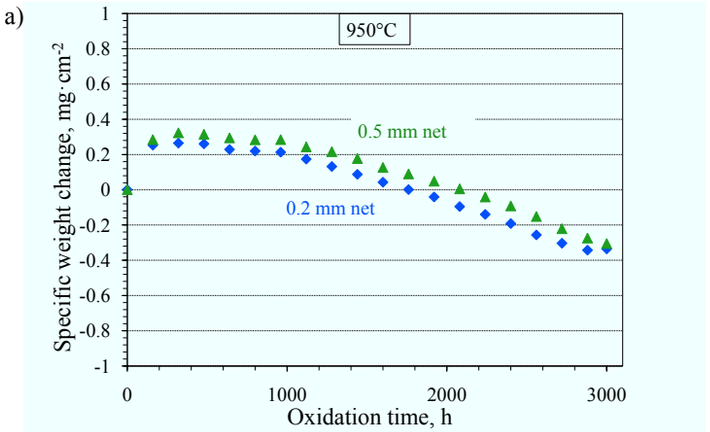

b)

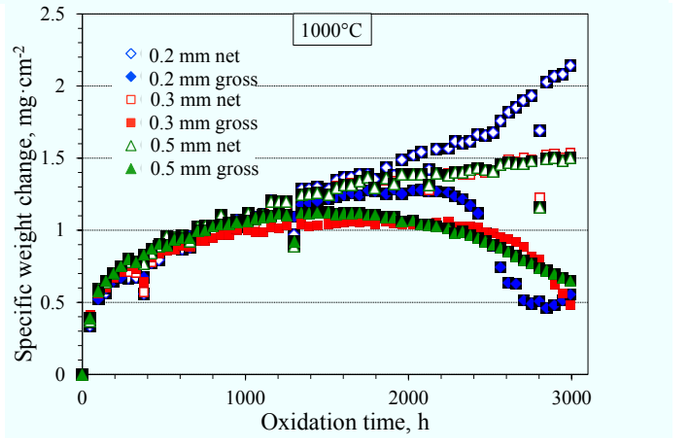

c)

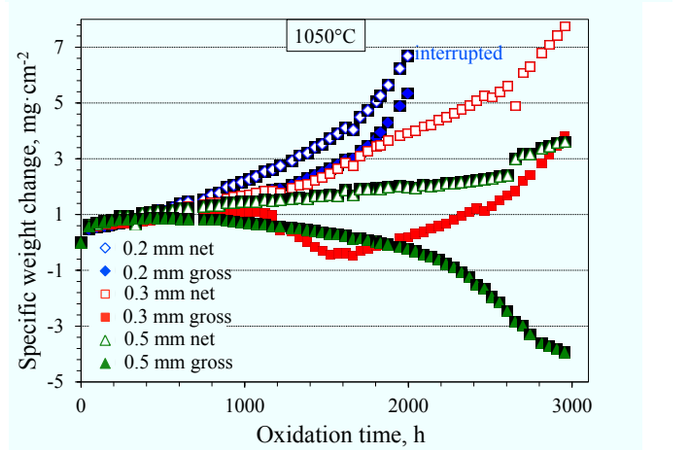

Figure 9.1: Weight change of alloy NiCr 8020 during air oxidation at a) 950, b) 1000, and c) 1050°C.

The reason for the difference is the weakness of the very thin substrate against substrate creep. The scale spallation of the 0.2 mm specimen becomes much faster after about 2400 h, which indicates a change of the oxidation mechanism or mechanical failure of the material (see **Figure 9.4 c**). After approximately 2800 h a substantial weight increase occurs.

Comparing the curves at 1000 and 1050°C, it seems that at both temperatures, the scale starts to spall on the 0.3 and 0.5 mm specimens when the weight gain is approximately 1 - 1.2 $mg.cm^{-2}$. At 1050°C, the critical weight gain for onset of scale spallation is reached much earlier (after about 600 h) than at 1000°C (approximately 1000 h). At 1050°C, the exposure of the 0.2 mm specimen was interrupted after 2000 h because of breakaway oxidation observed at the edges of the specimen (see **Figure 9.2 a**). The 0.3 mm specimen underwent breakaway oxidation after approximately 3000 h (see **Figure 9.2 b**). A similarity of the 0.2 and 0.3 mm specimens at 1050°C is that they are both subjected to a short period of scale spallation, and then start to exhibit a weight gain. Similar to the behavior of the 0.2 mm specimen oxidized at 1000°C for 3000 h discussed in the previous paragraph, these weight gains occurring after longer exposure times after a preceding scale spallation might also here be an indication for breakaway oxidation.

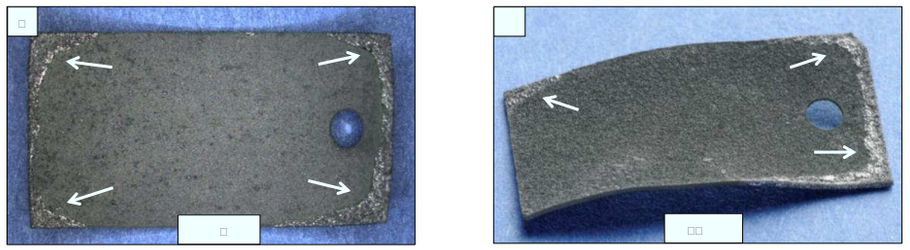

Figure 9.2: Macro pictures of alloy NiCr 8020 specimens after oxidation at 1050°C for a) 2000 h of 0.2 mm and b) 3000 h of 0.3 mm thick specimen.

9.3 Oxide scale formation and subscale depletion

Figure 9.3 shows the cross sections of the 0.2 and 0.5 mm specimens of alloy NiCr 8020 oxidized at 950°C for 3000 h. Cracks and voids pointed with red arrows are observed in the chromia scale. This is in agreement with the weight change curves, which show a large tendency to scale spallation (**Figure 9.1 a**) under 10 h thermal cycles at 950°C.

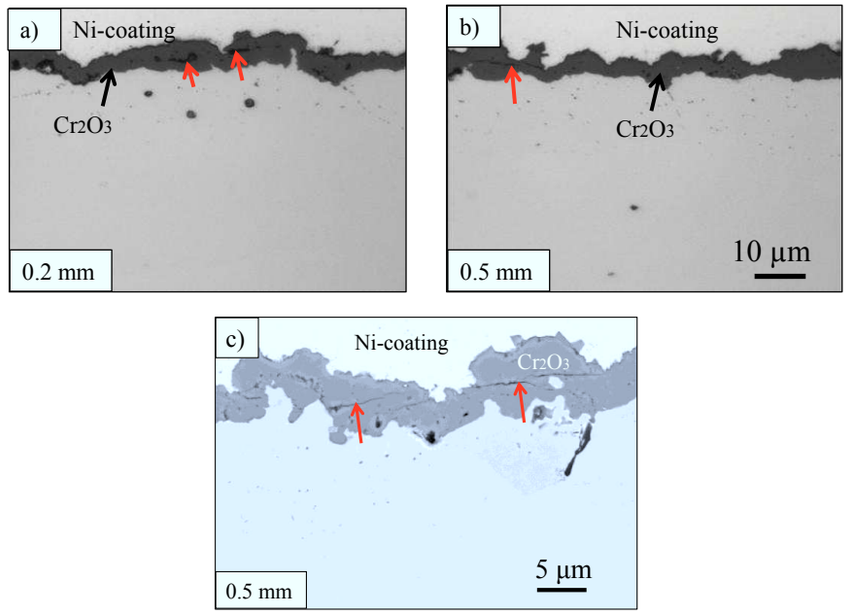

Figure 9.3: BSE images showing cross sections of the a) 0.2 and b) 0.5 mm specimens of alloy NiCr 8020 oxidized at 950°C for 3000 h. Images shown in a) and b) were investigated at ORNL. Fig. c) is a higher magnification image showing cracks in the scale of the 0.5 mm specimen analyzed at FZJ.

It was very often observed that the presence of internal oxides of e.g. Al_2O_3 and SiO_2 in the subscale region has the result, that protrusions of subscale alloy are pushed outward and are visible as metal protrusions or nodules of external oxide in the alloy/scale interface region [172-174]. This type of alloy/scale interface was observed for alloys 230 and X (see e.g. **Figure 5.2** and **Figure 8.4**, respectively). The oxide nodules at the alloy/scale interface can hinder the lateral propagation of cracks initiated by voids and therefore reduce the tendency of scale spallation. However, the lack of Al and Si additions in alloy NiCr 8020 leads during shorter times of exposure to relatively smooth alloy/scale interfaces. It has frequently been shown [175] that such flat oxide interfaces are not beneficial for oxide adherence. Cracks at the alloy/scale interface, e.g. induced by voids originating from vacancy condensation, may easily propagate along the flat interface [175], i.e. much easier than in case of the "undulated" interfaces formed in case of alloy 230 and X (see e.g. **Figure 5.2** and **Figure 8.4**, respectively). After longer time exposure, the compressive growth and/or thermally induced stress in the scale on NiCr 8020 results in the development of rumpling interfaces (see e.g.

Figure 9.3) as a result of plastic deformation of the alloy-near surface region. This results in crack formation, especially within the oxide scale (**Figure 9.3**). The large tendency for the formation of these rumpling interfaces is likely related to the substantially lower creep strength of alloy NiCr 8020 compared to alloys 230 and X.

For the 0.2 mm specimen oxidized at 1000°C during a 100 h TG test, the scale on the alloy consists of Cr_2O_3 with an average thickness of about 3 µm, which is in accordance with the weight gain of 0.5 mg.cm^{-2} (see **Figure 9.1 b**, knowing that 1 mg.cm^{-2} weight gain corresponds to 6.07 µm Cr_2O_3 thickness). Some Cr_2O_3 is dispersed along alloy grain boundaries in the subscale region in the form of small particles (**Figure 9.4 a**). The amount of internal oxide increases after 1000 h oxidation, and fragments of $NiCr_2O_4$ spinel can be observed on the top of the scale. After 3000 h, the thickness of the protective Cr_2O_3 scale seems similar to that after 1000 h, but the amount of outer Ni-rich spinel increases significantly and indication of spallation of the spinel can be seen in the right corner of **Figure 9.4 c**. This finding indicates, that the rapid spallation after 2400 h (**Figure 9.1 b**) mentioned above is related to spallation of the spinel instead of Cr_2O_3. The massive formation of the spinel indicates occurrence of a critical Cr depletion in the alloy. To be noted is that Ni-rich oxide (NiO) is observed in between the spinel and the Cr_2O_3 layer at the position of a deep crack of the substrate. From the thermodynamic point of view, the NiO oxide cannot form in between the spinel and the Cr_2O_3 phases due to its high dissociation pressure (see Section 3.1). Therefore, the local formation of the NiO must be the result of preceding scale cracking which allows the direct contact of the alloy surface with the atmosphere.

For the 0.3 mm specimen minor formation of the spinel phase was observed up to 3000 h oxidation at 1000°C (**Figure 9.5 a**). No indications of spinel formation were found for the 0.5 mm specimen (**Figure 9.6**). Some cracks at the spinel/Cr_2O_3 as well as the alloy/scale interfaces in parallel with the inhomogeneous scale thickness illustrate occurrence of scale spallation. This is in agreement with the weight gain data (**Figure 9.1 b**) and explains why the oxide scale after 3000 h is locally even thinner than that after 1000 h (see e.g. **Figure 9.5**).

The cross sections of the specimens oxidized at 1050°C are shown in **Figure 9.7** - **Figure 9.9**. Similar to the cross sections of the specimens oxidized at 1000°C, a wavy alloy/scale interface is observed after longer time. For the 0.2 mm specimen (**Figure 9.7**), hardly any Ni-Cr spinel was found after the 72 h TG test, but after 300 h, fragments of spinel could be

observed on top of the Cr_2O_3 scale. The spinel phase is not clearly apparent in the cross section of the specimen after 1000 h because of the scale spallation (see also **Figure 9.1 c**).

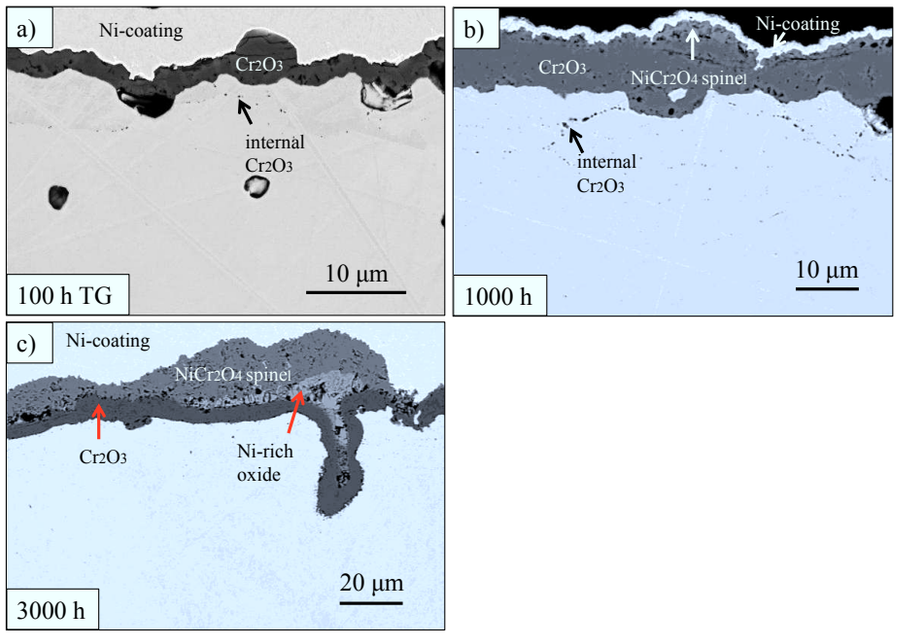

Figure 9.4: BSE images showing cross sections of 0.2 mm specimens of alloy NiCr 8020 oxidized at 1000°C for a) 100 h TGA, b) 1000 h, and c) 3000 h.

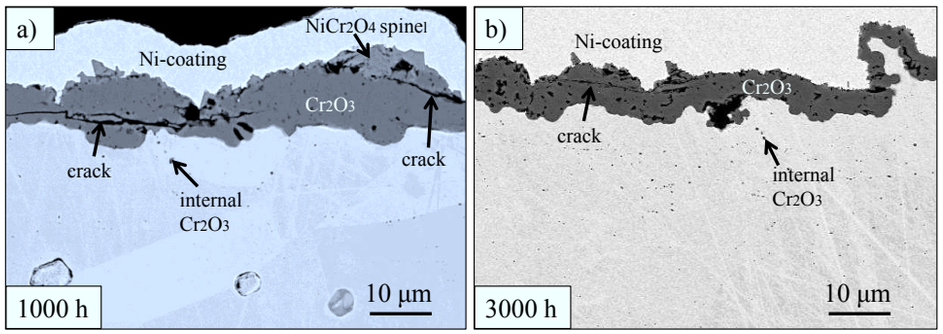

Figure 9.5: BSE images showing cross sections of 0.3 mm specimens of alloy NiCr 8020 oxidized at 1000°C for a) 1000 h and b) 3000 h.

Massive formation of spinel phase and formation of large voids as well as significant internal oxidation of Cr is observed after 2000 h of the 0.2 mm specimen (**Figure 9.7 d**), indicating

failure of the specimen. The Cr concentration profile of this specimen in **Figure 9.11 d** shows a Cr interface level of less than 10 wt. %. The formation of voids and internal Cr_2O_3 after long time oxidation is similar to that found for alloy X, which indicates the loss of protective property of the scale as shown in **Figure 8.14**.

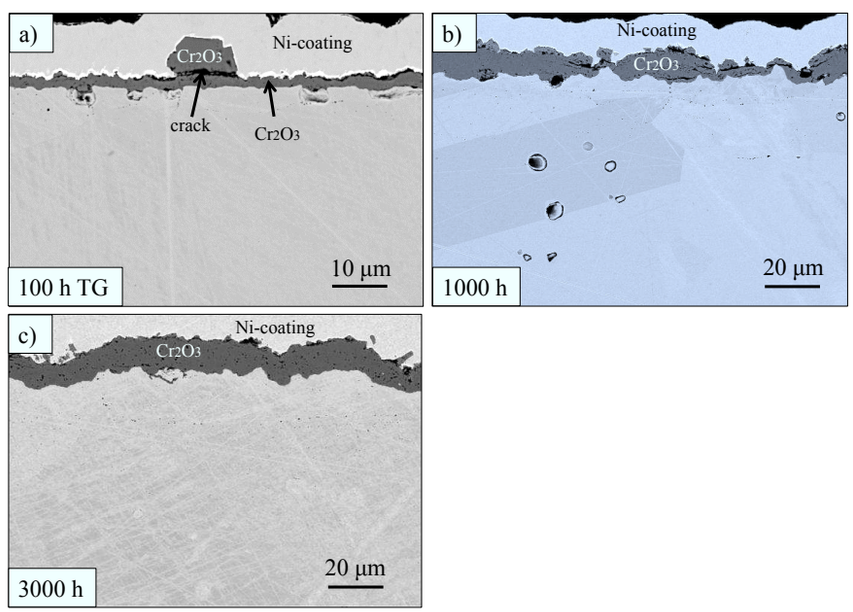

Figure 9.6: BSE images showing cross sections of 0.5 mm specimens of alloy NiCr 8020 oxidized at 1000°C for a) 100 h TGA, b) 1000 h and c) 3000 h.

The oxide scale on the 0.3 mm specimen is quite similar to that of the 0.2 mm specimen after oxidation at 1050°C (**Figure 9.8**). After 300 h, some spinel formed and then almost totally spalled after 1000 h. After 3000 h, the 0.3 mm specimen showed indications of failure by formation of spinel and the presence of large amounts of voids. For the 0.5 mm specimen (**Figure 9.9**), no obvious spinel formation was found until 1000 h oxidation at 1050°C. After 3000 h, the thickness of the scale is quite inhomogeneous due to repeated scale spallation (**Figure 9.1 c**). Similar to the observations of the 0.2 and 0.3 mm specimens, the appearance of significant formation of the spinel phase and internal voids indicate the failure of the specimen.

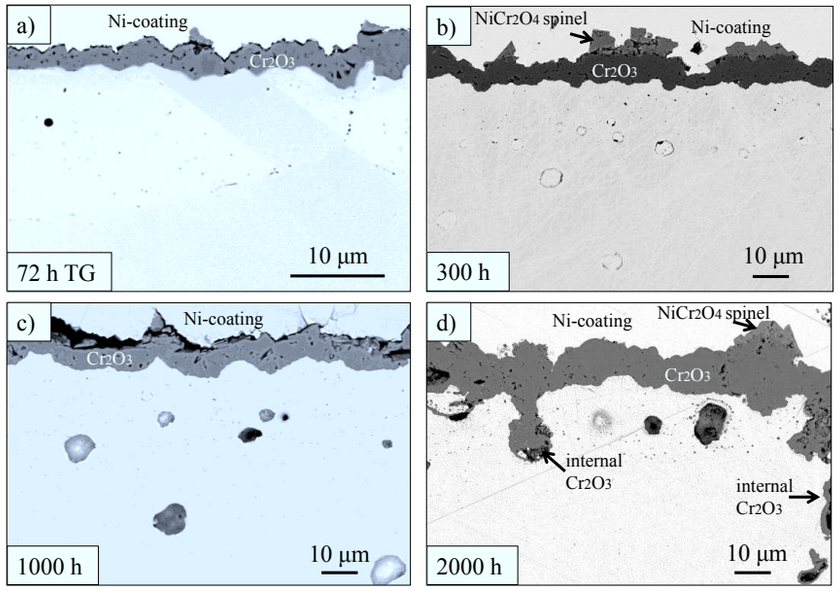

Figure 9.7: BSE images showing cross sections of 0.2 mm thick specimens of alloy NiCr 8020 after different times of oxidation at 1050°C.

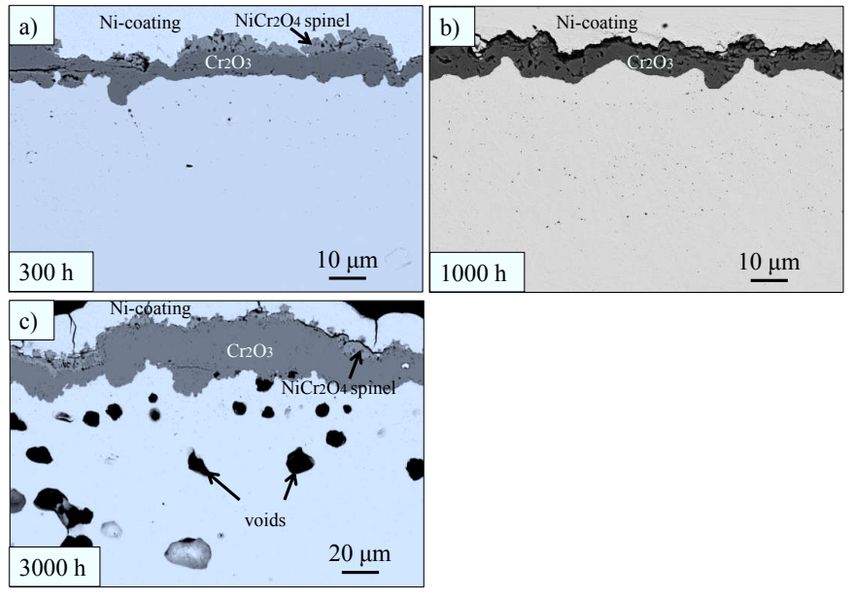

Figure 9.8: BSE images showing cross sections of 0.3 mm thick specimens of alloy NiCr 8020 after different times of oxidation at 1050°C.

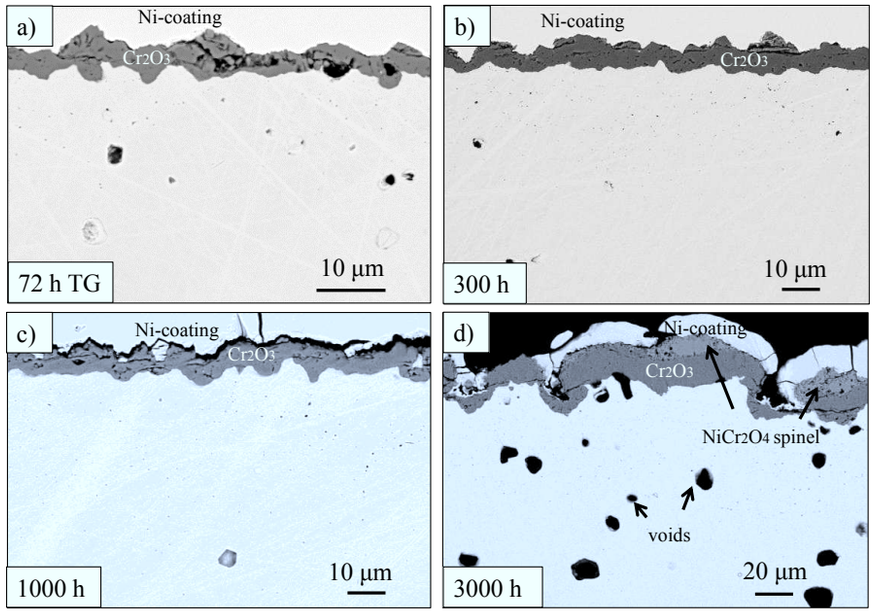

Figure 9.9: BSE images showing cross sections of 0.5 mm thick specimens of alloy NiCr 8020 after different times of oxidation at 1050°C.

Figure 9.10 shows the subscale concentration profile of Cr of the 0.5 mm specimen after oxidation at 950°C for 3000 h. The diffusion front has not reached the center of the specimen, and the interface Cr concentration is about 17 wt. %. Only limited data are available for the oxidation at 950°C, so a more detailed discussion of the Cr concentration profiles are done using the data at 1000 and 1050°C.

The subscale concentration profiles of Cr are plotted for each tested specimen thickness after various exposure times at 1000 and 1050°C in **Figure 9.11**. Similar to the profile shown in **Figure 9.10**, the interface Cr concentration is for all specimen thicknesses approximately 16 - 17 wt. % after 1000°C oxidation (**Figure 9.11 a b c**) i.e. before the depletion front reaches the center of the specimen (see Section 3.3.2). This interface Cr concentration of NiCr 8020 is similar to that of alloy 230 and alloy X during this oxidation stage (**Figure 7.1** and **Figure 8.17**). Taking into account that the original Cr content is about 20 wt. %, compared to 22 wt. % for alloys 230 and X, the decrease of the Cr interface concentration of alloy NiCr 8020 is smaller than in the other two studied Ni-base alloys.

As discussed in Section 3.3.2, the value of the interface Cr concentration remains constant during the first stage of the Cr depletion if parabolic kinetics prevail. Assuming parabolic oxidation kinetics, the difference between the original Cr concentration and the interface concentration (C_0-C_i) is a function of the ratio $\frac{x}{\sqrt{\tilde{D}t}}$ (see **Eq. (3.23)**). In case of the power law oxidation kinetics used in the present study, the ratio $\frac{x}{\sqrt{\tilde{D}t}}$ has to be modified to a relation between the power law rate constant k and the inter-diffusion coefficient $\tilde{D}$. An approximation may be derived using the following procedure:

The equation to describe the parabolic oxidation kinetics (**Eq. (3.18)**) can be rewritten as:

$$x = \sqrt{k_p \cdot t} \tag{9.1}$$

The power law rate constant of oxidation k in the equation $\Delta m / A = k \cdot t^n$ (i.e. **Eq. (6.2)**) can be replaced by k′ with a unit of $cm.h^{-0.4}$, corresponding to the thickness of the chromia scale x using the following expression:

$$k' = x \cdot \frac{M_O \cdot \nu_{Cr_2O_3}}{M_{Cr_2O_3} \cdot \nu_O} \cdot \frac{1}{\rho_{Cr_2O_3}} \tag{9.2}$$

Then, the power law kinetics can be written as:

$$x = k' \cdot t^{0.4} \tag{9.3}$$

Comparing **Eq. (9.1)** and **(9.3),** the $\sqrt{k_p}$ can be replaced by k and t:

$$\sqrt{k_p} = \frac{k'}{\sqrt{\tilde{D}}} \cdot t^{0.4} \tag{9.4}$$

Inserting in **Eq. (3.23)**, reveals that the difference between the original and the interface Cr concentration is proportional to $\sqrt{t/\tilde{D}}$:

$$C_0 - C_i \propto \sqrt{\frac{t}{\tilde{D}}} \tag{9.5}$$

Inserting **Eq. (9.4)** reveals the modified expression:

$$C_0 - C_i \propto \frac{k'}{\sqrt{\tilde{D}}} \cdot t^{0.4} \tag{9.6}$$

As already mentioned in Section 3.3.2, the interface concentration of Cr thus increases with oxidation time during steady state oxidation exhibiting power law kinetics with n<0.5. Ignoring the minor difference of M_{alloy} (average atomic weight of the alloy, see **Eq. (3.23)**) between the different studied Ni-base alloys, the (C_0-C_i) for the various alloys can directly be compared after a given oxidation time as long as steady state oxidation prevails.

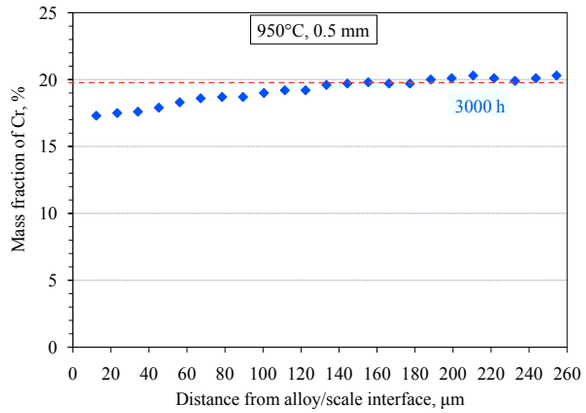

Figure 9.10: Subscale concentration profile of Cr in the 0.5 mm specimen of alloy NiCr 8020 oxidized at 950°C after 3000 h. Red dashed line indicates the original Cr concentration in the alloy.

Table 9.2 lists the values of the power law rate constants k (**Eq. (3.19)**) and k′, the inter-diffusion coefficients, here approximately replaced by the effective diffusion coefficients D, calculated using FDM (see Section 7.4), as well as the values of the ratio $k'/\sqrt{?}$ for the three studied Ni-base alloys. As mentioned in Chapter 7 the oxidation kinetics of alloy 230 is slower than that of alloy X. From **Table 9.2** it is apparent that the oxidation kinetics of NiCr 8020 is even slower than that of alloy 230. The larger amounts of alloying elements in alloy 230 and alloy X might be the reason of the faster oxidation kinetics. First, the concentration of point defects can be increased by the incorporation of the atomic solutes of the alloying elements like Fe. Additionally, as discussed in Section 3.3.4, Mn and Ti can enhance the growth of the Cr_2O_3 scale during air oxidation [109]. Besides, outwardly protruding alloy nodules due to the presence of internal oxides of Al_2O_3 in alloy 230 and X will cause micro damage of the scale, thus allowing a transport of gas molecules towards the alloy/scale interface resulting in an enhancement of scale growth [172, 174]. The slightly larger diffusivity of Cr in alloy NiCr 8020 compared to that in the other two alloys might be a result

of the lacking of heavy elements with large atomic radii such as W and Mo, which are expected to slow down the diffusion of Cr [176].

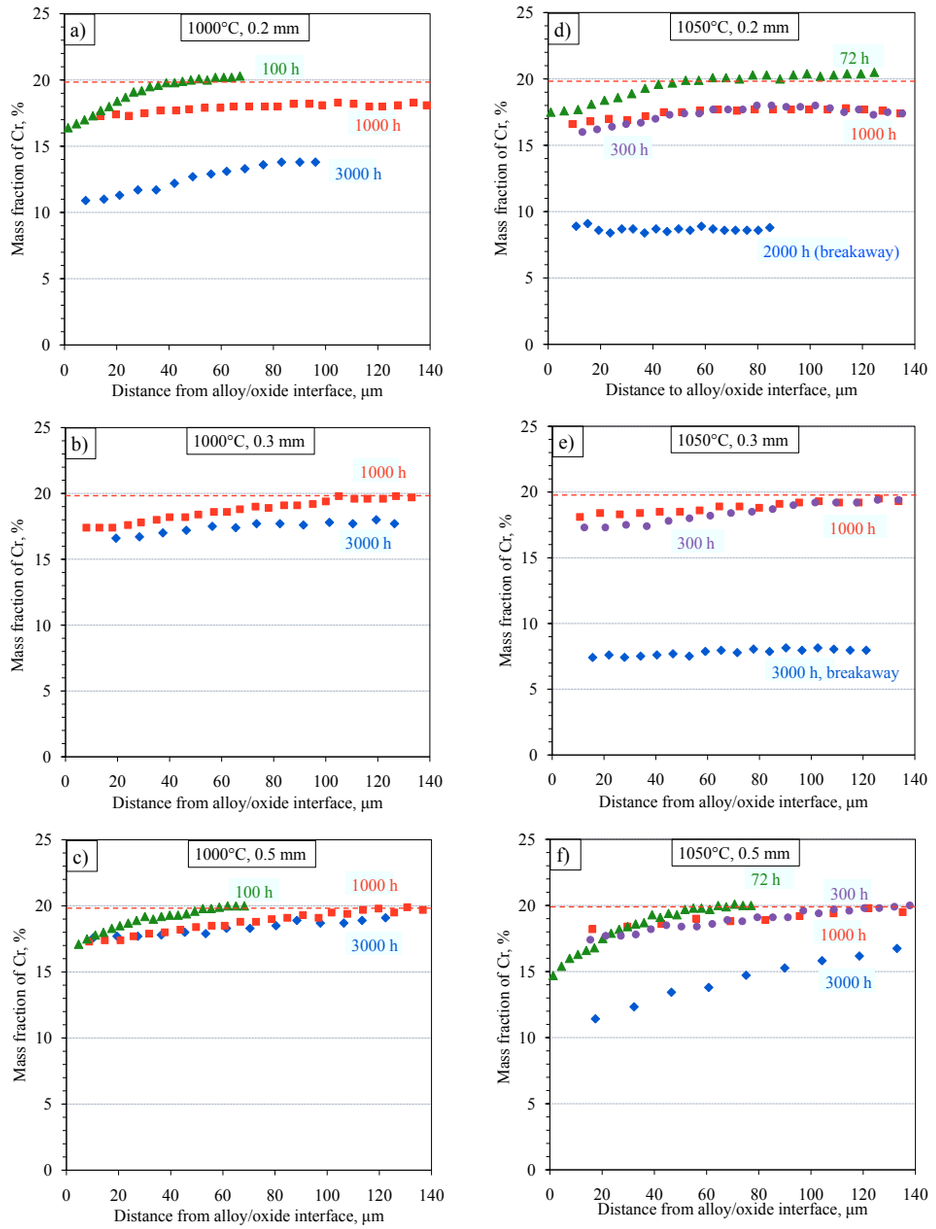

Figure 9.11: Time dependent subscale concentration profiles of Cr of NiCr 8020 with specimen thicknesses of 0.2, 0.3, and 0.5 mm after oxidation at a-c) 1000°C and d-f) 1050°C.

In reference [177], it was pointed out that the boundary diffusion coefficient of Cr in Ni-Cr-Fe alloys decreases with increasing carbon content in the alloy. The measured carbon content in alloy 230, alloy X and NiCr 8020 is 0.092 wt. %, 0.061 wt. % and 0.0018 wt. %, respectively. This agrees to the ranking of the D_{Cr} values of these alloys in **Table 9.2**, however, it is not sure whether this is in the studied alloys indeed the main reason for the observed ranking of D_{Cr}.

Table 9.2: Comparison of the power law rate constants of oxidation k, k′ and diffusivity of Cr, D as well as the ratio $k'/\sqrt{D}$ between the studied Ni-base alloys.

k (·)

	950°C	1000°C	1050°C
Alloy X	0.0639	0.1264	0.2056
Alloy 230	0.0464	0.1051	0.1584
NiCr 8020	0.0337	0.0796	0.1054

k′ (·)

	950°C	1000°C	1050°C
Alloy X	□□ □ −□	□□ □ −□	□□ □ −□
Alloy 230	□□ □ −□	□□ □ −□	□□ □ −□
NiCr 8020	□□ □ −□	□□ □ −□	□□ □ −□

D_{Cr} (·)

	950°C	1000°C	1050°C
Alloy X	□□ □ −	□□ □ −	□□ □ −
Alloy 230	□□ □ −	□□ □ −	□□ □ −
NiCr 8020	□□ □ −	□□ □ −	□□ □ −

$□'/\sqrt{□}$ ($h^{0.1}$)

	950°C	1000°C	1050°C
Alloy X	□□ □ −□	□□ □ −□	□□ □ −□
Alloy 230	□□ □ −□	□□ □ −□	□□ □ −□
NiCr 8020	□□ □ −□	□□ □ −□	□□ □ −□

At a given oxidation time and temperature, a larger value of $k'/\sqrt{t}$ corresponds to a larger value of the term (C_0-C_i) in **Eq. (9.6)**. The $k'/\sqrt{t}$ value of alloy NiCr 8020 is smaller than that of the other alloys. This explains a smaller (C_0-C_i) (20 wt. % - 16wt. % = 4 wt. %) of alloy NiCr 8020 compared to that of alloy X and alloy 230 (i.e. 22 wt. % - 16 wt. % = 6 wt. %). The $k'/\sqrt{t}$ values of alloys 230 and X are at a given temperature very similar; this also explains why the (C_0-C_i) values of both alloys are very similar.

The Cr interface concentration of the NiCr 8020 specimens showing the start of macroscopically visible breakaway oxidation (**Figure 9.2** and **Figure 9.11 d e)** are slightly lower than 10 wt. %, while the interface Cr concentrations of the other specimens were still above 10 wt. % (**Figure 9.11**). Therefore, the critical Cr concentration to define the pragmatic lifetime limits t* can also for this alloy reasonably be assumed to be 10 wt. %. Consequently, the same procedures of lifetime prediction as described in Chapter 6 can be applied to NiCr 8020 as will be shown in the next section.

9.4 Results of lifetime prediction using reservoir approach

Similarly as shown in Sections 6.4 and 8.5 for alloy 230 and alloy X, a lifetime diagram is constructed for NiCr 8020 (**Figure 9.12**). The calculations are based on the oxidation kinetics shown in **Figure 9.1**. At 1050°C, the 0.2 mm thick specimen shows significant “super-parabolic” behavior of oxide growth after approximately 300 h. The 0.3 mm specimen exhibits scale spallation after approximately 1000 h and a “super-parabolic” behavior after approximately 1300 h. Therefore the lines representing wall thickness loss of these two specimens in **Figure 9.12** deviate from the basic power law kinetics with a substantial inclination. At 950 and 1000°C, the main cause of enhanced Cr consumption is scale spallation. As a result, the deviations from the power law kinetics are not as significant as those observed at 1050°C. Because of the lack of experimental data, the value of t_{10} of the 0.3 mm at 950°C was interpolated using the same procedures as described in Section 6.4.4. At 1050°C, the 0.2 and 0.3 mm specimens already failed before the end of the experimental time of 2000 h and 3000 h, respectively (see **Figure 9.2** and **Figure 9.11 d e)**. Therefore the experimental lifetimes of these specimens in **Figure 9.12** (black open symbols) indicating measured breakaway are located higher than the predicted values which were calculated assuming the critical Cr interface concentration to be 10 wt. %.

With the extrapolation of the rate constant of oxidation k (**Figure 9.13**), the lifetime diagram is also extrapolated to higher and lower temperatures in **Figure 9.14**. The same procedures as described in Section 6.4.4 were used for extrapolation. The deviation of the lines from the steady state power law oxidation starts approximately when the total loss of wall thickness reaches 6 µm, assuming formation of a pure chromia scale corresponding to a weight gain of 1 mg.cm^{-2}.

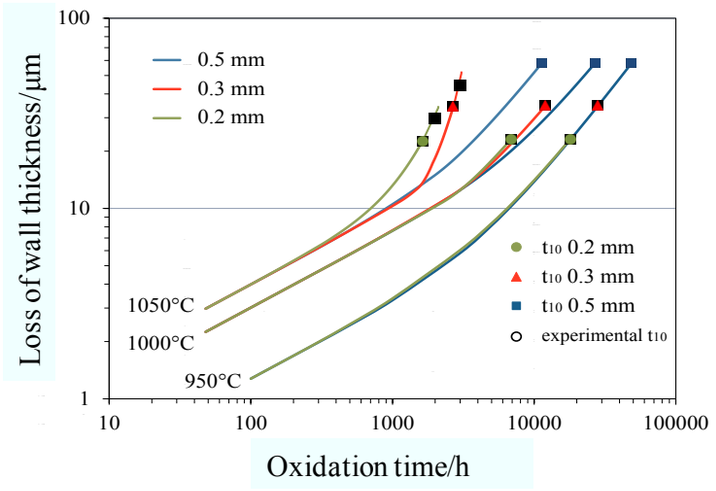

Figure 9.12: Lifetime diagram of alloy NiCr 8020 in the studied temperature range for specimens of different thicknesses calculated using the reservoir approach on the basis of the gravimetric data in **Figure 9.1**, and results of Cr depletion in **Figure 9.11**.

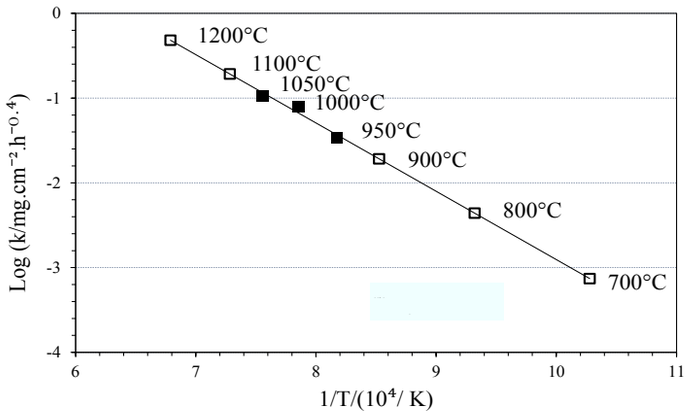

Figure 9.13: Oxidation rate constant k (**Eq. (3.19)** with n=0.4) as function of 1/T for steady state scale growth with extrapolation (open symbols) to higher and lower temperatures.

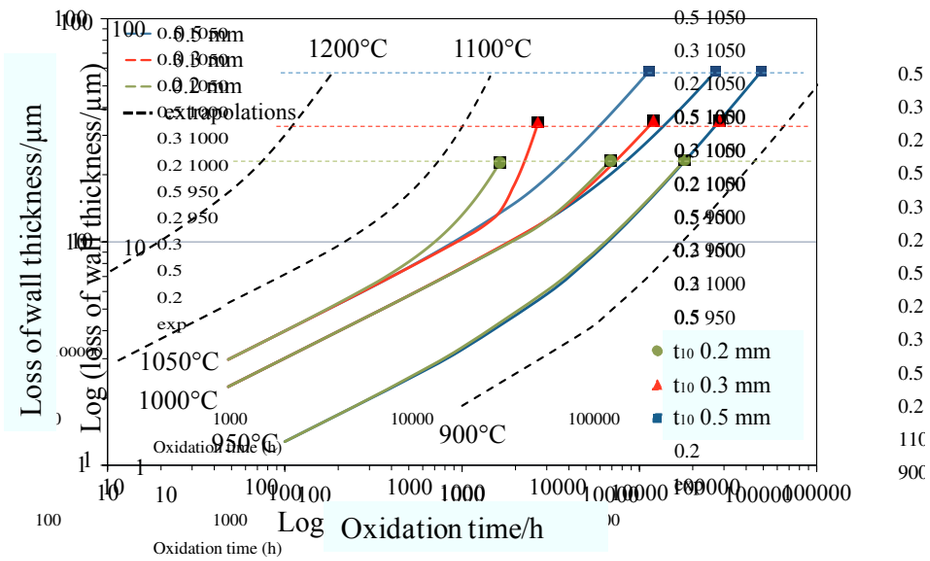

Figure 9.14: Lifetime diagram of NiCr 8020 shown in **Figure 9.12**, here with extrapolation to higher (1100, 1200 °C) and lower (900°C) temperatures.

In a similar manner as previously applied for alloy 230 and alloy X, **Figure 9.15** shows the times t_{10} as a function of specimen thickness at the studied and extrapolated temperatures. The large difference between the values of t_{10} of the 0.3 and 0.5 mm specimens at 1050°C is the result of the appearance of the "super-parabolic" behavior not only for the 0.2 mm but also for the 0.3 mm specimen. For the calculation of t_{10} at 1100°C, it is assumed that all the specimens may undergo "super-parabolic" oxidation. For the 900°C data, it is assumed that none of the specimens exhibits "super-parabolic" oxidation.

Figure 9.16 compares the predicted lifetime limits t_{10} for NiCr 8020 with those of the other two studied Ni-base alloys. The lines connecting the t_{10} symbols of NiCr 8020 show a relatively steady increase of t_{10} with increasing specimen thickness at 950 and 1000°C with a slight convex inflection at 0.3 mm. This is different from the obvious inflections at the thickness of 0.3 mm observed for alloy 230 and alloy X. This difference is mainly related to the fact that at 950 and 1000°C the rate of Cr consumption for alloy NiCr 8020 is the result of initial power law oxidation and subsequent scale spallation for all specimen thicknesses, and the enhancement of Cr consumption by scale spallation is not as significant as that caused by "super-parabolic" oxidation. At 1050°C, the line of NiCr 8020 is very similar to that of alloy

X, with a slight concave inflection at 0.3 mm, because both the 0.2 and 0.3 mm specimens of these two alloys show at 1050°C qualitatively similar “super-parabolic” oxidation. This is contrary to alloy 230 for which only the 0.2 mm specimen showed “super-parabolic” kinetics at this temperature.

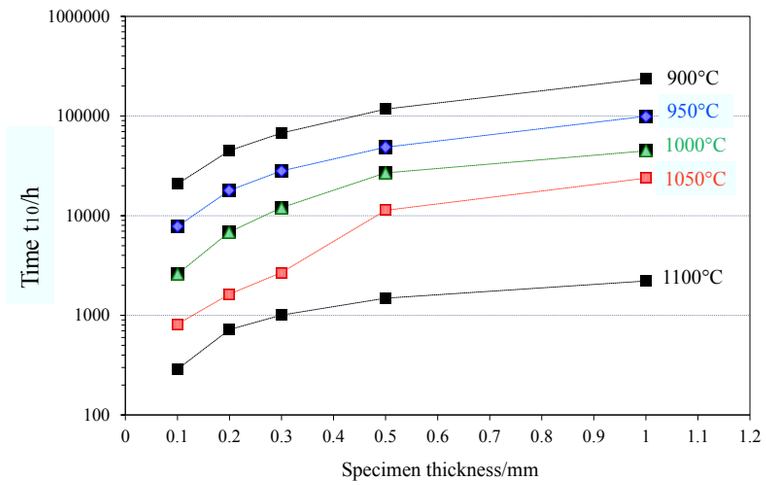

Figure 9.15: Calculated times t_{10} as function of specimen thickness for alloy NiCr 8020 with extrapolations (open symbols) to other temperatures and specimen thicknesses (0.1 and 1 mm) based on experimental results of specimens oxidized at studied temperatures (950 - 1050°C).

a)

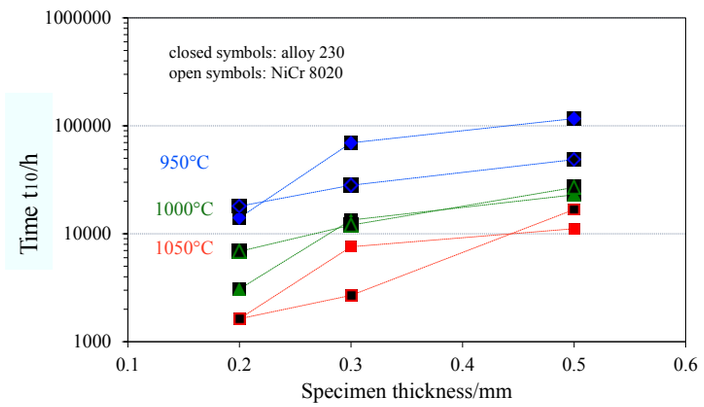

Figure 9.16: Calculated times t_{10} of alloy NiCr 8020 as function of specimen thickness compared with those of a) alloy 230 and b) alloy X at the studied temperatures (950 - 1050°C).

b)

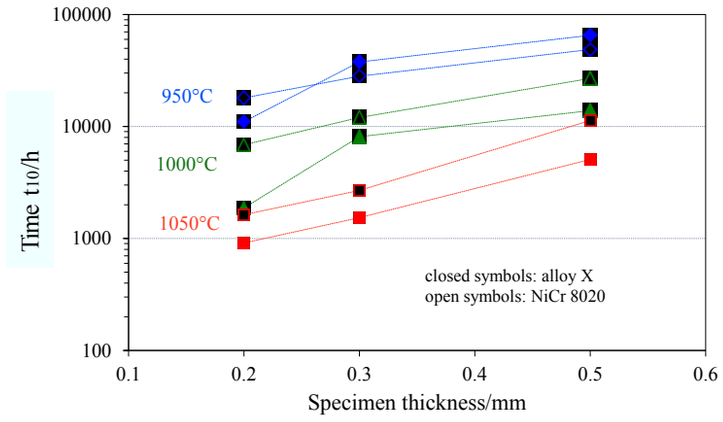

Figure 9.16 (continued)**.**

10 Oxidation behavior of austenitic steel Nicrofer 2020 LNi

10.1 Experimental

Table 1 shows the nominal and analyzed chemical compositions of the austenitic steel Nicrofer 2020 LNi. The alloy contains 20 wt. % of Ni, 20 wt. % of Cr and less than 0.6 wt. % of Al. It is expected that on Nicrofer 2020 LNi, an external Cr_2O_3 will form, whereas Al, which is commonly added as de-oxidant (together with Si) during alloy melting, will tend to oxidize internally. In general, Cr is a BCC stabilizer; while in contrast, the Ni, Mn, and Co and the elements C and N stabilize the austenitic structure [178]. As discussed in Section 3.3.4, Mn and Ti are known to increase the growth rate of Cr_2O_3 scale in high pO_2 environment.

Table 10.1: Chemical composition of studied alloy Nicrofer 2020 LNi (in wt. %) determined by ICP-OES and combustion infrared analysis compared with nominal composition supplied by manufacturing data sheet [121].

	Fe	Ni	Cr	Si	Mn	Ti	Al	C	N	O	S
Nominal	Bal.	19~22	19~22	1.0 (max)	1.0 (max)	0.6 (max)	0.6(max)	0.05(max)	-	-	-
Analyzed	Bal.	18.7	20.7	0.45	0.50	0.40	0.47	0.0069	0.0101	<0.001	<0.001

The creep strength of Nicrofer 2020 LNi under tensile load is substantially lower than that of Ni-base superalloys, such as alloys 230 and X. This makes the alloy vulnerable to substrate creep as a result of scale growth stress and tensile thermal stress during cooling. The yield stresses of the studied alloys at room and high temperatures are compared in **Table 10.2**.

Alloy Nicrofer 2020 LNi was supplied by VDM Metals in the form of sheet with a thickness of 0.6 mm and a width of 38.4 mm. The received alloy was cut into specimens with dimension of □ □ □ □ . As mentioned in Chapter 4, all specimens were ground with SiC grinding papers to three thicknesses (0.2, 0.3 and 0.5 mm) until the final surface finishing of P1200.

First, the ground specimens were prepared for long term (3000 h) and intermediate term (1000 h) air oxidation testing at 950 and 1000°C to have a direct comparison of the results with those of the Ni-base alloys discussed in the previous sections.

Table 10.2: Comparision of yield stress at room and high temperatures of the studied alloys [52, 121, 166].

	Yield stress ($Rp_{0.2}$) in Mpa Room temperature	Yield stress ($Rp_{0.2}$) in Mpa High temperature
Alloy 230	395	275(1000°C)
Alloy X	≥310	210(700°C)
NiCr 8020 SO	≥200	-
Nicrofer 2020 LNi	200	125(700°C) 55(1000°C)

However, during the actual tests at 1000°C the high oxidation rates observed (see following section) lead to the decision, to interrupt the exposures after shorter times (approximately 1560 and 500 h respectively). Longer exposure times would, especially for the thinner specimens, have resulted in a total oxidation thus preventing any useful metallographic cross section investigation. Even after 500 h, the specimens showed breakaway type oxidation. Similar to the observations at 1000°C, an exposure at 950°C for a 0.5 mm specimen with 10 h thermal cycles carried out at ORNL showed that the specimen failed after short exposure time (approximately 500 h) due to breakaway and subsequent substantial scale spallation. Therefore, further investigations were not conducted at this temperature. Additional exposures at lower temperature (900°C) were carried out to obtain a period of steady-state protective oxidation and make sure that oxidation kinetics and oxidation induced microstructural changes could be analyzed before occurrence of breakaway oxidation. Besides, isothermal TG tests for short times at 900, 1000 and 1050°C were carried out for obtaining more detailed information about the temperature dependence of oxidation kinetics.

10.2 Oxidation kinetics

Figure 10.1 shows the net and gross weight change curves of the Nicrofer 2020 specimens with different thicknesses during oxidation at 900, 950 and 1000°C. At 900°C, no specimen thickness dependence of the weight gain is obvious during the early stages of oxidation. After about 200 h it is apparent that the thinner specimen exhibits slightly faster oxidation kinetics than the thicker ones. At approximately 500 h, the curve of the 0.2 mm specimen starts to show an inclination towards more rapid oxidation. The 0.3 and 0.5 mm specimens exhibit onset of scale spallation after about 1000 h, while the scale on the 0.2 mm specimen does not show a clear indication of spallation up to about 1300 h. **Figure 10.2 a** shows a macro image of the 0.2 mm specimen after 640 h exposure at 900℃ , i.e. just after the enhanced oxidation

occurs. The oxide scale at the specimen edge is thicker than in other specimen areas. Cracks can clearly be seen in the oxide at the edge and are expected to allow ingress of oxygen resulting in faster oxidation. The proof for occurrence of scale spallation during the last period of the exposure is shown in **Figure 10.2 b** for the 0.5 mm specimen.

At 950°C, the net weight change curve (**Figure 10.1 b**) shows that the 0.5 mm specimen exhibits onset of significant scale spallation after approximately 500 h exposure, which indicates the occurrence of breakaway already after short time of oxidation at this temperature.

Similar to the studied Ni-base alloys, the steady state growth of the oxide at 900°C can be described by a power law time dependence with n=0.4. However, the rate constant k of Nicrofer 2020 is much larger than that of the studied Ni-base alloys (see **Figure 10.3**). The k values of Nicrofer 2020 in **Figure 10.3** are derived from the TG tests at 900, 1000 and 1050°C (closed black symbols) and the gravimetric data of the steady state oxidation stage at 900 and 950°C (open black symbols).

At 1000°C, the weight gains for all specimens reach approximately 6 - 8 mg.cm^{-2} after already 500 h. Comparison with the data of the Ni-base alloys leads to the conclusion that the surface scales formed on the austenitic steel in this time period are not protective chromia scales. Rather, breakaway type oxidation already occurred after very short exposure time as will be illustrated in the following section. The enhancement of the (gross) weight gains occurring after approximately 500 h for the 0.2 mm specimen and somewhere between 500 and 1000 h for the other two specimens (**Figure 10.1 c**) are related to a change in the composition of the breakaway scale. Protective chromia base scale formation at 1000°C was only observed for the TGA specimen exposed isothermally for 100 h.

The kink (see the enlarged figure of the area in the yellow square in **Figure 10.1 c**) of the net weight change of the 0.5 mm specimen at 1000°C after 50 h indicates that scale spallation already occurred after the first cooling cycle, i.e. after reaching a weight gain of 2 mg.cm^{-2}. This is in accordance with the weight gain at the starting point of scale spallation at 900 and 950℃ (**Figure 10.1 a b**). This means that the kinetics at 1000°C is so fast that after the first heating cycle (48 h), the thickness of the oxide scale on the 0.5 mm specimen has reached a value (2 mg.cm^{-2} oxygen uptake) resulting in a sufficiently large strain energy to cause spallation of the oxide. This again illustrates that during the cyclic oxidation at 1000℃ ,

already after very short oxidation time the scale formed on the surface is not a protective chromia scale, as mentioned above.

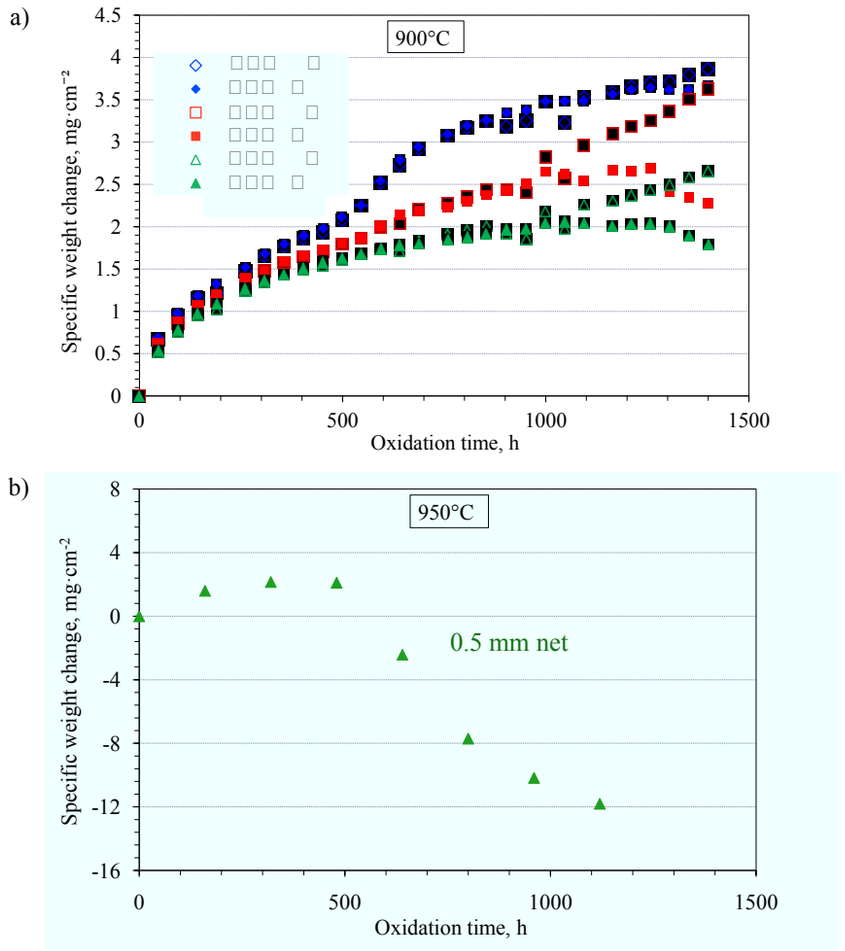

Figure 10.1: Oxidation kinetics of Nicrofer 2020 specimens with different thicknesses at a) 900, b) 950, and c) 1000°C.

c)

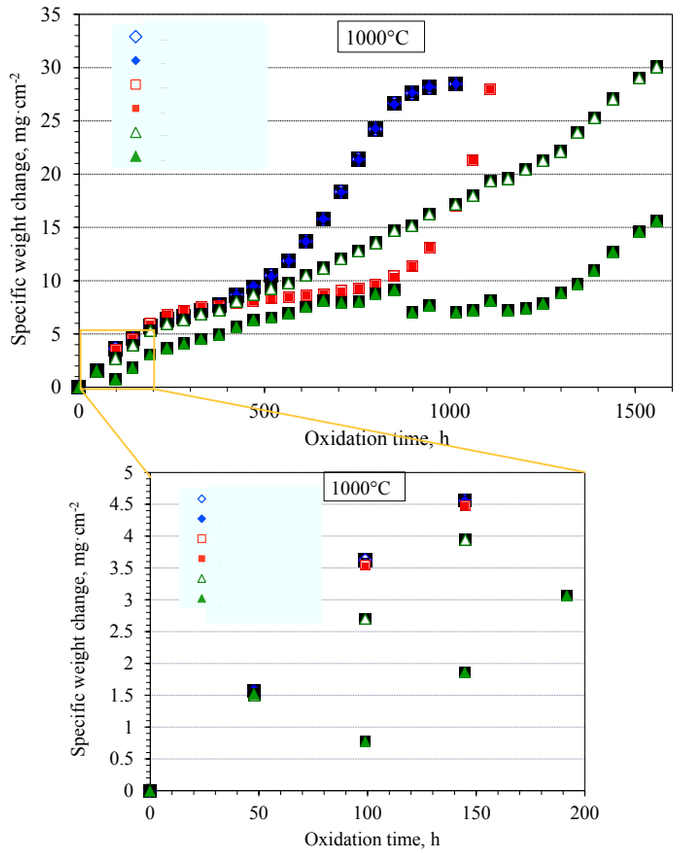

Figure 10.1 (continued).

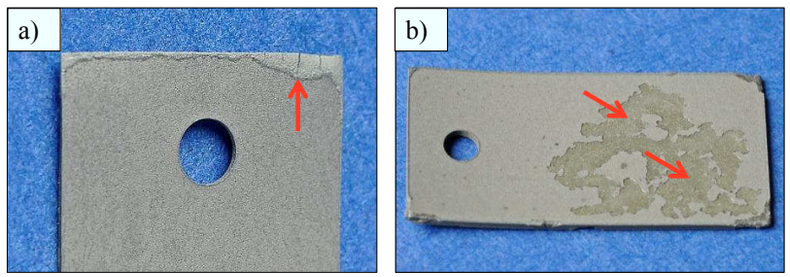

Figure 10.2: Macro images of Nicrofer 2020 oxidized at 900°C; a) specimen thickness 0.2 mm after 640 h and b) 0.5 mm after 1400 h. Arrows indicate a) occurrence of breakaway and b) scale spallation.

Figure 10.4 compares the weight gain curves during the 100 h TG tests in synthetic air at 1000°C of all the studied alloys. It can be seen that the oxidation rate of Nicrofer 2020 is higher than that of the Ni-base alloys, e.g. reaching a weight gain of 1.6 mg.cm^{-2} after 100 h oxidation for the 0.5 mm specimen, compared to 0.74 mg.cm^{-2} for alloy X, 0.62 mg.cm^{-2} for alloy 230, and 0.55 mg.cm^{-2} for alloy NiCr 8020. Unlike the weight gain curve of the 0.5 mm specimen during thermal cycling in **Figure 10.1 c**, the weight gain curve of the 0.5 mm in **Figure 10.4 a** shows that the specimen does not exhibit scale spallation after about 50 h during isothermal oxidation at 1000°C. This proofs that the thermal stress during the cooling process is the reason for scale spallation of the 0.5 mm specimen, and possibly also causes substrate creep during cooling and subsequently formation of tensile cracks in the scale during re-heating for thinner specimens. The scale spallation or scale cracking will allow local contact of the atmosphere to the bare metal. If the subscale Cr concentration is lower than the critical level required for re-healing, the Fe (and Ni) in the alloy will be oxidized, resulting in breakaway type oxidation.

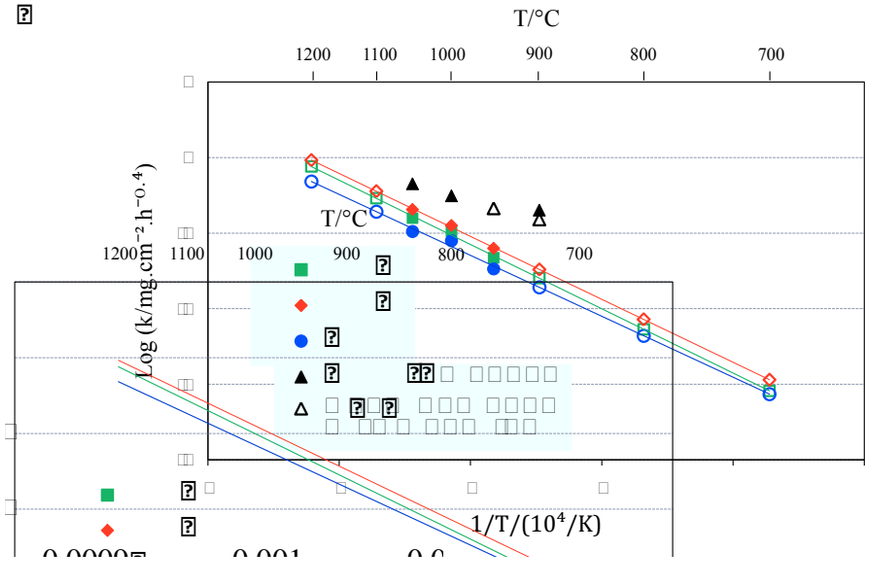

Figure 10.3: Power law rate constant k (**Eq. (3.19)** with n=0.4) of Nicrofer 2020 compared with the k values of the studied Ni-based alloys at the various test temperatures. For the alloys 230, X and NiCr 8020 the open symbols represent extrapolated data.

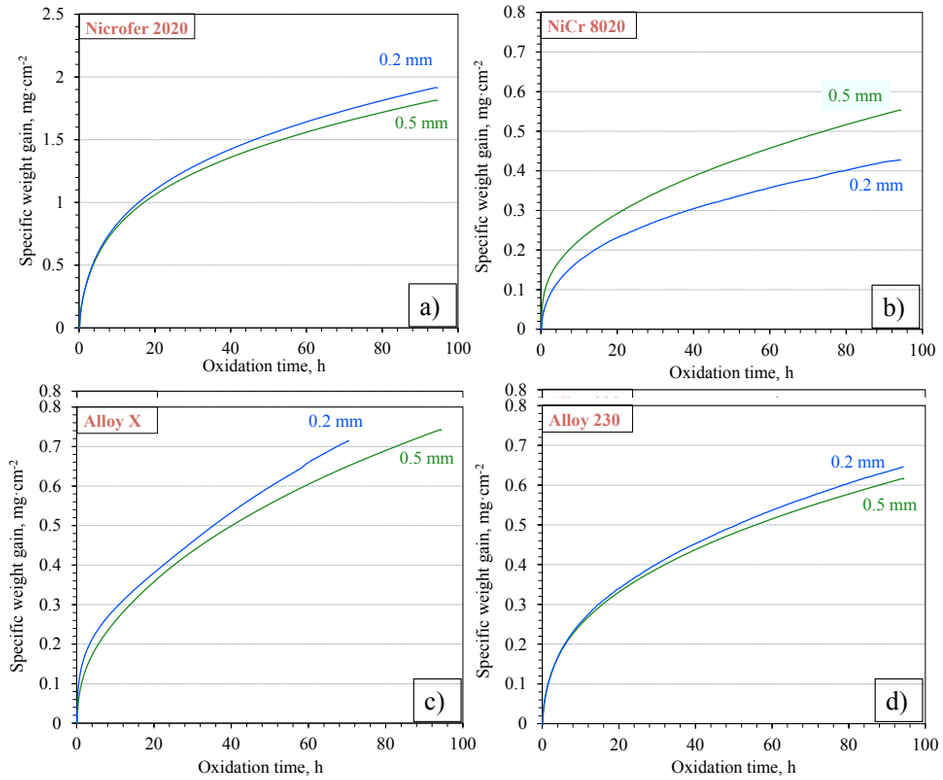

Figure 10.4: Weight gain curves during 100 h TG test at 1000°C for all the studied alloys showing a much higher rate of oxidation of Nicrofer 2020 compared to the Ni-base alloys. (The test of the 0.2 mm specimen of alloy X was stopped after 70 h because of a malfunction of the test facility.)

10.3 Microstructrual changes and oxide formation

In this section, observations of the oxide scale and alloy microstructures before occurrence of breakaway oxidation will be shown for the specimens oxidized at 900°C. The breakaway oxidation of Nicrofer 2020 is discussed using specimens oxidized at 1000°C as example.

Clear indications of breakaway oxidation were not observed in the SEM investigations of the cross sections in the middle of the specimens after oxidation at 900°C specimens either after 640 or 1400 h. **Figures 10.5 a b** present the BSE images showing cross sections of the 0.2 mm specimens after 640 h and 1400 h exposure. As mentioned in Section 10.2 for the edge effect

of the 0.2 mm specimen (see **Figure 10.2 a**), here it shows again the evidence of the reason of the appearance of the enhanced oxidation as a result of the formation of cracks perpendicular to the specimen surface in the scale (see the red circles in **Figure 10.5**). The vertical cracks in the scale are more apparent after 1400 h oxidation than after 640 h oxidation. No vertical cracks are observed in the scale on the thicker specimens (0.3 and 0.5 mm), e.g. the 0.5 mm specimen shown in **Figure 10.5 c d,** even after 1400 h oxidation at 900°C. These observations are in qualitative agreement with the oxidation kinetics shown in **Figure 10.1 a** showing that the thick specimens exhibit scale spallation instead of an inclination to accelerated oxidation.

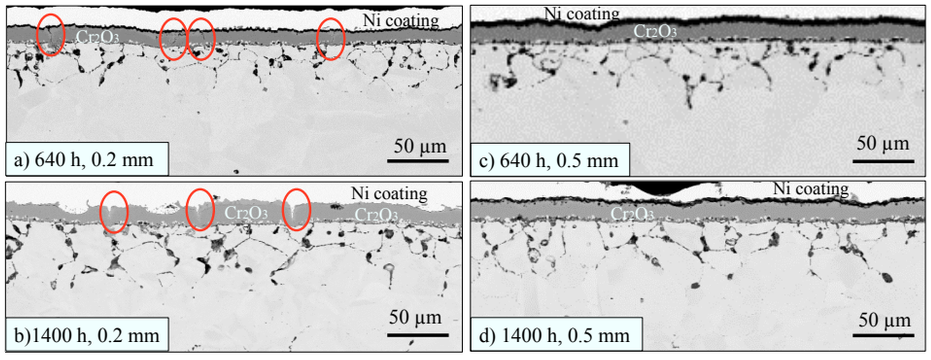

Figure 10.5: BSE images showing cross sections of a, b) 0.2 mm and c, d) 0.5 mm specimen of Nicrofer 2020 after a, c) 640 h and b, d) 1400 h oxidation at 900°C. Red circles indicate locations of cracks within the oxide perpendicular to the alloy/scale interface.

Figure 10.6 shows the oxide scale formation for the 0.5 mm specimens of alloy Nicrofer 2020 after oxidation at 900 and 1000°C for different times. During the oxidation at 900°C (**Figure 10.6 a-c**) and the steady-state isothermal oxidation for 100 h at 1000°C (**Figure 10.6 d**), it is generally observed that a layer of Cr/Mn spinel is formed on top of the chromia scale, and minor amounts of Ti-rich oxide are formed in the outermost layer of the scale. As discussed in Section 3.3.4, Ti and Mn are very frequently observed to be incorporated in chromia scales and finally diffuse into the outer layer of the scale to form, mostly, TiO_2 and $MnCr_2O_4$, respectively. The figure show that SiO_2 formed as internal precipitates near the alloy/scale interface and along the grain boundaries in the subscale region. Al_2O_3 internal oxide formed mainly along the alloy grain boundaries. It was sometimes not easy to unequivocally distinguish Al_2O_3 from SiO_2 in the image due to the similarity in contrast of the

two phases. The EDX point analyses of the scale and precipitates are shown in **Figure 10.7** taking the 0.5 specimen after oxidation of 1400 h at 900°C as example.

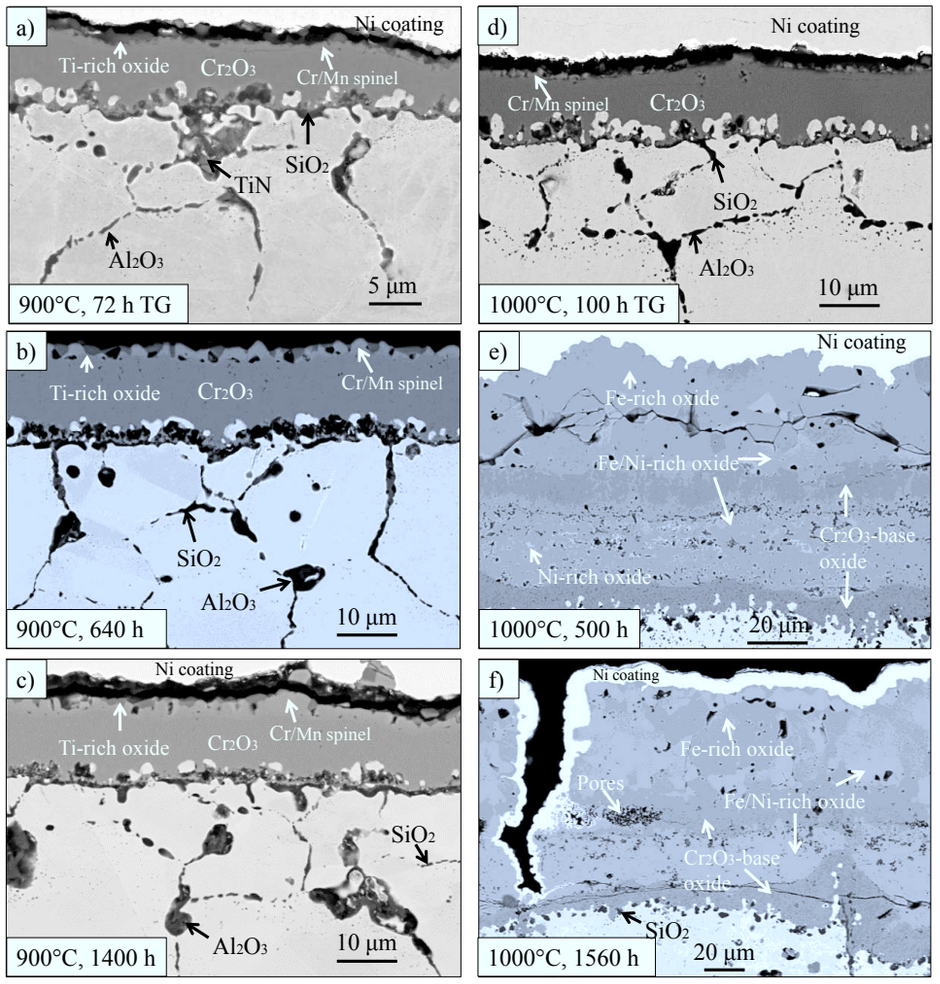

Figure 10.6: BSE images showing cross sections of 0.5 mm thick specimens of Nicrofer 2020 after oxidation at a-c) 900°C and d-e) 1000°C for different times.

After 500 and 1560 h oxidation at 1000°C, the scale on the 0.5 mm specimens of Nicrofer 2020 exhibited a breakaway type oxide (**Figure 10.6 e f)**. The morphologies of the breakaway type oxide after both oxidation times look quite similar. The EDX point analyses of the scale and precipitates are shown in **Figure 10.8** taking the 0.5 specimen after oxidation of 1560 h at 1000°C as example.

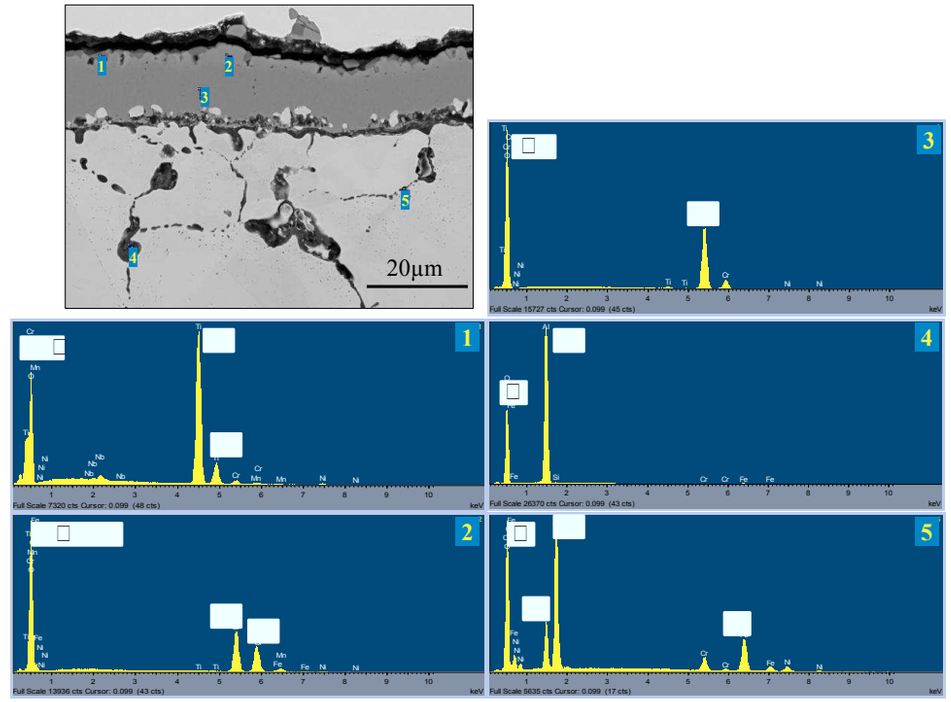

Figure 10.7: BSE image showing cross section of 0.5 mm thick specimen of Nicrofer 2020 after oxidation at 900°C for 1400 h with spectra of EDX point analyses, corresponding to the specimen shown in **Figure 10.6 c**.

On the top of the scale, a two-phase zone exists, in which irregular Fe/Ni-rich oxide is dispersed in an Fe-rich oxide matrix. Beneath the two-phase zone a region is present, which consists of two dark grey Cr-rich oxide layers and one light grey Fe/Ni-rich oxide. It is assumed that the upper Cr-rich layer is the original protective Cr_2O_3 oxide, however with a modified composition (likely $FeCr_2O_4$ and $NiCr_2O_4$) due to incorporation of part of the Cr_2O_3 into mixed oxide after breakaway oxidation. With the lateral and vertical cracks as well as the porous structure in the breakaway scale, the oxygen can penetrate deeper into the location beneath the original Cr_2O_3 oxide, where the Cr depletion zone exists. The Fe and Ni concentrations in the Cr depletion zone are substantially higher than in the original alloy, so the oxides of Fe and Ni can easily be formed. A continuous layer of relatively pure Cr_2O_3 is present beneath the Fe/Ni-rich oxide when the alloy is consumed to a depth where the Cr content is again sufficiently high to allow chromia-rich scale formation. Beneath this layer the

pO_2 is apparently at a level lower than the dissociation pressure of the various Fe- and Ni-rich oxides (see details in Section 3.1).

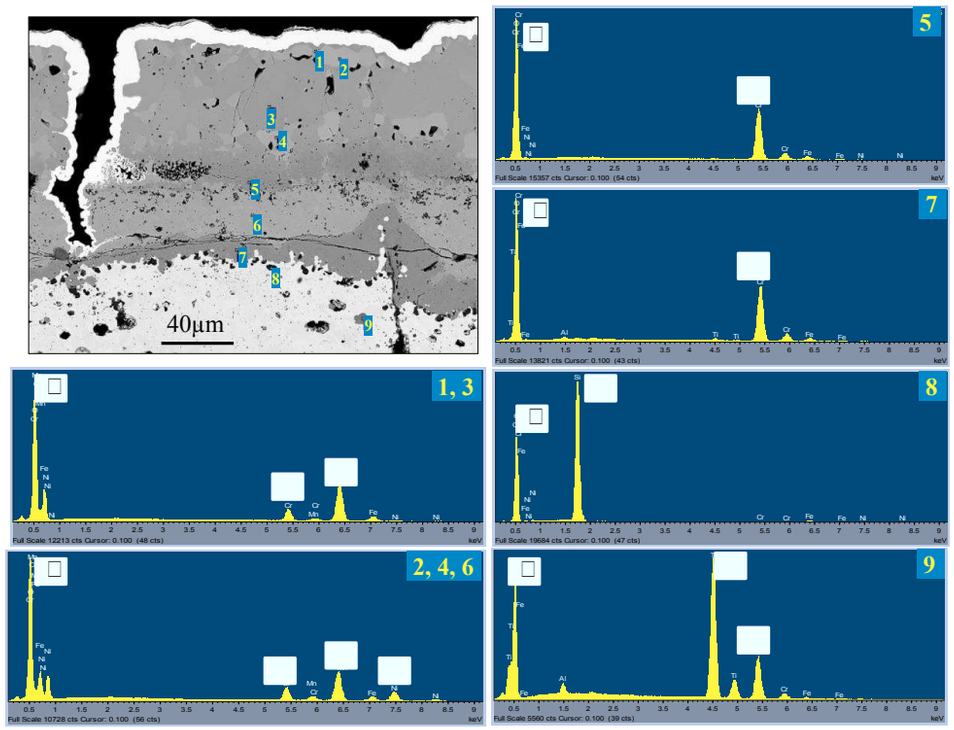

Figure 10.8: BSE image showing cross section of 0.5 mm thick specimen of Nicrofer 2020 after oxidation at 1000°C for 1560 h with spectrums of EDX point analyses, corresponding to the specimen shown in **Figure 10.6 f.**

The BSE images in **Figure 10.9** show the cross sections of 0.3 mm specimens oxidized at 900 and 1000°C for different times. At 900°C (**Figure 10.9 a b**), a protective chromia scale with Cr/Mn spinel and Ti-rich oxide in the outermost layer is formed, similar to that observed for the 0.5 mm specimens at this temperature (**Figure 10.6 a-c**). At 1000°C, a breakaway type oxide scale is observed after short as well as long oxidation times (**Figure 10.9 c d**). The morphology of the breakaway type scale, especially the scale formed after 500 h oxidation, is quite similar to that observed for the 0.5 mm specimens shown before in **Figure 10.6**.

However, after 1100 h oxidation at 1000°C, the breakaway scale on the 0.3 mm specimen (**Figure 10.9 d**) consists only of two main oxide phases. The outermost light grey layer is Fe-

rich (Fe=26.8 at. %) oxide; it also contains 11 at. % of Cr and small fractions of Ni, Mn and Ti. The dark grey layer, located beneath the light grey layer, is Cr-rich oxide; apart from Cr it contains small fractions of Fe, Ni, Mn and Ti. The outermost light grey layer is the oxide formed after occurrence of breakaway, whereas the dark grey layer is related to the original protective Cr_2O_3 formed during the very early stages of oxidation. However, it now became incorporated in the other oxide formed after the breakaway oxidation started. Unlike the type of oxide observed for the other breakaway specimens (see **Figure 10.6 e f**, **Figure 10.9 c**, and also later **Figure 10.10 e**), no Ni-containing oxides were found in the scale of this specimen. This is because the dissociation pressure of NiO is higher than that of Fe-rich oxide (Section 3.1), thus, oxidation of Ni can only occur in an environment with higher pO_2, which can be provided by the cracks and pores in the scale. However, the scale is relatively dense on the 0.3 mm specimen after 1100 h oxidation at 1000°C. The pO_2 in the inner part of the dense scale is expected to be lower than that in the porous scale, so Ni is in that case hardly oxidized.

Considering that no scale spallation was observed according to the weight gain data in **Figure 10.1 b**, the dense scale formed at 1000°C on the 0.3 mm specimen might be a result of subscale creep due to the reduction of the specimen thickness after long term oxidation, in combination with the relating low creep strength of the substrate material. The formation of fast growing Fe-rich oxide (see Section 3.2) during the breakaway oxidation is in agreement with the high weight gain of the 0.3 mm specimen after approximately 800 h at 1000°C shown in **Figure 10.1 b**.

The rapid oxidation of Fe after breakaway is believed to be controlled by the outward diffusion of cations through the existing oxide. For example, the cations diffuse outward from the alloy/scale interface through the protective Cr_2O_3 layer, but some of the cations are already oxidized by oxygen which diffuses inwardly. Therefore, small amounts of Fe and other oxygen active solute elements are found in the original Cr_2O_3 layer. The presence of nitrides in the center of this specimen is another indication of substantial transport of molecular gas species through the scale.

Figure 10.10 presents the BSE images of the cross sections showing the 0.2 mm specimens oxidized at 900 and 1000°C for different times. At 900°C the scale still mainly consists of protective chromia based oxide for the 0.2 mm specimen oxidized up to 1400 h, although breakaway appeared at the edge of the 0.2 mm specimen after 640 h oxidation at 900°C (**Figure 10.2 a**).

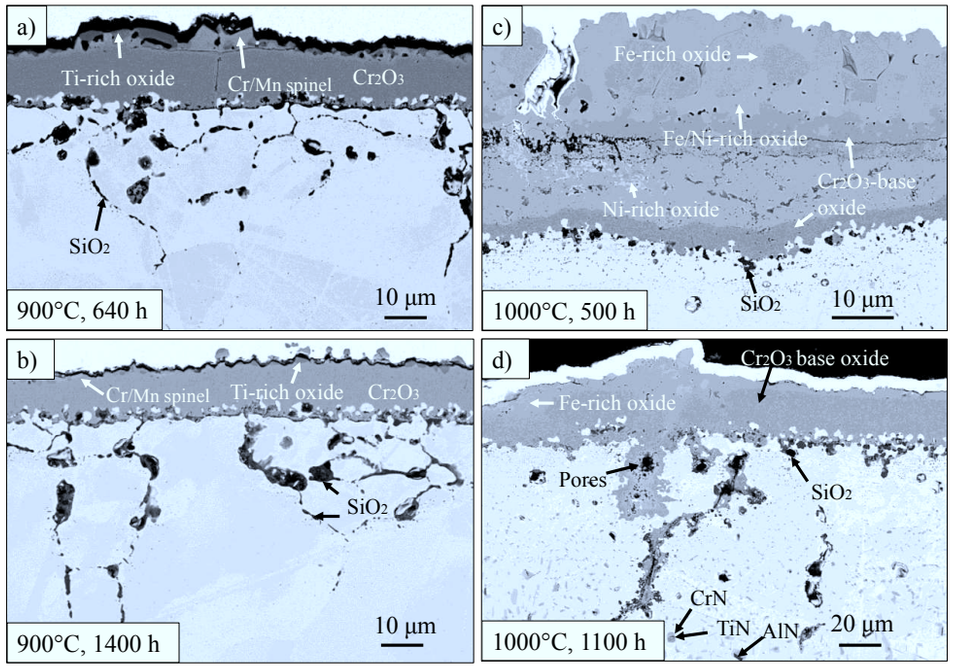

Figure 10.9: BSE images showing cross sections of 0.3 mm thick specimens of Nicrofer 2020 after different oxidation times at a, b) 900°C and c, d) 1000°C.

The scale and the subscale microstructures of the 0.2 mm specimens, either during the period of the growth of the protective Cr_2O_3 scale or after breakaway, are qualitatively similar to those described for the 0.5 mm specimens (**Figure 10.6**). The cross sections of the 0.2 mm specimens after 1000°C oxidation are only shown for the exposures after the 100 h TG test and after 500 h, because the specimen after longer term exposure was totally consumed by oxidation.

In the as-received microstructure of alloy Nicrofer 2020, small amounts of TiN precipitates are dispersed in the γ-Fe matrix. This can be e.g. seen in the cross section images of the center of the 0.5 mm specimens after the short time TG tests (**Figure 10.11 a** and **d**), for which the microstructure has not been affected by oxidation.

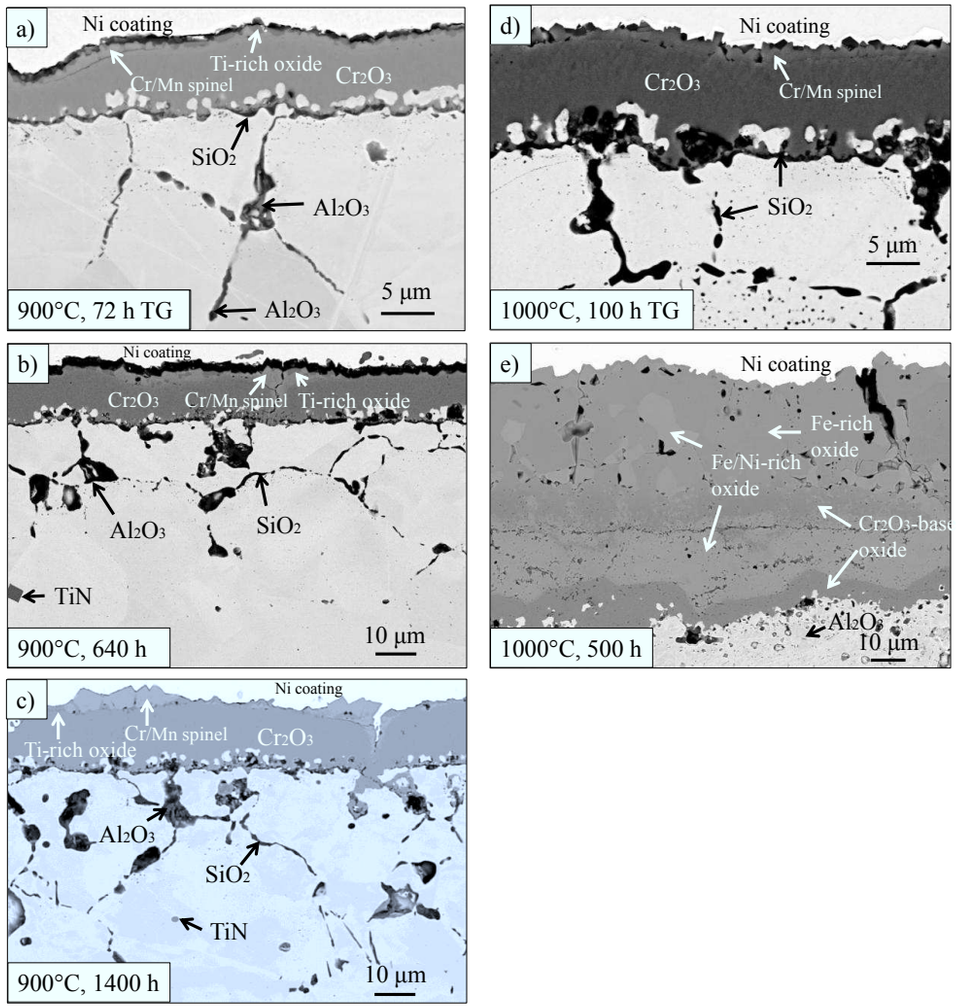

Figure 10.10: BSE images showing cross sections of 0.2 mm thick specimens of Nicrofer 2020 after oxidation at a-c) 900°C and d-e) 1000°C for different times.

During exposure at 900°C, the size and amount of the TiN precipitates do apparently not change up to 1400 h exposure (compare **Figure 10.11 a b c**). However at 1000°C, the amount of TiN increases with increasing oxidation time from 100 to 500 h. After 1600 h oxidation at 1000°C, numerous precipitates of nitrides in the form of small particles or needles are observed, i.e. not only TiN, but also CrN, and AlN (**Figure 10.11 f**).

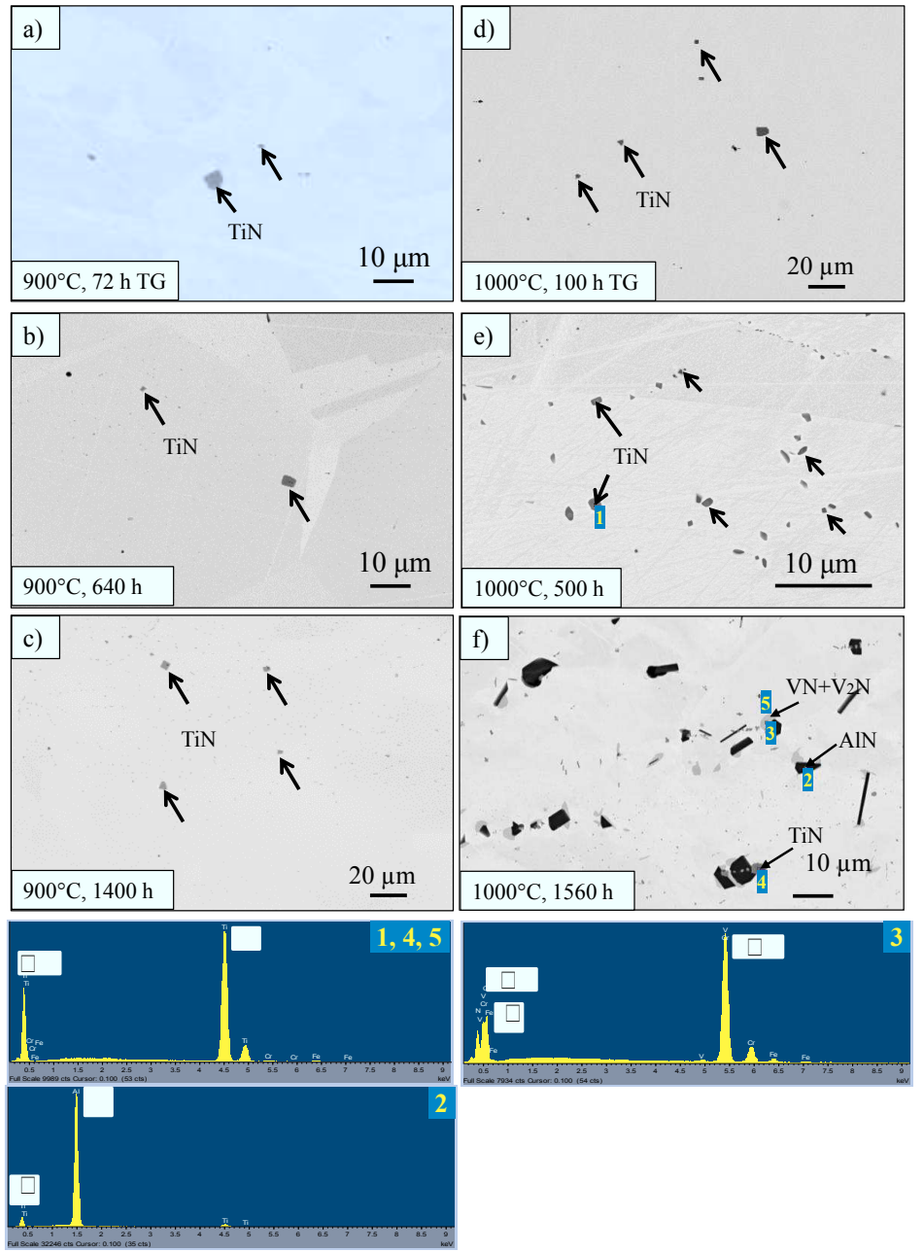

Figure 10.11: BSE images showing cross sections of the center of 0.5 mm thick Nicrofer 2020 specimens oxidized at a-c) 900°C and d-f) 1000°C for different times. The spectra of selected EDX point analyses of the precipitates are also shown.

The increasing amount of TiN as well as the presence of Cr- and Al-nitrides is a clear indication of N-ingress from the environment related to the loss of protective properties of the scale against ingress of molecular species such as nitrogen. **Figure 10.12** shows the cross sections of the 0.2 and 0.5 specimens after the 72 h TG test at 1050°C. A protective chromia scale is formed during this short time isothermal oxidation at 1050°C. Similar to the scale formed on the specimens after the TG tests at lower temperatures (**Figure 10.6** and **Figure 10.10**), Ti-rich oxide as well as Cr/Mn spinel is found in the outer layer of the scale. Internal oxides of Si and Al are dispersed near the alloy/scale interface as well as in the subscale region.

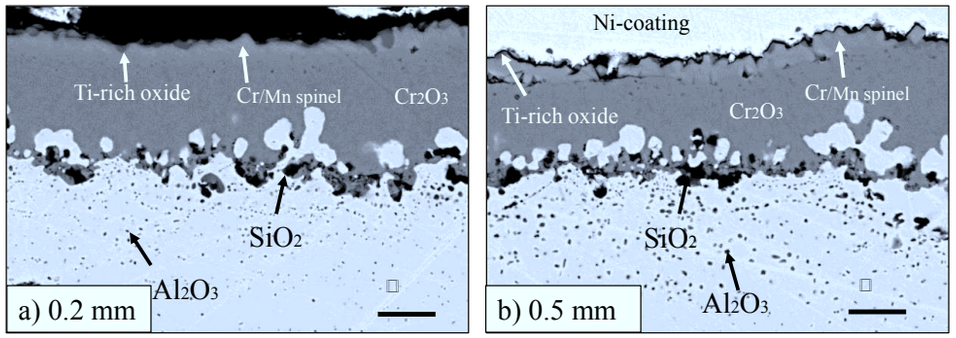

Figure 10.12: BSE images showing the cross sections of the a) 0.2 and b) 0.5 mm specimens of Nicrofer 2020 after 72 h TG test in synthetic air at 1050°C.

10.4 Subscale chromium depletion

Figure 10.13 shows the subscale Cr concentration profiles measured by EDX in specimens oxidized at 900 and 1000°C. At 900°C, the interface concentration of Cr is approximately 9 - 10 wt. % during the steady state oxidation stage, i.e. before the depletion front reaches the center of the specimen (**Figure 10.6 a b c**). The profile of the 0.2 mm specimen after discontinuous oxidation of 640 h at 900°C in **Figure 10.6 a** shows that the depletion just reached the center of the specimen. This coincides with the occurrence of the macroscopically observed breakaway on the specimen edges (**Figure 10.2 a**).

At 1000°C, the Cr profiles of the 0.2 and 0.5 mm specimens after the 100 h TG test are very steep with an interface concentration approaches 5 wt. %. However, for the 0.2, 0.3 and 0.5 mm specimens after 500 h exposure, the interface Cr concentration increases to approximately

13 wt. %. The profiles observed after the TG tests are caused by selective Cr oxidation due to formation of an external chromia based scale (**Figure 10.6 d**). Due to the low Cr interface concentration this protective scale is not retained during prolonged cyclic exposure and a breakaway type scale is formed containing substantial amounts of Fe and Ni (**Figure 10.6 e f**, **Figure 10.9 c d**, and **Figure 10.10 e**). This means that, in respect to the main alloying elements Fe, Ni, and Cr, the latter element is no longer exclusively oxidized. Consequently, the loss of Cr, relative to the alloy concentrations of Fe and Ni, becomes smaller than during the 100 h isothermal oxidation. This results in a higher Cr interface concentration after 500 h exposure than after 100 h isothermal oxidation (**Figure 10.13 d**). Accordingly, this kind of increase of the interface Cr concentration after prolonged exposure time is the result of the breakaway of the corresponding specimens (**Figure 10.6 e f**, **Figure 10.9 c** and **Figure 10.10 e**). Only after continuing oxidation to e.g. 1100 and 1560 h a further decrease in Cr interface concentration occurs for the 0.3 and 0.5 mm specimen, respectively.

The Cr concentration profiles in the 0.2 and 0.5 mm specimens after the 72 h TG test at 1050°C are shown in **Figure 10.14**. The interface Cr concentrations are clearly below 10 wt. % for both specimen thicknesses, which is qualitatively similar to that observed after the 100 h TG test at 1000°C (**Figure 10.13 d f**).

The GDOES profiles in **Figure 10.15 a1 and b1** show that after 72 h isothermal oxidation of the 0.2 and 0.5 mm specimens at 900°C the Cr concentration at the alloy/scale interface (dashed red line is an extrapolation of the Cr concentration to the alloy/scale interface) is close to 10 at. % (equals to ~9 wt. %). This value is very similar to the interface Cr concentration measured by EDX (**Figure 10.13 a**). According to the oxidation kinetics (**Figure 10.1 a**) and the BSE cross sections shown above, this concentration is apparently sufficiently large to retain chromia growth during long term thermal cycling at 900°C. At 950°C chromia based scale growth occurs up to approximately 500 h (**Figure 10.1 b**).

However, the fact that for the 0.2 mm specimen breakaway type oxidation was observed during exposure at 900°C on specimen edges (**Figure 10.2 a**) indicates, that for the Nicrofer 2020 austenitic steel, a Cr interface concentration of approximately 9 wt. % seems to be close to the value which is required to prevent breakaway type oxidation.

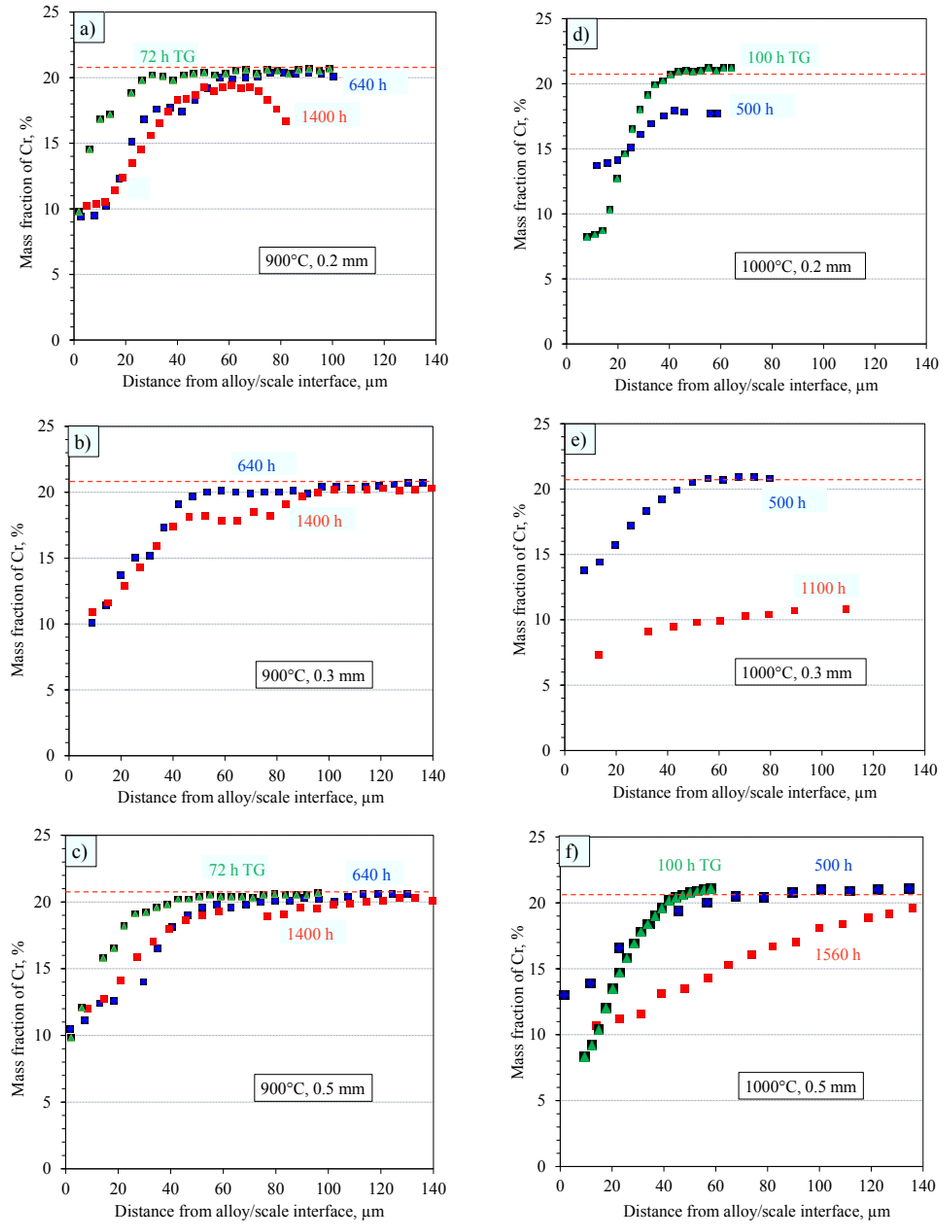

Figure 10.13: Subscale concentration profiles of Cr in Nicrofer 2020 after oxidation at a-c) 900°C and d-e) 1000°C after different times of exposure for specimen thicknesses of a, d) 0.2 mm, b, e) 0.3 mm, and c, f) 0.5 mm.

The GDOES depth profiles (**Figure 10.15 a1** and **b1**) also show that the surface scale mainly consists of chromia; only very small amounts of Fe and Ni, originating from the transient state of oxidation are present in the outer part of the scale. The outer scale region exhibits a very strong enrichment of Ti and Mn. The enrichment correlates with a substantial depletion in the subscale region for both elements. Ti shows a minor enrichment in the inner part of the chromia scale, in agreement with previous observations [109] and the pO_2 dependence of Ti-solubility in chromia [109]. Mn is enriched at the oxide surface, however, the amount of Mn dissolved in the inner part of the chromia (equals approximately 0.15 wt. %) seems to be virtually independent of the distance from the alloy/scale interface. Very similar enrichments of Ti and Mn are found in the 0.2 (**Figure 10.15 a2**) and the 0.5 mm specimen (**Figure 10.15 b2**), indicating that the depletion of e.g. Mn and Ti are not yet substantially affected by the limited reservoir of these elements in the thin specimen. Chromium is clearly depleted in the subscale region. Si and Al are, slightly enriched near the alloy/scale interface, probably in form of SiO_2 and Al_2O_3, respectively (e.g. **Figure 10.6**).

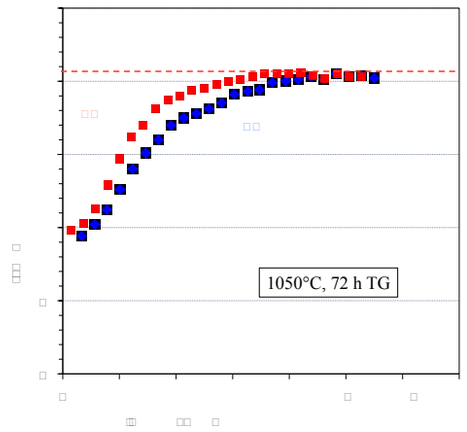

Figure 10.14: Subscale concentration profiles of Cr in Nicrofer 2020 specimens of different thicknesses isothermally oxidized at 1050°C for 72 h in TG test.

The results in **Figure 10.16** show that during the 72 h isothermal oxidation a protective chromia scale forms even at 1050°C, which is in agreement with the microstructure of the oxide scale shown in **Figure 10.12**. The distributions of the minor alloying elements Mn, Ti, and Si are qualitatively similar to those observed at 900°C, whereby the incorporation of Ti and Mn in the outer scale part seems to be more pronounced at 1050°C.

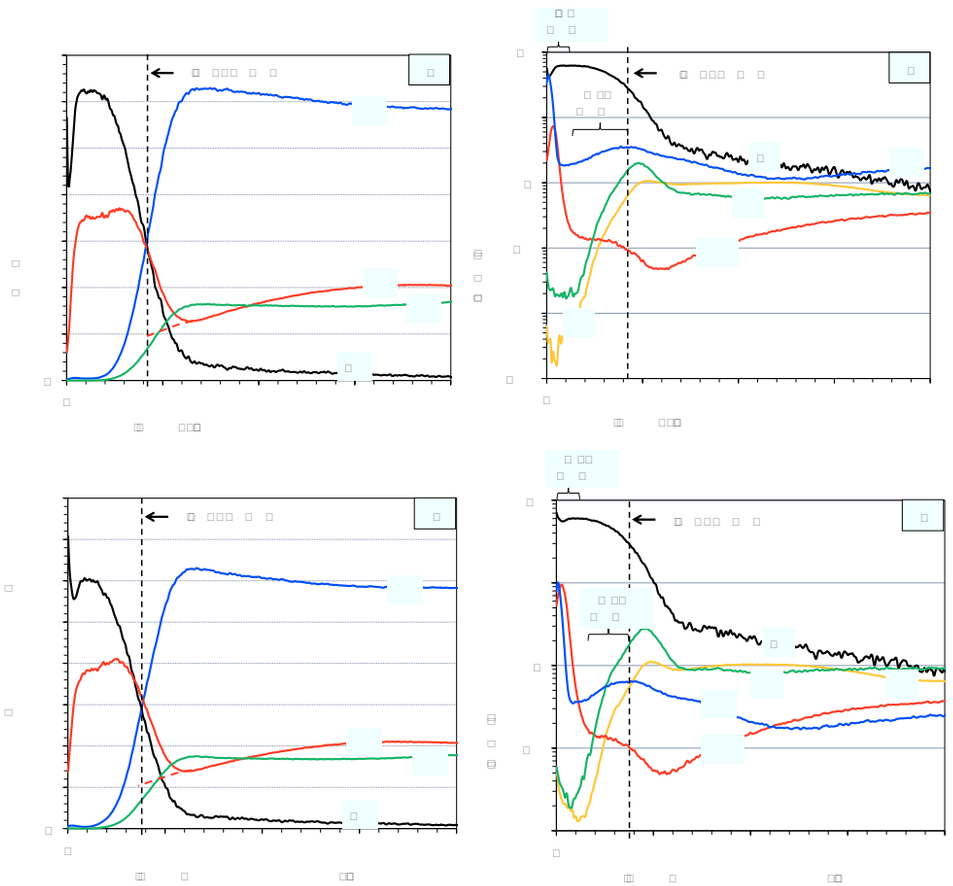

Figure 10.15: GDOES profiles of the a) 0.2 mm and b) 0.5 mm specimens of Nicrofer 2020 after 72 h isothermal TG test in synthetic air at 900°C.

As described in Section 3.3.4, incorporations of Ti as well as Mn in chromia enhance the growth rate of the subsurface scale [109]. As the incorporation of these elements will likely be temperature dependent, its effect on oxidation kinetics is expected to be temperature dependent. The dashed red lines in **Figure 10.16** indicating the extrapolation of the Cr concentration to the alloy/scale interface show that the Cr interface concentration after the 72 h TG test at 1050°C is approximately 8 - 9 at. % (equals to 7 - 8 wt. %). This value is clearly smaller than that observed after the TG test at 900°C of about 9 wt. % (**Figure 10.15**), in qualitative agreement with the EDX data. This indicates that the enhancement of the chromia growth rate by Ti and Mn increases with increasing temperature resulting in a decreasing Cr interface concentration with increasing temperature.

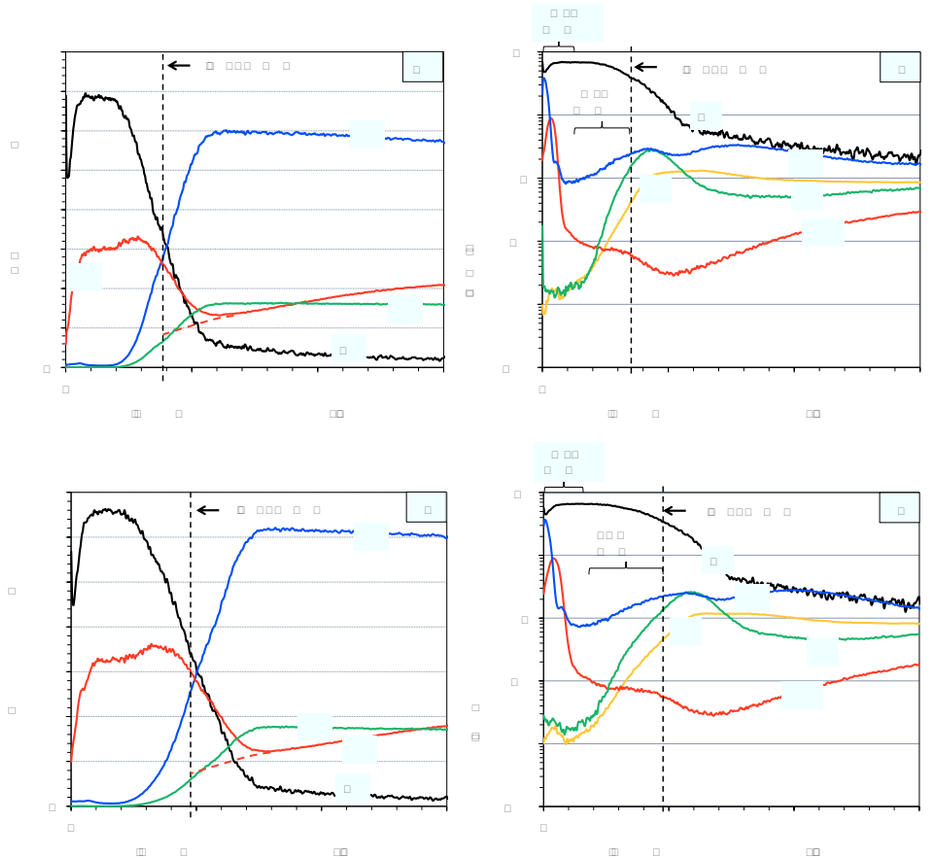

Figure 10.16: GDOES profiles of the a) 0.2 mm and b) 0.5 mm specimens of Nicrofer 2020 after 72 h isothermal TG test in synthetic air at 1050°C.

Even the very low interface Cr concentrations during the isothermal TG tests at 1000 and 1050°C are apparently sufficient to maintain the growth of the protective chromia base scale during oxidation up to the maximum isothermal test time of 72 hours. However, thermal cycling, resulting in initiation of micro-damage during the cooling and/or re-heating process, allows, for a certain time, direct local access of gaseous species to the alloy surface. The weight gain data in **Figure 10.1** illustrate that at 1000°C and above, the very low Cr interface concentration does not allow the micro-damage to be healed by re-formation of the protective chromia. At 900°C this healing is assured, however the macro image (**Figure 10.2**) shows indication of breakaway at the edges of the 0.2 mm specimen after 640 h oxidation.

10.5 Lifetime diagram of Nicrofer 2020

10.5.1 General remark

As shown above, the growth of protective chromia for prolonged oxidation was only observed at 900°C. Therefore, here the concept of lifetime prediction of alloy Nicrofer 2020 will be developed mainly based on the oxidation behavior at 900°C.

According to the discussions in the previous sections, it was found that the critical interface Cr concentration for maintaining the formation of a protective chromia scale during oxidation at 900°C with thermal cycles is about 10 wt. %. It was also observed that for the 0.2 mm specimens, the breakaway oxidation occurred when the Cr depletion front reached the center of the specimens (**Figure 10.13 a**). After the breakaway, the interface Cr concentration does not decrease with increasing oxidation time, rather, the Cr concentration at the center of the specimen decreases with increasing oxidation time. A similar depletion process can be observed for the 0.3 and 0.5 mm specimens after oxidation at 900°C, i.e. the interface Cr concentration does not show a clear time dependence (**Figure 10.13 b c**).

The observation that breakaway occurs at a time at which the subscale Cr concentration profile is still very steep leads to the conclusion that the reservoir approach applied for the Ni-base alloys considering the critical interface Cr concentration assuming a quasi-flat Cr profile at the time t* is not suitable for the lifetime prediction of alloy Nicrofer 2020. Instead, the time when the depletion front reaches the center of the specimen, designated as t_C might be more suitable to determine the lifetime limits. As already mentioned in Section 6.1 (see **Eq. (6.1)**) this criterion is considered to underestimate the lifetime limits of the studied Ni-base alloys compared to the t* approach.

10.5.2 Construction of lifetime diagram

According to the Cr concentration profile of the 0.2 mm specimen in **Figure 10.13 a**, the depletion reached the center of the specimen after approximately 640 h oxidation at 900°C. The time t_C for the other specimen thicknesses can then be calculated using the following relation, derived from **Eq. (6.1)**:

$$\frac{t_C}{t_C'} = \frac{l^2}{l'^2} \qquad (10.1)$$

The calculated t_C for the 0.3 mm specimen is 1440 h, and for the 0.5 mm specimen it equals 4000 h. **Figure 10.13 b** shows that the Cr depletion front of the 0.3 mm specimen almost reached the center of the specimen after 1400 h, which is in good agreement with the calculated value of 1440 h.

Figure 10.17 shows the lifetime diagram for alloy Nicrofer 2020 at the studied temperatures. The blue curve showing the loss of wall thickness as a function of oxidation time at 900°C was calculated based on the gravimetric data of the 0.5 mm specimen shown in **Figure 10.1 a** using the modified COSP model described in Section 6.4. Because of the short lifetime of the 0.2 and 0.3 mm specimens, no apparent inclination of the curve occurred before these specimens fail due to breakaway oxidation. Therefore the symbols indicating the approximate lifetime t_C of the 0.2 and 0.3 mm specimens are plotted on the curve calculated for the 0.5 mm specimen. The t_C of the 1 mm specimen was also calculated using **Eq. (10.1)**. The symbol representing the wall thickness loss of the 1 mm specimen at time t_C is plotted on the extrapolated curve for the 0.5 mm specimen according to the experience from the Ni-base alloys that no apparent differences of the oxidation and scale spallation kinetics were found between the 0.5 and 1 mm specimens (**Figure 6.19** and **Figure 8.2**). As discussed in the previous sections, even the 0.5 mm specimen failed after short time oxidation during cyclic exposure at 950 and 1000°C. Therefore, only one symbol indicating the lifetime of the 0.5 mm specimen is plotted on the curve of 950 and 1000°C.The lines showing the lifetime at 950 and 1000°C were also calculated on the basis of the gravimetric data shown in **Figure 10.1**.

Figure 10.18 shows a comparison between the lifetime limits of alloy Nicrofer 2020 and the Ni-base alloys 230 and X at 900°C. The values of t_{10} derived for alloy 230 and X were already shown in **Figure 6.18** and **Figure 8.20**, respectively. With the lifetime criterion based on t_C, the lifetime limits of alloy Nicrofer 2020 are much shorter than those of the Ni-base alloys for a given specimen thickness and temperature. As explained before, a major reason for this difference in behavior between the nickel base alloys and the austenitic steel is the high oxide growth rate of the latter material. It is important to note that, according to the product sheet of Nicrofer 2020 [121], this alloy can be used at temperatures up to 1050°C. However, according to the present study, a component with a wall thickness of 0.5 mm can, at temperatures higher than 1000°C, only safely be operated under isothermal conditions. At these high temperatures, thermal cycling will cause early breakaway oxidation.

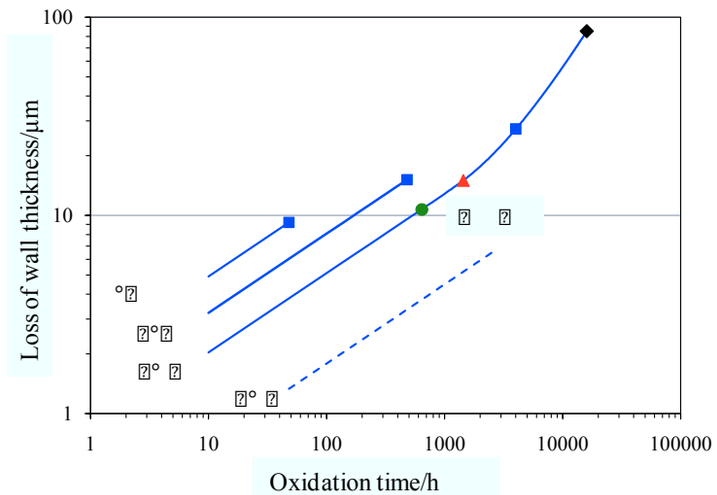

Figure 10.17: Lifetime diagram calculated for alloy Nicrofer 2020 showing the dependence of wall thickness loss as a function of oxidation time. Symbols show the calculated times t_C for specimens of different thicknesses. The dashed line for 800°C is extrapolated based on the weight gain kinetics during discontinuous oxidation at 900 and 950°C.

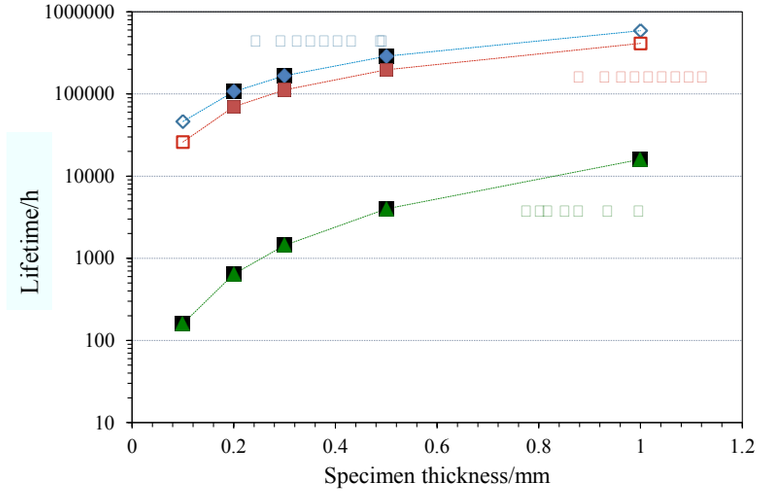

Figure 10.18: Comparison between lifetime limits t_C of alloy Nicrofer 2020 and of the studied Ni-base alloys (t_{10}) at 900°C.

Summary and conclusions

In the present investigation, an attempt was made to develop a generalized oxidation lifetime model for chromia-forming FCC alloys that can be incorporated into alloy data sheets and easily understood and employed by component designers. The model captures the most important damaging oxidation effects relevant for component design: wall thickness loss, scale spallation and the occurrence of critical depletion of the scale forming element Cr, which eventually results in “breakaway” oxidation. The material used for development of the concept was the wrought NiCrW base alloy 230.

For obtaining input data for the modeling and for verification of the predictions of the developed modeling approaches, specimens of alloy 230 with thicknesses varying between 0.2 - 0.5 mm (in selected cases 1 mm) were oxidized at 950 - 1050°C in laboratory air for up to 3000 h. After exposure, the specimens exhibited a microstructure consisting of a γ-Ni matrix, Ni/W-rich M_6C and/or Cr-rich precipitates ($M_{23}C_6$ and π-nitrides); type and amount of precipitates depend on specimen thickness, temperature and time. The oxidation induced loss of Cr resulted in a Cr-depleted subsurface zone in which the Cr-rich precipitates dissolved. In addition, the Cr-lean M_6C was also depleted in this zone. The width of the M_6C-free zone was always smaller than that of the zone which was free of Cr-rich precipitates (carbides and/or nitrides). In the center of the specimens, Cr-rich $M_{23}C_6$ and π-nitrides were formed. These effects increased with oxidation time, temperature and decreasing specimen thickness. Using thermodynamic and kinetic modeling, a mechanism was developed to explain these observations wherein the Cr depletion in the subsurface zone increased the local C and N activity, resulting in an activity gradient that drove C and N back to the center of the specimen. In case of the Cr-lean M_6C the destabilization of the carbide phase in the subscale zone was related to a decrease of the W activity as a result of the decreasing Cr concentration. Because the specimens were thin, the relative change in C and N content is sufficient to stabilize the Cr-rich carbide ($M_{23}C_6$) and nitride (π-phase) near the specimen center. Thermocalc and DICTRA calculations using the measured oxidation kinetics as input data successfully predicted the measured Cr depletion profiles and qualitatively explained the other above mentioned microstructural changes. With increasing exposure time and decreasing specimen thickness, precipitate formation in the specimen center gradually became affected by N uptake from the environment. This process resulted in enhanced nitride formation at the expense of

the Cr-rich carbides, in qualitative agreement with the thermodynamic calculations. Ongoing Cr depletion eventually resulted in an eventual dissolution of the M_6C precipitates.

For developing the lifetime diagram, a Matlab based tool was developed to describe the oxide growth and spallation kinetics on the basis of a modified COSP approach. The calculated Cr consumed by oxidation was then correlated with measured kinetics of Cr depletion in the bulk alloy. A critical value for subscale Cr depletion at the alloy/scale interface of 10 wt. % was used based on the measured Cr concentration profiles, and macroscopically visible "breakaway" at specimen edges and occurrence of extensive nitridation. In this approach, a quasi-flat Cr concentration profile was assumed at the end of the lifetime. Therefore, the calculated lifetime limits are dependent on the reservoir of Cr in the specimens which decreases with decreasing specimen thickness.

For getting a more precise description of the lifetime limits, a finite difference (FD) method was set-up to describe the subscale Cr concentration profiles of alloy 230 after long time oxidation in the studied temperature range 950 - 1050°C. This FD method allowed obtaining a more detailed correlation between the non-steady state oxidation kinetics as a result of scale spallation or "super-parabolic" oxide growth occurring with the subscale depletion kinetics. In the FD calculations an instantaneous Cr flux was used as the boundary condition for the calculations. This approach resulted in calculated subscale Cr profiles which showed very good agreement with the measured profiles. Therefore, the finite difference method for non-steady-state oxidation was used to calculate the lifetime of the alloy 230 specimens. The calculated values of lifetime for the alloy 230 specimens by the FD method were, as expected, generally shorter than the values calculated using the reservoir approach, however the actual differences between the critical times calculated by the two methods were not very significant.

After development of the lifetime diagram for alloy 230, a similar procedure was used to develop the same type of lifetime diagrams for the Ni base alloys X and NiCr 8020 as well as the austenitic steel Nicrofer 2020.

The as-received alloy X exhibited after exposure a microstructure which consisted of a γ-Ni matrix and M_6C carbide precipitates. After 3000 h oxidation at 1000°C, the thin (0.2 and 0.3 mm) specimens exhibited significant formation of nitride (π-phase) due to the ingress of N from the environment as well as a partial change of the oxidation of Cr from external to internal. Both observations indicated the loss of protective properties of the external chromia

scale. Far less substantial formation of nitride was observed in the thin specimens of alloy X after 2000 h oxidation at 1050°C, in spite of a very low level of subscale Cr concentration (about 5 wt. %). The phase diagram obtained by equilibrium calculations using Thermal-Calc showed that at 1050°C the nitride dissolved with decreasing Cr concentration in the alloy. At 950°C, no formation of nitride was observed even after 3000 h exposure because of the relatively small consumption of Cr in the alloy and thus maintenance of the protective scale properties.

A lifetime diagram for alloy X was constructed using the same procedures and criteria for evaluating the experimental results as done for alloy 230. The times to critical subscale Cr depletion were shorter than those for alloy 230, the main reason being the higher scale growth rate in case of alloy X. The difference in lifetime was especially pronounced for the 0.3 mm specimen at 1050°C because this tended to exhibit “super-parabolic” oxidation whereas in case of alloy 230 this was only observed for the thinnest specimen of 0.2 mm.

Alloy NiCr 8020 exhibited a single phase microstructure due to the lack of alloying additions such as W and/or Mo and especially because of the extremely low C content. Due to the lack of minor alloying additions of Al and Si hardly any internal oxidation occurred and thus the “undulated” alloy/scale interfaces typically formed on alloy 230 and X, were not found for NiCr 8020. The smooth alloy/scale interface on the latter alloy is believed to promote propagation of void related cracks along the interface, resulting in poor scale adhesion during cyclic oxidation. The poor creep resistance of the material has as result that oxide growth stresses and thermally induced stresses during cycling lead to plastic deformation of the alloy in the subsurface zones, accompanied by crack formation within the oxide scale. The steady-state oxide growth rate of the NiCr 8020 is smaller than that of alloys 230 and X, mainly due to the lack of Mn and Ti, i.e., elements which are known to enhance the growth rate of chromia during air oxidation. In spite of the lower growth rates the times t_{10} until occurrence of critical Cr interface concentrations were for alloy NiCr 8020 shorter than for alloy 230. This was mainly related to the poorer scale adherence and the lower initial Cr content of only 20 wt. %.

The oxidation kinetics of the austenitic steel Nicrofer 2020 was found to be significantly higher than that of the studied Ni-base alloys. The GDOES profiles showed substantial enrichments of Ti and Mn in the outer part of the chromia scale and characteristic concentrations of dissolved elements in the inner part of the scale. These distributions are in

accordance with the known pO_2 dependence of the solubility of these elements in chromia thus explaining the high growth rate of the surface scale. This high growth rate results in very low Cr interface concentrations during short term isothermal oxidation, the concentration decreasing with increasing temperature. During cyclic oxidation at 950°C and above, this results in very early breakaway oxidation of Nicrofer 2020. Only at 900°C, a long term growth of a protective chromia scale was sustained. Therefore, only a simplified lifetime diagram could be constructed for this material taking into account temperatures at and beneath 900°C.

The philosophy and significance of the used approach for the development of lifetime diagrams for chromia forming FCC materials is illustrated in **Figure S 1 a,** showing the results of alloy 230 at 1000°C as example. The loss of wall thickness is plotted as function of time using the data presented in Section 6.4 for the 0.5 mm specimen. Based on the results in Section 6.4.4, it was assumed that specimens with a thickness of 0.3 mm or more exhibit the same kinetics for scale spallation and re-healing. The times t_{10} for different specimen thicknesses were calculated using the procedure explained in Section 6.4.4. The results are compared with oxidation data of an alumina forming alloy (here the ODS alloy PM 2000) taken from reference [179]. The oxidation kinetics and estimated times to breakaway (the latter occurring after the Al content decreased from 5.2 to 1.2 wt. %) [179] for specimens of different thickness were re-calculated and transferred into a presentation as used in the Lifetime Diagrams developed in the present project.

Apart from the differences in absolute times to occurrence of critical depletion of scale forming element (Cr or Al) the figure clearly shows the fundamental difference when estimating design relevant oxidation damage of the two types of materials. For both material types the main lifetime criterion for the thinnest specimens (a few tenths of a mm) is the time for occurrence of “breakaway oxidation” due to critical Cr or Al depletion. For components of several mm thick, however, the chromia forming alloy 230 exhibits severe wall thickness loss and substantial amounts of spalled oxide (**Figure S 1 b**) before the critical Cr depletion at t_{10} is reached. For such components the lifetime considerations will in most cases not be governed by critical Cr depletion but by the extent of wall thickness loss and/or spalled oxide. For the selected alumina forming material, however, the loss in wall thickness and the amount of spalled oxide are still small if the time for critical Al depletion e.g. for a specimen of 3 mm thickness is reached.

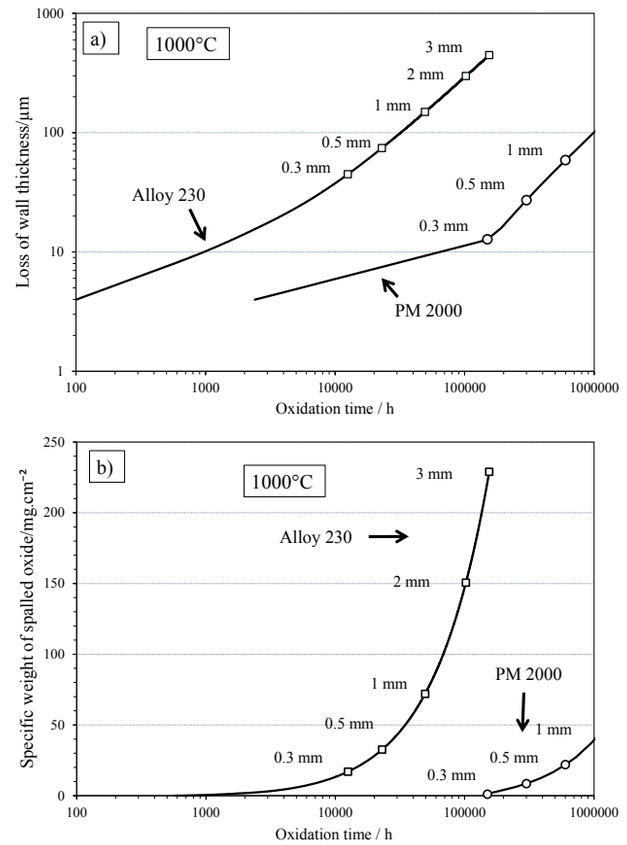

Figure S 1: Fig. a) shows the loss of wall thickness as function of time for alloy 230 at 1000°C. The data are derived from the results shown in **Figure 6.15** and extrapolated assuming that the kinetics of scale spalling and healing was independent of specimen thickness; thus, the "super-parabolic" oxidation observed for the thinnest (0.2 mm) specimen was ignored. Inserted symbols indicate calculated times t_{10} for specimens of 0.3, 0.5, 1, 2 and 3 mm. The results are compared with those for the alumina forming material PM 2000. Weight gain data for this alloy were taken from reference [179] and recalculated into the governing oxidation damage parameters used in the present study. Symbols indicate times to breakaway oxidation derived from [179] for specimens of different thickness. Fig. b) shows the specific weight of spalled oxide as a function of oxidation time corresponding to the calculated results shown in Fig. a).

The approach used to construct lifetime diagrams using time to breakaway as function of component thickness for various temperatures [21, 26, 32, 74] is thus for the alumina forming materials fully adequate. However, for the chromia forming FCC materials discussed in the present studies, this is obviously not the case.

The developed lifetime diagrams are thus believed to be very useful tools for taking oxidation induced damage into account in component design. The application of such diagrams might likely be extended if future developments would allow taking additional damage mechanisms, e.g. formation of volatile Cr species in rapidly flowing, water vapour rich gases, into account.

Bibliography

[1] M. J. Donachie and S. J. Donachie, Superalloys: A Technical Guide, 2nd Edition, ASM International, **2002**.

[2] N. Birks, G. H. Meier and F. S. Petit, Introduction to the High-Temperature Oxidation of Metals, Cambridge University Press, **2006**.

[3] INSG Insight, INSG Secretariat Briefing Paper, No.20, April 2013. [Online]. Available: http://www.insg.org/%5Cdocs%5CINSG_Insight_20_Nickel_Alloys_2013.pdf. [Accessed 09 September 2015]

[4] [Online]. Available: http://www.brookings.edu/blogs/techtank/posts/2015/08/06-engine-design-fuel-costs [Accessed 15 December 2015].

[5] H-H. Angermann, M. Brenner, H. Damsohn, K-G. Krumbach, K. Luz, C. Pfender and M. Watzlawski., *ATZ -Automobiltechnische Zeitschrift.* vol. 108, no. 5, pp. 382-389, **2006**.

[6] R. C. Reed, The Superalloys, Fundamentals and Applications, Cambridge University Press, **2006**.

[7] D. Naumenko, V. Shemet, L. Singheiser and W. J. Quadakkers, *Journal of Materials Science*, vol. 44, pp. 1687, **2009**.

[8] C. T. Sims, N. S. Stoloff and W. C. Hagel, Supperalloys II- High Temperature Materials for Aerospace and Industrial Power, New York: Wiley, **1987**.

[9] R. H. Cook, *Nucl. Technol.*, vol. 66, pp. 283, **1984**.

[10] H. M. Tawancy, *J. Mater. Sci*, vol. 27, pp. 6481, **1992**.

[11] B. Gleeson and M. A. Harper, *Oxidation of Metals*, vol. 49, pp. 373-99, **1998**.

[12] D. J. Young, High Temperature Oxidation and Corrosion of Metals, Oxford: Elsevier Corrosion Series, 1st Edition, **2008**.

[13] A. J. Strutt and K. S. Vecchio, *Metallurgical and Materials Transactions A*, vol. 30A, pp. 355-361, **1999**.

[14] A. Chyrkin, S. L. Schulze, J. Piron-Abellan, W. Bleck, L. Singheiser and W. J. Quadakkers, *Advanced Engineering Materials*, vol. 12, no. 9, pp. 873-883, **2010**.

[15] M. Schütze, *Oxidation of Metals*, vol. 44, nos. 1/2, pp. 29-61, **1995**.

[16] H. Nickel, P. J. Ennis and W. J. Quadakkers, *Mineral Processing and Extractive Metallurgy Review: An International Journal,* vol. 22, no. 1, **2001**.

[17] H. E. Evans and R. C. Lobb, *Corr. Sci.*, vol. 24, no. 3, pp.223-233, **1984**.

[18] C. E. Lowell, C. A. Barrett, R. W. Palmer, J. V. Auping and H. B. Probst, *Oxidation of Metals*, vol. 36 nos. 1/2, pp. 81-112, **1991**.

[19] J. L. Smialek, *Acta Materialia*, vol. 51, pp. 469-483, **2003**.

[20] D. Poquillon and D. Monceau, *Oxidation of Metals*, vol. 59, nos. 3/4, pp.409-431, **2003**.

[21] W. J. Quadakkers and K. Bongartz, *Materials and Corrosion*, vol. 45, pp. 232-241, **1994**.

[22] D. P. Whittle, *Corrosion Science*, vol. 12, pp. 869-872, **1972**.

[23] H. C. Cowen, S. J. Webster, in *B.N.E.S. International Conference on Corrosion of Steels in CO_2*, paper 28, pp. 349-358, **1974**.

[24] D. J. Young, A. Chyrkin and W. J. Quadakkers, *Oxidation of Metals*, vol. 77, pp. 253-264, **2012**.

[25] W. J. Quadakkers and M. J. Bennett, *Material Science and Technology*, vol. 10, pp. 126-131, **1994**.

[26] I. Gurrappa, S. Weinbruch, D. Naumenko and W. J. Quadakkers, *Materials and Corrosion,* vol. 51, pp. 224-235, **2000**.

[27] M. Shütze, W. J. Quadakkers and J. R. Nicholls, Lifetime Modeling of High Temperature Corrosion Processes, *Proceedings of an EFC Workshop*, G. Strehl, V. Guttmann, D. Naumenko et al., pp. 107-122, **2001**.

[28] M. Shütze, W. J. Quadakkers and J. R. Nicholls, Lifetime Modeling of High Temperature Corrosion Processes, *Proceedings of an EFC Workshop*, J. R. Nicholls, R. Newton, M. J. Bennett et al. pp. 83-106, **2001**.

[29] I. G. Wright, R. Peraldi and B. A. Pint, *Materials Science Forum*, vols. 461-464, pp. 579-590, **2004**.

[30] W. J. Quadakkers, D. Naumenko, E. Wessel, V. Kochubey and L. Singheiser, *Oxidation of Metals*, vol. 61, pp. 17-37, **2004**.

[31] B. A. Pint, L. R. Walker and I. G. Wright, *Materials at High Temperatures*, vol. 21, no. 3, pp. 175-185, **2004**.

[32] P. Huczkowski, N. Christiansen, V. Shemet, J. Piron-Abellan, L.Singheiser and W. J. Quadakkers, *Materials and Corrosion,* vol. 55, no. 11, pp. 825-829, **2004**.

[33] B. A. Pint, L. R. Walker and I. G. Wright, *Materials at High Temperatures*, vol. 26, no. 2, pp. 211-216, **2009**.

[34] I. G. Wright, B. A. Pint, L. M. Hall, P. F. Tortorelli; M. Shütze, W. J. Quadakkers and J. R. Nicholls, Lifetime Modeling of High Temperature Corrosion Processes, *Proceedings of an EFC Workshop*, pp. 358-339, **2001**.

[35] H. E. Evans and A. T. Donaldson, *Oxidation of Metals,* vol. 50, nos. 5/6, pp. 457-475, **1998**.

[36] H. E. Evans, A. T. Donaldson and T. C. Gilmour, *Oxidation of Metals*, vol. 52, nos. 5/6, pp. 379-402, **1999**.

[37] R. Bauer, M. Baccalaro, L. P. H. Jeurgens, M. Pohl and E. J. Mittemeijer, *Oxidation of Metals*, vol. 69, pp. 265-285, **2008**.

[38] J. A. Nesbitt, NASA-TM2000-209271.

[39] T. J. Nijdam, L. P. H. Jeurgens and W. J. Sloof, *Acta Mateliaria*, vol. 51. pp. 5295-5307, **2003**.

[40] W. M. Pragnell and H. E. Evans, *Modeling and Simulation in Material Science and Engineering,* vol. 14, pp. 733-740, **2006**.

[41] J. A. Nesbitt, *J. Electrochem. Soc.*, vol. 136, no. 5, pp. 1518-1527, **1989**.

[42] C. S. Tedmon, *Journal of the Electrochemical Society*, vol. 113, no. 8, pp. 766-768, **1966**.

[43] C. A. Barrett and A. F. Presler, NASA TN D-8132, **1976**.

[44] D. Wajszel, *Journal of the Electrochemical Society*, vol.10, no. 6, pp. 504-507, **1963**.

[45] C. E. Lowell, C. A. Barrett, R. W. Palmer, J. V. Auping and H. B. Probst, *Oxidation of Metals*, vol. 36, nos. 1/2, pp. 81-112, **1991**.

[46] J. L. Smialek and J. V. Auping, *Oxidation of Metals*, vol. 57, nos. 5/6, pp.559-581, **2002**.

[47] E. N¨dah, M. P. Hierro, K. Borrero and F. J. Perez, *Oxidation of Metals*, vol. 68, nos. 1/2, pp. 9-21, **2007**.

[48] J. L. Smialek, *Metallurgical Transaction A*, vol. 9A, pp. 309-320, **1978**.

[49] J. L. Smialek, *Acta Materialia,* vol. 51, pp. 469-483, **2003**.

[50] D. Poquillon, D. Oquab and D. Monceau, *Materials Science Forum*, vols. 461-464, pp. 737-746, **2004**.

[51] R. Orosz, U. Krupp, H.-J. Christ and D. Monceau, *Oxidation of Metal*, vol. 68, pp. 165–176, **2007**.

[52] “High Temperature Tech Brief” Haynes International, 2009. [Online]. Available: http://www.haynesintl.com/pdf/h3060.pdf. [Accessed 16 July 2015].

[53] W. J. Quadakkers, Materials in Energy Systems, *Manuscript in University of Applied Science Aachen/Jülich*, **2013**.

[54] [Online] http:/www.thermocalc.com.

[55] [Online] http:/www.factsage.com.

[56] S. C. Tsai, A. M. Huntz and C. Dolin, *Materials Science and Engineering*, vol. A212, pp. 6-13, **1996**.

[57] Z. Zeng, K. Natesan, Z. Cai, D. Gosztola, R. Cook and J. Hiller, *Journal of Materials Engineering and Performance*, vol. 23, no. 4, pp. 1247-1262, **2014**.

[58] H. M. Tawancy, *Oxidation of Metals*, vol. 45, no. 3/4, pp. 323-348, **1996**.

[59] S. Cruchley, H. E. Evans, M. P. Taylor, M. C. Hardy and S. Stekovic, *Corrosion Science*, vol. 75, pp. 58-66, **2013**.

[60] C. Wagner, *J. Electrochem, Soc.*, vol. 63, no. 7, pp. 772-782, **1959**.

[61] D. Kim, C. Jang and W. S. Ryu, *Oxidation of Metals,* vol.71, pp. 271-293, **2009**.

[62] C. Desgranges, F. Lequien, E. Aublant, M. Nastar and D. Monceau, *Oxidation of Metals*, vol. 79, pp. 73-105, **2013**.

[63] E. O. Kirkendall, *Transaction the Metallurgical Society of AIME*, vol. 147, pp. 104, 1942.

[64] A. H. Rosenstein, J. K. Tien and W. D. Nix, *Metallurgical Transaction A*, vol. 17A, pp. 151, **1986**.

[65] H. V. Atkinson, *Oxidation of Metals*, vol. 24, nos. 3/4, pp. 177-197, **1985**.

[66] M. T. Tinker and L. W. Hobbs, *Proceedings of the 39th Annual Meeting of Electron Microscopy Society of America*, G. W. Bailey, ed. (Claitor"s Publishing Division, Baton Rouge, pp. 86, **1981**.

[67] M. Michalik, M. Hänsel, J. Zurek, L. Singheiser and W. J. Quadakkers, *Materials at High Temperature*, vol. 22, pp. 213, **2005**.

[68] W. J. Quadakkers, H. Holzbrecher, K. G. Briefs and H. Beske, *Oxidation of Metals*, vol. 32, no. 1, pp. 67-88, **1989**.

[69] J. Jedlinski, *Materials at High Temperatures*, vol. 22, nos. 3/4, pp. 485-495, **2005**.

[70] H. E. Evans and R. C. Lobb, *Corrosion Science*, vol. 24, no. 3, pp. 209-222, **1984**.

[71] V. K. Tolpygo and D. R. Clarke, *Oxidation of Metals*, vol. 49, nos, 1/2, pp. 187-212, **1998**.

[72] W. W. Smeltzer and D. P. Whittle, *Journal of the Electrochemical Society*, vol. 125. no. 77, pp. 1116-1126, **1978**.

[73] W. J. Quadakkers and H. Viefhaus, "EFC workshop", in *Methods and Testing in high Temperature Corrosion*, Frankfurt, **1995**.

[74] P. Huczkowski, V. Shemet, J. Piron-Abellan, L. Singheiser, W. J. Quadakkers and N. Christiansen, *Materials and Corrosion*, vol. 55, no. 11, pp. 825-830, **2004**.

[75] B. D. Bastow, D. P. Whittle and G. C. Wood, *Oxidation of Metals*, vol. 12, no. 5, pp. 413-438, **1978**.

[76] P. Kofstad, Microscopy of Oxidation I, edited by M. J. Bennett and G.W. Lorimer, London: Institute of Metals, pp. 2-9, **1991**.

[77] B. A. Pint, *JOM*, pp. 42-43, **2009**.

[78] A. Agüero, V. Gonzalez, P. Mayr and K. Spiradek-Hahn, *Materials Chemistry and Physics*, vol. 141, pp. 432-439, **2013**.

[79] M. Machkova, A. Zwetanova, V. Kozhukharov and S. Raicheva, *Journal of the University of Chemical Technology and Metallurgy*, vol. 43, no. 1, pp. 53-58, **2008**.

[80] J. Ehlers, D. J. Young, E. J. Smaardijk, A. K. Tyagi, H. J. Penkalla, L. Sinheiser, et al., *Corrosion Sci*., vol. 48, pp.3428-3454, **2006**.

[81] H. Asteman, J-E. Svensson and L-G. Johansson, *Oxidation of Metals*, vol. 57, nos. 3/4, pp.11-26, **2002**.

[82] K. Segerdahl, J-E. Svensson and L-G. Johansson, *Corrosion Sci.*, vol. 44, pp. 2635-2649, **2002**.

[83] A. Yamauchi, K. Kurokawa and H. Takahashi, *Oxidation of Metals*, vol. 59, nos. 5/6, pp. 517-527, **2003**.

[84] E. J. Opila, *Mater. Sci. Forum,* vol. 461-464, pp. 765-774, **2004**.

[85] H. Asteman, J-E. Svensson, M. Norell and L-G. Johansson, *Oxidation of Metals*, vol. 54, nos. 1/2, pp. 11-25, **2000**.

[86] H. Asteman, J-E. Svensson, L-G. Johansson and M. Norell, *Oxidation of Metals*, vol. 52, nos. 1/2, pp.95-111, **1999**.

[87] C. Pettersson, T. Jonsson, C. Proff, M. Halvarsson, J-E. Svensson and L-G. Johansson, *Oxidation of Metals*, vol. 74, pp. 93-111, **2010**.

[88] M. Auchi, S. Hayashi, K. Toyota and S. Ukai, *Oxidation of Metals*, vol. 78, pp. 51-61, **2012**.

[89] D. M. England and A. V. Virkar, *Electrochem Soc*, vol. 148, pp. A330-338, **2001**.

[90] D. M. England and A. V. Virkar, *Electrochem Soc*., vol. 146, pp. 3196-3202, **1999**.

[91] N. Hussain, A. H. Qureshi, K. A. Shahid, N. A. Chughtai and F. A. Khalid, *Oxidation of Metals,* vol. 61, nos. 5/6, pp. 355-364, **2004**.

[92] N. Hussain, K. A. Shahid, I. H. Khan and S. Rahman, *Oxidation of Metals*, vol. 41, pp. 251-270, **1994**.

[93] G. R. Holcomb, *Oxidation of Metals*, vol. 69, pp.163-180, **2008**.

[94] G. R. Holcomb and D. E. Alman, *JMEPEG*, vol.15, pp. 394-398, **2006**.

[95] S. R. J. Saunders, M. Monteiro and F. Rizzo, *Progress in Materials Science*, vol. 53, pp. 775-837, **2008.**

[96] G. R. Holcomb, D. E. Alman, *Scripta Materialia*, vol. 54, no. 10, pp. 1821–1825, **2006**.

[97] B. A. Pint, *Transactions of ASME*, vol. 128, pp. 370-376, **2006**.

[98] W. J. Quadakkers, J. Piron-Abellan, V. Shemet and L. Singheiser, Mater. High Temp., vol. 20, pp. 115, **2003**.

[99] J. Zurek, M. Michalik, F. Schmitz, T. -U. Kern, L. Singheiser and W. J. Quadakkers, *Oxidation of Metal*, vol. 63, no. 5, pp. 401-422, **2005**.

[100] H. Asteman, J.-E. Svensson, L.-G. Johansson, *Oxidation of Metal*, vol. 57, no. 3, pp. 193-216, **2002**.

[101] A. V. Dean and P. J. Ennis, *Nucl. Technol.*, vol. 66, pp. 117, **1984**.

[102] W. R. Johnson, L. D. Thompson and T. A. Lechtenberg, Nucl. Technol., vol. 66, pp. 88-101, **1984**.

[103] Th**.** Malkow, W. J. Quadakkers, L. Singheiser and H. Nickel, *Report Forschungszentrum Jülich*, Jülich, FRG, Jül-3589, ISSN 0944-2952, **1998**.

[104] S. N. Basu, G. J. Yurek, *Oxid. Met.*, vol. 36, pp. 281-315, **1991**.

[105] G. J. Yurek, D. Eisen, A. Garratt-Reed, *Metall. Trans. A*, vol. 13A, pp. 473-485, **1982**.

[106] P. J. Ennis and W. J. Quadakkers, Conf. High Temperature Alloys – *Their Exploitable Potential*, JRC Petten, NL, 15-17th Oct 1985, Proceedings, Elsevier Applied Science London, New York, EUR 11365, J. B. Marriot, M. Merz**,** J. Nihoul and J. O. Ward (eds)**,** p. 465, **1987.**

[107] A. Naoumidis, H.A. Schulze, W. Jungen, P. Lersch and J. Eur, *Ceram. Soc.,* vol. 7, pp. 55-63, **1991**.

[108] M.G.C. Cox, B. McEnaney and V.D. Scott, *Phil. Mag.*, vol. 26, pp. 839, **1972**.

[109] J. Zurek, D. J. Young, E. Essumana, M. Hänsel, H. J. Penkalla, L. Niewolak and W. J. Quadakkers, *Materials Science and Engineering*, vol. A 477, pp. 259-270, **2008**.

[110] W. J. Quadakkers, *Materials Science and Engineering*, vol. 87, pp. 107-112, **1987**.

[111] R. Pillai, H. Ackermann and K. Lucka, *Corrosion Science*, vol. 69, pp. 181, **2013**.

[112] H. Ackermann, G. Teneva-Kosseva, H. Köhne, K. Lucka, S. Richter and J. Mayer, *Materials and Corrosion*, vol. 59, pp. 380, **2008**.

[113] D. P. Whittle, J. Stringer, *Phil. Trans. R. Soc. Lond,* vol. 295, no. 1413, pp. 309-329, **1980**.

[114] D. P. Moon, *Materials Science and Technology*, vol. 5, pp. 754-764, **1989**.

[115] P. Hou and J. Stringer, *Oxidation of Metals*, vol. 38, pp. 323, **1992**.

[116] F. Golightly, H. Stott and G. Wood, *Oxidation of Metals*, vol. 10, no. 3, pp. 163, 1976.

[117] B. A. Pint, *Oxidation of Metals*, vol. 45, nos. 1/2, pp. 1-37, **1996**.

[118] B. A. Pint, A. J. Garratt-Reed and L. W. Hobbs, *Materials at High Temperature*, vol. 13, no. 1, pp. 3-16, **1995**.

[119] “Hastelloy X technical data” [Online]. Available: http://www.hightempmetals.com/techdata/hitempHastXdata.php. [Accessed 20 August 2015]

[120] [Online]. Available: http://en.wikipedia.org/wiki/Nichrome. [Accessed 20 August 2015]

[121] “Bänder von ThyssenKrupp VDM” [Online]. Available: www.thyssenkruppvdm.com. [Accessed 20 Jan 2013]

[122] H. C. Graham and H. H. Davis, *J. Am. Ceram. Soc.*, vol. 54, pp. 89, **1971**.

[123] D. Young and B. A. Pint, *Oxidation of Metals*, vol. 66, pp. 137, **2006**.

[124] “MNX-MEMS and Nanotechnology Exchange” [Online]. Available: http://www.memsnet.org/material/chromiumoxidecr2o3bulk/?keywords=chromium%20oxide. [Accessed 08 July 2015].

[125] H. Evans, *Int. Mater. Rev.*, vol. 40, pp. 1-40, **1995**.

[126] W. J. Quadakkers, P. Huczkowski, D. Naumenko, J. Zurek, G. H. Meier, L. Niewolak and L. Singheiser, *Mater. Sci. Forum*, vol. 595-598, pp. 1111-1118, **2008**.

[127] J. Zurek, G. H. Meier, E. Essuman, M. Hänsel, L. Singheiser and W. J. Quadakkers, *J. Alloys Compd.*, vol. 467, pp. 450, **2009**.

[128] W. J. Quadakkers and L. Singheiser, *Mater. Sci. Forum.*, vol. 369, pp. 77, **2001**.

[129] S. Osgerby, K. Berriche-Bouhanek and H. E. Evans, *Mater. Sci. Eng.*, vol. A412, pp. 182, **2005**.

[130] A. Baldan, *J. Mater. Sci.*, vol. 37, pp. 2171-2202, **2002**.

[131] D. L. Klarstrom and G. Y. Lai, *Proceedings 6th International Symposium on Superalloys*, Seven Spring, PA, Sept. 18-22, **1988**.

[132] D. L. Klarstrom, *Corrosion*, vol. 407, pp. 1-12, **1994**.

[133] L. Jiang, R. Hu, H. Kou, J. Li, G. Bai and H. Fu, *Mater. Sci. Eng.*, vol. A536, pp. 37, **2012**.

[134] P. Subramanya Herle, M. S. Hegde, K. Sooryanarayana, T. N. Guru Row and G. N. Subbanna, *J. Mater. Chem.*, vol. 8, pp. 1435, **1998**.

[135] V. Gavriljuk and H. Berns, High Nitrogen Steels, Structure, Properties, Manufacture, Applications, Berlin: Springer, **1999**.

[136] C. S. Giggins and F. S. Pettit, *J. Electrochem. Soc.*, vol. 118, pp. 1782, **1971**.

[137] "Thermo-Calc Database Guide", [Online]. Available: http://www.mie.uth.gr/ekp_yliko/TC_Database_Guide.pdf. [Accessed 10 June 2015].

[138] A. Chyrkin, P. Huczkowski, V. Shemet, L. Singheiser and W. J. Quadakkers, *Oxidation of Metals*, vol. 75, pp. 143, **2010**.

[139] P. J. Ennis, W. J. Quadakkers and H. Schuster, *Mater. Sci. Technol.*, vol. 8, pp. 78, **1992**.

[140] R. Pillai, H. Ackermann, H. Hattendorf and S. Richter, *Corros, Sci.*, vol. 75, pp. 28, **2013**.

[141] K. Ledjeff, A. Rahmel and M. Schorr, *Werkst. Korros.*, vol. 30, pp. 767, **1979**.

[142] P. Berthod, C. Vebert, L. Aranda, R. Podor and C. Rapin, *Oxidation of Metals*, vol. 63, pp. 57, **2005**.

[143] R. Petkovic-Luton and T. A. Ramanarayanan, *Oxidation of Metals*, vol. 34, pp. 381, **1990**.

[144] A. Chyrkin, R. Pillai, H. Ackermann, H. Hattendorf, S. Richter, W. Nowak, D. Grüner and W. J. Quadakkers, Corros. Sci., vol. 96, pp. 32, **2015**.

[145] W. J. Quadakkers, *Mat. Sci. Eng.*, vol. 87, pp. 107, **1987**.

[146] B. Fernandez, N. Bordel, R. Pereiro, A. Sanz-Medel and J. Anal, *Atom. Spectrom.*, vol. 18, pp. 151-156, **2003**.

[147] F. Präßler,V. Hoffmann, J. Schumann, K. Wetzig, *Fresenius J. Anal. Chem*., vol. 355, pp. 840-846, **1996**.

[148] W. J. Quadakkers, A. Elschner, Q. Speier and H. Nickel, *Appl. Surf. Sci.*, vol. 52, pp. 271, **1991**.

[149] "MNX-MEMS and Nanotechnology Exchange" [Online]. Available: http://www.memsnet.org/material/nickelnibulk/?keywords=nickel. [Accessed 08 July 2015].

[150] P. Villars, "Material Phases Data System (MPDS)", Springer Verlag GmbH, Heidelberg, 2014. [Online]. Available: http://materials.springer.com/isp/crystallographic/docs/sd_0540673. [Accessed 09 July 2015].

[151] P. Villars, "Material Phases Data System (MPDS)", Springer Verlag GmbH, Heidelberg, 2014. [Online]. Available: http://materials.springer.com/isp/crystallographic/docs/sd_1008647. [Accessed 09 July 2015].

[152] H. S. Carslaw and J. C. Jaeger, Conduction of Heat in Solids, Oxford, Clarendon Press, **1959**.

[153] C. Asensio-Jimenez, L. Niewolak, H. Hattendorf, B. Kuhn, P. Huczkowski, L. Singheiser and W. J. Quadakkers, *Oxidation of Metals*, vol. 79, pp. 15-28, **2013**.

[154] C. Zhu, X. Zhao, I. S. Molchan, G. E. Thompson, G. Liang and P. Xiao, *Materials Science and Engineering A*, vol. 528, pp. 8687-8697, **2011**.

[155] H. E. Evans and M. P. Taylor, *Surface and Coatings Technology*, vols.94-95, pp. 27-33, **1997**.

[156] J. Jedlinski, M. J. Bennett and H. E. Evans, *Workshop on mechanical properties of protective oxide scales*, Teddington Mddx. Royaume-Uni, **1994**.

[157] M. Brunner, M. Bensch, R. Völkl, E. Affeldt and U. Glatzel, *Materials Science and Engineering A*, vol. 550, pp. 245-262, **2012**.

[158] C. A. Barrett and C. E. Lowell, *Oxidation of Metals*, vol. 9, no. 4, pp. 308-355, 1975.

[159] M. N. Özisik, Finite Difference Methods in Heat Transfer, CRC Press, **1994**.

[160] V. C. Walton, Applications of a General Finite-Difference Method for Calculating Bending Deformations of Solid Plates, NASA, **1960**.

[161] J. Crank, The Mathematics of Diffusion, Oxford University Press, **1975**.

[162] E. W. Hart, *Acra. Met. Metall.*, vol. 5, pp. 597, **1957**.

[163] W. W. Smeltzer, R. R. Haering and J. S. Kirkaldy, Acta. Metall., vol. 9, pp. 880, **1961**.

[164] G. Gottstein, Physical Foundations of Materials Science, Springer Press, **2005**.

[165] W. J. Quadakkers, Werkstoffe und Korrosion, vol. 36, pp. 335-347, **1985**.

[166] “Haynes 230 Technical Data”. [Online]. Available: http://www.hightempmetals.com/techdata/hitempHaynes230data.php. [Accessed 16 Jan 2016].

[167] C. Xu, W. Gao, *Met. Res. Innovat.*, vol. 3, pp. 231-235, **2000**.

[168] V. K. Tolpygo, J. R. Dryden and D. R. Clarke, *Acta Mater.*, vol. 46, no. 3, pp. 927-937, **1998**.

[169] D.R. Clarke, *Acta Mater.*, vol. 51, pp. 1393-1407, **2003**.

[170] R. W. Evans and B. Wilshire, Introduction to Creep, The Institute of Materials, London, **1985**.

[171] B.A. Pint, P.F. Tortorelli, I.G. Wright, *Oxidation of Metals*, vol. 58, no. 1, pp. 73-101, **2002**.

[172] M. Schiek, L. Niewolak, W. Nowak, G. H. Meier, R. Vaßen, W. J. Quadakkers, *Oxidation of Metals*, vol. 84, pp. 661-694, **2015**.

[173] A. Chyrkin, W. G. Sloof, R. Pillai, T. Galiullin, D. Grüner, L. Singheiser and W. J. Quadakkers, *Materials at High Temperatures*, vol. 32, pp. 102, **2015**.

[174] P. Huczkowski, S. Ertl, J. Piron-Abellan, N. Christiansena, T.Höfler, V. Shemet, L. Singheiser and W.J. Quadakkers, *Materials at High Temperatures*, vol. 22, no 3-4, **2005**.

[175] D. Naumenko, V. Shemet, L. Singheiser, W. J. Quadakkers, *Journal of Materials Science*, vol. 44, no. 7, pp 1687-1703, **2009**.

[176] Z. Tökei, K. Hennesen, H. Viefhaus, H. Grabke, *Mater. Sci. Technol.*, vol. 16, pp. 1129, **2000**.

[177] T-F. Chen, G. P. Tiwari, Y. Iijima and K. Yamauchi, *Materials Transactions*, vol. 44, no. 1, pp. 40-46, **2003**.

[178] W. Bleck (ed.), Materials Science of Steel-Textbook for RWTH Students, Department of Ferrous Metallurgy Aachen University, Aachen: Mainz, **2007**.

[179] D. Naumenko, Ph. D thesis, RWTH Aachen University, **2001**.

Schriften des Forschungszentrums Jülich
Reihe Energie & Umwelt / Energy & Environment

Band / Volume 361
Calibration and large-scale inversion of multi-configuration electromagnetic induction data for vadose zone characterization
C. von Hebel (2017), ix, 123 pp
ISBN: 978-3-95806-210-8

Band / Volume 362
Process-based modelling of regional water and energy fluxes taking into account measured neutron intensities by cosmic-ray probes
R. Baatz (2017), xvi, 135 pp
ISBN: 978-3-95806-211-5

Band / Volume 363
Quantitative Analyse der Lithiumverteilung in Kathoden- und Elektrolyt-Dünnschichten für Festkörperbatterien
C. Dellen (2017), vi, 161 pp
ISBN: 978-3-95806-214-6

Band / Volume 364
Intragruppentrennung Seltener Erden mittels neuer phosphororganischer Liganden
S. Hadić (2017), VIII, 164 pp
ISBN: 978-3-95806-215-3

Band / Volume 365
Automated Magnetic Divertor Design for Optimal Power Exhaust
M. Blommaert (2017), xxiv, 220 pp
ISBN: 978-3-95806-216-0

Band / Volume 366
PEM-Elektrolyse-Systeme zur Anwendung in Power-to-Gas Anlagen
G. Tjarks (2017), IV, 135 pp
ISBN: 978-3-95806-217-7

Band / Volume 367
Fundamental Insights into the Radium Uptake into Barite by Atom Probe Tomography and Electron Microscopy
J. Weber (2017), IX, 160 pp
ISBN: 978-3-95806-220-7

Band / Volume 368
Entwicklung von elektronenleitenden Schutzschichten gegen die anodische Auflösung von Stromsammlern in neuartigen „Dual-Ionen“-Energiespeichern
G. Teucher (2017), VIII, 120 pp
ISBN: 978-3-95806-222-1

Schriften des Forschungszentrums Jülich
Reihe Energie & Umwelt / Energy & Environment

Band / Volume 369
Herstellung und Charakterisierung oxiddispersionsverstärkter Haftvermittlerschichten
J. Bergholz (2017), V, 133, II pp
ISBN: 978-3-95806-223-8

Band / Volume 370
Performance of Plasma Facing Materials under Thermal and Plasma Exposure
I. Steudel (2017), XVI, 150 pp
ISBN: 978-3-95806-226-9

Band / Volume 371
The Impact of Transient Thermal Loads on Beryllium as Plasma Facing Material
B. Spilker (2017), XII, 134 pp
ISBN: 978-3-95806-227-6

Band / Volume 372
Analysis and Simulation of Macroscopic Defects in Cu(In,Ga)Se_2 Photovoltaic Thin Film Modules
B. Misic (2017), iv, 147 pp
ISBN: 978-3-95806-228-3

Band / Volume 373
Chemical and physical properties of sodium ionic conductors for solid-state batteries
M. Guin (2017), ix, 126 pp
ISBN: 978-3-95806-229-0

Band / Volume 374
Prediction of Oxidation Induced Life Time for FCC Materials at High Temperature Operation
R. Duan (2017), vi, 180 pp.
ISBN: 978-3-95806-230-6

Weitere ***Schriften des Verlags im Forschungszentrum Jülich*** unter
http://wwwzb1.fz-juelich.de/verlagextern1/index.asp

Energie & Umwelt
Energy & Environment

374

Oxidation induced lifetime prediction for FCC

Ran Duan

Mitglied der Helmholtz-Gemeinschaft

JÜLICH
FORSCHUNGSZENTRUM

Prediction of Oxidation Induced Life Time for FCC Materials at High Temperature Operation

Ran Duan

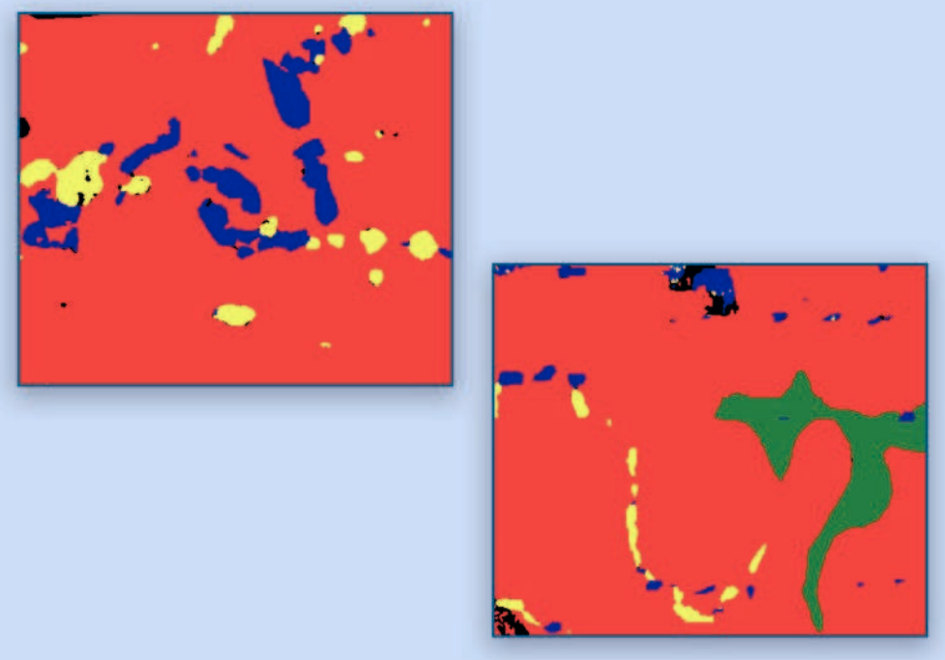

Energie & Umwelt /
Energy & Environment
Band / Volume 374
ISBN 978-3-95806-230-6

JÜLICH
FORSCHUNGSZENTRUM

Energie & Umwelt /
Energy & Environment
Band / Volume 374
ISBN 978-3-95806-230-6

JÜLICH
FORSCHUNGSZENTRUM